HYPOXIA-MEDIATED CHANGES IN THE MICROGLIAL PHENOTYPE OF AGE-ASSOCIATED WHITE MATTER LESIONS AND A ZEBRAFISH MODEL

Dissertation by

Taghreed Saud M. Almansouri

The University Of Sheffield.

In Partial Fulfillment of the Requirements

For the Degree of Doctor of Philosophy of Neuroscience

Sheffield Institute for Translational Neuroscience – SITraN

The Medical School - University of Sheffield

November 2022

ABSTRACT

Introduction:

Age-associated white matter lesions (WML) are a common feature of the ageing brain, and an independent risk factor for dementia. Deep subcortical lesions (DSCL) are associated with chronic cerebral hypoperfusion resulting in a hypoxic environment, and are characterised by high levels of microglia with an amoeboid phenotype, suggesting that sustained activation of the hypoxia-inducible factor (HIF) signalling pathway modifies the microglial phenotype. We hypothesised that the hypoxic environment of DSCL drives the microglia to a pro-inflammatory phenotype which contribute to lesion pathogenesis. The aims of this project were:

1. To characterize the transcriptomic profile of microglia in DSCL and the surrounding radiologically normal-appearing white matter (NAWM) compared to the non-lesional control white matter
2. To perform a detailed characterisation of the microglial response associated with hypoxia in *vhl*$^{-/-}$ zebrafish, a model which displays up-regulated hypoxic signalling

Methods:

CD68^{+} microglia were isolated from post-mortem white matter regions of interest by immuno-laser capture microdissection. The transcriptomic profile was attempted using the RNA-seq; it was then assessed using Human Clariom S Arrays. Within the WM groups, genes were considered significantly differentially expressed if they had a fold change ≥ of ±1.2 and a p-value <0.05. The datasets were interrogated using DAVID to identify significantly altered functional groups and pathways. Immunohistochemistry was performed to validate gene expression changes at the protein level.

In order to exploit the *in vivo* imaging capabilities of zebrafish, microglial morphology in response to sustained HIF signalling was characterised in double transgenic *vhl* $^{hu2117/+}$ *(mpeg1::mCherryCAAX, phd3::GFP)* line for both *vhl* $^{-/-}$ mutant larvae and its wildtype sibling via high-resolution confocal microscopy. Both pro- and

anti-inflammatory cytokines were assessed at basal level and in post-wounded larvae using qPCR.

Results:

RNAseq is incompatible with low-quality and highly degraded RNA extracted from the immuno-LCM samples.. Microarray profiling of microglia in DSCL compared to non-lesional control white matter identified 181 differentially expressed genes. Functional clustering analysis identified dysregulation of haptoglobin-haemoglobin binding (Enrichment score 2.15, p=0.017), supported by increased levels of CD163 as characterized by immunostaining. In the microglia from NAWM versus control white matter, functional clustering analysis identified significant dysregulation of protein de-ubiquitination (Enrichment score 5.14, p<0.0001).

At 5 and 7 dpf, there was a sustained significant increase in microglia number and morphology changes within the *vhl* $^{-/-}$ larvae relative to their siblings. The pro- and anti-inflammatory cytokine levels were comparable in the ZF genotypes.

Conclusions:

The post-mortem microarray findings reveal complex roles for microglia within the DSCL, suggesting a potential neuroprotective role for microglia in DSCL. In contrast, the NAWM findings indicate that microglial dysfunction may contribute to lesion spread.

At 5 and 7dpf, microglia in the *vhl* $^{-/-}$ display a similar morphology to those in age-associated DSCL. The activation of HIF as a result of the loss of *vhl* does not affect cytokine mRNA levels in the ZF brain.

ACKNOWLEDGEMENTS

First and foremost, thank you, my Almighty Allah, for the countless blessings and all I have achieved. I would greatly like to thank all those who helped me complete this research, especially the Faculty of Applied Medical Science at King Abdulaziz University, for funding my scholarship.

I would like to express my deepest appreciation to my supervisors, Dr Julie Simpson and Dr Fredericus van Eeden, who believed in my work and for their continuous support, encouragement, and guidance. Working with them was inspiring, enthusiastic, and full of outstanding achievements. I extend my thanks to their laboratory groups, who supported me throughout my experiments and became my good friends.

I had the great pleasure of working with Noemie Hamilton, Deepak Ailani, Pamela Ellis, Paul Heath, Dirk Sieger, Julie Mazzolini, Sue Clark and Nicholas J Van Hateren; I gratefully acknowledge their assistance and advice that contributed to my research. My sincere thanks also go to the committee members, Dr Paul Kasher and Dr Janine Kirby, for their insightful suggestions and feedback.

My deepest heartfelt gratitude to my angels, Siba, Hashim, and Shaden, who have joined me during my PhD journey and made it enjoyable in their unique way; they are the reason for my smile every day. A special mention to Shaden, who arrived in the world three months before thesis submission; I consider her the spirit of this thesis. Thanks to my better half, Hussein Alattas, for his endless support and being there for me during the most challenging stages of the PhD.

Infinite love and gratitude to my parents (Badiah and Saud) for their unlimited love, support and inspiration; words cannot thank you enough. May Allah reward you for everything. Heartfelt gratitude to my brothers, sisters, nephews and nieces for taking care of me and supporting me ever since.

I am deeply indebted to myself, Taghreed; thank you for completing this journey and making me proud.

Thank you to all of my friends here in Sheffield, especially Motaz Fadul, Eleanor Markham, Wafa Bamofleh, Marrwa Alasharif, Sara Bin Mahfoz, Tarub Bin shahlan, Arwa Abugabel, Fayza Alahmadi, Malak Algamdi, and Sondus Hajuj; I wish them all the best in their future.

TABLE OF CONTENTS

LIST OF ABBREVIATIONS

Ab	Antibody
ABC-HRP	Avidin-biotinylated complex-horse radish peroxidase
AD	Alzheimer's Disease
ALS	Amyotrophic Lateral Sclerosis
ASR	Aquatic surface respiration
ATP	Adenosine triphosphate
Aβ	Amyloid Beta
BBB	Blood brain barrier
BDNF	Brain-derived Neurotrophic Factor
CAA	Cerebral Amyloid Angiopathy
CD163	CD163 molecule, Scavenger Receptor Cysteine-Rich Type 1 Protein
CD74	histocompatibility antigen gamma chain
CD80	Cluster of differentiation 80, B7-1
CD86	Cluster of differentiation 86, B7-2
CFAS	Cognitive Function and Ageing Study
CNS	Central Nervous System
CSF	Cerebrospinal Fluid
CT	Computed Tomography
DAB	3,3'-Diaminobenzidine tetrahydrochloride
DAVID	Database for Annotation Visualisation and Integrated Discovery
dH2O	Distilled water
DNA	Deoxyribonucleic acid
dpf	Day post fertilisation
DSCL	Deep Subcortical Lesion
ds-DNA	Double Stranded Deoxyribonucleic acid
dT	Oligonucleotide
EVs	Extracellular vesicles
FC	Fold Change
FU	Fluorescence unit
GABA	Gamma-Aminobutyric Acid
GFP	Green Fluorescence Protein
H&E	Haematoxylin and eosin
H2O2	Hydrogen Peroxide
Hb	Haemoglobin
HBA	Haemoglobin α subunit
HBB	Haemoglobin β subunit
Hb-Hp	Haemoglobin-haptoglobin complex
HIF	Hypoxia Inducible Factor
Hp	Haptoglobin
hpf	Hours post fertilisation
hpi	Hours post injury

Hrs	Hours
HVR	Hypoxic ventilatory response
Iba-1	Ionized calcium-binding Adaptor Molecule 1
ICH	Intracerebral haemorrhage
IFN-γ	Interferon Gamma
IgG	Immunoglobulin G
IHC	Immunohistochemistry
IL	Interleukin
LCM	Laser Capture Microdissection
LFB	Luxol Fast Blue
LSM	Light-sheet microscopy
MHC-II	Major Histocompatibility Class II
min	Minutes
MRI	Magnetic Resonance Imaging
mRNA	Messenger RNA
Ms	Multiple sclerosis
MTZ	Metronidazole
n/a	Not available
NAWM	Normal Appearing White Matter
NTR	Bacterial nitroreductase-expressing transgenic
PD	Parkinson's disease
PI	Propidium iodide
PM	Post Mortem
PVL	Periventricular Lesion
QC	Quality control
qPCR	Quantitative Polymerase Chain Reaction
RNA-Seq	Ribonucleic acid-Sequencing
ROS	Reactive Oxygen Species
RT	Room Temperature
ss-cDNA	Single Stranded cDNA
SVD	Small Vessel Disease
TBI	Traumatic brain injury
tg	Transgenic
TGF-β	Transforming Growth Factor-Beta
TNF- α	Tumour Necrosis Factor α
USP	Ubiquitin Specific Protease
USP17	Ubiquitin specific peptidase 17
VaD	Vascular Dementia
VHL	Von Hippel Lindau
Vs	Versus
WM	White Matter
WMC	White Matter Change
WMH	White Matter Hyperintensities
WML	White Matter Lesion

WT	Wildtype sibling
µl	Microliter
µm	Micrometre

LIST OF FIGURES

LIST OF TABLES

Declaration

I, Taghreed Almansouri, confirm that the Thesis is my own work. I am aware of the University's Guidance on the Use of Unfair Means (*www.sheffield.ac.uk/ssid/unfair-means*). This work has not been previously been presented for an award at this, or any other, university.

Poster and Flash talk presentations

- ZDM15 (September, 2022)
- ARUK (March, 2022)
- ARUK-dementia network (November, 2021)
- Yorkshire - ARUK (May, 2021)
- ARUK (March, 2019)

Chapter 1 **Introduction**

Age-associated white matter lesions (WML) are recognised as hyperintensities on T2-weighted magnetic resonance imaging (MRI) scans (Prins and Scheltens, 2015, Moscoso et al., 2020). Different terminologies equivalent to WML are used in the literature, including white matter changes (WMC) and white matter hyperintensities (WMH). The Greek descriptive, Leukoaraiosis, refers to the lesion's hypointensities on computed tomography (CT) scans, where 'leuko' means 'white' and 'araiosis' means 'rarefaction' (Hachinski et al., 1986). In the current study, the terminology WML will be used to refer to these hyperintensities.

1.1 Age-Associated White Matter Lesions: Classification and clinical manifestations

Neuropathological post-mortem studies of ageing population-representative cohorts, such as the Cognitive Function and Ageing Study (CFAS), show that WML are commonly observed in individuals aged 65 and above (Fadul et al., 2020, Esiri et al., 2001). Based on their anatomical location, WML are classified into two major categories: the periventricular white matter lesions (PVL) which are located adjacent to the ventricles and the deep subcortical lesions (DSCL) which occur distant from the ventricles (Prins and Scheltens, 2015), as shown in Figure 1.1. Population-representative cohort studies indicate that the prevalence of PVL is 90% among the ageing population. In contrast, DSCL are found in 60% of the aged population (De Groot et al., 2002, Fernando et al., 2004a).

Discrete WML tend to spread and become confluent, however, whether this is specific for a subclass of either PVL or DSCL or both is currently unknown (Barkhof et al., 2006).

The age-associated WML are associated with neurological diseases, such as Alzheimer's disease (AD) (Lee et al., 2016) and dementia (Fernando et al., 2004b, Hu et al., 2021). In ageing population studies, vascular pathologies (including WML) were reported in 84% of patients with dementia compared to 71% of non-demented patients (Matthews et al., 2009). The clinical manifestation associated with WML include the impairment of subcortical frontal function, psychiatric disorders including depression (O'brien et al., 1996, Lee et al., 2015), balance disturbance (Baezner et al., 2008, Veselý et al., 2016) , cardiovascular diseases (Verhaaren et al., 2013), cerebrovascular diseases (Kim et al., 2008), and gait dysfunction (de Laat et al., 2010, Rosario et al., 2016).

Cognitive decline is a common clinical feature in people with WML, however the lesion-types involved in cognitive deterioration are debated (Griffanti et al., 2016). While some ageing population-representative studies have linked cognitive impairment directly to PVL (Gupta et al., 1988, de Groot et al., 2000), others report that cognitive decline correlates with an extension of WML to areas of the white matter immediately underlying cortex, and not exclusively PVL (Damian et al., 1994), while yet other studies have shown similar impacts on cognitive function associated with both PVL and DSCL (Burns et al., 2005).

WML are associated with dementia and cognitive decline in the ageing population, where the WML volumes are proportionally related to the risk of cognitive decline and

dementia (Prins and Scheltens, 2015). In fact, WML are a significant independent risk factor for dementia (Fernando et al., 2004b, Matthews et al., 2009).

The most common risk factor for the formation of WML is ageing (Garnier-Crussard et al., 2020). However, several predictive factors correlate with the progression of the WML, including cardiovascular disease, hypertension (Verhaaren et al., 2013, Zhao et al., 2015, Zhao et al., 2019), and smoking (Garnier-Crussard et al., 2020).

1.2 Mechanisms Underlying the Pathogenesis of WML

Several theories have been proposed for the mechanisms underlying the pathogenesis of WML , including chronic cerebral hypoperfusion giving rise to a hypoxic environment (Tomimoto et al., 2003, Duncombe et al., 2017), dysfunction of the blood-brain barrier (BBB) causing extravasation (Simpson et al., 2007, Freeze et al., 2020) and accumulation of plasma proteins which trigger an inflammatory response, and overlying cortical pathology (Leys et al., 1991, Huang et al., 2007, McAleese et al., 2017) leading to Wallerian degeneration and demyelination and underlying WML formation (Wharton et al., 2015). However, the exact mechanism(s) remains unknown.

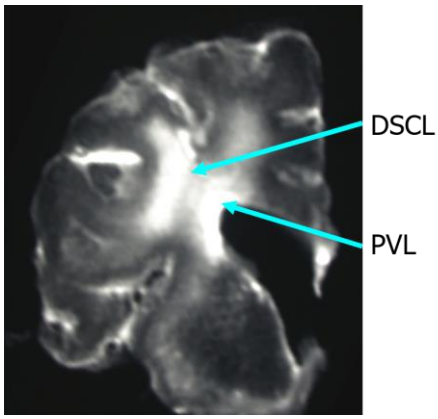

Figure 1.1 - MRI detection of age-associated white matter lesions. T2-weighted resonance imaging of a formalin-fixed post-mortem coronal brain slice. WML appear as hyperintensities, and classified according to their anatomical locations; the PVL and DSCL are identified with arrows, PVL: Periventricular lesions; DSCL: Deep subcortical lesions.

1.2.1 Hypoperfusion/ Hypoxia Hypothesis

The occurrence of age-associated WML is increased in patients with vascular risk factors such as hypertension, hyperlipidaemia and a history of stroke (van Dijk et al., 2008, Sonohara et al., 2008, Rastogi et al., 2021). The cognitive decline in patients with WML relates to cerebral small vessel disease (SVD) (Prins and Scheltens, 2015). It has been suggested that a reduction in cerebral blood flow results in cerebral hypoperfusion and gives rise to a hypoxic environment causing tissue damage, which underlies the pathogenesis and progression of WML in the ageing brain (Prins and Scheltens, 2015, Wong et al., 2019).

Several lines of evidence support the role of hypoxia as a mechanism of white matter damage. Histological characterisation of vessels in WML has demonstrated thickening of arterioles, perivascular widening, capillary loss and perivenous collagenosis, suggesting vascular insufficiency and cerebral hypoperfusion underlie lesion pathogenesis (Brown et al., 2009, Prins and Scheltens, 2015). Further evidence for the role of hypoxia includes the increased expression and nuclear translocation of hypoxia-inducible transcription factors (HIF-1α and HIF-2α), and expression of the hypoxia-associated proteins they regulate, including matrix metalloproteinase-7 (MMP7) and vascular endothelial growth factor (VEGFR2) (Fernando et al., 2006, Sosa and Smith, 2017).

Cerebral hypoperfusion and hypoxia are features of both WML subtypes but are predominantly associated with the DSCL compared to PVL (Fernando et al., 2006), and are associated with the increased nuclear translocation of HIF-α and microglial activity

within the DSCL (Kaelin Jr, 2008). These differences may reflect differences in the vascular supply to these regions (Auriel et al., 2012). The periventricular white matter is supplied by long, penetrating arterioles forming a watershed area. In contrast, the deep subcortical WM is supplied by medullary arteries, which are more prone to arteriolosclerosis and vascular changes and hence more likely to result in hypoperfusion and hypoxia (Xiong and (Xiong and Mok, 2011, Sosa and Smith, 2017).

In a rat model of cerebral hypoperfusion, where hypoxia is induced via bilateral occlusion of the common carotid artery (Washida et al., 2019), the model exhibits cognitive decline in addition to white matter pathology, similar to the human cerebral WML (Farkas et al., 2004). These findings support the proposed role of hypoxia and hypoperfusion underlying the development of age-associated WML (Schachtele et al., 2014, Fernando et al., 2006).

1.2.2 Blood-Brain Barrier (BBB) dysfunction

The blood-brain barrier (BBB) is a highly selective, semi-permeable barrier formed by fenestration-free cerebral endothelial cells that are held together by tight junction proteins (TJP), the basement membrane and astrocyte endfeet (Lin et al., 2017, Bai et al., 2018). The barrier is essential to maintain homeostasis within the central nervous system (CNS) by acting as a regulator interface for the bidirectional movement of molecules (Yang et al., 2018). Disruption of the BBB is commonly associated with the ageing process and neurodegenerative diseases, and is characterised by the loss of TJP (Jalal et al., 2015). The loss of TJP has been reported in both WML and radiologically normal-appearing white

matter (NAWM); suggesting that WM pathology extends beyond the WML and into the surrounding NAWM (Farrall and Wardlaw, 2009, Topakian et al., 2010).

The correlation between WML and BBB dysfunction has been demonstrated in both post-mortem human and animal studies (Ueno et al., 2002, Lin et al., 2017). Post-mortem studies of age-associated WML have exhibited increasing permeability of the BBB characterised by the accumulation of plasma proteins, such as albumin, thrombin, and fibrinogen in the cerebral parenchyma and elevation of the CSF/serum albumin ratio (Lin et al., 2017). Extravasation of these proteins may promote inflammatory processes and/or cause oedema leading to hypoperfusion (Winkler et al., 2014, Kalaria, 2018).

While several lines of evidence support the role of BBB dysfunction in the pathogenesis of age-associated WML, it should be noted that there are conflicting reports in the literature including an MRI study suggesting that BBB dysfunction is unrelated to WM pathology (WAHLUND and Bronge, 2000).

1.2.3 Cortical Pathology

WML have also been suggested to arise due to the classical cortical neuropathology of AD (Aβ plaques and neurofibrillary tangles), causing axonal loss through Wallerian degeneration (McAleese et al., 2017).

In cerebral amyloid angiopathy (CAA), the cortical vascular pathology caused by the abnormal deposition of β-amyloid (Aβ) within vascular walls is predicted to affect the vascular supply to the WM, causing ischaemia and initiating the cascade of WML

formation (Weller et al., 2015, Kalaria, 2018), suggesting that WML are caused by the extension of cortical pathology (Bozzali et al., 2002).

Overall, hypoperfusion and hypoxia, BBB dysfunction and cortical pathology are considered potential factors underlying the formation of WML. Whether all factors play equal roles is as yet unknown.

1.3 Dementia

Dementia is a broad category of diseases characterised by progressive impairment in cognitive function. Worldwide, it is considered one of the most significant reasons for disability and dependency among the elderly (over 60y). Still, it is not an inevitable part of the ageing process (Bailey et al., 2013). The World Health Organisation (WHO) reports approximately 55 million people currently have dementia, with 10 million new cases yearly. The number of affected individuals is increasing, and with the increasing elderly population, it is predicted to reach 78 million in 2030 and 139 million in 2050 (WHO, 2022).

Symptoms of dementia usually accompany deterioration in emotional control, social behaviour, or motivation. The onset of dementia occurs gradually, and early-stage symptoms, which include poor memory and loss of orientation in relation to places and time, are often overlooked (Bailey et al., 2013). Dementia symptoms become apparent and confirmed when a patient's memory is impaired, with difficulty recalling recent events and disorganised speech ability. Moreover, patients often get lost in their homes and neglect personal care (WHO, 2022).

According to etiologic, neuropathology and clinical presentation, dementia can be categorised into four main groups: Alzheimer's disease (AD); vascular dementia (VaD) (including large and small vessel disease); dementia with Lewy Bodies (DLB); and frontotemporal dementia (FTD), ordered by the most common type, respectively. AD is the most common type of dementia based on clinical and autopsy surveys and contributes to 60–70% of the dementia cases. AD is neuropathologically characterised by selective neuronal loss associated with extracellular plaques of β-amyloid and intracellular neurofibrillary tangles composed of hyperphosphorylated tau (Uzun et al., 2011). VaD, the focus of the current study, is the second most common form of dementia and contributes to at least 20% of dementia cases (Iadecola, 2013). VaD arises as a result of inadequate blood supply to the brain caused by disease and/or injury (Kirshner, 2012). DLB accounting for 4-8% of all cases (Prasad et al., 2022). Its neuropathological characterised by the accumulation of α-synuclein within neurones of the cortex and substantia nigra, and often co-occurs with amyloid-β plaques and tau neurofibrillary tangles (Yousaf et al., 2018). FTDs are neuropathologically associated with neurodegeneration within the frontal and temporal cortices (Bang et al., 2015). It account for 1.6 to 7% of dementia cases (Bottero et al., 2021). However, the classification of dementia is difficult because subtypes are often indistinct and mixed forms frequently co-exist. An early diagnosis of the disease prompts optimal management and support. Studies suggest regular exercise, a healthy lifestyle and cognitive activities play a role in preventing or delaying the onset of dementia (Uzun et al., 2011).

Dementia is a chronic or progressive disease with significant burdens (WHO, 2022). In addition to their cognitive decline, affected individuals are at risk of psychosocial (emotional)dysfunction, causing potential difficulties in everyday life. The increasing numbers of patients represent an increased cost to society since severe dementia patients depend heavily on assistance. In many cases, the patient's family and friends fulfil caregiving roles, which can be stressful and demanding, leading to health consequences for the careers. The WHO recognises dementia as a public health priority. Dementia also has economic burdens; health costs associated with dementia were estimated to be US$ 1.3 trillion in 2019 (WHO, 2022). Further understanding of the disease mechanism(s) and identification of novel therapeutic targets to ease the symptoms and/or delay/prevent the onset of the disease are urgently required. Given the minimal success of current therapies, which offer limited efficacy, it is highly likely that successful treatment of dementia will require the identification and modulation of alternative mechanisms contributing to cognitive decline.

1.4 Vascular Dementia

1.4.1 Definition and Risk Factors

Vascular dementia (VaD) is a progressive disease caused by the reduction of the blood supply to the brain, typically involving multiple minor strokes, which results in cognitive impairment. VaD is the second most common form of dementia after Alzheimer's disease and contributes to at least 20% of dementia cases (Kalaria, 2018, Cai

et al., 2017). The severity of the disease symptoms depends on the brain region where strokes have occurred and the size of the affected vessels (Kirshner, 2012).

VaD shares risk factors with vascular diseases and cerebrovascular disease (CVD) (Venkat et al., 2015, Ding et al., 2020). While the most predictive factors for VaD are age, gender and history of stroke, other risk factors contribute to VaD, including; genetic, atherogenic vascular factors, ischaemic heart disease, atrial fibrillation, raised cholesterol, homocysteine concentrations, psychological stress in early life and regular exposure to stress (Brien and Thomas, 2015, Perneczky et al., 2016). Additional studies are needed to evidence these factors and determine the mechanism(s) underlying disease pathology.

1.4.2 VaD Diagnosis Criteria, Treatment and Prevention

The primary tool of VaD diagnosis involves the patients' detailed history identifying certain criteria, neuropathological features, neuropsychological status evaluation and neuroimaging (T O'Brien and Thomas, 2015). The diagnosis criteria for VaD is defined by several guidelines, including the Diagnostic and Statistical Manual of Mental Disorders, Fourth Edition (DSM-IV) criteria, International Classification of Diseases -Tenth Edition (ICD-10) criteria and the National Institute of Neurological Disorders and Stroke-Association Internationale pour la Recherche et l'Enseignement en Neurosciences (NINDS-AIREN), the Alzheimer's Disease Diagnostic and Treatment Center criteria (ADDTC), and the Hachinski Ischemic Score (Perneczky et al., 2016). Each of these have different diagnosis criteria of core signs and symptoms to diagnose dementia. The DSM-

IV and the NINDS-AIREN criteria are widely used to diagnose VaD. According to DSM-IV, VaD patients must show symptoms for at least one domain of cognitive function impairment (Chui et al., 2016). The criteria of NINCDS-AIREN require memory loss in addition to a decline of two or more cognitive domain functions.

There is no current medical or surgical treatment for VaD as the ischemic changes are irreversible. A critical prevention plan is to minimise the risk of stroke by committing to healthy food intake and an active lifestyle. After the onset of VaD, controlling these risk factors may stabilise or slightly improve cognitive function (Kalaria et al., 2016, Ding et al., 2020). Medication used for hypertension and hypercholesterolemia treatments in patients diagnosed with VaD stabilises or shows improvements in cerebral perfusion and cognition performance. Neuropsychiatric drugs also minimise behaviour and psychological symptoms (T O'Brien and Thomas, 2015).

1.4.3 Vascular diseases

Vascular diseases are classified into large and small vessel diseases. The large vessel diseases (LVD), such as atherosclerosis, involve the obstruction of the blood flow within the large arteries caused by the abnormal accumulation of plasma proteins and lipids in the walls, eventually reducing the blood flow through these arteries. The relationship between atherosclerosis and dementia is correlative (Suemoto et al., 2011).

Small vessel disease (SVD) manifesting on MRI and CT scans as diffuse white matter lesions (WML), lacunar infarcts (LACI) and/or microinfarcts (Sahathevan et al., 2012, Horsburgh et al., 2018), affects the small vessels of the brain including arterioles

and capillaries (Pantoni, 2010, Wardlaw et al., 2013). The common underlying cause of SVD is a series of minor strokes. It is associated with several vascular risk factors, including hypertension, lipid disorders, diabetes mellitus, tobacco smoking and cardiovascular diseases. However, the mechanism(s) underlying their pathology remains unknown (Venkat et al., 2015). SVD is considered to be the main contributor to the development of dementia and cognitive impairment (Brun et al., 1987, Weller et al., 2015).

1.5 Microglia

Microglia are distributed through the CNS and account for 5-20% of the neuroglia within the brain, and spinal cord (Waisman et al., 2015); and are considered the primary immune cells involved in neuroprotection. While they are located in all brain regions, higher levels of microglia are situated in the myelinated tissue (white matter), compared to cortical areas (Olah et al., 2011). Microglia perform a similar function to peripheral macrophages, including antigen presentation and phagocytosis of cell debris (Waisman et al., 2015). Microglia are constantly surveying their local environment (Verkhratsky and Butt, 2013, Rohan Walker et al., 2013, Hashemiaghdam and Mroczek, 2020), and this feature is fundamental to enable the rapid defense function of the microglia.

Under normal conditions, resting (steady) stage microglia are characterised by their ramified morphology, composed of a small cell body and long branching processes. While the microglial cell body generally remains fixed, its processes are continually moving and extending to scan the surrounding area (Ginhoux et al., 2013, Rohan Walker et al., 2013, Verkhratsky and Butt, 2013). Mildly activated microglia, also called hyper-

ramified, are characterised by increased numbers of branching processes and the secretion of pro-inflammatory cytokines (Crews and Vetreno, 2016). Intermediate-activated microglia are characterised by enlarged swollen cell bodies and truncated processes with a 'bushy' morphology (Crews and Vetreno, 2016).

When activated, microglia transform rapidly from a ramified, resting morphology state to an amoeboid morphology, which is the maximally immune-responsive form. At this stage, microglia have a rounded, macrophage-like morphology with no or few processes, (Aloisi, 2001, Crews and Vetreno, 2016). The amoeboid microglia play a major role in phagocytosis (Karve et al., 2016). The different microglia morphologies are illustrated in Figure 1.2.

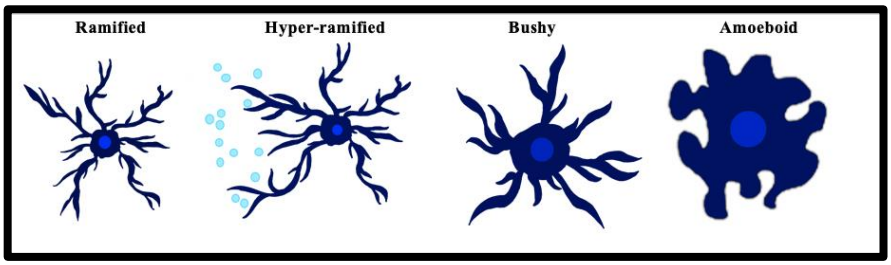

Figure 1.2 - The main features of microglial morphology. Ramified microglia are characterised by long, branched processes and a small cellular body to support the surveillance of the surrounding environment. In contrast, amoeboid microglia have a large, round cell body with retracted processes. Original figure created using biorender.

1.5.1 M1 and M2 activated Microglial

Microglial activation results in two major phenotypes, M1 and M2, where microglia have a major pro-inflammatory neurotoxic or anti-inflammatory neuroprotective role, respectively (Tang and Le, 2016). The mechanism of microglial activation is described in Figure 1.3.

'Classical' activation drives microglia to an M1 phenotype, and is induced by interferon-gamma (IFN-γ) and lipopolysaccharide (LPS) (Satoh, 2018, Boche et al., 2013), which stimulate the production of pro-inflammatory mediators such as tumour necrosis factor-α (TNF-α), interleukin-1β (IL-1β) and IL-6, superoxide, nitric oxide (NO), reactive oxygen species (ROS), and proteases (Michaud et al., 2013, Tang and Le, 2016). These pro-inflammatory molecules will eventually cause damage to the surrounding environment and are neurotoxic. The alternative M2 microglia phenotype reduce pro-inflammatory immune responses and release anti-inflammatory cytokines. M2 microglia are associated with the expression of IL-4 or IL-13 and the anti-inflammatory cytokines IL-10 and Arginase 1 (Arg1) (Michaud et al., 2013), which have been shown to stimulate myelin repair and extracellular matrix reconstruction (Jiao et al., 2018).

It should be acknowledged that the M1/M2 phenotype classification was first reported in animal studies to explain the pro- and anti-inflammatory states observed in the peripheral macrophages (Mills et al., 2000). Microglia are versatile cells characterised by their shifting capability to unique activation states and are not limited to the simple M1/M2 classification (Ransohoff, 2016). The simple classification of M1/M2 phenotypes represents extreme states, and it is likely that both states, as well as intermediate forms,

are present in the ageing brain (Tang and Le, 2016), where microglia respond to ageing, ischemia, infections, and several neurodegenerative diseases (Ransohoff, 2016).

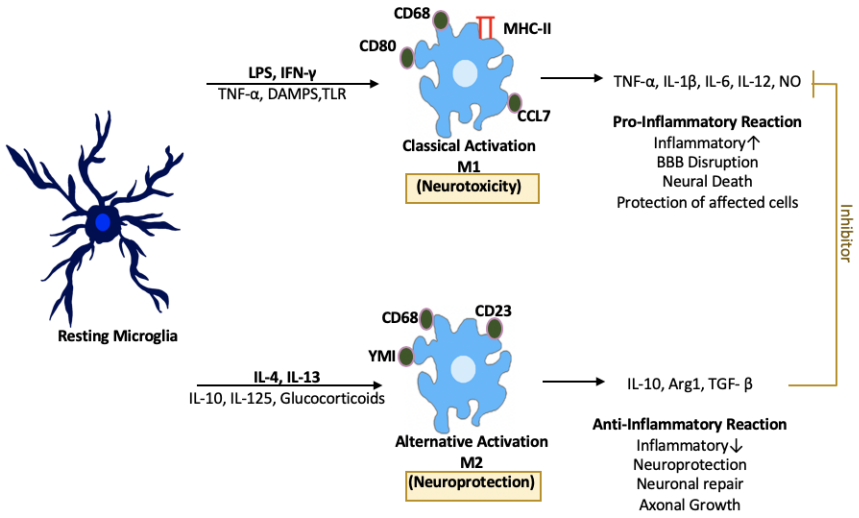

Figure 1.3 - Microglia-activation phenotypes. LPS and IFN- γ signals mainly activate the classically activated microglia (M1), which release neurotoxic products and induce pathogenic phagocyte and immune presenting functions. In contrast, the neuroprotective microglia (M2) are commonly activated by IL-4 and IL-13 signals and release neurotrophic factors. M2 microglia phagocytose cellular debris in the brain and are involved in neuronal repair mechanisms. CD, cluster of differentiation; DAMPs, damage-associated molecular patterns; ECM, extracellular matrix; IFN-γ, interferon γ; IL, interleukin; LPS, lipopolysaccharide; NO, nitric oxide; PAMPs, pathogen-associated molecular patterns; RNS, reactive nitrogen species; ROS, reactive oxygen species; TGF-β, transforming growth factor β; TLR, toll-like receptor; TNF-α, tumor necrosis factor α.

1.5.2 Microglial Phenotypes in the Ageing Brain

The normal ageing process is a significant risk factor for neurodegenerative diseases and impacts various cell types, including microglia (Von Bernhardi, 2007, Beltrán-Castillo et al., 2021). Extensive innate immune activation occurs during brain ageing and is associated with cognitive decline. Microglia become primed during neurodegeneration, neuroinflammation and as part of the normal ageing process. Primed microglia have a lower activation threshold, resulting in an exaggerated and heightened response that may contribute to neurodegeneration and cognitive impairment (Olah et al., 2011, Perry and Holmes, 2014). During normal ageing, microglia acquire an activation morphology associated with increased production of pro-inflammatory mediators (IL-1β and IL-6) and increased DNA-binding activity of NF-κB, which promotes IL-6 expression and enhances classical microglial activation (Olah et al., 2011, Harry and therapeutics, 2013). The alternative microglia activation diminishes, and the IL-4/IL-13 signalling pathway declines in activity. Accordingly, the age-associated inflammation profile alters the microglia phenotype to be more M1-like, which increases the neuroimmune response during the onset of neurodegenerative diseases (Michell-Robinson et al., 2015).

Dystrophic (senescent) microglia have also been reported in AD, where they co-localise with neuropil threads, neurofibrillary tangles, and neuritic plaques (Streit et al., 2009). These dystrophic microglia have an altered morphology characterised by fragmentation and de-ramification of their processes. Their dysfunctional roles are characterised by reduced surveillance, processing speed, motility, and cellular migration (Davies et al., 2017, Hefendehl et al., 2014, Damani et al., 2011). The dystrophic

(senescent) microglia are thought to contribute to disease progression through a loss of neuroprotection and reduced phagocytic activity, causing a failure of the immune responses towards stimuli (Floden and Combs, 2011, Olah et al., 2011, Hefendehl et al., 2014). It is possible that both primed and/or dystrophic microglia are present during the ageing process and increase the risk of neurodegeneration (Olah et al., 2011).

1.5.3 The Microglial phenotype in WML

Several factors can influence the microglial phenotype in WML, including myelin attenuation, leakage of plasma proteins, and the denudation of the ependymal with exposure to CSF factors (Kobayashi et al., 2002, Weller et al., 2015). Although the histopathological features of demyelination, axonal damage, astrogliosis and oligodendrocyte loss exist in both types of WML, the microglial profile is one of the most significant differences between the two groups: PVL and DSCL (Schmidt et al., 2011, Hase et al., 2018).

In an ageing population-representative neuropathology cohort study, microglia in the PVL predominantly display a ramified morphology, immune-activated and proliferative profile evidenced by the expression of MHC II and the immune co-stimulatory molecules (B7-2 and CD40) (Schwartz et al., 2006, Peferoen et al., 2015). In contrast, microglia within DSCL exhibit large amoeboid morphology and phagocytic phenotype with the expression of $CD68^{+}$, a lysosomal marker. The findings suggest an ongoing immune activation in the former and an innate pattern in the latter, where

microglia have a role in demyelination, phagocytosis and the removal of degraded myelin (Simpson et al., 2007, Waller et al., 2019). The difference in microglial phenotypes within the two lesion types suggests a different role of microglia in the pathogenesis of PVL and DSCL (Fernando et al., 2006). The microglia phenotypes, whether M1 or M2, within these lesions are undetermined.

The microglia within the radiologically NAWM from lesional cases express significantly elevated levels of MHC II^+ compared to microglia from control non-lesional WM cases (Simpson et al., 2007). Whether the abnormal microglia phenotypes within the NAWM are inhibiting the lesion spread or contributing to lesion progression is currently unknown.

1.5.4 Microglia Pathology - Response to Hypoxia in the DSCL

As discussed earlier, chronic cerebral hypoperfusion, along with disruption of the BBB, play a crucial role in the pathogenesis of age-associated WML, which likely activates microglia to induce a pro-inflammatory response. Pro-inflammatory microglial cells are associated with the depletion of oligodendrocytes, activation of astrocytes and demyelination (Fazekas et al., 1987).

M1 microglia secrete pro-inflammatory cytokines that may directly affect the BBB, leading to extravasation of plasma proteins, and act as positive feedback for further microglial activation. Additionally, the sustained secretion of pro-inflammatory cytokines may activate the surrounding glial cells, impacting myelination and axonal function (Liu et al., 2006, Winkler et al., 2014). Further, activated microglia may secrete damaging

molecules, such as cathepsins, a lysosomal protease. These protein degradation enzymes were found to be highly expressed by amoeboid microglia within DSCL, suggesting they contribute to the degradation of myelin and, subsequently the pathogenesis of WML (Simpson et al., 2009).

Further, the oxidative stress and the DNA damage response are features of both WML and the surrounding radiologically normal appearing white matter (NAWM) (Al-Mashhadi et al., 2015). Oxidative stress is defined by the excessive production of reactive oxygenated species (ROS), which cannot be neutralised by the action of antioxidants, resulting in accumulation and causing cellular damage. ROS include free radicals, hydrogen peroxides and nitric oxide (NO) (Pisoschi and Pop, 2015). Within the brain, the cerebral WM mainly consists of myelinated axons and oligodendrocytes that are highly vulnerable to the effect of these oxidative stresses, resulting in their damage (Takase et al., 2018). Oxidative stress and the DNA damage response are features of both WML and the surrounding radiologically normal-appearing white matter (NAWM) (Al-Mashhadi et al., 2015).

A summary of the proposed WML pathogenic mechanism(s) and the potential role of microglia in the pathogenesis of DSCL is presented in Figure 1.4. However, whether microglia contribute to lesion formation or prevent lesion spread is currently unknown. Overall, the current literature suggests that the pathogenesis of WML is complex and likely reflects the contribution of multiple factors (Weller et al., 2015). Given the limited success of current therapies, it is highly likely that successful treatment of dementia will require the identification and modulation of alternative mechanisms causing cognitive

decline. Understanding how WML arises may identify novel drug targets and enable new treatments to be identified (Lin et al., 2017, Wharton et al., 2015).

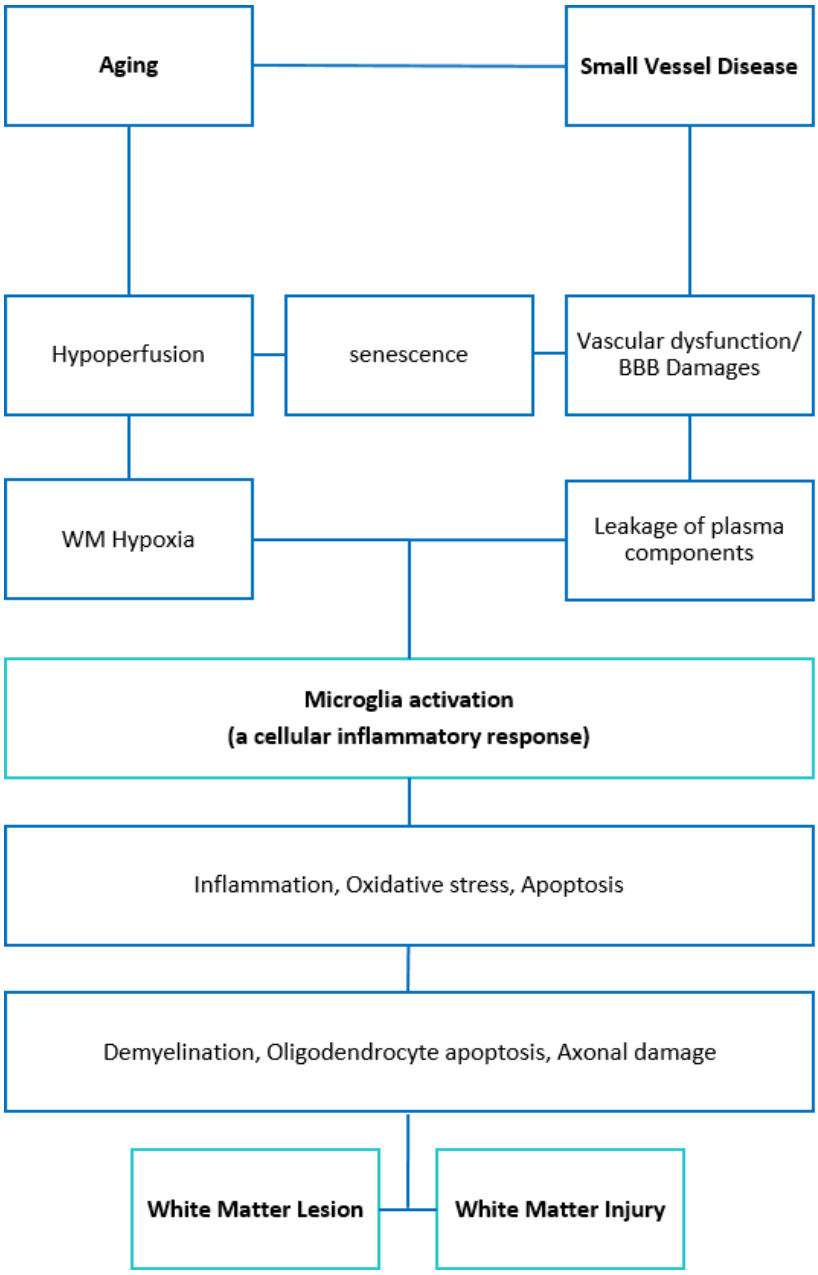

Figure 1.4 - The hypothesised pathway for the formation of age-associated WML. The cascade illustrates possible pathogenic mechanisms for WML development. The ageing process and the small vessel disease are the primary factors affecting vascular integrity, leading to chronic cerebral hypoperfusion and disruption of the BBB that initiates lesion pathogenesis. The cascade progression will induce the microglia's pro-inflammatory response, oxidative stress and cellular death that contribute to the demyelination and development of white matter lesions. Original figure modified from (Wharton et al., 2015).

1.6 Hypoxia and the Hypoxia-Inducible Factor pathway

As previously discussed, age-associated DSCL are associated with chronic cerebral hypoperfusion and a hypoxic environment. These hypoxic lesions are characterised by the presence of microglia with a phagocytic amoeboid morphology, which displays significant nuclear localisation of HIF-α. Microglial pathology is not restricted to the DSCL but extends into the surrounding radiologically normal appearing white matter (NAWM). While several studies have linked hypoxia with changes in microglial function, whether microglia are contributing to the pathogenesis of WML or preventing lesion spread in the ageing brain is currently unknown (Fernando et al., 2006, Wharton et al., 2015, Lin et al., 2017).

The reduction of the level of oxygen tension in tissues directly impacts the body's biophysiological and metabolic processes and indirect effects that eventually activate HIF-α. Under normoxic conditions, when sufficient oxygen levels exist, the HIF-α subunit is hydroxylated and binds to the tumour suppressor Von Hippel–Lindau (VHL) protein, enabling HIF-α to become ubiquitylated and degraded. In response to hypoxia, or without functional VHL, the ubiquitylation step is prevented, causing accumulation and the nuclear translocation of HIF-α, where it binds to the HIF-β subunit, and together they regulate transcription of the hypoxia-inducible genes (HIG) (Harris, 2002, Lappin and Lee, 2019); as demonstrated in Figure 1.5.

The HIF pathway is one of the main cellular sensors of hypoxia and has a critical regulatory role in homeostatic responses at both systemic and cellular levels (Weidemann et al., 2008). Within the brain, it is possible that cerebral hypoxia activates the HIF

pathway, which in turn promotes microglial activation and neuronal cell death, ultimately resulting in impairment of brain function. However, it should be noted that the HIF response may also enable adaptation of the cell to hypoxia, thereby eliciting a neuroprotective effect. As the HIF pathway represents a major response to hypoxia, it may potentially play a crucial role in the formation of age-associated WML.

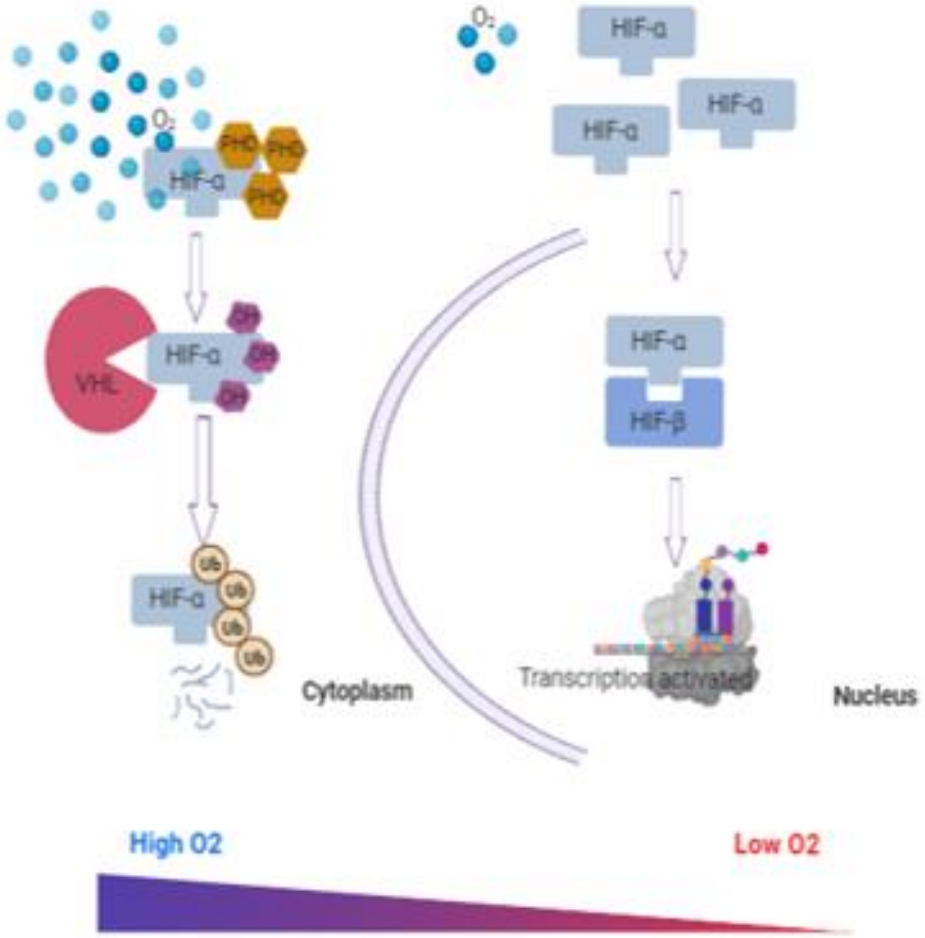

Figure 1.5 - HIF-α processing under normal and hypoxic conditions. Under normoxia: With the presence of both adequate oxygen and prolyl hydroxylases (phd), HIF-α subunits are hydroxylated and bind to VHL, followed by polyubiquitination and degradation of the HIF-α subunits. In contrast, under hypoxia: The reduction of oxygen will prevent the degradation process of HIF-α, resulting in stabilisation, translocation of HIF-α to the cell nucleus and forming a transcription complex with HIF-β. Eventually, theheterodimer composed of HIF-α and HIF-β continuously activates HIG, which in turn regulates the cell's biological processes, including proliferation, angiogenesis, metabolism, apoptosis and migration. Original figure created using biorender.

1.7 Animal Models of Hypoxia

Animal models are often utilised to determine the mechanisms underlying diseases, define potential targets for therapeutic trials, and measure the effectiveness of therapeutic medications. Utilising a variety of hypoxia models is crucial to understand the effects of hypoxia on brain functioning and other metabolic encephalopathies that accompany hypoxia, such as the age-related disorders Alzheimer's and dementia (Gibson and Huang, 1992, Venkat et al., 2015).

Several animal models of hypoxia exist, and the findings of these models have enabled a better and more reliable understanding of hypoxic-associated brain changes. The *in vivo* models are produced by a variety of means, whether by reducing the oxygen accessibility (hypoxic hypoxia), lowering the oxygen-carrying capacity of the blood (anaemic hypoxia), or altering the tissues' capability to consume the available oxygen (histologic hypoxia). The hypoxia-induced changes are better-examined either (1) *ex vivo*, where the animal is made hypoxic, and subsequent effects are assessed *in vitro*, or (2) *in vitro*, where the isolated tissue being examined for effects is made hypoxic (Gibson and Huang, 1992). A genetic knockout mutation(s) targeting the HIF pathway components has also been utilised to induce hypoxia in an animal model (Strohl, 2007, van Rooijen et al., 2009, Azad and Haddad, 2013, Lappin and Lee, 2019).

1.7.1 Rodent Animal Models – the mouse

Several rodent studies support the role of microglia in developing WML in response to hypoxia. Animals treated with the microglia inhibitor minocycline show minimal white matter damage in response to surgical occlusion of the carotid artery (Cho et al., 2006). Furthermore, in mice, hypoxia-induced by bilateral carotid artery stenosis is associated with microglia proliferation and elevated production of pro-inflammatory cytokines. Additionally, treating mice with dimethyl fumarate, an anti-inflammatory agent, decreases the microglial response, implicating a role of M1-activated microglia in response to hypoxia (Fowler et al., 2018). In an aged mice study, intermittent hypoxia resulting from obstructive sleep apnea causes low-grade neuroinflammation in the dorsal hippocampus, temporary cytokine elevations and longstanding microglial changes. These changes are associated with cognitive impairment and pathological brain ageing (Sapin et al., 2015).

1.7.2 Aquatic Animal Model - Zebrafish

The zebrafish is a tropical freshwater fish native to Southeast Asia. Its Latin name, Danio rerio, equals Bengali's meaning 'from the rice fields' (Nusslein-Volhard and Dahm, 2002). Zebrafish embryos and larvae are transparent, while the adult bodies contain black horizontal stripes on each side, giving rise to the name 'zebra' (Nusslein-Volhard and Dahm, 2002, Howe et al., 2013). The cost of housing and maintaining zebrafish is considered economical compared to rodents. Zebrafish adults are small (2.5-4cm long),

requiring less living space. Breeding occurs about every ten days and produces up to 300 eggs. The rapid development and generation time allows high-throughput testing with both time and cost-effectiveness (Lieschke and Currie, 2007, Caroline Brennan, 2014).

The popularity of zebrafish in research has rapidly increased due to their genetic homology with humans; ~70% of the fish genes are similar to humans, rising to 82% of the genes linked to human diseases (Howe et al., 2013). Moreover, the transparency of the early stages enables optical observation of cell development and high-quality *in vivo* imaging. This feature is helpful for real-time observation of developing pathologies and tracking genetic manipulation or pharmacological treatment (Lieschke and Currie, 2007, Chakraborty et al., 2009). The *ex vivo* fertilisation and embryogenesis facilitate the insertion of transgenic modifier genes and the usage of mutagenesis (knock-out) assays (Howe et al., 2013, Caroline Brennan, 2014). These valuable attributes of zebrafish, in addition to their high similarity to the human nervous system in terms of representative anatomy, behaviours and aetiology, make them an ideal model to study neurodegenerative disease pathogenesis (Lieschke and Currie, 2007, Simonetti et al., 2015). The zebrafish has been successfully utilised to study the pathology of human neurodegenerative diseases including Parkinson's, Alzheimer's and Huntington's (Wang and Cao, 2021).

1.8 Microglia establishment on embryonic zebrafish Brain

Microglia originate from macrophages, where a subpopulation from the primitive macrophages in the yolk sac colonise in the larval CNS; later, these macrophages

differentiate into microglia followed by a proliferation and migration phase into the head mesenchyme (Herbomel et al., 2001). The process occurs at the third-day post fertilisation (3 dpf) of the larval embryogenesis, when the first neural apoptosis initiates in zebrafish brains. The apoptotic neurons require an efficient removal mechanism to prevent the build-up of damaging degradation products in the surrounding tissue (Mazzolini et al., 2020).

The early macrophage arrives in the brain via an invasion process that involves crossing the brain, retinal and epidermal basal laminae. Initially, at 23-30 hours post fertilisation (hpf), the macrophages invade through the cephalic mesenchyme close to the brain boundaries, adhering to the pial surface and roof of the fourth ventricle. Macrophage cells emerge slowly, and are found throughout the brain compartment by 35 hpf onwards. The macrophage continues colonisation in the forebrain, midbrain and hindbrain, optic tectum and mesenchyme, and optic nerves by 48 hpf. Between 55 and 60 hpf, all macrophages in the brain and retina undergo a phenotypic transformation into early amoeboid microglia. By 60 hpf, the microglia colonise the midbrain and the optic tectum, in response to neural apoptosis and are found throughout most brain areas by 78 hpf (Herbomel et al., 2001). Microglia change from highly motile amoeboid cells involved in phagocytosis of apoptotic cells (at 3 dpf) into morphing microglia, this is an intermediary transition status, characterised by speedily transforming back and forth between phagocytic and ramified profiles. The morphing microglia finally settle into a typical mature ramified morphology by 5 dpf, and become highly ramified by 7 dpf. The microglial population motility peaks between the age of 3.5 and 4.5 dpf, followed by a

substantial decline at 5 dpf (Svahn et al., 2013). During further development, the larval microglia are gradually replaced by definitive microglia that persist throughout adulthood.

1.9 Microglia Function and Gene Expression in Zebrafish

In the zebrafish brain, microglia have similar defensive response roles toward any homeostatic disturbance or pathology as in the human brain (Sieger and Peri, 2013); they respond to injuries firstly by polarising cellular branches followed by migration toward the injury site (Casano et al., 2016). Microglial loss leads to neutrophil accumulation that can eventually hinder the resolution of inflammation. The high similarity in both morphology and behaviour of microglia between mammalian and zebrafish microglia suggest a high degree of conservation across species (Sieger and Peri, 2013).

The larval microglia mature promptly and express specific microglial genes, including *apoeb*, *p2ry12*, *hexb*, *csf1ra*, and *mpeg1.1*, *mafbslc7a7*, and *sall1a*. While some genes display constant expression throughout the developing larva, others are upregulated at 3 dpf compared to days 5 and 7 (Mazzolini et al., 2020). Comparison of the gene expression profile during the larval stage have revealed a significant upregulation of many genes at 3 dpf, followed by major gene expression changes occurring between day 3 and 5 dpf (Mazzolini et al., 2020). These gene expression changes correlate with invading primitive macrophages into the larval CNS and their differentiation into microglia.

In a comparative expression analysis, the core microglia genes of larval and adult zebrafish are also expressed in human microglia, indicating a highly conserved core microglia signature across species. The core expression signatures of human microglia matched most with microglia of the 7dpf larval stage. These core genes mainly represent 'cellular processes', 'metabolic processes', 'development', and 'Immune system process' categories (Mazzolini et al., 2020). These expression profile findings strengthen the larval zebrafish as a valid model to study human neurological diseases.

1.10 The *vhl*$^{-/-}$ Zebrafish as a Model

The mutant zebrafish line, *vhl* $^{hu2117/hu2117}$, also referred to as *vhl*$^{-/-}$, was originally isolated by mass-sequencing of an N-Ethyl-N-Nitrosourea (ENU) mutagenesis “library” of F1 fish. It was selected because it carried a nonsense mutation at the 23rd amino acid of the *vhl* gene (c.361.c>t/T, p.Q23X.); where an amino acid, Glutamine (Q), is substituted and replaced by a stop codon on chromosome 6 at position Q23X within the zebrafish *vhl* orthologue, as shown in Figure 1.6. The premature stop is predicted to severely truncate the vhl protein rendering it unable to bind HIF, which prevents the polyubiquitination and consecutive hydroxylation of HIF-α (van Rooijen et al., 2009). The non-functional protein consequently permits HIF-α to accumulate and translocate into the nucleus provoking chronic hypoxic signalling (van Rooijen et al., 2009), a similar activation is seen in the hypoxic environment linked with human WML (Ramakrishnan et al., 2017).

*Figure 1.6 - The Q23X mutation in the HIF-α binding site. The figure shows a section of a vhl amino acid alignment sequence for human and zebrafish. The HIF-α binding site is boxed in orange. The C/T Q23X mutation within the vhl -/- is identified with a red box. The vhl sequence of 175-amino-acid protein within vhl -/- and human VHL is identical by 52% and similar by 70%, where * represent an exact amino acid match, and: represent a similar match. Original figure modified from (van Rooijen et al., 2009).*

It is important to stress that while the human HIF pathway is activated in response to a hypoxic condition, the net result of the *vhl* mutation is activated HIF in a normoxic condition. Moreover, while activation of the HIF pathway causes the majority of hypoxia response, some responses caused by oxygen deprivation are not driven by the activated HIF pathway. As such, the *vhl*$^{-/-}$ mutant may allow for the isolation of direct effects of the HIF activation on microglia.

1.11 The vhl$^{-/-}$; phd3::EGFP; mpeg::mCherry1 Lines

Mutant *vhl*$^{-/-}$ zebrafish survive for up to 10 days, unlike the *vhl*$^{-/-}$mutant mouse, which die during early embryonic stages, therefore it is an ideal model to provide an insightful view of hypoxia signalling during embryonic and post-embryonic stages (van Rooijen et al., 2009). The *vhl* model can be used to study the microglial response to

hypoxia. For the current research, the *vhl*$^{hu2117/+}$ line (*vhl* $^{-/+}$) was backcrossed to wildtype line several times to minimise background mutations. To study HIF signalling, an *in vivo* reporter for HIF activity was developed, where enhanced green fluorescent protein (EGFP) was driven by the promoter of *prolyl hydroxylase 3* (*phd3*), a highly responsive HIF target gene, *phd3::*EGFP*,* (Sahathevan et al., 2012)and crossed into the *vhl*$^{-/+}$background (van Rooijen et al., 2009). In the presence of the *phd3::EGFP* transgene, high EGFP expression in the homozygous *vhl*$^{-/-}$ zebrafish from approximately 36 hpf allowing easy identification of mutants in clutches of embryos.

In order to exploit the *in vivo* imaging capabilities of the zebrafish and track the microglia, another reporter was crossed into the *vhl*$^{-/+}$; *phd3::EGFP* background: *mpeg1::mCherry*. The *macrophage-expressed gene-1* (*mpeg1*) transgenic expression is driven by the *mpeg1* promoter of macrophage cells, including microglia. The macrophage-exclusive expression of *mpeg1* has enabled its usage as a recognition marker within a live zebrafish at embryonic and larva stages. Hence, in the presence of the *mpeg1::*mCherry transgene, the macrophages are recognisable by the co-expression of mCherry seen as red fluorescent cells within the homozygous *vhl*$^{-/-}$ zebrafish, enabling real-time *in vivo* examination of macrophage behaviour and function in the zebrafish model (Ellett et al., 2011).

1.12 The *vhl*$^{-/-}$ zebrafish successfully induces hypoxia responses

The *vhl*$^{-/-}$ mutation induces a cellular response to hypoxia which is highly similar to that observed under oxygen deprivation, and is present in the early embryonic stages (van

Rooijen et al., 2009). The loss of *vhl* in zebrafish has previously been characterised as a model of vascular response to hypoxia (van Rooijen et al., 2009); where hypoxia initiates vascular proliferation and remodelling to ensure adequate oxygen availability to the tissues. The *vhl*$^{-/-}$ embryos' vascular network is characterised by hyper-branching, which enables the differentiation between *vhl*$^{-/-}$ mutants and their wildtype sibling (van Rooijen et al., 2009).

The cardiovascular system is also altered in the *vhl*$^{-/-}$; the heart rate of the *vhl*$^{-/-}$ embryo is significantly higher than the wildtype sibling from 7 dpf to 10 dpf (Van Rooijen et al. 2009). While the cardiac output of the wildtype embryo declines during early development (Kopp et al., 2005), in contrast, the *vhl*$^{-/-}$ cardiac output increases from 3.2-fold at 4 dpf to 15-fold by 10 dpf, resulting in cardiomegaly, oedema and high output cardiac failure, which eventually contributes to the death of the homozygous embryo between 8 and 11 dpf (Van Rooijen et al. 2009). These changes are associated with an enlarged heart, indicating a response to chronic hypoxia exposure where the fish attempt to increase the cardiac output to increase the supply of oxygenated blood (Fan et al., 2005, Villamor et al., 2004).

The hypoxic responses enable the identification of the *vhl*$^{-/-}$ larval zebrafish from their wild-type (wt) sibling clutchmates by their behavioural and physiological appearance, as illustrated in Figure 1.7. From the age of 4 dpf, even under normoxic conditions, *vhl*$^{-/-}$fish display an enlarged heart size, Figure 1.7 A. The *vhl*$^{-/-}$mutant fish also have more extensive vascular growth into the dorsal fin, as displayed in Figure 1.7 B, and hyperventilate, recognisable by their rapid buccal movement.

As mentioned earlier, the vhl zebrafish were maintained on a transgenic background(*phd3*::eGFP) which enables the expression of GFP under the phd3 promoter; where the phd3 promoter is active in hypoxic areas or when HIF is activated via other means, for instance, by loss of Vhl function (Santhakumar et al., 2012). The *phd3* gene is strongly induced by HIF signalling and, therefore, a typical 'negative feedback regulator' as the Phd3 protein typically acts to keep HIF-α hydroxylated and the pathway switched off.

The expression of eGFP in the transgenic *phd3::egfp* zebrafish correlates to the levels of *phd3* expressed in hypoxic areas (Santhakumar et al., 2012). While both *vhl*$^{-/-}$ zebrafish and their wildtype siblings show some expression of GFP, it is significantly elevated in the *vhl*$^{-/-}$ mutant fish. This can be observed more prominently in the brain of the *vhl*$^{-/-}$ mutant larvae and extends along the entire body, as shown in Figure 1.8, confirming hypoxia signalling in the *vhl*$^{-/-}$mutant fish.

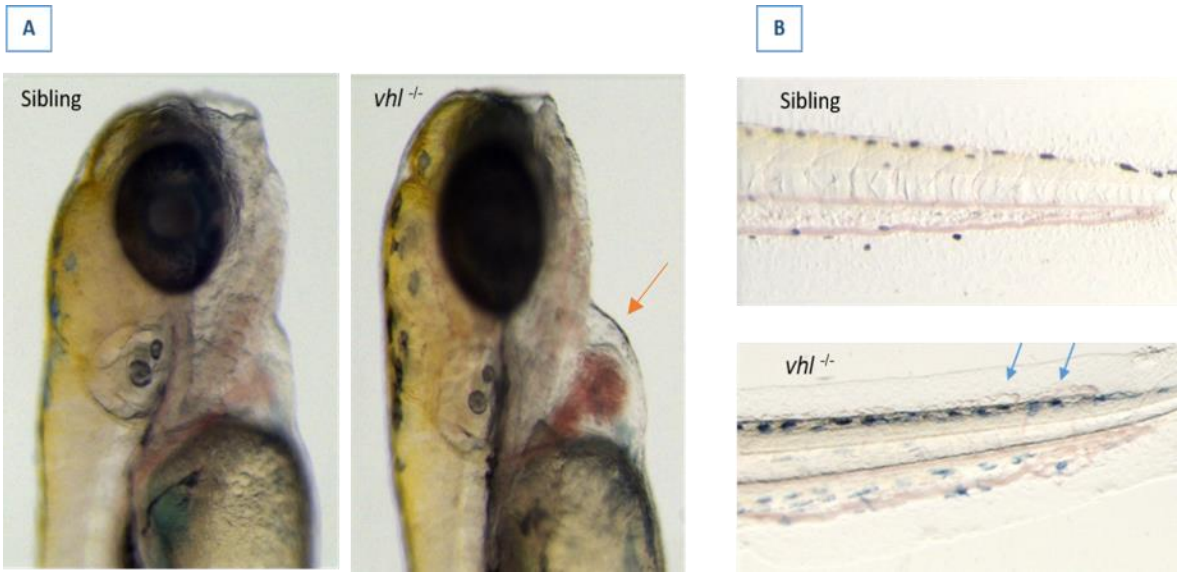

*Figure 1.7 - Differences in physiological appearance of the two larval genotypes. The vhl$^{-/-}$ shows (**A**) enlargement of the heart and heart cavity (orange arrows) and (**B**) vascular loops in the tail (blue arrows) at 4.5 dpf, compared to their wildtype sibling.*

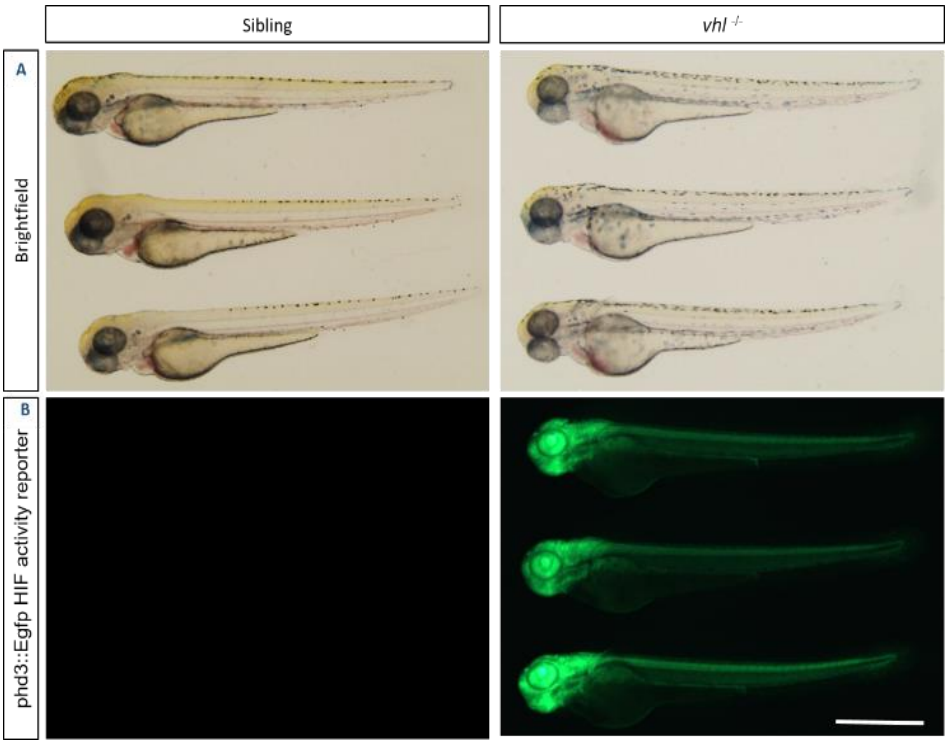

Figure 1.8 - Expression of GFP enables in vivo visualising of hypoxic signalling in 3dpf vhl$^{-/-}$ zebrafish. Representative image of sibling and vhl$^{-/-}$ mutant zebrafish under (A) bright-

field, and (B) GFP fluorescence. GFP is driven by a phd3::EGFP transgene, where the highly responsive phd3 promoter drives it. The scale bar represents 1 mm length.

1.13 Conservation of the Hypoxia Signalling Pathway in Zebrafish

A successful animal model must be translatable to human pathology, where the essential proteins share resemblances in their sequencing and functions. A representative model generally shares more than 30% of its genetic identification with the target human genes (Pearson, 2013). The zebrafish model displays high genetic homology to humans and conserves at least one recognisable orthologue for ~70% of human genes (Howe et al., 2013). Notably, the vhl/HIF pathway, crucial to initiate hypoxia signalling observed, is highly conserved in zebrafish (see below). Hence, the zebrafish is considered an exemplary informative organism for studying the HIF pathway under both physiological and pathophysiological conditions (Schaaf et al., 2009, Santhakumar et al., 2012, van Rooijen et al., 2011, Vettori et al., 2017).

Zebrafish share all the components of the human HIF pathway (van Rooijen et al., 2011, Santhakumar et al., 2012, Elks et al., 2015). The zebrafish ortholog for the human *VHL* encodes for a protein that is 52% identical and 70% similar to the peptide sequence of the human protein. In addition, the location of *vhl* within zebrafish at chromosome 6, position 27.3 mb, has a syntenic location to the human *VHL* (Van Rooijen et al. 2009), suggesting similar protein functions (Zhang et al., 2014).

In addition, the HIF proteins are highly conserved in zebrafish. In zebrafish, the amino acid structure of the HIF-α proteins is 61% similar to humans' (Van Rooijen et al. 2009). The key motifs of the HIF-α proteins are 90% identical between humans and zebrafish (van Rooijen et al., 2009), proposing conservation of binding and interaction of these proteins. Together, the zebrafish's high conservancy of the VHL/HIF pathway and

the hypoxic signalling proteins, which are crucial for hypoxia signalling and responses in the human WML, supports the suitability of the fish to present a model of sustained HIF signalling.

1.14 Hypothesis and Aims:

Most multicellular organisms are heavily dependent on oxygen for survival. They adopt mechanisms to cope with oxygen deficiency, which can occur both in the environment and within the organism's tissues. The fundamental cellular response to hypoxia is conserved throughout the phylogeny (Krug, van Rooijen et al., 2011, Santhakumar et al., 2012). Hypoxia is a feature of several neurodegenerative diseases, including age-associated WML. Microglia play essential roles in maintaining homeostasis within the CNS. Environmental cues can influence the microglial phenotype, driving them to adopt either a pro-inflammatory (M1) or an anti-inflammatory (M2) phenotype. The relationship between hypoxia and neuroinflammation is still far from being completely understood. In this project, we **hypothesise** that sustained activation of the HIF signalling pathway in both age-associated DSCL and zebrafish drives microglia to a neurotoxic pro-inflammatory M1 phenotype. We aimed to:

1. Characterise the transcriptomic profile of microglia associated with DSCL and the surrounding NAWM to identify significant gene expression changes and dysregulated biologically relevant pathways and functional groups, which may contribute to age-associated WM pathology.

2. Assess the morphology and cytokine profile of microglia in a zebrafish model of sustained HIF signalling
3. Develop a robust protocol to isolate microglia from zebrafish and obtain sufficient quality and quantity of RNA to perform transcriptomic profiling
4. Compare the microglial transcriptomic profiles from DSCL and the zebrafish model of sustained HIF signalling to identify candidate genes/pathways that could potentially be targeted to modulate the neuroinflammatory response. Unfortunately the impact of the COVID-19 pandemic meant that this aim could not be completed.

Chapter 2

Characterising the microglial phenotype and gene expression profile in age-associated DSCL

2.1 Introduction

Age-associated white matter lesions (WML) appear as hyperintensities on T2 weighted magnetic resonance images (MRI). WML can be classified into periventricular lesion (PVL) and deep subcortical lesion (DSCL) based on their anatomical location (Fernando et al., 2004b). Several theories have been proposed as to the mechanism(s) underlying the formation of WML, including cerebral hypoperfusion, dysfunction of the BBB and neurodegeneration due to overlying cortical pathologies (Nelson et al., 2022). Nevertheless, the exact mechanism(s) of WML formation remains unknown.

To expand our understanding of deep subcortical WML, the current research has been performed on samples obtained from the Cognitive Function and Ageing Study (CFAS) neuropathology cohort. CFAS is a UK-based prospective longitudinal study of an ageing population-representative cohort. The study focuses on the neuropathology associated with cognitive decline and covers north and south, urban and rural populations. CFAS began in 1989 when over 18,000 people aged 65 or older were selected and invited to the study via their general physician (GP). The core characteristics of the population were obtained by regular cognitive testing and from questionnaires regarding their lifestyle, medication and general health, enabling longitudinal data to be collected.

A subgroup was invited to participate in the neuropathology study; currently, 525 participants have donated their brains to CFAS, and collection is still ongoing. These donated brains have enabled the evaluation of cellular and molecular pathologies of ageing, frailty and dementia (Wharton et al., 2011, Brayne et al., 2006).

Previous CFAS research assessed WML in formalin-fixed brains using MRI, where WML appear as hyperintensities on T2 weighted images. Fazekas proposed the following rating system for deep white matter hyperintensities; (0) absent; (1) punctate; (2) early confluent; and (3) confluent (Fazekas et al., 1987, Wharton et al., 2015). Years later, the scale was modified by Schelten and designed based on four areas: periventricular white matter hyperintensities (WMH), deep subcortical WMH, infratentorial WMH and basal ganglia WMH. The region of interest, WMH in the deep and subcortical WM, was further separately rated in the frontal, temporal, parietal and occipital regions and scored between 0 to 6: where (0) represents an absence of white matter hyperintensities; (1) represents a DSCL < 3 mm, and the number of the lesions (n) ≤5; (2) represents a DSCL < 3 mm, and n > 6; (3) represents a DSCL 4-10 mm, n ≤5; (4) represents a DSCL 4-10 mm, n>6; (5) represents a DSCL >11 mm, n>1; and (6) confluent, which encompass both the periventricular and deep subcortical regions (Fernando et al., 2004b, Scheltens et al., 1993).

Previous histological characterisation of DSCL (Schelten's rating 5) in the CFAS cohort have demonstrated that microglia adopt an amoeboid phenotype which may reflect BBB dysfunction or cerebral hypoperfusion and an associated hypoxic environment (as discussed in chapter 1). However, it is currently unknown whether these

microglia may have a damaging or beneficial role and adopt a pro-inflammatory M1 phenotype or an anti-inflammatory M2 phenotype. Since the microglial activation profile within DSCL is as yet undefined, research is required to characterise the transcriptomic profile of microglia within DSCL, compared to the radiologically normal-appearance white matter (NAWM) surrounding the lesion and control WM from non-lesional cases, to determine the microglial phenotype contributing to pathology or acting to restrict the lesion spread.

Characterising the transcriptomic profile of selected cells/tissue regions has provided comprehensive information on gene expression under physiological and pathological conditions. Transcriptomic profiling of DSCL and the surrounding NAWM in the CFAS cohort has identified the alteration of cell metabolic pathways and glial cell injury contribute to DSCL pathogenesis (Simpson et al., 2009). However, this approach examined mRNA extracted from the entire region of interest, which may have masked microglial specific gene expression changes. Laser capture microdissection (LCM) of immunolabelled cells enables the isolation of an enriched population of the cells of interest from post-mortem tissue, including $CD68^{+}$ microglia (Waller et al., 2012) and can therefore be employed to assess the transcriptomic profile of cells of interest.

Transcriptomic profiling techniques include ribonucleic acid-sequencing (RNA-Seq) technologies. The RNA-Seq workflow begins with the conversion of RNA into cDNA fragments to build a cDNA library. These short transcripts are then sequenced and analysed as reads per gene of interest (Marguerat and Bähler, 2010). It is a next-generation sequencing (NGS)-based technique, where large numbers of individual RNA

molecules within the sample are sequenced; thus, it enables differences in expression levels to be detected, based on how often a particular gene sequence is encountered in the dataset. The NGS-based procedure requires low RNA input. It can, with high accuracy, identify SNPs, novel transcripts, splice junctions, non-coding RNA and novel RNA sequences present in the sample with high sensitivity, making it a more advanced approach than microarray analysis. The issue with this high-throughput approach is its high cost, where the price of a sample is more than five times that of microarray analysis. Another highly relevant disadvantage of this technique is that the RNA-seq protocol cannot sequence poor-quality RNA, a common feature of post-mortem tissue. Despite this, the RNA-seq approach has been successfully employed in several instances to characterise several neurological diseases including, Parkinson's and Alzheimer's disease (Marguerat and Bähler, 2010, Wu et al., 2017).

Hypothesis, Aims and Objectives

Our study hypothesised that microglia adopt an M1 phenotype in age-associated DSCL and the surrounding NAWM, contributing to the progression of lesion pathology. This chapter aimed to:

1. Perform histological characterisation of deep subcortical white matter in an ageing neuropathology cohort and identify DSCL, NAWM and control WM cases for analysis.
2. Characterise the transcriptomic profile of microglia in these three WM groups using RNA-seq and identify significant gene expression changes and dysregulated

biologically relevant pathways and functional groups, which may contribute to age-associated WM pathology.

The objectives of the study were to:

1. Histologically confirm white matter pathology and identify suitable lesional and non-lesional cases for transcriptomic profiling.
2. Provide a qualitative description of the basic histology of the cases identified.
3. Identify suitable cases for laser capture microdissection (LCM) and evaluate the RNA quality for downstream transcriptomic analysis.
4. Isolate microglia from frozen post-mortem cases using immuno-LCM.
5. Perform transcriptomic profiling of microglia in control, NAWM and DSCL samples using RNA-seq.
6. Perform bioinformatics analysis of the datasets generated by RNA-seq to identify significantly differentially expressed genes and dysregulated pathways, and functional groups.

2.2 Material and Methods

2.2.1 Ethics Statement and Case Selection

Frozen post-mortem deep-subcortical white matter blocks were acquired from the CFAS neuropathology brain bank in accordance with Research Ethics Committee approval (REC No: 15/SW/0246), Appendix I. All research was conducted blind to any clinical information.

MRI analysis of the formalin-fixed hemisphere and consultant radiologist scores using a modified Schelten's rating system enabled the identification of the control and DSCL white matter cases, where control WM cases had a score of 0, and DSCL had a score of 5 on the modified Schelten's rating. The sampling of the contralateral frozen white matter was performed by Dr Julie Simpson and Mrs Lynne Baxter. The list of all cases used in this study is shown in *Table 2.1*. The final cohort details are provided in Table 2.4.

Table 2.1 - Frozen deep-subcortical white matter cases obtained from CFAS neuropathology cohort

Case	Gender	Age	Post-Mortem Interval (hours)
RH23	M	73	23
23/94	M	92	33
RH11	F	84	6
100/00	F	78	75
RH6	M	88	11
RH6	M	88	11
NA47/97	M	75	29
121/96	F	85	12
105/94	F	76	36
178/96	F	96	15
31/00	M	90	79
03-00	unknown	unknown	unknown
11/98	M	74	20
127/94	M	83	28
RH3	F	82	unknown
106/94	F	88	27

-Post-Mortem Interval is the time between death and brain retrieval

2.2.2 Neuropathological Assessment of the sampled white matter blocks

Classification of the frozen post-mortem blocks as control white matter from non-lesional cases, DSCL and NAWM from lesional cases were confirmed using basic histological stains: haematoxylin and eosin (H&E), Luxol fast blue (LFB) and immunohistochemistry for CD68.

To prepare samples for the histological classification, 6 µm sections were collected on charged slides (Leica, UK) and stored at -20^{o}C until required. The sections were warmed to room temperature (RT) for 5 minutes (min), fixed in ice-cold acetone (Fisher Scientific, UK) at 4˚C for 5 min and air-dried for 3 min at RT. This fixation step is crucial to preserve the cellular structures within the tissue and permeabilize the tissue to enable penetration of the stain/antibody.

2.2.3 Haematoxylin and Eosin (H&E)

Haematoxylin and eosin (H&E) is a primary histological stain used to assess the architecture of a tissue (Bancroft and Gamble, 2008). The basic haematoxylin interacts with the acidic components of basophilic structures in the tissue section, including cell nuclei and ribosomes, staining them blue. In contrast, the acidic eosin stain interacts with the acidophilic cytoplasmic components and connective tissue, staining them red/pink (Bancroft & Gamble, 2008).

Sections were prepared as previously described in section 2.2.2. The sections were submerged in filtered Harris's haematoxylin (CellPath Ltd, Powys, UK) for 2 min at RT, and then differentiated in 1% acid/alcohol for approximately 30 seconds (sec). The sections were placed in 1M Scott's Tap water (where 8.75 g sodium bicarbonate and 50.0 g magnesium sulphate were dissolved in 2.5 L water) for 10 sec and rinsed in tap water for a few sec. Sections were placed in 1% eosin (CellPath Ltd, Powys, UK) for 5 min at RT. The sections were washed with tap water and then dehydrated through a graded series of alcohols (70%, 95%, twice in absolute ethanol) (Fisher Scientific, UK), for 30 sec each. The sections were cleared in xylene for 5 min, before being permanently mounted in distyrene plasticizer xylene (DPX) (Leica Biosystems), covered with a glass coverslip (Fisher Scientific, UK), and dried overnight at 40ºC in an oven.

2.2.4 Luxol Fast Blue (LFB)

Myelinated axons were visualised using Luxol Fast Blue (LFB), where regions of demyelination are recognised by loss of LFB stain. This basic histological stain involves an acid-base reaction,This basic histological stain involves an acid-base reaction, with the base of the lipoprotein in myelin replacing the base of the dye and this reaction causes a colour change to green/blue (Bancroft & Gamble, 2008).

Sections were prepared as previously described in 2.2.2 and immersed in LFB (0.1% LFB in 500 ml 95% ethanol [Fischer, UK] and 2.5 ml of glacial acetic acid added) for 2 hours (hrs) at 60^{o}C. Any excess stain was removed by washing in 70% ethanol

(Fisher Scientific, UK) before being rinsed with distilled water (dH_2O). The sections were differentiated in freshly prepared 0.5% lithium carbonate for 30 sec until the white matter and cortex were clearly defined. Sections were washed in tap water and dehydrated through a graded series of ethanol (70%, 95%, twice in absolute) (Fisher Scientific, UK) for 30 sec in each, cleared in xylene for 5 min, mounted in DPX permanent mounting media and dried at 40ºC in an oven overnight.

2.2.5 Immunohistochemistry for CD68: Standard protocol

The microglial lysosomal marker CD68 was detected in the sections using immunohistochemistry (IHC). The biochemical principle of IHC enables the visualisation and cellular localisation of proteins in tissue sections using a specific primary antibody directed against the antigen of interest (Bancroft & Gamble, 2008). In this study, the antigen:antibody binding signals were further amplified using a biotinylated secondary antibody and visualised using a standard horseradish peroxidase-conjugated avidin-biotin complex (ABC-HRP) technique (Vectastain Elite kit; Vector Laboratories UK) with 3,3'-diaminobenzidine (DAB) (Vector Laboratories UK) as the substrate. The IHC principle is illustrated in Figure 2.1.

IHC was performed using the Vectastain Elite Mouse IgG kit (Vector Laboratories, Peterborough, UK). Sections were prepared as previously described. Sections were covered with 1.5% normal horse blocking solution in Tris-buffered saline (TBS; 50 mM Tris, 150mM NaCl, pH 7.6) for 30 min at RT. Following serum removal from the sections, mouse monoclonal anti-human CD68 antibody (Dako, UK) was applied at a concentration

of 1:100, diluted in 1.5% blocking solution, and incubated for 1 hr at RT. Negative controls were included in every run and comprised either omission of the primary antibody or an isotype control at the same concentration as the primary antibody. The sections were rinsed with TBS for 5 min and incubated with 0.5% biotinylated secondary antibody for 30 min at RT. The sections were rinsed with TBS for 5 min and incubated with ABC-HRP (freshly prepared at least 30 min prior to use) for 30 min at RT. Sections were washed in TBS for 5 min, and antibody binding was visualised using the peroxidase enzyme substrate 3,3'-diaminobenzidine tetrahydrochloride (DAB) (Vector Laboratories, Peterborough, UK). The reaction was observed under a microscope, and once developed, the enzyme reaction was quenched by washing the slides with dH_2O. Sections were counterstained with Harris haematoxylin (Leica, UK) for 15 sec before being dehydrated through a graded series of ethanol for 30 sec each [70%, 95%, twice in absolute (Fisher Scientific, UK)], and then cleared in xylene (Fisher Scientific, UK) for 5 min, before mounting in DPX (Leica Biosystems), and dried overnight at 40ºC in an oven.

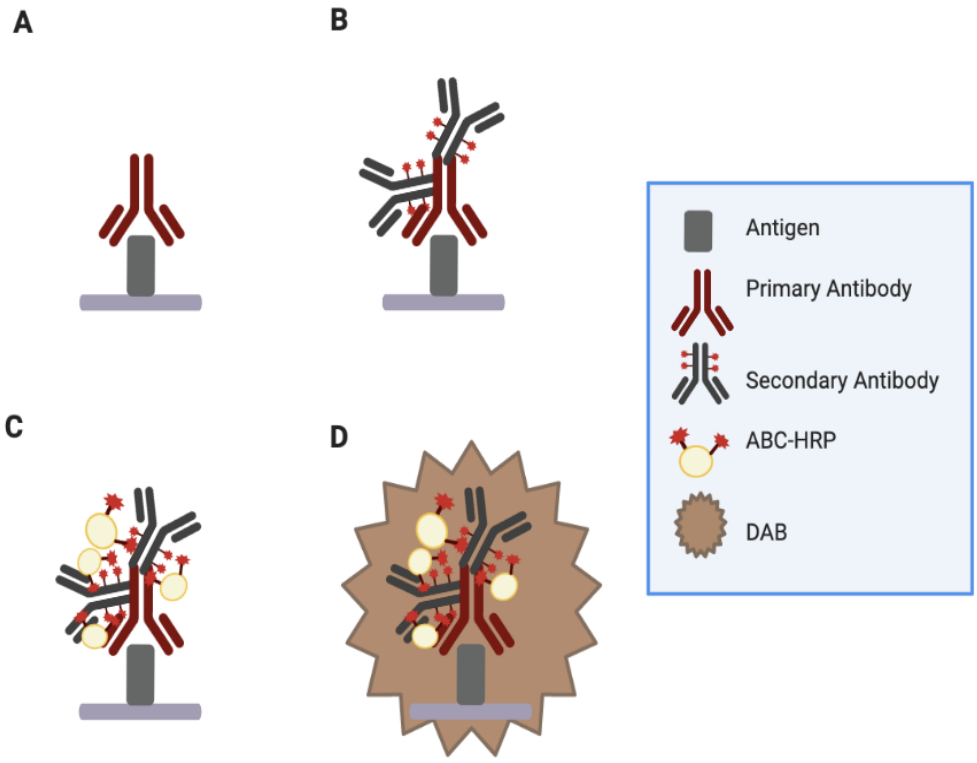

Figure 2.1 - Overview of Immunohistochemistry. (A) The primary unlabelled antibody binds with high affinity to the antigen of interest. (B) The specific biotinylated secondary antibody binds to the primary antibody. (C) ABC-HRP irreversibly binds to the biotinylated secondary antibody. (D) DAB, the HRP substrate, produces an insoluble reaction product, which is visualised as a brown precipitate; where ABC-HRP: horseradish peroxidase-conjugated avidin-biotin complex, DAB: 3, 3'-diaminobenzidine. Original figure created using biorender.

2.2.6 Histological Characterisation and Image Analysis

Histological characterisation of the deep-subcortical regions of interest confirmed whether the snap-frozen samples represented lesional or non-lesional white matter. The H&E and LFB staining enabled the location of the deep-subcortical regions and the visualisation of myelin attenuation, respectively. In addition, IHC allowed the presence of CD68 microglia to be assessed. Representative images for each case were captured using a Nikon Eclipse 80i microscope (Nikon Instruments Inc.).

Initially, twenty-three cases were assessed for evidence of demyelination and the presence of amoeboid CD68 microglia to enable white matter classification. The histological assessment of the cases was evaluated by three independent observers (Taghreed Almansouri, Olivia Jennings and Dr Julie Simpson), and confirmed by consultant neuropathologist Professor Stephen B. Wharton, blinded to the MRI scores. A qualitative description of each staining pattern across the entire section was noted using a light microscope. Subsequently, the frozen post-mortem blocks were categorised as either lesional (DSCL), normal-appearing white matter (NAWM) from lesional cases or control white matter from non-lesional cases.

In addition, all radiologically and histologically confirmed DSCL cases were matched with a separate NAWM block from the same case. For a block with a small discrete DSCL (<50% area of the total section), the same block was used to collect both NAWM and DSCL. Any DSCL case with no NAWM-matched case was excluded from the study.

2.2.7 Pre-LCM: Trizol RNA isolation and Integrity Analysis

In addition to histological classification, the starting RNA was also evaluated using a bioanalyser assay, Aligent 2100 (Agilent, UK). The RNA integrity number (RIN) is a numerical value to determine RNA degradation on a scale that ranges from 1-10, where 10 represents intact RNA, and 1 indicates degradation of the sample. The RIN quality is based on the 28S/18S ribosomal peak ratio, where the ratio is inversely related to degradation (Masotti and Preckel, 2006).

To determine RNA integrity, a 20-µm section of each block was collected into a sterile 1.5 ml Eppendorf tube, and RNA was extracted using the Trizol method (Life Technologies, Inc). In a fume hood, 500 µl Trizol reagent (Invitrogen, UK) was added to each Eppendorf and mixed with the tissue by a handheld homogeniser. Next, 200 µl chloroform (Fisher Scientific, UK) was added, vortexed vigorously for 5 sec, and incubated for 10 min at RT. The samples were centrifuged (Sigma centrifuges, UK) at maximum speed (20,000 g) for 15 min at 4°C. The upper aqueous layer was transferred into a fresh sterile 1.5 ml Eppendorf tube prior to adding 250 µl isopropanol and incubated for 10 min at RT. The samples were next centrifuged at 20,000 g for 10 min at 4°C. The supernatant was discarded, and the pellet was resuspended in 1 ml ice-cold (4°C) 75% ethanol (Fisher Scientific, UK) and mixed by vortexing for 5 sec. The samples were centrifuged at 15,000 g at 4°C for 5 min. After removing the supernatant, the samples were left to air dry for 5 min, and the pellet was resuspended in 25 µl sterile RNA-free water.

After extraction, the RNA quantity was assessed using a NanoDrop spectrophotometer (Thermoscientific, UK). The RNA samples were stored at -80°C for a later date when the RIN was evaluated using a picochip on the bioanalyser (Agilent, UK)

2.2.8 Sample Preparation for LCM

For RNA quality preservation and to avoid RNA degradation due to repeated freeze-thawing of the sample, LCM was performed on freshly prepared cryosections (CM3050S, Leica Microsystems, Milton Keynes, UK). Additionally, a rapid immunostaining protocol (discussed in 2.2.9) was used to preserve RNA quality, which reduced the protocol to around 20 min.

For LCM, 6-µm sections of each case were collected onto five uncharged sterile glass slides, one section per slide (Leica, UK) and warmed to RT for 1 min. The sections were fixed in ice-cold acetone (4°C) (Fisher Scientific, UK) for 3 min and then immunostained using a modified rapid ABC-HRP staining method.

2.2.9 Immunohistochemistry for CD68: Rapid protocol

The protocol was performed at RT, using sterile solutions made with diethylpyrocarbonate (DEPC)-treated water and under RNase-free conditions throughout the experiment.

The sections were blocked in 2% normal horse serum in TBS (Vectastain Elite kit; Vector Laboratories UK) for 3 min. Sections were incubated with anti-CD68 antibody

(Dako, UK), diluted in the blocking serum to a concentration of 1:10 for 3 min, and then rinsed briefly with TBS (150 µl in 10 ml Tris-buffered saline). Sections were incubated with 5% biotinylated secondary antibody (Vectastain Elite kit; Vector Laboratories UK) for 3 min. After rinsing in TBS, sections were incubated with 4% ABC-HRP (Vectastain Elite kit; Vector Laboratories UK), prepared at least 30 min before use, for 3 min and rinsed in TBS. The antibody binding was visualised using DAB (Vector Laboratories, UK) and incubated for 3 min. The sections were dehydrated in a graded series of alcohol (70%, 95%, twice in absolute ethanol) for 15 sec each; cleared in xylene (Fisher Scientific) for 2 min and left to air dry in a flow hood for a minimum of 60 min before LCM.

2.2.10 Laser Capture Microdissection

Laser capture microdissection (LCM) enables an enriched population of microglia, the particular cells of interest, to be isolated from a relevant white matter area of human post-mortem tissue. Previously this method demonstrated enrichment of the microglia within the collected cells (Waller et al., 2012). LCM was performed using the Veritas laser-capture microdissection system (Arcturus Engineering, Mountain View, CA, USA) and CapSure Macro caps, composed of a thermoplastic film mounted on a transparent cap (Arcturus Engineering, Mountain View, CA). The LCM system was set to ~12 µm spot size and ~70 mW power parameters. The immunostained sections and CapSure caps were loaded into the Veritas machine. Immunopositive cells were targeted by a focused infrared laser, causing the film to melt and the $CD68^{+}$ cells to adhere. Upon removing the cap, the targeted microglia were microdissected, leaving the non-targeted tissue behind

(Emmert-Buck et al., 1996). The LCM collection process is demonstrated in Figure 2.2. After approximately 2 hr of microdissection, a minimum of 2500 microglia were isolated. The film was carefully removed from the cap using sterile forceps and transferred to a sterile 0.2 ml Eppendorf tube with 50 µL extraction buffer (a component of the RNA PicoPure Isolation kit, Applied Biosystems, USA) and stored at -80°C until required for RNA extraction.

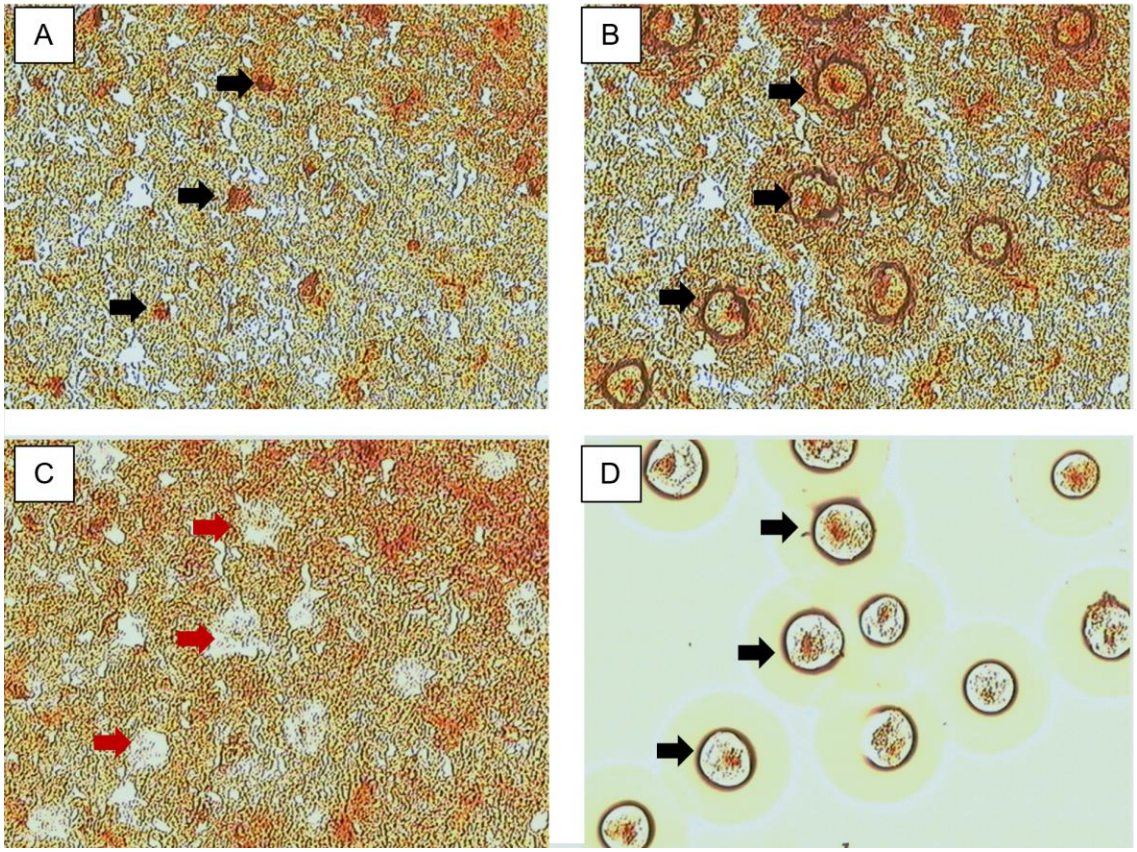

Figure 2.2 - Overview of the Laser Capture Microdissection procedure; a mechanism of isolating a cell of interest from a tissue section (A) microglia are visualised as darkly stained cells using the CD68 marker (B) CD68 cells are targeted for microdissection with an IR laser beam (C) Firing the laser causes the thermoplastic film to melt and adhere to the underlying microglia leaving empty spots (as indicated by the red arrows) within the tissue (D) Removal of the cap isolates the CD68 microglia from the surrounding tissue. CD68 microglia are indicated by the black arrows.

2.2.11 Post-LCM: RNA Extraction and Integrity Analysis

Total RNA was extracted from the LCM-isolated cells using the PicoPure RNA isolation kit (Life technologies: Applied Biosystems, USA). The film was incubated with 50 µl extraction buffer at 42°C for 30 min in a heat block. In the meantime, an extraction column was prepared by adding 250 µl conditioning buffer and incubated for 5 min at RT, before being centrifuged at 13300 g for 1 min, and the flow-through discarded. Next, 50 µl of 70% ethanol was added to the sample, mixed by gentle pipetting and transferred to the pre-prepared extraction column. The column was centrifuged at 100 g for 2 min to allow the RNA to bind to the column before being centrifuged at 13300 g for 1 min. 100 µl of wash buffer 1 was added, and the column was centrifuged at 8000 g for 1 min. 100 µl of wash buffer 2 was then added, and the column was centrifuged at 8000 g for 1 min. This step was repeated with the centrifugation speed increased to 13300 g for 1 min. The flow-through was discarded, and the column was transferred to a new sterile 1.5 ml Eppendorf tube. In the final extraction step to elute the RNA from the isolated cells, an 11 µl elution solution was added to the column and incubated for 1 min at RT. Following 1,000 g for 1 min centrifugation, the column was centrifuged at 13,300 g for 2 min. The isolation process enabled total cellular RNA to be obtained in a low ionic strength buffer volume. The quantity and quality of extracted RNA were measured using a NanoDrop 1000 spectrophotometer (Labtech International, Uckfield, UK) and a 2100 Bioanalyzer,

respectively (Agilent, UK). All RNA samples were stored under sterile conditions at −80°C for future downstream applications.

2.2.12 Sample selection to proceed with RNA-sequencing

Post-LCM RNA Integrity Analysis was performed. At this stage, only samples with two prominent ribosomal peaks were chosen to proceed with RNA-sequencing; post-LCM samples with no ribosomal peaks were eliminated from the study. In total, 4 control cases and 4 matched NAWM and DSCL cases were identified to proceed. For easier tracking, sample identification numbers were replaced by order numbers 1-12, as indicated in Table 2.2. The final cohort details are provided in Table 2.4.

Table 2.2 - The final list of 12 samples identified for RNA-sequencing

Case number	White matter group	Respective number
100/100 (8)	Control	1
23/94(11)		2
RH23H6		3
RH11H5		4
31/00 (8)	NAWM	5
178/96 (12)		6
11/98 (11) NA		7
127/94(9)		8
31/00 (9)	DSCL	9
178/96 (10)		10
11/98 (9)		11
127/94(9)		12

2.2.13 RNA-sequencing: Protocol

The twelve chosen RNA samples were transferred to the Sheffield Diagnostic Genetics Service at the Sheffield Children's Hospital NHS Foundation Trust. Dr Timothy Wright, a genetic technologist at the aforementioned unit, performed the entire experiment, including library preparation and RNA-sequencing. Due to the COVID-19 pandemic restrictions, neither participation nor observation of the experiment were permitted. The entire procedure was conducted by Dr Wright who then provided a summary report of the data obtained.

- **cDNA Library Preparation and Sample Sequencing**

The sequencing services processed the samples using a low input RNA library prep kit for Illumina (NEB, US), using a maximum input of 8 µl. As per the NEBNext Ultra II Low input RNA kit protocol, the mRNA was first fragmented and then converted to cDNA, and amplified by 20 cycles of amplifying PCR. The next step was adding adapters to each fragment, permitting recognition of the DNA and creating the library (Library preparation index illustrated in Table 2.3).

The cDNA library underwent amplification, which involves reverse transcription followed by a DNA polymerase chain reaction (PCR). Afterwards, quality control checks were performed to assess both the library concentration and the library fragment length. The DNA library was then sequenced at a single 100 bp read (a reasonable length to detect

low-expression transcripts) using the Illumina HiSeq 2500 platform and aimed for a 5% PhiX spike to cope with any low diversity.

Table 2.3 - Index used for library preparation.

Sample No	ID	Index no.	Sequence
1	100/100 (8)	2	CGATGT
2	23/94 (11)	7	CAGATC
3	RH23H6	8	ACTTGA
4	RH11H5	10	TAGCTT
5	31/00 (8)	11	GGCTAC
6	178/96 (12)	13	AGTCAA
7	11/98 (11) NA	14	AGTTCC
8	127/94 (9)	15	ATGTCA
9	31/00 (9)	16	CCGTCC
10	178/96 (10)	18	GTCCGC
11	11/98 (9)	20	GTGGCC
12	127/94 (9)	21	GTTTCG

- **Quality Control of Sequenced Samples**

The Sheffield Diagnostic Genetics Service performed four quality control measurements throughout the entire process. The quality checks involved initial sample evaluation (once samples arrived at the department), post-cDNA-preparing evaluation, library preparation evaluation, and a final quality control check after the post-sequencing metrics assessment. The quality control checks were achieved using both the Qubit 2.0 fluorometer (Qubit assay, Thermofisher) and Tapestation System (Agilent 2200) to evaluate sample concentrations and size/profile, respectively. The Agilent 2200 Tapestation System can be used for all measurements (sample concentration, size and profile); however, it is less accurate than the Qubit. Hence, both systems were combined for precise measurements.

2.2.14 RNA-sequencing: Data Analysis

Data analysis comprised several stages; it began with multiple quality control assessments for the sequenced transcript datasets. The sequenced profiles were then aligned to the reference human genome and assembled to generate an RNA sequencing map that expands the transcriptome. Following this, the data were tested for differential expression, which enables the recognition of the functional profile. For these analyses, Galaxy, Degust and Gorilla software were used. The outcome results were checked and confirmed by Dr Mark Dunning, director of the Sheffield Bioinformatics Core Facility at the University of Sheffield.

The Galaxy web platform, a public server at usegalaxy.org version 1.9, was used for quality assessment, alignment, quantification and differential expression testing. Firstly, the fastq files, the raw data standard storing format generated from the sequencing experiment, were uploaded to the Galaxy website. Initially, the data reads per sample were spread across two fastq files. The Concatenate Datasets tool was used to combine the two fastq files for each sample and the resulting file used in the subsequent analysis.

The FastQC tool determined the quality scores associated with the concatenated fastq files for quality assessment. The tool interprets the results using a traffic light system, where green refers to quality checks passed, while red indicates the failing of quality checks. The multiple quality-control reports were then aggregated into a single report using the MultiQC tool; to enable comparisons and quickly analyse data across all samples.

Following quality assessment and the HISAT2 tools, the reads from the concatenated fastq files were mapped and aligned to a build-in reference human genome (an annotation-based genome-guided assembly). Since the data originated from genomic material that crosses exon/intron boundaries, a splice-aware mapper for RNA-seq reads (HISAT2) was used to identify splice junctions between exons. Afterwards, a Compact Idiosyncratic Gapped Alignment Report (CIGAR) was generated to pair the given sequences with their assigned position at the reference genome. The CIGAR involves a series of letters and numbers that indicates the number of consecutive bases that have been mapped, for example, alignment matched, insertion, deletion, skipped, and soft or hard clipping.

The quality-control statistics for aligned reads were calculated using samtools, enabling analysis of high-throughput sequencing data. The quality control for the aligned data flagged any unmapped, unpaired, failed QC and duplicated PCR reads. A high aligned percentage (80%) is expected for RNA-sequencing.

Quantification of gene expression levels were identified based on the frequency of reads per sample. The HTSeq-count tool generates a count matrix table that displays the frequency of gene reads mapped in each sample. In order to prepare the data for further gene expression tests and visualisation steps, the generated read tables were collected in a single table using the Column-Join-on tool. The generated count matrix table has a specific design where each row is a measured gene, and each column is a different biological sample. The file was then converted to CSV format.

- **Interactive exploration of the results with DEGUST**

Degust is a tool used to test differential gene expression; it produces an interactive view of the results by plotting the data using principal component analysis (PCA). PCA facilitates data expression by showing the relationships in three axes and enables the identification of outliers which can then be excluded from downstream analysis. For this purpose, the CSV count files produced from the previous step were uploaded to Degust. No further investigation was carried out on the data.

2.3 Results

2.3.1 Histological characterisation of Control, DSCL, and NAWM samples

MRI classification of the formalin-fixed hemisphere guided the contralateral frozen hemisphere sampling. The sampled white matter blocks then underwent histological characterisation to determine whether control, DSCL, or NAWM had been sampled, as previously detailed.

The LFB staining pattern for both the control WM from non-lesional cases and the NAWM from lesional cases displayed a regular pattern of LFB and H&E staining, indicative of intact myelin (Figure 2.3 A-B and D-E). The lesional cases, in contrast, were histologically characterised by a reduction in LFB staining and pale H&E staining, indicating myelin loss; Figure 2.3 C and Figure 2.3 F.

Immunohistochemistry for CD68 within the control WM and NAWM cases displayed few microglia cells with a ramified morphology. While the microglia in DSCL cases had a dense distribution with an amoeboid morphology, as shown in Figure 2.3 G, Figure 2.3 H, Figure 2.3 I, respectively.

Generally, all DSCL cases had large lesions encompassing the majority of the tissue section and were characterised by prominent demyelination. There was one case that contained a smaller discrete lesion, which was easily distinguished from the surrounding NAWM. In this case, the DSCL exhibited focal loss of LFB staining indicating demyelination compared to the regular pattern of blue staining in the surrounding NAWM. When the LFB was cross-referenced with the CD68 immunostaining, the focal lesion was characterised by prominent CD68 microglia with an amoeboid morphology; in contrast, microglia within the surrounding NAWM displayed a ramified profile: Figure 2.4. For this tissue block that contained the discrete lesion, and where both the DSCL and NAWM were readily identifiable and clearly differentiated, both DSCL and NAWM samples were collected from this case block.

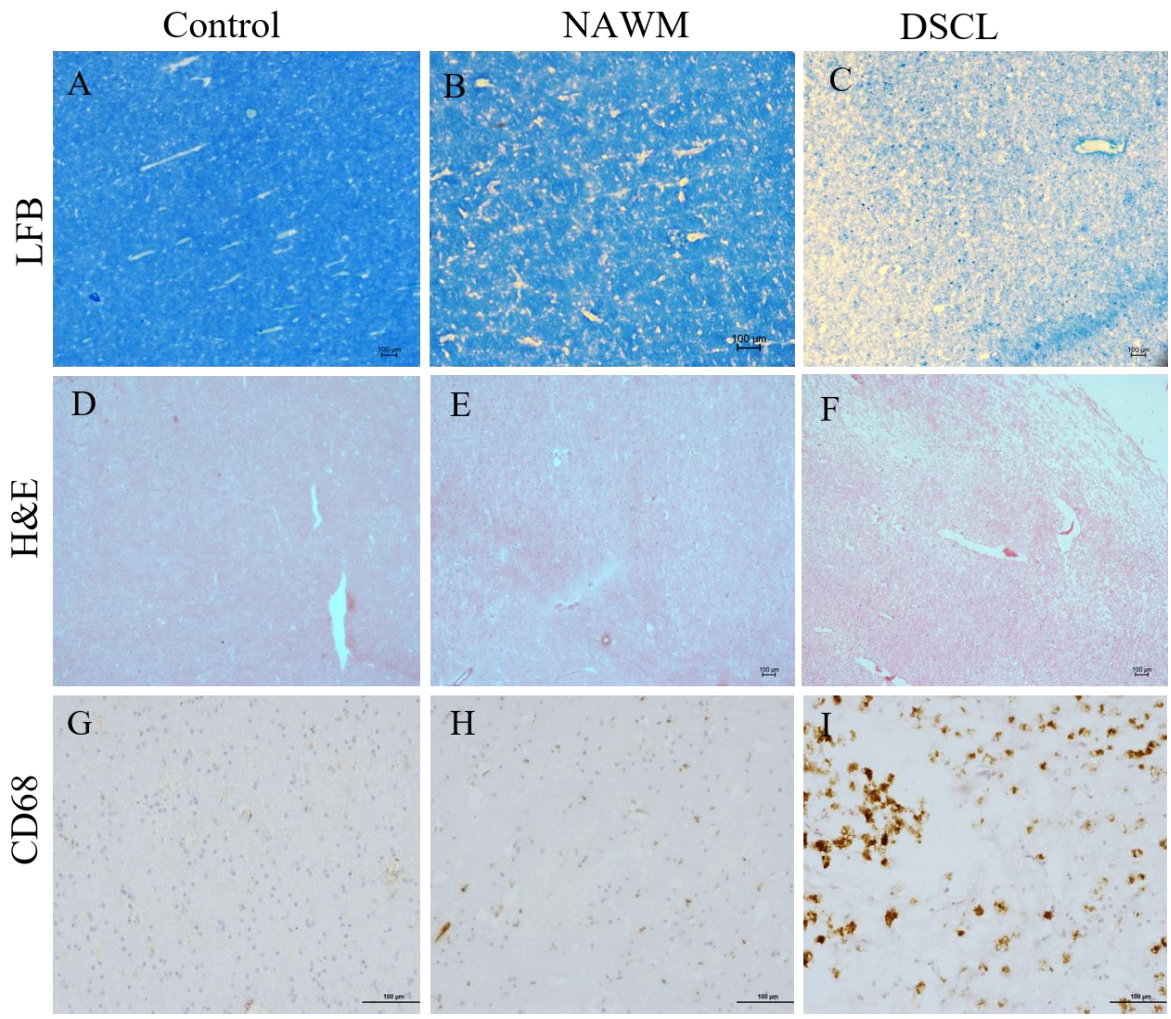

Figure 2.3 - Histological characterisation of deep-subcortical WM. Luxol fast blue (LFB), H&E staining and immunohistochemistry for CD68 were used to classify the deep subcortical white matter. Both the control white matter from non-lesional cases and NAWM from lesional cases displayed a regular pattern of LFB and H&E histological staining and a regular distribution of CD68 immunoreactive microglia with a ramified profile (A, B, and C, respectively). In contrast, the associated DSCL presented pale LFB and H&E and prominent CD68 immunoreactive microglia with an amoeboid morphology (D-F, respectively). Scale bar represents 100 µm.

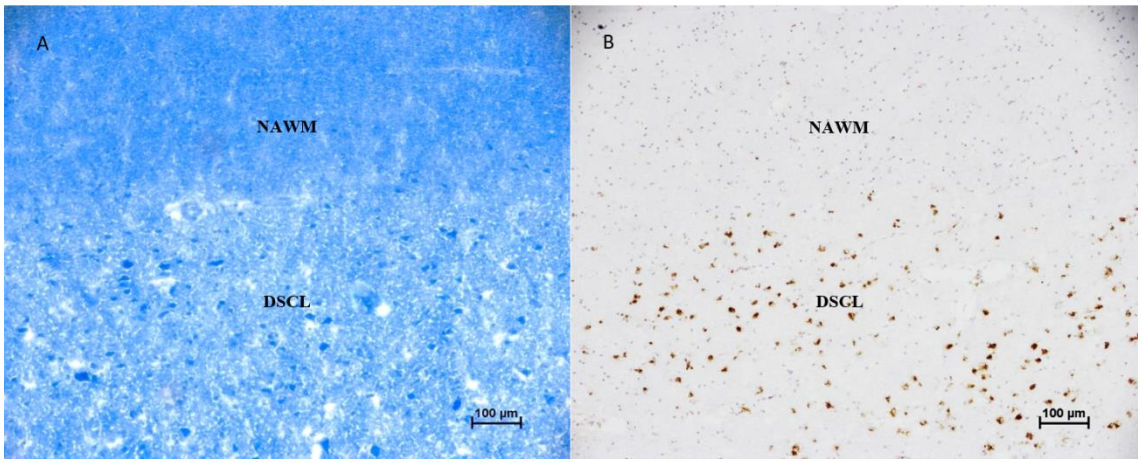

Figure 2.4 - LFB and CD68 staining of a discrete lesion. (A) LFB staining demonstrates myelin loss within the lesion, surrounded by intact myelin in the NAWM. (B) Large CD68+microglia are a prominent feature of DSCL, while the microglia in the adjacent NAWM are smaller with a ramified morphology. The dense blue cell-associated stain seen in the LFB stained lesion likely indicates microglia, which have phagocytosed the myelin (Boven et al., 2006). Scale bar represents 100 µm. The representative figure is for sample 127/94(9).

2.3.2 Cases excluded from the study

Where MRI classification was not compatible with the histological characterisation, these cases were excluded from the study (n=6). Two cases were radiologically classified as non-lesional NAWM, however, histological examination revealed the presence of high levels of amoeboid CD68 microglia; therefore, they were not included in the study. Similarly, one block was radiologically classified as DSCL; however, it displayed no evidence of demyelination or high levels of CD68 microglia following histological evaluation; therefore, it was excluded from the study. Furthermore, any DSCL case with no matched NAWM block was excluded from the study (n=3).

In addition to the histological evaluation, the RNA quality was also evaluated. All LCM samples with no visible ribosomal peaks were eliminated from the study (n=3). A summary of the original case list and the elimination reasons are displayed in Table 2.4.

Table 2.4 - The original list of CFAS blocks used for the current project. The columns compare MRI reports and histological classification findings. Samples were excluded from the study if the MRI and histological classifications did not match, if no matched NAWM and DSCL blocks were obtained from the same case, or if the RNA profile was poor. Cases excluded from the study are highlighted in blue. Noticing that sample 127/94 (9) was used for both DSCL & NAWM.

Case	MRI classification	Histological classification	For the Excluded samples- Reason for elimination
RH23 H6	Control	Non-lesional	
23/94 (11)	Control	Non-lesional	
RH11 H5	Control	Non-lesional	
100/00 (8)	Control	Non-lesional	
RH6	Control	Non-lesional	Post-LCM sample had a poor RNA profile
NA47/97	NAWM	Lesion	Classifications Mismatched
121/96 (11)	NAWM	Non-lesional	Post-LCM sample had a poor RNA profile
11/98 (11)	NAWM	Non-lesional	
105/94 (10)	NAWM	Lesion	Classifications Mismatched
178/96 (12)	NAWM	Non-lesional	
31/00 (8)	NAWM	Non-lesional	
03-00(4)	DSCL	Non-lesional	Classifications Mismatched
11/98 (9)	DSCL	Lesion, large	
105/94 (11)	DSCL	Lesion, large	Matched cases were excluded
178/96 (10)	DSCL	Lesion, large	
31/00 (9)	DSCL	Lesion, large	
127/94 (9)	DSCL	Lesion, small	
121/96 (10)	DSCL	Lesion, large	Post-LCM sample had a poor RNA profile
RH3 H3	DSCL	Lesion, large	No matching block
106/94 (25)	DSCL	Lesion, large	No matching block

2.3.3 RNA Quantity and Quality Assessments

A total of twelve deep subcortical white matter samples were identified from the CFAS neuropathology cohort to be taken forward for transcriptomic profiling by RNA-seq. These samples were classified as Control (from non-lesional cases), DSCL and NAWM (both areas matched from the same case), n=4 per group.

Prior to LCM, RNA was extracted using TRIzol, and the RNA quality was assessed. During LCM, the microglia were collected from the deep-subcortical region; afterwards, the RNA quality was assessed. The pre-and post-LCM RIN numbers for the samples are shown in Table 2.5. In addition to the RIN values, the picochip assay provides a profile of the RNA; while the RIN values are a suitable indicator of RNA integrity, the RNA profile should also be considered, as it provides a visual representation of the RNA quality of the samples.

Representative picochip profiles displaying the range of RNA qualities are shown in Figure 2.6 These include a representative electrogram of a case containing well-preserved RNA, evidenced by the clear 18s and 28s ribosomal peaks (Figure 2.6A), a case with moderate degradation levels, where ribosomal peaks are present but not as prominent as those seen in Figure A (Figure 2.6 B), and a case with highly degraded RNA with indiscernible ribosomal peaks and no associated RIN value (Figure 2.6 C).

Table 2.5 - Pre- and Post-LCM RIN values.

Case number	Pre-LCM RIN number	Post-LCM RIN number
1	2.9	n/a
2	2.2	n/a
3	-	n/a
4	6.4	n/a
5	2.9	n/a
6	4.5	n/a
7	6.4	n/a
8	-	n/a
9	2.3	n/a
10	3.5	n/a
11	n/a	n/a
12	2.3	n/a

n/a = no RIN value obtained

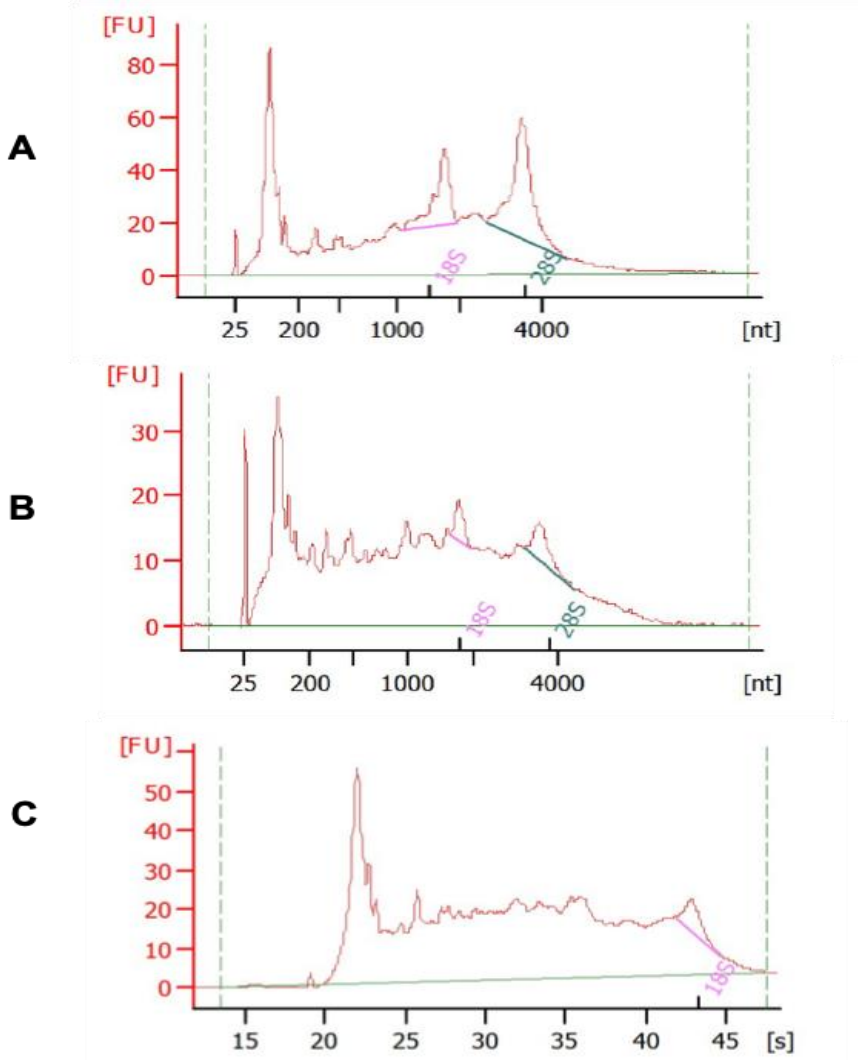

Table 2.6 - RIN integrity profile of frozen post-mortem tissue. Representative electrograms of cases with (A) high levels of intact RNA, and RIN value of 6.4 (B) reasonable RNA preservation with a RIN value of 2.9 and (C) highly degraded RNA with no RIN measurement obtained. The peaks represent 18s and 28s ribosomal RNA, respectively. (FU): fluorescence units, (nt): runtime in seconds

2.3.4 Quality Control Measurements

Several quality control measurements were performed at the Sheffield Diagnostic Genetics Service throughout the sequencing preparation process. Due to the pandemic restricting access to the Facility, Dr Timothy Wright performed all the experiments and provided the illustration figures in this section.

2.3.4.1 Initial Quality Control

In addition to the bioanalyzer assays performed for post-LCM RNA samples, a further initial quality control check was performed using the Qubit assay (Qubit RNA HS Assay Kit), and sample qualities were all too low to be detected. A second initial quality assessment was performed using Tapestation (High Sensitivity RNA Screentape). The results showed low RNA concentrations (Table 2.7) and highly degraded RNA, which is likely to reflect both the use of PM tissue and the LCM approach of sample collection, Figure 2.5; which was not optimal for the low input RNA workflow (which recommends RIN >8). After discussion with the people involved, it was decided to continue using the maximum input volume and then assess quality control after library preparation.

Notably, the warning in the file below indicated expired Screentapes. Due to the pandemic, the unit was having supply problems at this point, and hence they had to use a very slightly expired tape rather than delaying the project to assess the inputs that were going into the workflow.

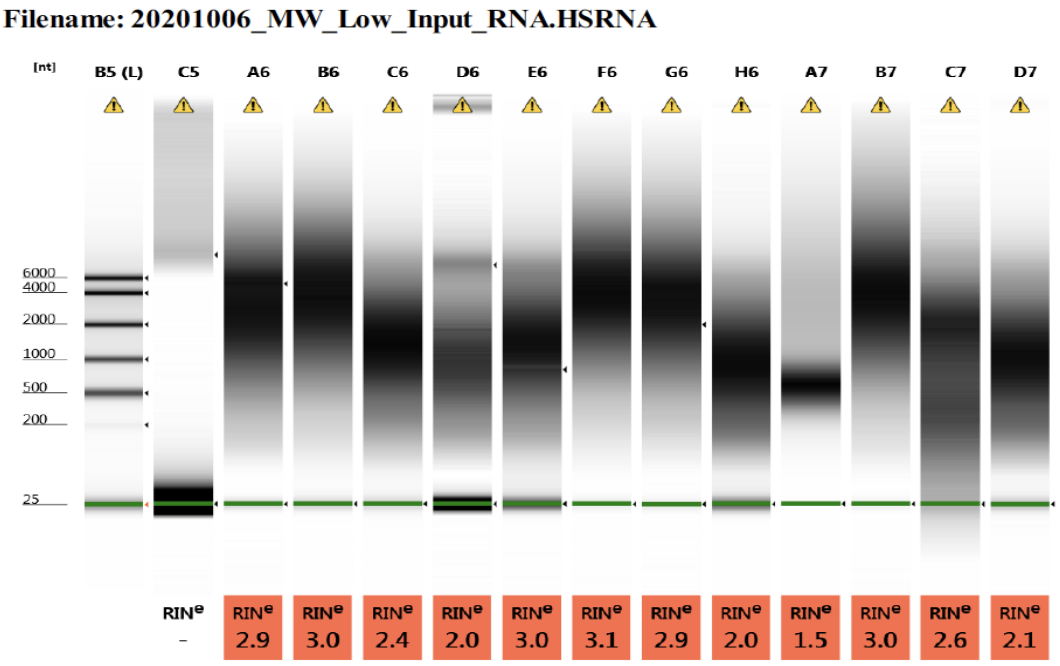

Figure 2.5 - Initial QC Tapestation results indicating the RIN values of all LCM-ed samples

Table 2.7 - Initial RNA concentration for the 12 samples RNA-seq, measured by Tapestation

Case number	RNA Conc (pg/ µl)
1	28400
2	22300
3	19300
4	1650
5	4680
6	58300
7	54200
8	5540
9	23200
10	84400
11	12400
12	12300

2.3.4.2 cDNA Quality Control

A second quality control measurement was taken after creating the cDNA using DNA Qubit (Qubit dsDNA HS Assay kit). Table 2.8 displays the Qubit concentration readings and how much cDNA was used for the library preparations. Tapestation quality measurements did not show anything, possibly due to the size of the product at this point.

Table 2.8 - Summary of cDNA Qubit reads and the cDNA statistic input for library preparation

Sample ID	cDNA Conc. (Ng/µl)	Volume (µl)	Total Yield (ng)	ng cDNA to use (ideal range 1-20ng)	Vol to use	Vol of 1X TE (to make up to 26µl)
1	0.63	15	9.45	9.45	15.00	11.00
2	1.43	15	21.45	20.00	13.99	12.01
3	4.52	15	67.80	20.00	4.42	21.58
4	0.916	15	13.74	13.74	15.00	11.00
5	0.388	15	5.82	5.82	15.00	11.00
6	1.24	15	18.60	18.60	15.00	11.00
7	1.05	15	15.75	15.75	15.00	11.00
8	0.696	15	10.44	10.44	15.00	11.00
9	2.24	15	33.60	20.00	8.93	17.07
10	1.74	15	26.10	20.00	11.49	14.51
11	0.442	15	6.63	6.63	15.00	11.00
12	0.852	15	12.78	12.78	15.00	11.00

2.3.4.3 Library Quality Control

Quality measurements were taken using both DNA Qubit (Qubit dsDNA HS Assay kit, Table 2.9, and following advice from Dr Wright, it was decided to proceed with the sequencing. The libraries were pooled using their molarity calculated from the Qubit concentration and Tapestation sizing (Equimolar pooling).

Table 2.9 - Table summarising the Qubit check for the prepared library and the statistical measurements for sequencing input

Sample ID	Estimated cDNA input (ng)	Final library Qubit ng/µl	Yield (in 30µl)	Peak Size (bp)	Molarity nM
1	9.5	3.5	105	310	17
2	20.0	6.5	195	335	29
3	20.0	8.5	255	315	41
4	13.7	5.36	161	328	25
5	5.8	2.62	79	320	12
6	18.6	9.07	272	338	41
7	15.8	6.18	185	332	28
8	10.4	3.38	101	321	16
9	20.0	7.03	211	308	35
10	20.0	7.5	225	314	36
11	6.6	2.55	77	309	13
12	12.8	3.79	114	315	18

2.3.4.4 Sequencing Summary Metrics

The last quality control check concerned the sequenced materials, a run of the metrics is presented in Table 2.10. To start with, the cluster density was poor (~420Kmm2, about half of the expected levels). % Clusters were slightly low (~80%, as opposed to the preferable >90%) and %> =Q30 was very low (~54%). PhiX (Aligned %) was higher than expected at 20%. This suggests the library did not cluster well. The thumbnail images confirm the library is under clustered, rather than over clustering masquerading as under clustering. This suggested issues with both the quantity and the quality with these libraries, likely due to the low quality of the starting material.

Despite the low cluster density and high PhiX, the quality metrics are imperfect. There are around 80% reads passing filters (which is low considering the density), %Q30 is about 50%, and the phasing is relatively high (>0.5). Looking at the % base metric, Figure 2.6, the library has shallow diversity and very high GC content (despite PhiX being at 20% and therefore mediating this effect somewhat).

Table 2.10 - Run summary data generated by the Illumina

Level	Yield total (G)	Project total yield (G)	Aligned (%)	Error rate (%)	Intensity cycle 1	%>= Q30
Read 1	12.6	12.6	20.24	1.34	4140	54.0
Read 2	0.6	0.6	0.00	0.00	12559	40.0
Total	13.2	13.2	20.24	1.34	8349	53.2

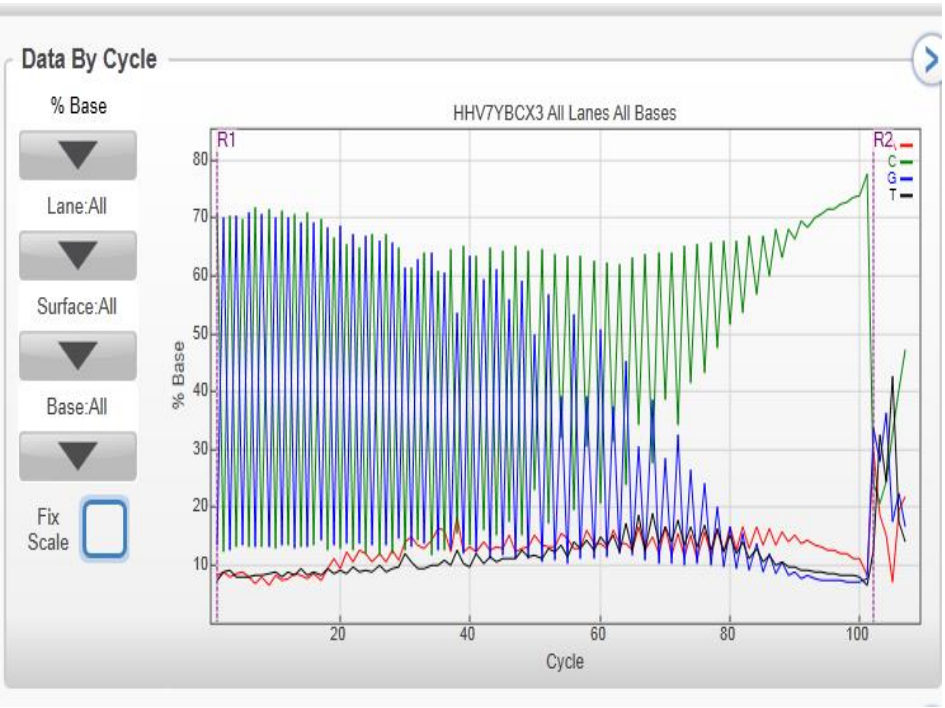

Figure 2.6 - Metric read for the base percentage, where the GC content was high across the reading, and only C toward the ends. The AT % is very low, less than 20%.

2.3.5 Data Analysis: The Galaxy MultiQC report

The MultiQC report produced an overview of the main findings, plus individual quality scores, including: sequence counts; a sequence quality histogram; per sequence quality scores; per base sequence contents; per sequence GC contents; per base N content; sequence length distribution; sequence duplication levels; over representative sequences; adapter content and status checks, each of which are illustrated below (from Figure 2.7 to Figure 2.13). Studying these graphs on an active page within the software had additional advantages, such as shifting over each spot to provide further related information including: the sample identification number; base-pair position and zoom-in/out of a specific region across the particular area of the gene(s).

To start with, the broad statistical outlines were assessed, Table 2.11 confirmed that the samples were sequenced for a singlelength 101 bp to generate a read that varied between 3.1 - 16.8 million. The table also identified the poor sample quality; all samples had a partial readfailure, with a range between 36-45%. In addition, all the samples had a high GC enrichment content, and a high level of duplication.

For whole-genome data, a high level of data coverage is expected where almost all the data reads will be unique. However, as demonstrated in Figure 2.7, the sequenced data in the current study had a small number of unique reads, less than a third, with a percentage ranging between 17.7 - 33.3%, indicating a poor report for the of the target sequences.

Table 2.11 - A general statistics overview for the sequenced material presenting the length of sequence, the number of reads (in Million), the percentage of fail reads, the GC content ration, and the duplication ratio.

Sample Name	Length	M Seqs	% Failed	% GC	% Dups
Sample__pd__1-Combine_fastq	101 bp	3.1	45%	87%	76.5%
Sample__pd__10-combine_fastq	101 bp	8.4	36%	89%	80.1%
Sample__pd__11-combine_fastq	101 bp	9.6	36%	89%	81.2%
Sample__pd__12-combine_fastq	101 bp	8.6	45%	90%	80.8%
Sample__pd__2-combine_fastq	101 bp	6.0	36%	87%	77.7%
Sample__pd__3-combine_fastq	101 bp	6.9	36%	90%	82.3%
Sample__pd__4-combine_fastq	101 bp	7.8	36%	88%	80.0%
Sample__pd__5-combine_fastq	101 bp	16.5	45%	83%	67.3%
Sample__pd__6-combine_fastq	101 bp	6.3	36%	89%	80.9%
Sample__pd__7-combine_fastq	101 bp	6.1	45%	90%	81.7%
Sample__pd__8-combine_fastq	101 bp	9.5	45%	80%	66.8%
Sample__pd__9-combine_fastq	101 bp	16.8	45%	83%	78.8%

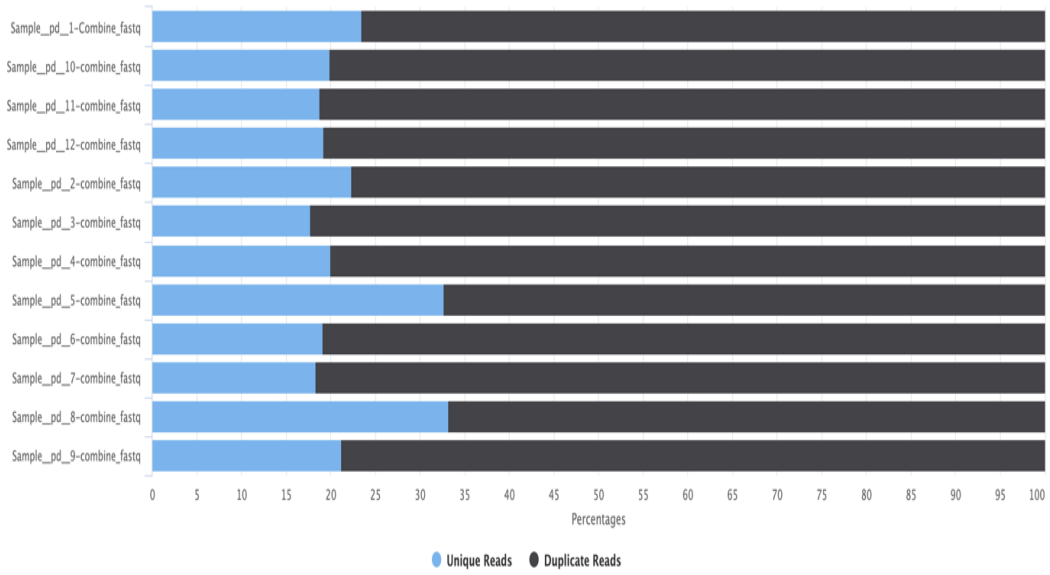

Figure 2.7 - The percentage sequence counts for the sequenced samples. Generally, across all samples, less than a third was a unique sequence while the remaining reads were duplications.

The *per-base sequence content* measures the proportion of each of the four nucleotides called per base position across all reads in the input sequence file. For whole-genome DNA sequencing, the four-nucleotide diversity is relatively constant with %G=%C and %A=%T. The per-base sequence content failed for the current sequenced data, indicated by red dashes next to each raw sample presented in Figure 2.8 A.

Figure 2.8 A is an overview of all the samples, where an individual detailed chart with the position of base-pair reads and TACG ratio content across the total reads can be seen. Figure 2.8 B is an exemplary representative for sample 1. As seen in the chart, there was a low diversity of nucleotides as the sequenced data is dominated by reads that are almost all G and C bases, and just Gs at the end of the read. The GC enrichment sequence indicated poor material quality across all the sequenced samples.

The average GC content displayed the number of GC bases per read. The diagram is comparable to the theoretical distribution based on a constant GC content assumption for all reads, which naturally appears as a peak curve. However, the current sequenced data curve shifted from the normal distribution, causing the failure of FastQC data (illustrated in Figure 2.9) and indicating the low nucleotide diversity of the samples.

A

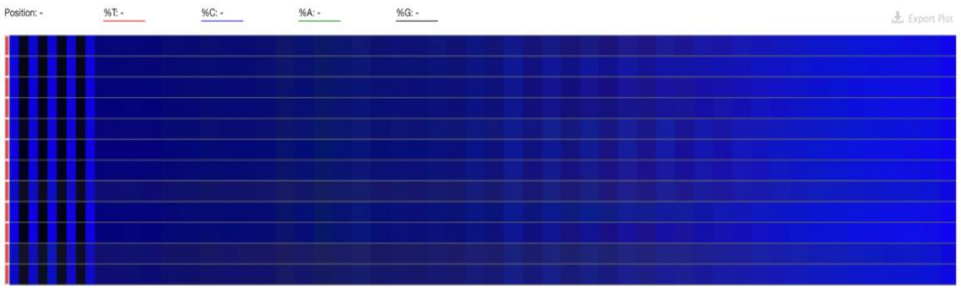

B

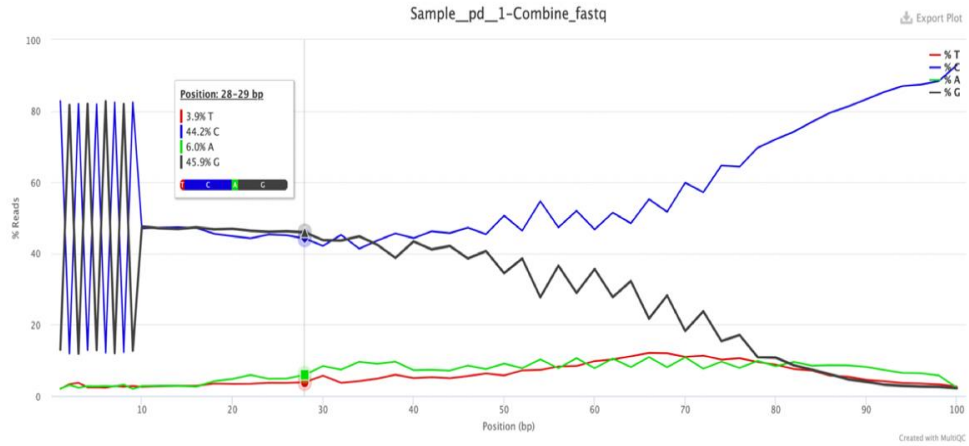

Figure 2.8 - Per-Base Sequence Content, where distribution of the four nucleotides is measured. (A) is an overview of nucleotide counts across the read, where shifting across the chart will display the base-pair location and nucleotide percentage, (B) a representative chart for an individual per base count representative of sample 1, where the GC content is dominant across the whole read, and G elevates towards the end of the read.

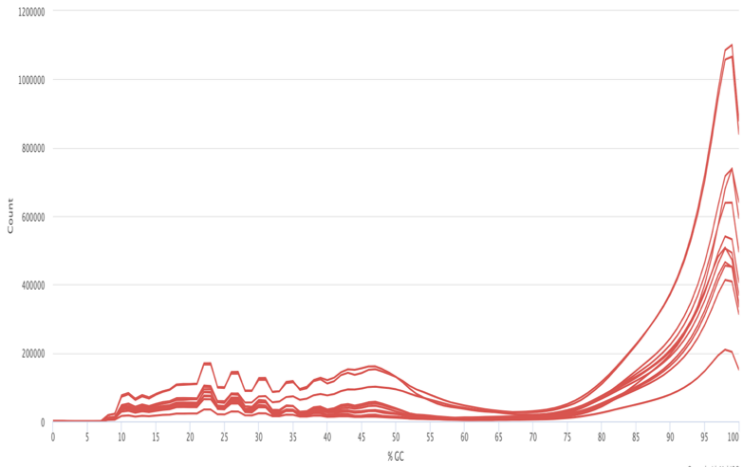

Figure 2.9 - Per-Sequence GC Content distribution curve. The peak curve shifts from a normal distribution due to the low nucleotide diversity of the samples.

During the sequencing, and when the sequencer is incapable of making a base call with satisfactory confidence, the program will substitute an N rather than a conventional base. Typically, with sequencing, a low proportion of Ns appears, particularly toward the sequence's end. The per-base N plotted diagram for the 12 sequenced samples is presented in the Figure 2.10, where it follows the traffic-light system. The sequencing reads had six warning flags for samples 2, 3, 4, 6, 10 and 11 for the N ratio passing 5% of the total reads. The remaining samples 1, 5, 7, 8, 9 and 12 failed for having the N ratio higher than 20%.

The sequenced data output was considered over-representative for having a sequence that makes up more than 0.1% of the total; Figure 2.11. For the over-representative sequence, matching sequences were looked for, and the best matching sequences are listed in Table 2.12. As the table displays, some of the over-representative sequences were compared with a Clontech SMART primer used during cDNA synthesis at the start of the library preparation.

Checking the adapter content is a cumulative plot of the proportion of adapter sequences identified at each position. Searching for the specific adaptors used during the library preparation demonstrated that the sequence outputs were clear of any contaminated reads from the adaptors, and all samples fell within the green zone, as shown in Figure 2.12.

A summary of the entire MultiQC quality check is presented in Figure 2.13.

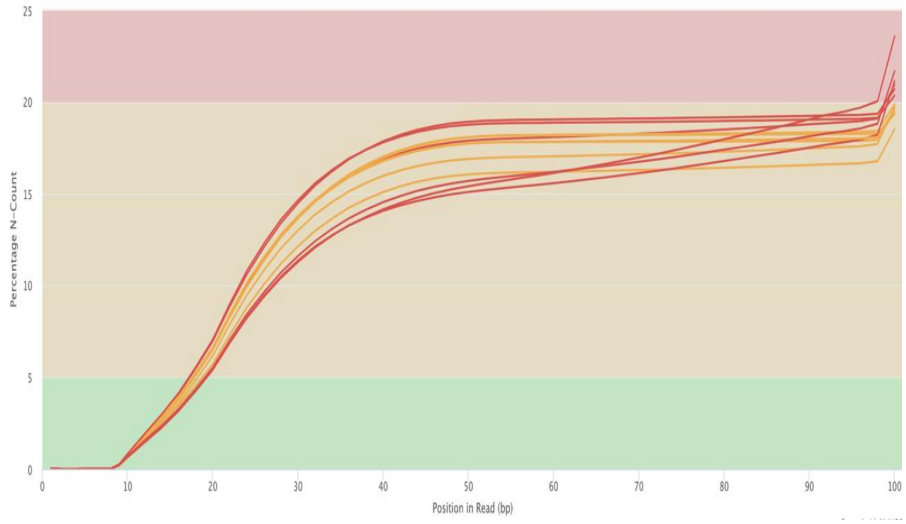

Figure 2.10 - The graph represents the Per-Base N Content for each sample. The 12 samples presented either warning or failing reads, where the N ratio was above 5% and 20%, respectively.

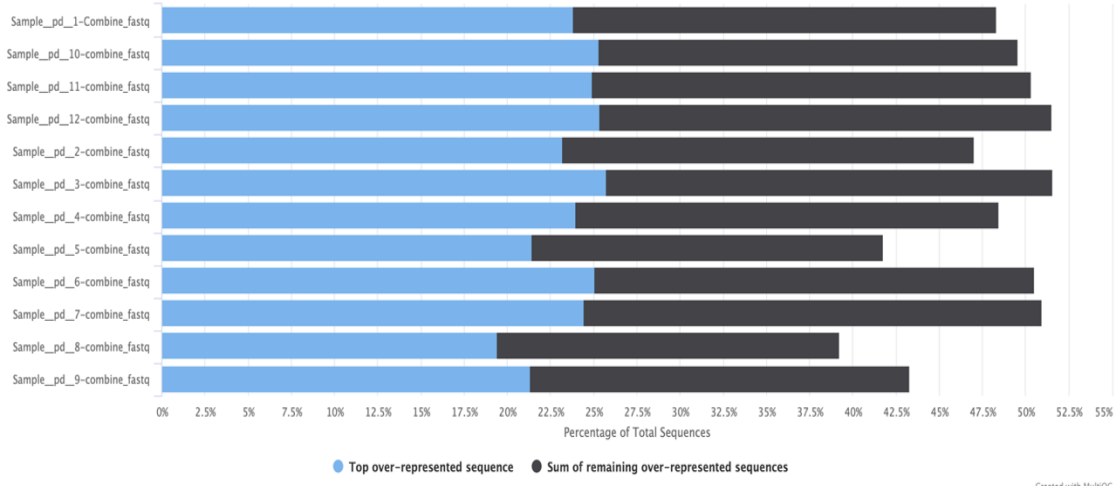

Figure 2.11 - A summary review of the over-representative sequence percentage across all samples.

Table 2.12 - An individual overrepresented sequence list of hits for sample number 1, where the GC content was very high, as well as a library preparation primer sequence.

Overrepresented sequences

Sequence	Count	Percentage	Possible Source
CGCGCGCGCGCGCGCGCGCGCGCGCGCGCGCGCGCGCGCGCGCGCGCG	946137	19.822499091774937	No Hit
CGCGCGCGCGCGCGCGCGCGCGNNNNNNNNNNNNNNNNNNNNNNNNNNNN	62941	1.3186757471015365	No Hit
CGCGCGCGCGCGCGCGCGCGCGCGCGCGCGCGCGCGCGCGCGCGCGCC	55390	1.1604748833344578	No Hit
AAGCAGTGGTATCAACGCAGAGTACTTTTTTTTTTTTTTTTTTTTTTTT	48708	1.0204804227740525	Clontech SMART CDS Primer II A (100% over 26bp)
CGCGCGCGCGCGCGCGCGCGCGCGNNNNNNNNNNNNNNNNNNNNNNNN	47449	0.9941031366552932	No Hit
CGCGCGCGCGCGCGCGCGCGCGCGCGCGNNNNNNNNNNNNNNNNNNNN	34397	0.7206509218641514	No Hit
CGCGCGCGCGNNNNNNNNNNNNNNNNNNNNNNNNNNNNNNNNNNNNNN	33159	0.694713606363735	No Hit

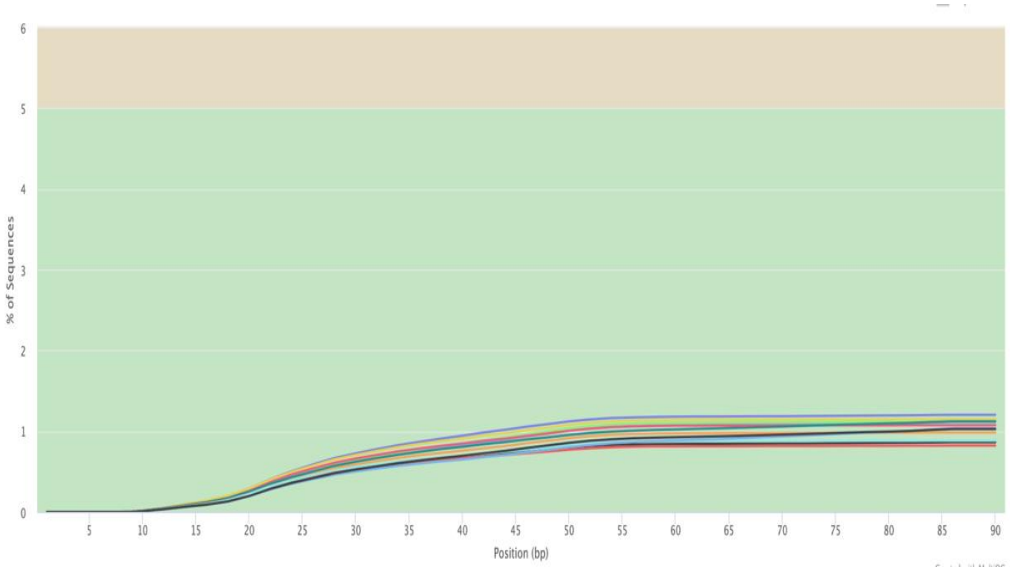

Figure 2.12 - The adaptors quality graph, which indicates a minimal read of adaptor content across all the sequence outputs

Figure 2.13 - Summary of the MultiQC checks. The sample identification numbers are listed vertically, where the quality checks are horizontal. The traffic light system visually represents normal (green), slightly abnormal (amber), or very unusual results (red). The basic statistics, per sequence quality, sequence length distance and the adaptor content are all green. Warning flags were raised for the per base sequence quality, and for specific samples for having per base N content above 5%. However, the per base sequence, per base GC content, per base N content, sequence duplications and overrepresented sequencing were all red.

2.3.5.1 Alignment Quality Control

The Samtool QC-report presents critical statistics for several different tools, as shown in Table 2.13. The general statistic is built on the total number of million reads found within each sample. In the current study, the sequence ranged between 3.1-16.8 million counts, as displayed in Table 2.13. The sequencing was accurate with minimal mismatching and base mapped errors were less than 1%.

A good mapping percentage occurs when 80-90% of the sequenced material is mapped and roughly around 10-20% remains unmapped. Unfortunately, in the current study only two samples reached a million mapped reads, and the proportion of reads ranged between 0.1% - 9.4% (Data are presented in Table 2.13 and Figure 2.14). Moreover, none of these reads were adequately paired.

2.3.5.2 Interactive exploration with DEGUST

Since the mapping ratio was so low it was not possible to proceed further with the sequencing output analysis. For clarification, when the alignment report was uploaded to Degust, an error message (Figure 2.15) appeared as no reads, no genetic differentiation, and no expressions were identified.

Table 2.13 - Data for the sequencing alignments summarising the total sequence read (in millions), the error rates, the M reads mapped, the mapped sequence ratio and the proper pairs ratio.

Sample Name	M Total seqs	Error rate	M Reads Mapped	% Mapped	% Proper Pairs
Samtools stats on sample__pd__1	3.1	0.84%	0.1	3.7%	0.0%
Samtools stats on sample__pd__10	8.4	0.84%	0.2	1.8%	0.0%
Samtools stats on sample__pd__11	9.6	0.86%	0.0	0.5%	0.0%
Samtools stats on sample__pd__12	8.6	0.84%	0.1	1.5%	0.0%
Samtools stats on sample__pd__2	6.0	0.83%	0.2	2.9%	0.0%
Samtools stats on sample__pd__3	6.9	0.83%	0.0	0.2%	0.0%
Samtools stats on sample__pd__4	7.8	0.81%	0.0	0.1%	0.0%
Samtools stats on sample__pd__5	16.5	0.88%	1.1	6.6%	0.0%
Samtools stats on sample__pd__6	6.3	0.83%	0.1	0.9%	0.0%
Samtools stats on sample__pd__7	6.1	0.84%	0.1	1.3%	0.0%
Samtools stats on sample__pd__8	9.5	0.85%	0.9	9.4%	0.0%
Samtools stats on sample__pd__9	16.8	0.85%	1.1	6.7%	0.0%

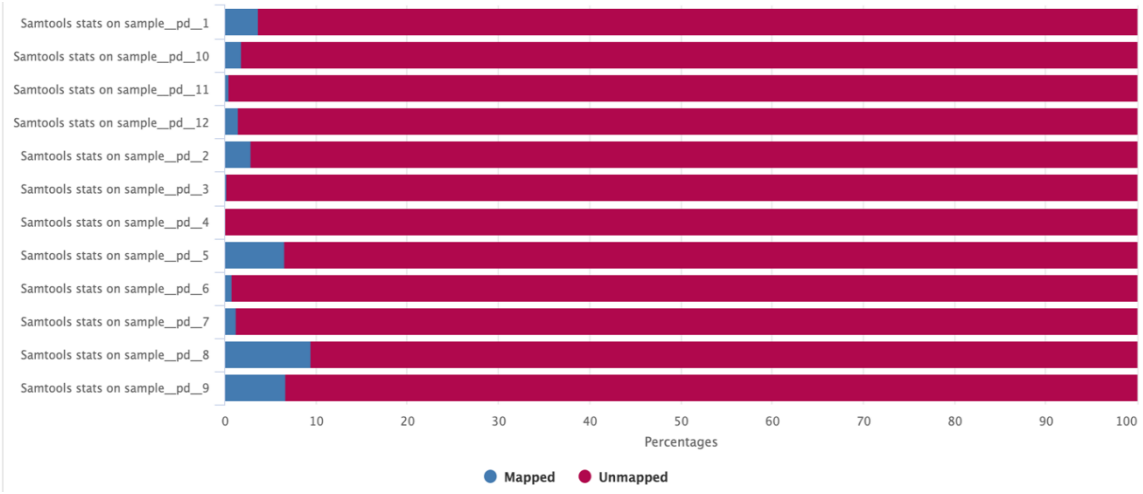

Figure 2.14 - SamTools Alignment Quality Control. The alignment metrics are presented as mapped versus unmapped reads percentages. The proportion of sample reads which were mapped was 0.1-9.4%.

Figure 2.15 - DEGUST note error explains where the poor alignments of the sequence output have prevented further analysis of the data.

2.4 Discussion

Large scale population-based studies have shown that age-associated WML are an independent risk factor for dementia (Hu et al., 2021), yet they remain understudied in the field. DSCL are characterised by extensive demyelination, astrogliosis and high levels of microglia with an amoeboid phenotype (Fernando et al., 2004b, Prins et al., 2004). The gene expression profile of DSCL and their surrounding NAWM has previously been characterised (Wharton et al., 2015), but these studies may have masked biologically relevant cell-specific transcriptomic changes. Therefore, the current study aimed to characterise the microglial transcriptomic profile in order to elucidate their role in lesion pathology

2.4.1 Histological characterization of MRI-guided sampling is essential

In the current study, MRI of the formalin-fixed hemisphere was used to guide sampling of the frozen contralateral hemisphere. Age-associated WML appears as MRI hyperintensities, which correlate with myelin loss. However, the MRI detection of WML is less sensitive and less specific than histological assessment of WM pathology (Fernando et al., 2004b). In a study comparing post-mortem MRI with histological characterisation of 33 cases from an ageing population-representative cohort, the MRI detection sensitivity for DSCL was 86% (79–93%), and specificity was 80% (72–88%). The same study reported that the sensitivity and specificity for PVL was 95% (87–99%) and 71% (44–90%), respectively. Further, false-negative MRI was associated with milder pathology.

Therefore, post-mortem MRI of the formalin-fixed brain is a reliable method to detect larger WML, which are more likely to have a clinical impact and to obtain data on the severity and distribution of WML. However, combining MRI data with histological assessment of the WM region of interest is essential to confirm the presence or absence of pathology.

Previous studies have shown that CD68 microglia with an amoeboid morphology are a prominent feature of DSCL, while the microglia within the NAWM and control WM have small cell bodies, a ramified morphology and extended processes (Waller et al., 2019). In the current study, CD68 immunostaining was combined with the basic histological stains H&E and LFB to confirm the pathology of the sampled deep subcortical white matter regions of interest. Interestingly while studies have suggested that WML are symmetrical within the two hemispheres (Potter et al., 2012), the current findings provide evidence that this is not always the case and highlight the importance of performing histological evaluation of MRI-guided samples.

2.4.2 What role do microglia play in DSCL?

Microglia are the primary immune cells poised for rapid responses to CNS injury resulting from inflammation, damage, and infection (Cowan et al., 2022). Microglia respond to any homeostatic imbalance and pathological cue by becoming activated, reflected by their morphological and functional changes (Cowan et al., 2022). Human PM Studies have shown an increase in the number of microglia in the ageing brain,

particularly in the WM, where the number of phagocytic microglia is significantly upregulated (Ahn et al., 2022). It has been suggested that this increase in phagocytic microglia is in response to the accumulation of myelin debris within the aged brain (Safaiyan et al., 2016).

The pathological activation of microglia within age-associated DSCL may result from several factors, including demyelination, chronic hypoxia and vascular hypoperfusion (Tomimoto et al., 2003, Duncombe et al., 2017), dysfunction of the BBB (Simpson et al., 2007) and overlying cortical pathology (Leys et al., 1991, Huang et al., 2007, McAleese et al., 2017). In response to these factors, microglia may be polarised to either M1 or M2 and produce neurotrophic factors or neurotoxins, respectively, which can either contribute to or prevent the progression of pathology (Wharton et al., 2015). However, it should be noted that this is an oversimplification of the microglial activation status and that studies characterising microglial activation in age-associated PVL indicate that they are a heterogeneous population (Fadul et al., 2020). In a comparison study involving control, NAWM, and PVL cases, the PVL histological evaluation indicated the presence of immune-activated microglia within the lesions. In contrast, the microarray transcriptomic profile of PVL identified significant downregulation of microglial activation markers, implicating that PVL are a continuous spectrum of white matter injury (Fadul et al., 2020).

Previous transcriptomic profiling of DSCL in the CFAS cohort demonstrated these lesions are associated with an increased expression of hypoxia-related genes in addition to the dysregulation of immune-regulatory genes, including genes associated with

antigen processing, presentation, phagocytosis and signalling pathways associated with pro-inflammatory cytokines (Simpson et al., 2009). However, it should be noted that the previous gene expression profiling characterised the transcriptome of total tissue extracts, which may have masked microglial specific changes. To determine whether the microglia of DSCL and the surrounding NAWM adopt an M1 or M2 phenotype, immuno-LCM was employed in the current study to isolate the microglia and assess their transcriptomic profile.

2.4.3 RNA-Seq is not compatible with immuno-LCM for transcriptomic profiling of PM tissue

The RNA-sequencing technique was used to investigate differences in the transcriptomic profile of microglia isolated from control non-lesional and lesional aged white matter cases. The study aimed to identify the significantly differentially expressed genes, which may elucidate the role of microglia in the formation of age-associated WML.

PM tissue is a valuable resource to increase our understanding of potential mechanisms underlying neurological diseases (Ozsolak and Milos, 2011). Ideally, samples with a high RIN of 8 or more are used in RNA sequencing experiments; however, it is not always possible to obtain high-quality RNA sourced from PM samples (Sigurgeirsson et al., 2014). Although a low RIN index is commonly associated with the PM samples, no consensus exists on the cut-off of RIN values in RNA-seq (Wu et al., 2017).

All the samples in the current study had a highly degraded RNA profile which can negatively impact RNA-seq (Wu et al., 2017, Ferreira et al., 2018). PM tissue is a hugely

valuable resource to identify relevant biological changes which may underlie disease pathogenesis; however, there are several factors which negatively influence the RNA integrity index including, the post-mortem interval (PMI), environmental parameters, the agonal state of the patient, methods of tissue collection, and the freezing interval (FI) (Wu et al., 2017, Ferreira et al., 2018).

A study has shown the RNA degradation level is dependent on both the PMI and the duration of the FI in a large sample set of brain biospecimens (Birdsill et al., 2011). A total of 79 brain specimens from both neurodegenerative disease and neurologically normal controls were stored at -80^{o}C before analysis for an unspecified length of time. Regardless of diagnosis, the PMI significantly and negatively correlated to RNA yield and RIN value (Birdsill et al., 2011).

Pre-mortem agonal factors, such as patients being on a ventilator or prolonged terminal hypoxia, impact on the brain pH and subsequently the post-mortem yield of RNA (Johnston et al., 1997). A brain pH of less than 6.0 correlates with the reduction or absence of detectable mRNA levels (Kingsbury et al., 1995). In contrast, brains with a high pH strongly associate with preserved mRNA levels. Therefore, measurement of brain pH is advised to identify post-mortem tissue most likely to contain preserved mRNA.

The repetitive freeze-thaw cycles of snap-frozen samples may also accelerate RNA degradation (Wu et al., 2017). A study assessed the impact of the repeated freeze-thaw cycles on RNA integrity using samples, which were either left to thaw at room temperature or were placed on ice. The findings indicated that RNA degradation results from repeatedly using the samples during their lifecycle. For the RNA-degraded samples,

the study also detected changes in gene expression, including the housekeeping gene (Ji et al., 2017).

The RNA quality of the PM tissue used in the current study was further challenged during the immuno-LCM procedure. While immuno-LCM can generate a sample enriched for a specific cell type or region of interest, this procedure can have a direct impact on RNA quality as indicated by a reduction in the RIN (Wang et al., 2020, Nichterwitz et al., 2018). The fixation step, which occurs before the rapid IHC staining protocol, has been shown to impact RNA quality by creating non-specific crosslinking of proteins and nucleic acids, which can impact the transcriptome (Kim et al., 2015). Furthermore, the LCM approach requires a relatively long time to obtain a relatively small number of cells, and hence a small RNA yield. The outcome of low quality and highly degraded RNA requires more PCR cycles for amplification, which eventually leads to poor quality RNA-seq data (Wang et al., 2020).

Previous studies on the CFAS cohort successfully analysed the transcriptomic profile of DSCL by microarray analysis (Simpson et al., 2009); however, the current study demonstrates that RNA extracted from immuno-LCMed PM tissue is not compatible with RNA-seq. Low-quality RNA is highly challenging in whole-genome gene expression profile studies and can obscure inter-individual differences (Gallego Romero et al., 2014) and skew gene expression profiles (Wu et al., 2017). The combination of low RNA quality with low RNA input can cause inefficient amplification of differentially expressed transcripts which may mask biologically relevant gene expression changes and impact the interpretation of the datasets (Bhargava et al., 2014). In the literature, the QCTapeStation

is more frequently used than the picochip to assess the RIN values for RNA-seq samples; however, it should be noted that these two techniques give different values. In the current project, the RNA profiles for samples were assessed twice, once using the picochip (where RIN values were unidentified except for one sample) and once using QCTapeStation (where RIN values ranged between 1.5 - 3.1).

There are, however, several proposed solutions to deal with RNA-seq analysis of highly degraded mRNA obtained from PM tissue. One approach is to normalise the RNA-seq output data and eliminate any gene expression resulting from a low RIN index, but it should be noted that this profiling approach only works with PM samples with a RIN of at least 4 (Gallego Romero et al., 2014). Other studies have developed a computational normalising method which is compatible with a RIN of at least 2 (Nichterwitz et al., 2018, Xiong et al., 2019), however determining the transcriptomic profiles of samples with RIN <2 by RNA-seq remains a challenge. A ribosomal RNA depletion step to remove the most abundant RNA species from highly degraded and low amount samples has been suggested (Hrdlickova et al., 2017). This could be performed using sequence-specific rRNA probes to generate biotinylated cDNA which can be depleted using streptavidin beads (Hrdlickova et al., 2017). In a study comparing protocols it was found that the TruSeq Ribo-Zero rRNA Removal Illumina protocol (Schuierer et al., 2017, Li et al., 2014b) gave the best results compared to TruSeq Stranded mRNA, TruSeq Ribo-Zero rRNA Removal, and TruSeq RNA Access protocols (Schuierer et al., 2017).

Another depletion process with a different elimination approach uses the Ribonuclease H (RNase H), which cleaves the RNA strand that binds to DNA oligos. The

sample is then digested and cleaned up with DNase, a process which removes more than 80% of the ribosomal RNA (Bhargava et al., 2014). In comparison studies that assessed the data generated alongside the time and cost of the commercially available deletion systems, it has been suggested that RNase H is the best option for highly degraded RNA profile samples (Bhargava et al., 2014). Other advances in the field include library preparation kits designed explicitly for degraded RNA samples and include an rRNA depletion step, thereby removing the need to conduct this step separately (Qiu et al., 2012).

The development of the exome-capture transcriptome protocol has been shown to increase the performance of RNA-seq on highly degraded RNAs. The capture transcriptome libraries can accurately measure differential gene expression and record the genetic variants for all specimen sources, even formalin-fixed paraffin-embedded material (Schuierer et al., 2017, Hrdlickova et al., 2017).

While there have been significant advances in RNA-seq profiling of poor-quality starting material, the current study results suggest this approach is not compatible with immuno-LCM. LCM itself can impact RNA quality, as demonstrated in the pre-and post-LCM bioanalyzer analysis of RNA quality, supporting previous observations of a decrease in the RIN following LCM (Nichterwitz et al., 2018, Qiu et al., 2012, Waller et al., 2012). In contrast to studies which have shown that transcriptomic profiles can be generated from mRNA extracted from immuno-LCMed cells obtained from PM tissue using microarrays (Waller et al., 2012), the current study suggests that the mRNA is not suitable for gene expression profiling using RNA-seq. Alternatives to immuno-LCM have been suggested,

including basic H&E staining of the tissue (Wang et al., 2020), or LCM-seq techniques that combine LCM isolation of a single cell with polyA-based Smart-seq2 RNA sequencing (Nichterwitz et al., 2018). However, while these approaches may be a suitable alternative to isolate neurons, which are clearly visible following H&E staining, neither technique will enable the identification and isolation of microglia from PM tissue.

2.5 Summary of the major findings

1. DSCL are not always symmetrical, therefore histological confirmation of the white matter changes identified by MRI analysis of the contralateral hemisphere is essential.

2. While PM tissue is a valuable resource for identifying disease-relevant gene expression changes, the current RNA- seq technology is not compatible with the immuno-LCM-ed material; however, we cannot rule out technical issues contributed to the failure here. Further optimisation of extraction protocols may be required in the future.

Chapter 3 **Characterising the transcriptomic profile of DSCL**

3.1 Introduction

Transcriptomic profiling provides information on all genome transcribed RNAs under physiological and pathological conditions. This technology also elucidates the genetic alterations, the biological changes, and the potential mechanisms underlying pathological conditions (Casamassimi et al., 2017). The two major techniques employed for transcriptomic profiling are Ribonucleic Acid-Sequencing (RNA-seq) and microarray. The RNA-seq relies on quantification and identification of the RNA (Wang et al., 2009, Nelson, 2001), where briefly, the RNA is converted into complementary DNA (cDNA) fragments, followed by the cDNA library synthesis. The short fragments transcripts are then sequenced and analysed, providing reads for specific genes (Wang et al., 2009, Ozsolak and Milos, 2011).

Microarray transcriptomic profiling is a hybridisation-based technique. Depending on the species to be analysed, the microarray chip can either cover the whole genome or be specifically designed to inspect the expression of a selected panel of genes (Affymetrix, 2009). The Human Clariom ™ S Arrays, used in this study, quantify the expression of over 47,000 transcripts representing over 20,000 genes (Zwemer et al., 2014). The microarray process involves the synthesis of cDNA by the reverse transcription of RNA. The cDNA is then fragmented, labelled, and hybridised onto the microarray chip for scanning (Lonergan et al., 2007). The amount of labelled cDNA is directly proportional to the signal

intensity of each spot bound to the microarray chip. The signal intensity measurements statistically compare the samples to identify differentially expressed genes.

The microarray transcriptomic profiling technique has been used to identify significant gene expression changes in biologically relevant pathways and functional groups in a variety of neuropathological conditions (Ding and Cantor, 2004), including the assessment of the astrocytic transcriptomic profiling in relation to Alzheimer's disease (AD) pathology (Simpson et al., 2011), white matter pathology in multiple sclerosis (Waller et al., 2016), and the blood-brain barrier changes (BBB) in ageing brains (Goodall et al., 2019). The molecular analysis of post-mortem tissue using this microarray approach has been successfully utilised in combination with immuno- Laser capture microdissection (LCM). The conjugated technique has enabled the transcriptomic gene profiling of specific regions or cells of interest in human post-mortem tissue (Simpson et al., 2009, Fadul et al., 2020, Cunnea et al., 2011) and animal models (Parakalan et al., 2012) and provided a perception of the causes and molecular mechanisms of pathogenesis.

Although not all the alteration of mRNA gene expression is defined at a proteomic level, the correlation between the mRNA and the protein level of the differentially expressed transcripts has been evidenced (Koussounadis et al., 2015). In fact, the correlation between mRNA and proteomic levels in differentially expressed transcripts has a stronger association than mRNA and proteomic levels with insignificantly expressed transcripts. This correlation has enabled the immunohistochemistry (IHC) technique to assess the changes in the expressed protein encoded by the candidate genes, which were identified by the transcriptomic study. In addition to increasing the microarray outcome

reliability (validation), the IHC enables the determination of the cellular localisation of the protein.

Hypothesis, Aims and Objectives

Our study hypothesised that microglia adopt an M1 phenotype in age-associated DSCL and the surrounding NAWM, contributing to the progression of lesion pathology. The transcriptomic profile of the microglia within the three classified brain cases was attempted using RNA-sequencing (in chapter 2). This chapter aimed to:

- Characterise the transcriptomic profile of LCM-ed microglia from the age-associated DSCL cases compared to the control WM and normal NAWM using the experimental microarray technique.

The objectives of the chapter were to:

1. Perform bioinformatic analysis of microglial-associated gene expression and identify the dysregulated biologically relevant pathways and functional groups using DAVID.
2. Investigate changes at the proteomic level of the proteins encoded by a panel of candidate genes using the IHC approach.

3.2 Material and Methods

3.2.1 Histological evaluation and RNA integrity assessment

The sample criteria for transcriptomic profiling using either RNA- sequencing or Microarray analysis are identical. For both approaches, a complete histological evaluation and RNA integrity assessment were carried out, as previously detailed in 2.2.6.

While matched DSCL and NAWM regions were available for 3 cases, 1 unmatched DSCL and NAWM were used (due to the restricted lab access caused by the COVID-pandemic). In total, 4 control cases and 3 matched NAWM and DSCL cases, and 1 unmatched NAWM and DSCL were identified for the analysis, as detailed in Table 3.1.

Table 3.1 - The final list of 12 samples identified for microarray analysis

Case number	White matter group	Respective number
100/100 (8)	Control	1
RH23H6		2
23/94 (11)		3
RH11H2		4
31/00 (8)	NAWM	5
11/98 (11)		6
127/94 (9)		7
178/96 (11)		8
31/00 (9)	DSCL	9
11/98(9)		10
127/94(9)		11
03-00 (5)		12

3.2.2 Microarray

Microarray analysis was used to evaluate the gene expression profile of the twelve white matter regions of interest. The samples were processed by Dr Rachel Waller, a Post-doctoral Research Associate at Sheffield Institute for Translational Neuroscience (SITraN), as the COVID-pandemic restrictions meant no training was permitted but shadowing and some limited participating opportunities were available.

3.2.2.1 Protocol Overview

The microarray analysis using the Human Clariom ™ S Arrays cartridge (ThermoFisher Scientific, MA, USA) requires around 10 ng of hybridisation-ready target DNA purified from the RNA extracted from the WM samples. To prepare the samples, the GeneChip 3' IVT Pico Kit (ThermoFisher Scientific, MA, USA) is used, which is able to deal with the degraded RNA samples associated with post-mortem studies. The kit aims to produce biotinylated double-stranded cDNA (ds-cDNA) hybridisation targets, starting with reverse transcription of the LCM-isolated mRNA into single-strand complementary-DNA (cDNA). Subsequently, a 3' adaptor is added onto the cDNA to act as a template for double-strand (ds-cDNA) synthesis, which in turn acts as a template for in-vitro transcription (IVT) using adaptor-specific primers and Taq DNA polymerase. The complementary RNA (cRNA) is then synthesised using T7 RNA polymerase on the IVT of the double-stranded cDNA, and purified by the removal of enzymes, salts, inorganic phosphates and unincorporated nucleotides. The purified cRNA is used to synthesise second-cycle sense-strand cDNA (ss-cDNA), achieved by reverse transcription using second-cycle primers. The ss-cDNA is purified from the template RNA by adding RNase-H

to hydrolyse the cRNA template. The purified ss-cDNA is fragmented and labelled using a DNA labelling reagent bonded to biotin. The biotinylated double-stranded cDNA (ds-cDNA) is hybridised onto the GeneChip and the arrays scanned using the GeneChip Scanner 3000.

3.2.2.2 GeneChip 3' IVT Pico Kit: Assay steps

1. Poly-A RNA Control mixture

The poly-A RNA control is a specifically designed exogenous positive control consisting of polyadenylated transcripts for the *B*. *subtilis* genes which are absent from all eukaryotic samples. It binds to a control probe for *B*. *subtilis* that is present on the eukaryotic GeneChip to enable the success and efficiency of the entire target preparation process to be assessed. In this experiment 2 µl of poly-A RNA control was added to 3 µl mRNA (relatively equal to 50 ng) extracted from the LCM-isolated microglia of the deep subcortical white matter.

2. First-strand cDNA synthesis

To generate the first-strand cDNA, total RNA was primed with a T7 promoter sequence, then reverse transcribed to a single-stranded cDNA (ss-cDNA) that contains a T7 promoter sequence at the 5' end. The first-strand master mix consisted of 4 µl of pico first-strand buffer and 1 µl of pico first-strand enzyme; the mixture was gently vortexed and briefly centrifuged. On ice, 5 µl of the master mix were added to 5 µl of the total RNA and mixed thoroughly. The samples were briefly centrifuged to remove any trapped air bubbles and collect the reaction mix at the bottom of the tube. The mixture was incubated at 25°C for 5 min, then placed in a thermal cycle at 42°C for 1 hr. At the end of

the reaction, the mixture was cooled to 4°C for at least 2 min and briefly centrifuged. For clean-up, 2 µl of the pico clean-up reagent was added to each sample and mixed thoroughly before incubation at 37°C for 30 min then at 80°C for 10 min, and at 4°C for at least 2 min, it was then briefly centrifuged.

3. 3' adaptor cDNA synthesis

The 3’ adaptor was added to the ss-cDNA to act as a template for ds-cDNA synthesis in the pre-IVT amplification reaction. The reaction was accomplished using DNA polymerase and RNase H to remove the RNA concurrently and to synthesise ss-cDNA with 3’ Adaptor. On ice, the 3’ adaptor master mix was prepared by combining 7 µl of 3’ adaptor buffer with 1 µl of 3’ adaptor enzyme in a nuclease-free tube; the mixture was gently vortexed and briefly centrifuged before adding 8 µl of the 3’ master mix to each of the ss-cDNA samples. Following another gentle vortex and brief centrifugation the samples were incubated at 15°C for 15 min, 35°C for 15 min, 70°C for 10 min, and at 4°C for at least 2 min. The tubes were briefly centrifuged to collect the samples at the bottom.

4. Double-strand cDNA synthesis

The ds-cDNA, which acts as a template for in vitro transcription (IVT), was converted from ss-cDNA; the reaction uses Taq DNA polymerase and adaptor-specific primers to synthesise and pre-amplify ds-cDNA. The pre-IVT amplification master mix was prepared on ice, where 29 µl of IVT Pico PCR buffer and 1 µl of IVT Pico PCR enzyme were added to a nuclease-free tube, then mixed thoroughly and briefly centrifuged. Following this 30 µl of the pre-IVT mix were added to each 3' adaptor cDNA sample followed by another gentle vortex and brief centrifugation. The mixture was incubated at 95°C for 2

min, 94°C for 30 sec and at 70°C for 5 min, and then at 4°C for at least 2 min. The samples were briefly centrifuged to collect ds-cDNA at the bottom of the tube.

5. Synthesis of cRNA by in vitro transcription

The complementary RNA (antisense, cRNA) was synthesised and amplified by in vitro transcription (IVT) of the ds-cDNA template using T7 RNA polymerase. The master mix for this procedure was prepared at room temperature by adding 24 µl of IVT buffer to 6 µl of IVT enzyme, then mixed thoroughly and centrifuged briefly. 30 µl of the IVT master mix was added to each ds-cDNA sample before being incubated at 40°C for 16 hrs, and cooled to 4°C.

The cRNA was purified from enzymes, salts, inorganic phosphates, and unincorporated nucleotides to act as a template for the second cycle of cDNA synthesis. At room temperature, 80 µl of each cRNA sample was mixed with 140 µl of magnetic purification beads in a well of a round bottom plate, (Thermo Scientific™, Abgene 96 well polypropylene storage microplates). The mixture was pipetted up and down at least 10 times and left at room temperature for 10 min, allowing the cRNA within the samples to bind to the purification beads. After incubation, the plate was placed on a magnetic stand for 5 min to capture the purification beads. When completed and the mixture became transparent, the supernatant was removed carefully, avoiding disturbing the purification beads. The purification beads were washed on the magnetic stand by adding 200 µl of 80% ethanol wash solution to each well and incubating for 30 sec. The washing step was repeated three times to enhance cRNA purification and left to air dry for 5 min. cRNA was eluted by adding 27 µl of pre-heated (65 °C) nuclease-free water and incubated for 1 min,

followed by gently pipetting up and down 10 times. The plate was removed from the magnetic holder and allowed to stand at room temperature for 5 min; the supernatant, which contains the eluted cRNA, was transferred to a fresh nuclease-free tube. Following the elution step, the quantity of the amplified cRNA was assessed on the Nanodrop™ 1000 Spectrophotometer (ThermoFisher Scientific, MA, USA). The quality of cRNA was checked using a Nano LabChip 6000 assay in the Agilent 2100 Bioanalyzer.

6. Double-strand cDNA synthesis- second cycle

The purified cRNA was reverse transcribed to create sense-strand DNA; the antisense-strand cDNA was synthesised using DNA polymerization and the 2nd-cycle primers. The 2nd-Cycle ds-cDNA master mix was prepared on ice by mixing 4 µl pico 2nd-cycle primers with 8 µl of ds-cDNA Buffer and 4 µl of pico 2nd-cycle ds-cDNA Enzyme. The mixture was mixed thoroughly and centrifuged briefly before adding 16 µl of the master mix to each (24 µl) cRNA sample. The reaction mixture was mixed, centrifuged briefly, and incubated at 25°C for 10 min, at 42°C, 50 min, at 70°C for 10 min, and then at 4°C for at least 2 min. The samples containing the 2nd- cycle-cDNA were centrifuged briefly to collect the 2nd-cycle ds-cDNA at the bottom of the tube.

7. Hydrolysis of RNA using RNase H

By using a combination of hydrolysis buffer and heat, the cRNA template was hydrolyzed from the ss-cDNA. On ice,7 µl of pico hydrolysis buffer was added to each 2nd-cycle ss-cDNA sample and mixed thoroughly via vortexing and briefly centrifuged. The mixture was incubated at 65°C for 20 min and then at 4°C for at least 2 min.

8. Purification of ds-cDNA

The purification of 2nd-cycle ds-cDNA aimed to prepare cDNA for the labelling stage by removing enzymes, salts, and unincorporated dNTPs. The procedure is similar to the cRNA purification. Firstly, the ds-cDNA bound to the purification beads by mixing 57 µl of 2nd-cycle ds-cDNA sample with 100 µl purification beads in a round bottom well, and the samples were mixed by pipetting up and down 10 times. The plate was left on the bench for 10 min before placing it on a magnetic stand for 5 min. The supernatant was carefully aspirated to avoid any disturbance of the purification beads. The purification of the beads was carried out on the magnetic stand by adding 200 µL of 80% ethanol wash solution, incubated for 30 sec and the wash buffer removed by pipetting ensuring that the beads were not disturbed (repeating this step for 3 times). Before the elution step, the samples were left for 5 min to air-dry. To elute the ds-cDNA, the plate was removed from the magnetic stand, 27 µl of pre-heated (65 °C) nuclease free-water added and incubated for 1 min before pipetting up and down 10 times. The plate was replaced on the magnetic stand for 5 min, and the supernatant, which contains the purified ds-cDNA, was transferred to a 0.5ml Eppendorf nuclease-free tube.

9. ds-cDNA fragmentation and labelling

The purified ds-cDNA was fragmented using the enzymes uracil-DNA glycosylase (UDG) and apurinic/apyrimidinic endonuclease 1 (APE 1). Subsequently, the fragmented cDNA was labelled by terminal deoxynucleotidyl transferase (TdT) using DNA labelling reagent covalently linked to biotin (provided within the kit). The ds-cDNA was first normalised by transferring 6.6 µg of ds-cDNA and then making a final volume of 46 µL using RNase free dH_2O to have a final concentration of ds-cDNA 143.5 ng/µL. The

fragmentation and labelling master mix were prepared by adding 12µl of pico fragmentation and labelling buffer with 2 µl of pico fragmentation and labelling enzyme and mixed thoroughly, before adding 14 µl of the master mix to 46 µl of the purified ds-cDNA sample. The mixture was incubated at 37°C for 1 hour, 93°C for 2 min, and at 4°C for at least 2 min.

At this stage, the success of fragmentation was confirmed using the Agilent 2100 Bioanalyzer (Agilent, UK) to detect a single peak of fragment DNA size of 40 and 70 nucleotides, as shown in Figure 3.1.

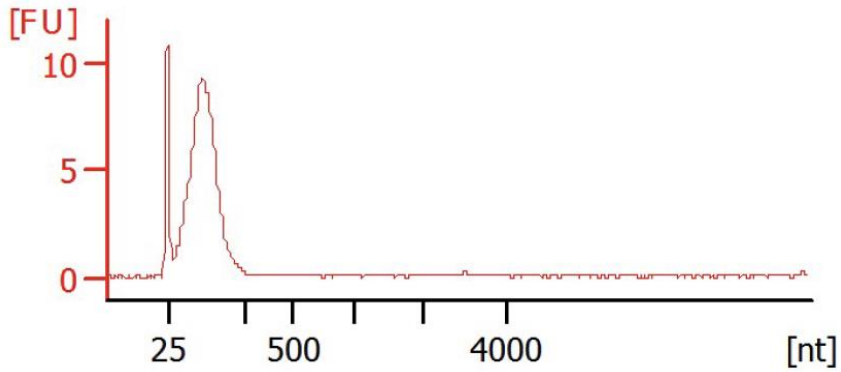

Figure 3.1 - Assessment of fragmented ds-cDNA. The fragmented ds-DNA appears as a single peak within the expected size of 40-70 nucleotides, indicating the success of fragmentation. Where, FU: fluorescence unit, NT: nucleotide size.

10. Cartridge array hybridization

In this final stage the fragmented and labelled ds-cDNA was hybridised to Human Clariom ™ S Arrays (ThermoFisher Scientific, MA, USA). Initially, the microarray chips were preconditioned with 200 µl pre-hybridization mix at 45°C for 25 min, rotating at 60 rpm in a hybridisation oven (Affymetrix, UK). Meanwhile, the hybridisation master mix was prepared by combining 11 µl of 20X hybridisation controls (containing serial concentrations of bioB, bioC, bioD, and cre genes), 3.7 µl of Oligo B2 (positive control), 110 µl of the hybridisation mix (preheated at 65 °C), 22 µl of DMSO and 13.3 µl of nuclease-free water in a nuclease-free tube. The mixture was mixed by gentle vortexing and centrifuged. The hybridisation cocktail was completed by adding 60 µl of ds-cDNA samples. To aid the reaction, the mixture was incubated at 99°C for 5 min, at 45°C for another 5 min, and centrifuged briefly.

After conditioning the gene chips, a total of 200 µl of the hybridisation cocktail replaced the preconditional hybridisation solution. The cocktail was injected into the GeneChip® probe array cartridges and incubated in a hybridisation oven for 16 hours (overnight) at 45°C and 60 rpm. Upon completion of the hybridisation, the cocktail mix was removed. The arrays were washed in the GeneChip Fluidics Station 400 (Affymetrix, UK) and left to equilibrate at room temperature before staining with Affymetrix GeneChip® Command Console Fluidics Control (ThermoFisher Scientific, MA, USA). Scanning of the arrays was performed using a GeneChip® Scanner 3000 with a high-resolution laser to determine the fluorescent intensity of hybridised transcripts. Lastly, the Affymetrix Expression Console generated the raw signal intensity values (CEL files).

3.2.2.3 Transcriptomic Data Analysis

3.2.2.3.1.1 Quality control assessments

The transcriptional profile of microglia isolated from control, NAWM, and DSCL were first assessed for quality control and then compared among the three categorised groups. The Affymetrix Expression Console software and the Qlucore Omics Explorer software (Qlucore, Lund, Sweden) were utilised to evaluate all samples' amplification, hybridisation, housekeeping genes and signal intensity. Prior to statistical analysis, the CEL file containing the data created from the microarray scanner was imported to GeneSpring version 7.0 (Agilent, USA) and normalised to the median of all genes.

The sample distribution was identified using the Qlucore Omics Explorer software with the Principal Component Analysis (PCA). Genes were considered significantly differentially expressed if they had a minimum fold change ≥1.2 (either up-or down-regulated) and a P-value ≤0.05; where fold change values above 1.2 and below -1.2 represent upregulated and downregulated genes, respectively, compared to the comparison group.

Transcriptome Analysis Console software, version 4.1.1 (Affymetrix®, UK) was also used for quality assessment with interactive visualising. The software features focus on genes and pathways to explore interaction and compare differential gene expression profiles between the three groups: control, NAWM and DSCL, using the stringency parameters. Genes with a fold change below 1.2 and a p-value greater than 0.05 were excluded. Comparison tables of the significantly differentially expressed genes were

generated to compare the profile between DSCL vs control; NAWM vs DSCL and NAWM vs control cases in downstream bioinformatic analysis.

3.2.2.3.1.2 Bioinformatic analysis

The transcriptomic datasets and comparisons of the aged white matter cases' transcriptomic profiles were analysed using the Database for Annotation Visualisation and Integrated Discovery (DAVID) version 6.8 (NIAID, NIH, USA; Huang *et al.*, 2009), an online bioinformatics resource. The gene comparison tables were imported separately to identify pathways and processes that differed significantly between groups. The select identifier was set for "OFFICIAL-GENE-SYMBOL", species selection 'Homo-Sapiens' and 'gene list'.

Firstly, each dataset (from each of the three comparisons) were uploaded to DAVID to identify significant KEGG (Kyoto Encyclopedia of Genes and Genomes) pathways. Furthermore, the clustering tool on DAVID was used at the highest stringency setting to enable genes to be grouped according to their clinically related pathways, interactions and altered functional groups. Subsequent analysis was repeated to assess the upregulated and downregulated genes separately.

3.2.3 Validation of candidate gene expression changes using IHC

IHC was carried out to validate and identify the expression and localisation of protein encoded by a panel of candidate genes. The selection of antibodies was based on a literature search of antibodies that detect the proteins associated with the differentially expressed genes. All recommended antibodies that are compatible with PM tissue and

were commercially available were selected for this validation study. Initial primary antibody optimisation was carried out to determine the optimal concentration that provided specific immunolabeling with minimal nonspecific background stain. Based on the manufacturer's recommendation, a range of dilutions was used (Table 3.2) followed by a qualitative assessment for each concentration. IHC was performed using the standard ABC-HRP protocol technique and Vectastain Elite kit (Vector Laboratories, UK) with DAB (Vector Laboratories, UK) as substrate (as detailed in section 2.2.5). The validation IHC was then performed using the optimal primary antibody concentration determined from the titration study. Appropriate isotypes and negative controls were included in all runs.

3.2.3.1 Image acquisition and Statistical Analysis

The IHC and histological studies performed on the stained sections were assessed using the Nikon microscope and NIS-Elements Imaging Software (Nikon UK, Kingston Upon Thames). A qualitative description of each antibody's staining pattern and localisation was assessed across all specimens; DSCL, NAWM and control non-lesional cases.

The stained slides were first scanned using the Nanozoomer Digital Pathology software (Hamamatsu, Uk). For image acquisition, NDP.view 2 Software was used to image 5 white matter regions of the deep subcortical white matter for each case, at 20x magnification. The quantification of specific immunoreactivity was calculated using Analysis^D software (Nikon UK, Kingston Upon Thames) to assess the % area of

immunoreactivity per image. For the data analysis, the mean % area of immunoreactivity was calculated based on the total number of images per case.

Statistical analysis was performed using IBM SPSS Statistics version 26.0 (SPSS Inc., Chicago, IL, USA). The data were not normally distributed; thus, analyses were conducted using non-parametric methods. Statistical comparisons of quantitative data between groups were carried out using the Kruskal Wallis. The P-values were adjusted for multiple testing using the Post hoc method and considered significant if $p < 0.05$.

Table 3.2 - Primary antibody panel used to validate the microarray candidate genes; the optimum concentration used in the study is shown in bold

Primary Antibody	Species	Clonality	Isotype	Dilution	Supplier
CD163	Rabbit	Monoclonal	IgG	1:250 **1:500** 1:1000	Abcam, UK
Dub3	Rabbit	Polyclonal	IgG	1:50 **1:100** 1:200	Novusbio, UK
SRBI	Rabbit	Monoclonal	IgG	**1:500** 1:1000 1:2500	Abcam, UK
UCHL1	Mouse	Monoclonal	IgG	1:50 1:100 1:200	Sigma, UK

3.3 Results

3.3.1 RNA Quantity and Quality Assessments

Twelve samples were identified from the CFAS neuropathology cohort to study the microglial transcriptomic profile of age-associated WM pathology by microarray analysis. These cases were classified into control WM from non-lesional cases (4 cases), NAWM from lesional cases (4 cases), and DSCL (4 cases).

The RNA quality and quantity were assessed pre and post -LCM using the Agilent 2100 bioanalyzer; presented in Table 3.3. Prior to the LCM, RNA was extracted using TRIzol and the RNA quality was assessed. Pre-LCM, the RIN values in the control WM ranged from n/a-2.9, in DSCL the range was n/a-4.5, and in NAWM the range was n/a-6.4. A representative electropherogram of pre-LCM profiles in shown in Figure 3.2A-B. During LCM, an enriched population of microglia were collected from the deep subcortical region; afterwards, the RNA quality was assessed. Overall, the RIN value decreased across all groups, in control WM the range was n/a-2.4, in DSCL the range was n/a-2.5-, and in NAWM the range was n/a-6.2. While RIN values are a suitable indicator of RNA integrity, the RNA profile should also be considered, as it provides a visual representation of the RNA quality of the samples. For samples where RINs were unavailable, the pico-chip profile was examined to ensure similar profiles were assessed; Figure 3.2 C.

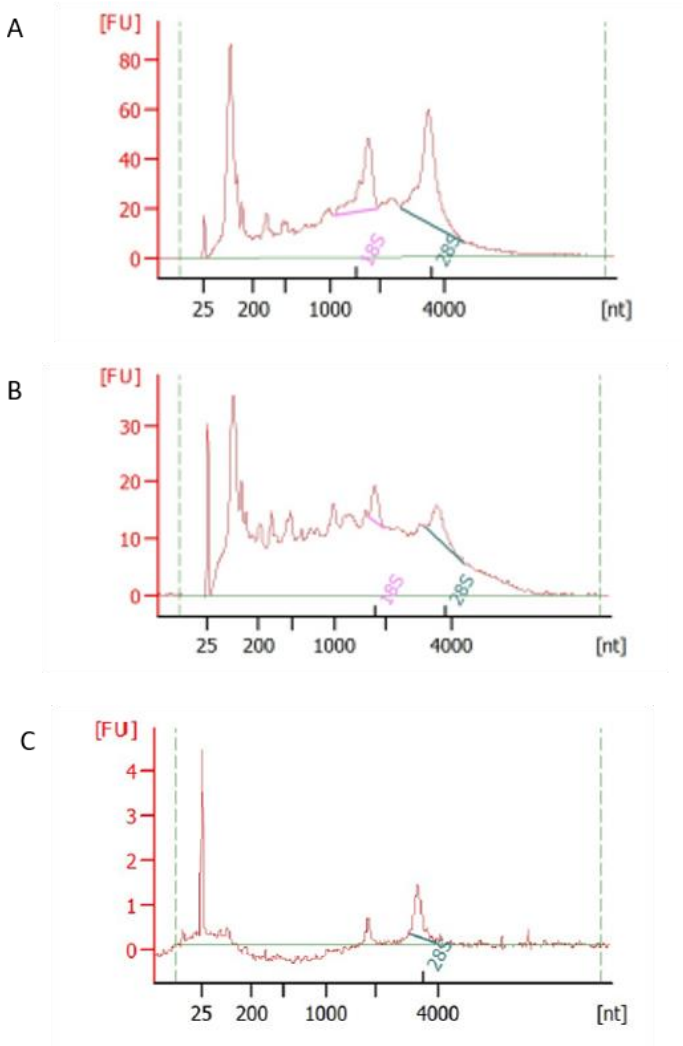

Figure 3.2- Pre- and post-LCM RNA integrity. Representative electropherograms for two different frozen cases, where the mRNA profile was assessed before LCM and detected (A) high (6.4) and (B) low (2.9) RIN values. Ribosomal RNA is represented by two peaks of 18S and 28S. (C) A representative electropherogram for post-LCM samples with no RIN value FU= fluorescent unit.

Table 3.3 - Pre- and Post-LCM RIN values measured using the Agilent 2100 bioanalyzer. The cases were selected for the downstream transcriptomic profiling using the microarray approach.

Case number & Conditions	**Pre-LCM RIN**	**Post-LCM RIN**	**Post-LCM RNA concentration (pg/µl)**
Control			
1	2.9	n/a	11086
2	2.7	2.2	4268
3		2.4	4223
4		2	615
RIN values range	n/a- 2.9	n/a-2.4	615-11086
NAWM			
5	2.9	n/a	2935
6	6.4	n/a	4707
7		6.2	3798
8	4.5	n/a	5244
RIN values range	n/a-6.4	n/a-6.2	2935-5244
DSCL			
9	2.3	n/a	7238
10	2.4	2.3	3459
11	n/a	n/a	4459
12	4.5	2.5	1148
RIN values range	n/a-4.5	n/a-2.5	1148-7238

3.3.2 RNA preparation for microarray Analysis

The initial steps of the microarray protocol used approximately 50 ng of mRNA per sample. During the process, there were two points at which the concentration of the genetic material and the success of the protocol was assessed. The first checkpoint was for the yield of cRNA, and the second check followed the purification of ss-cDNA. As seen in Table 3.4, all samples had a cRNA value above 3000 ng/ µl, except sample 4, where its original sample had low RNA concentration. The second checkpoint was for the synthesised ss-cDNA. Again, all cases, except for sample 8 had a ss-cDNA concentration above 400ng/ul as shown in Table 3.4

Table 3.4 - Concentrations of cRNA after ss-cDNA synthesis and ss-cDNA obtained after the second amplification cycle.

Case number	Condition	cRNA concentration (ng/µl)	ss-cDNA concentration (ng/µl)
1	Control	3347.05	506.56
2		3622.54	508.75
3		3000.11	588.73
4		2284.84	378.40
5	NAWM	3576.86	526.81
6		3265.58	480.27
7		3580.86	410.91
8		3442.89	406.30
9	DSCL	3574.03	482.70
10		3589.55	480.45
11		3394.13	580.24
12		3659.33	440.86

3.3.3 Microarray bioinformatic Analysis

3.3.4 Quality Control assessments

The Affymetrix Expression Console, the Qlucore Omics, and the Transcriptome Analysis Console software were employed to assess the quality controls and enable visual inspection of the data.

Labelling controls

The Poly-A spikes, derived from *Bacillus Subtilis* (*Dap, Thr, Phe, Lys*), were added to each sample and used as a positive control. The fluorescent intensity of the Poly-A spikes was assessed and all samples passed the quality check, except sample 4 which had low levels of Poly-A Phe, as presented in Figure 3.3 A.The Poly-A spikes showed a relatively similar intensity for all other *Bacillus Subtilis*, therefore sample 8 remained in the subsequent analysis.

Hybridisation and signal quality

A hybridisation control was used to evaluate the efficiency of the hybridisation step and included biotin-labelled cRNA transcripts from *E.Coli* (*BioB*, *bioC*, *bioD*) and various concentrations of the P1 bacteriophage (*Cre*). The intensity of the hybridisation signal was measured and demonstrated an increased signal intensity, which directly correlated to the concentration of the hybridisation controls, suggesting a good hybridisation efficiency across all samples. As seen in Figure 3.3 B. All samples passed the

hybridisation control check, except sample 8; however, since it is still comparable to the other samples, sample 4 remained in the subsequent analysis.

Signal intensities across the arrays

The signal intensities generated from the arrays were measured using a plotted histogram generated by the Affymetrix Expression Console Software. All twelve samples had a comparable signal intensity as illustrated in Figure 3.3 C. There were slight divergences between two samples (5 and 11), where they had a slight shift from the curve, however all samples underwent subsequent bioinformatics analysis.

The Relative Log Expression (RLE) signal is a calculation method used to detect signal intensity for each probe set in the arrays against the median signal value across all arrays. RLE data representative plots help to assess and compare the signal intensity across the samples. In the current study, the RLE data showed a similar spread across all samples, as demonstrated in Figure 3.3 D.

Overall, all quality control checks were within range, and so all samples underwent subsequent bioinformatic analysis.

A

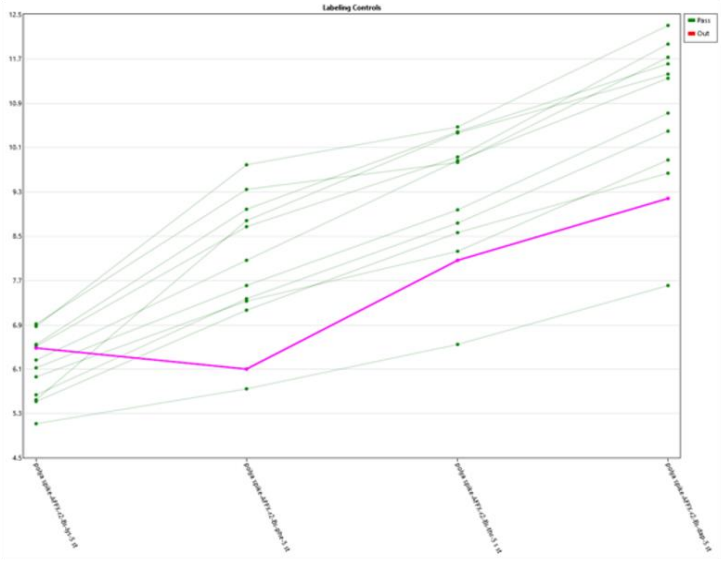
Labeling Controls
Pass
Out

B

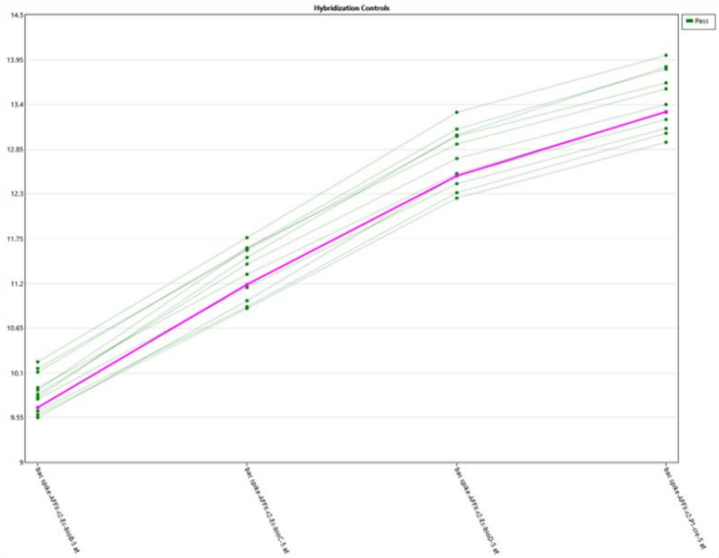
Hybridization Controls
Pass

C

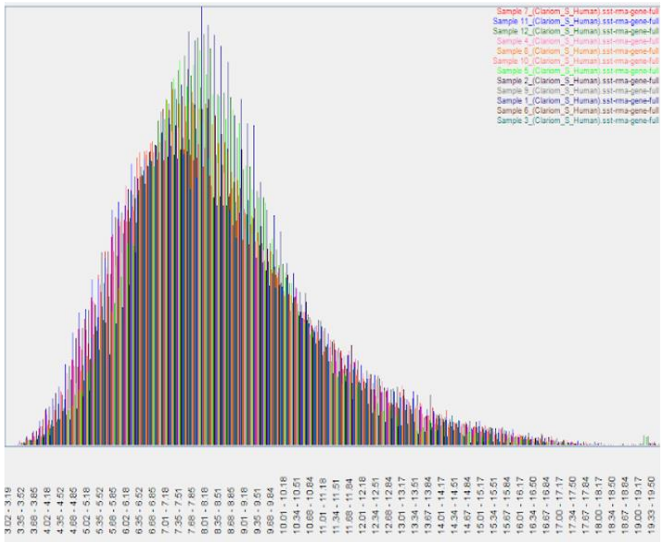
Sample 7_(Clariom_S_Human).sst-rma-gene-full
Sample 11_(Clariom_S_Human).sst-rma-gene-full
Sample 12_(Clariom_S_Human).sst-rma-gene-full
Sample 4_(Clariom_S_Human).sst-rma-gene-full
Sample 8_(Clariom_S_Human).sst-rma-gene-full
Sample 10_(Clariom_S_Human).sst-rma-gene-full
Sample 5_(Clariom_S_Human).sst-rma-gene-full
Sample 2_(Clariom_S_Human).sst-rma-gene-full
Sample 9_(Clariom_S_Human).sst-rma-gene-full
Sample 1_(Clariom_S_Human).sst-rma-gene-full
Sample 6_(Clariom_S_Human).sst-rma-gene-full
Sample 3_(Clariom_S_Human).sst-rma-gene-full

D

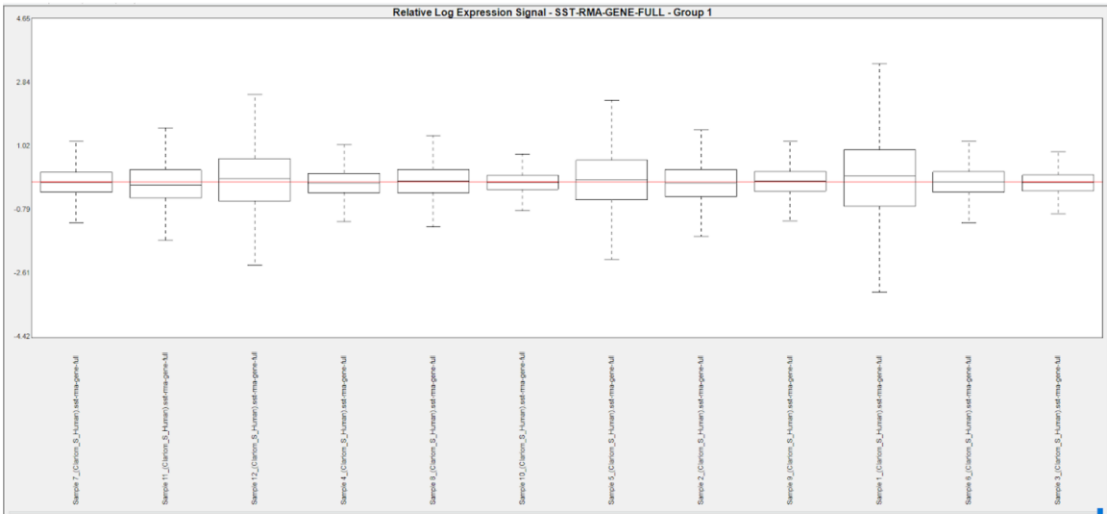

Figure 3.3 - Quality control assessments. (A) The sample ID number 178/96 (11) (labelled in pink) has not reached the threshold for the Poly-A Bacillus Subtilis Phe spike in control; however, the sample remained through all subsequent analyses. (B) The mean signal intensity plots of the hybridization control are relatively comparable across all the microarray samples. (C) Ten out of the twelve samples showed comparable signal intensity profiles, while two samples showed slight shifted and higher signal intensity (D) The Relative Log Expression plot for the microarray sample, where the median gene expression (red line) in the twelve microarray samples (X-axis) correlated with the relative log expression signal (Y-axis).

3.3.5 Transcriptomic analysis and comparison of the gene expression

The Qlucore Omics Explorer software, with parameters: fold change ≥ +/-1.2, p ≤0.05, was used to visually inspect the differentially expressed genes of the three white matter groups by producing a three-way comparison PCA plot presented in Figure 3.4. There was a clear separation between the 3 groups, while the clustering of cases within groups suggests transcriptomic similarity within each WM group, as shown in Figure 3.4.

Using the stringency setting outlined above, 181 genes were significantly differently expressed between DSCL and non-lesional control (93 genes were upregulated, and 88 genes were downregulated), 299 genes were significantly differentially expressed between DSCL cases and NAWM (97 genes were upregulated, and 202 genes were downregulated), and 374 genes were significantly differentially expressed between NAWM and the control non-lesional cases, (209 genes were upregulated, and 138 genes were downregulated); the data is summarised in Figure 3.6 and Table 3.5. While the MRI and basic histological characterisation of the NAWM may initially suggest that the microglia in this region have similarities to control WM, it is very interesting to note that the greatest number of significantly differentially expressed genes were in this comparison group. These findings highlight the importance of extensive characterisation based in more than one approach, and also suggest that microglia play an important role in lesion spread in contrast to the established lesion. ~~**Error! Reference source not found.**~~

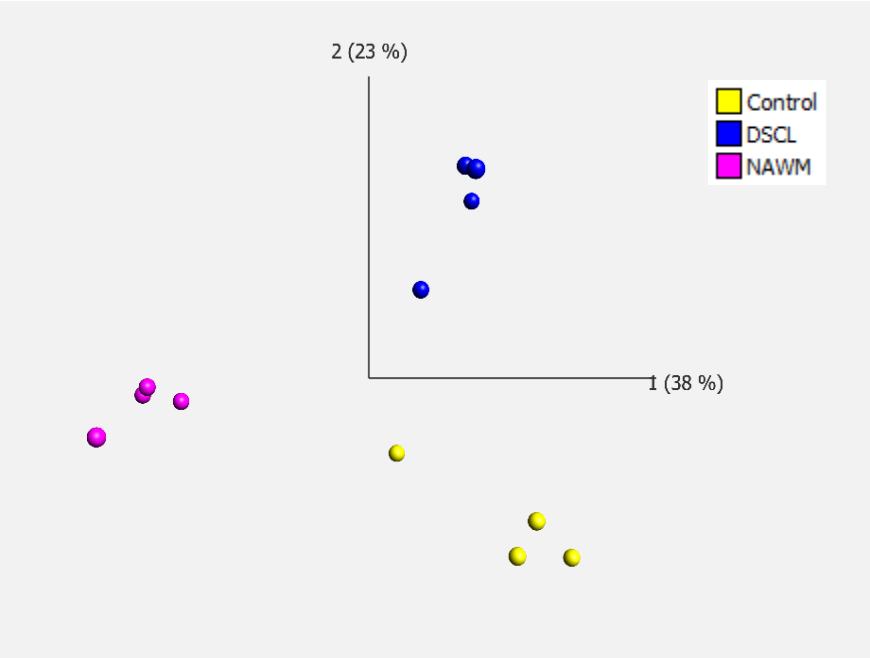

Figure 3.4 - PCA of the microglial transcriptome in ageing white matter. The principal component analysis (PCA) plot of the transcriptomic profile of microglia in ageing white matter demonstrates distinct separation between the three groups, demonstrating genetic differences between the three groups while displaying genetic similarities within the three groups. The outliner sample is within the NAWM group.

Table 3.5 - Number of differentially expressed genes for each of the 3 comparisons computed by Qlucore Omics Explorer

Two group comparisons	Total number of significantly differentially expressed genes	Number of Up regulated genes	Number of Down regulated genes
DSCL vs Control	181	93	88
DSCL vs NAWM	299	97	202
NAWM vs Control	374	209	138

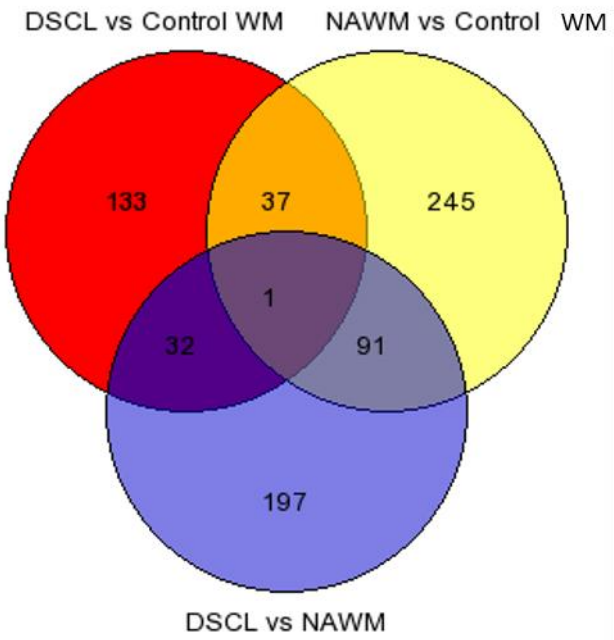

Figure 3.5 - Differential gene expression by Venn diagram analysis. The number of differently expressed genes common among the comparison group.

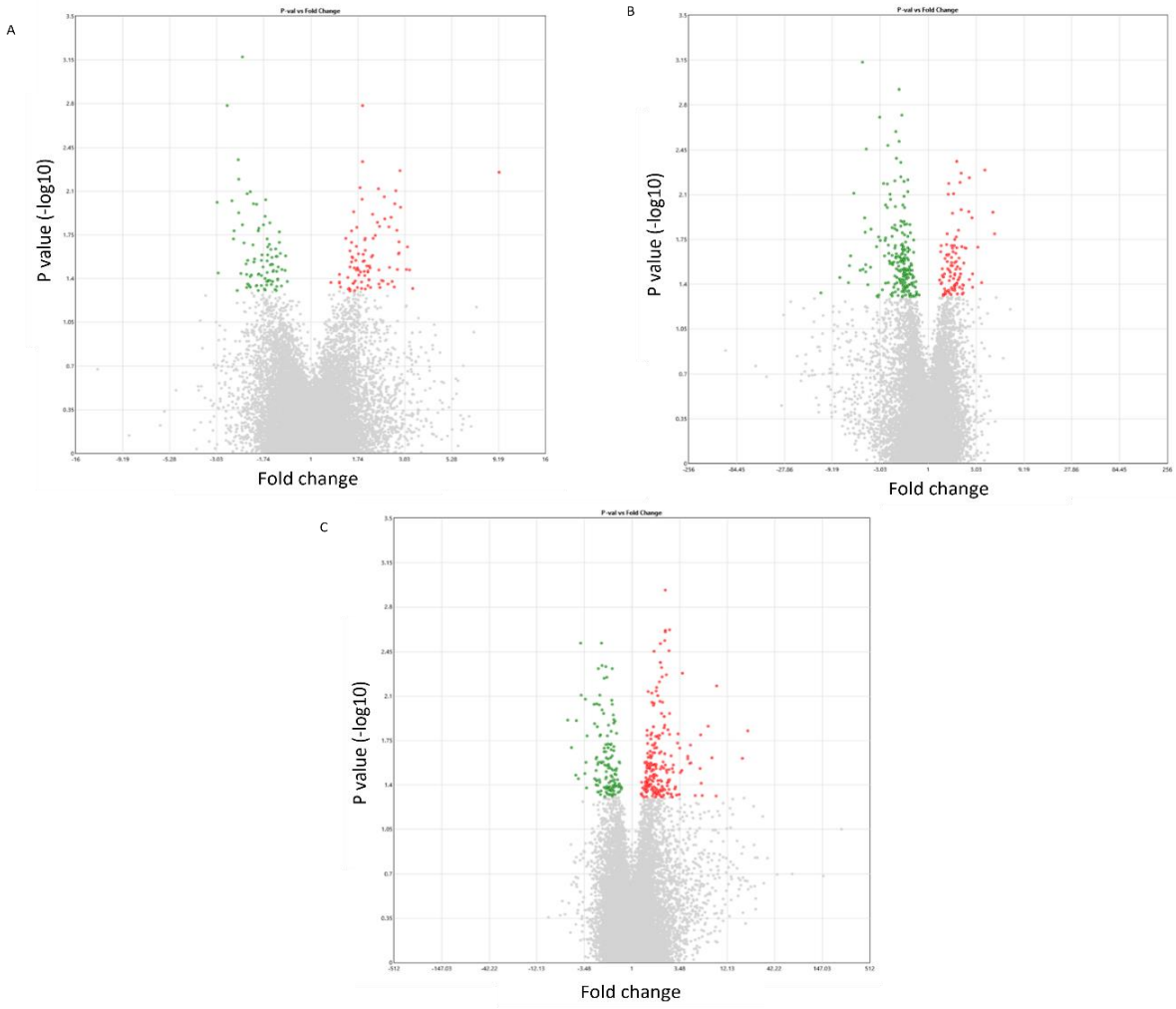

Figure 3.6 - Volcano plot of differential gene expression among the age-associated white matter cases (A) where 181 genes were significantly differentially expressed in DSCL versus non-lesional control WM; 88 are upregulated (red) while 93 are downregulated (green) (B) 299 genes were significantly differentially expressed in DSCL versus NAWM; 97 genes were upregulated (red), whilst 202 were down-regulated (green) (C) 347 genes were significantly differentially expressed in NAWM versus non-lesional control WM 138 genes were upregulated (red) whilst 209 genes were down-regulated (green). The volcano plot parameters were set for ≤ 1.2-fold change and a p-value ≤ 0.05 to identify the significantly differentially expressed genes. Each gene location is signified by a dot (•); where a red dot denotes the upregulated genes, whilst downregulated genes are signified using a green dot. The log2 (fold change) and the negative log10 p-value are the X and Y-axes, respectively.

3.3.6 Significant differential expression profiles

DAVID was used to analyse the functional groupings and KEGG pathways and identify altered genes with the highest stringency setting. The full list of significantly expressed genes was initially imported to DAVID to analyse the functional group alternation and affected pathways using the highest stringency setting for functional clusters. Afterward, the gene list of up-regulated and down-regulated genes were imported to DAVID independently for further analysis.

The KEGG pathways analysis (using DAVID) displayed no significant differences in output between all the compared groups, where all Benjamini p-values were >0.05.

DSCL vs Control

A total of 181 genes were significantly expressed differently by microglia in DSCL compared to non-lesional control cases; 93 genes were upregulated while 88 were down-regulated. A Gene annotated clustering classification was used to identify the significantly dysregulated functional groups, which included clusters of the Haptoglobin binding, haptoglobin-haemoglobin complex, TBC domain family member and Rab-GTPase genes, as shown in Table 3..

NAWM vs Control

347 genes were significantly expressed differently in NAWM from lesional cases compared to non-lesional control cases; 209 genes were upregulated while 138 were down-regulated. Significantly dysregulated functional groups included protein deubiquitinating and ubiquitin-dependent protein catabolic processes: Table 3..

In addition, looking at the data set that identifies microglia-associated gene expression, the scavenger receptor class B, member 1 gene (*SCB1*) was upregulated in NAWM compared with the control WM group, (FC = 9.13, p = 0.0486).

DSCL vs NAWM

Lastly, a comparison analysis was run between the DSCL and the non-lesional NAWM cases, where 299 genes were significantly expressed differently in DSCL cases compared to NAWM from lesional cases; 97 genes were upregulated while 202 were down-regulated. Table 3.8 shows the down regulated differentially functional groups, which included TBC and Rab-GTPase TBC domain genes.

full data set for different gene expression is presented in Appendix II.

Table 3.6 - Dysregulated functional group analysis of DSCL compared to control WM

Annotated cluster	Enrichment score	Gene count	Benjamini Value P-value ≤ 0.05	Up/Down-regulated	Dysregulated genes
Haptoglobin binding	2.5	3	$1.7*10^{-2}$	Up-regulated	Haemoglobin-α1 (*HBA1*) Haemoglobin-α2 (*HBA2*) Haemoglobin- β(*HBB*)
haptoglobin-haemoglobin complex		3	$2.4*10^{-2}$		
TBC	2.66	7	$6.3*10^{-6}$	Down-regulated	TBC1 domain family member: (*TBC1D3B, TBC1D3E, TBC1D3F, TBC1D3G, TBC1D3H, TBC1D3I, TBC1D3L*)
Rab-GTPase-TBC domain			$4.3*10^{-3}$		

Table 3.7 - Dysregulated functional group analysis of NAWM compared to control WM. Results of DAVID analysis found two main annotated cluster groups were downregulated in NAWM cases. None of the upregulated gene list reached statistical significance.

Annotated cluster	Enrichment score	Gene count	Benjamini Value P-value ≤ 0.05	Dysregulation type	Responsible gene(S)
Protein deubiquitination	5.14	9	$1.3*10^{-4}$	Down-regulated	Ubiquitin specific peptidase 17-like family member: *USP17L5, USP17L19, USP17L24, USP17L25, USP17L26, USP17L27, USP17L28, USP17L29, USP17L30,* Ring finger protein 8 (*RNF8*) Toll interaction protein (*TOLLIP*)
Ubiquitin-dependent protein catabolic process		11	$1.3*10^{-4}$		

Table 3.8 - Dysregulated functional group analysis of DSCL compared to NAWM. Results of DAVID analysis found two main annotated clusters were downregulated in NAWM cases. None of the upregulated nor the downregulated gene list reached statistical significance.

Annotated cluster	**Enrichment score**	**Gene count**	**Benjamini Value P-value ≤ 0.05**	**Dysregulation type**	**Responsible gene(S)**
TBC	1.94	5	$2.1*10^{-1}$	Down-regulated	TBC1 domain family member: (*TBC1D3B, TBC1D3E, TBC1DE3F, TBC1DE3G, TBC1DE3H, TBC1DE3I, TBC1DE3L*)
Rab-GTPase- TBC domain		5	$6.1*10^{-1}$		

3.3.7 Primary antibody optimisation and qualitative assessment of candidate gene expression changes

The correlation between mRNA and proteomic levels in differentially expressed transcripts has a stronger association than mRNA and proteomic levels with insignificantly expressed transcripts (Koussounadis et al., 2015). Thus, the IHC validation was used to increase the microarray outcome reliability. The IHC method is preferable over the RT-qPCR as it enables the determination of the cellular localisation of the protein.

The chosen antibody panel is based on the significantly expressed data (presented in Tables 3.6 and 3.7) to increase its validity. From the tables, The haptoglobin-haemoglobin complex is dysregulated, rapidly recognised and degraded via the macrophage scavenger receptor CD163. Hence, the CD163 antibody was used. Further, the downregulation of genes associated with the protein ubiquitin and deubiquitination process can be identified using the DUB3 and UCHL antibodies. The SRB1 protein antibody was correlated with the SCB1 gene expression.

To optimize antibody concentration, we selected for the lowest concentration of the primary antibody, which produced clear visualisation of specific binding to the microglial cell body and processes, with minimal background staining. For the CD163, the two tested primary antibody concentrations produced good quality stains; hence, the lowest concentration was selected (Figure 3.7 A).

The Dub3 immunoreactivity positive cells with detailed cell morphology were observed at the two higher concentrations (1:50 and 1:100); however, the intensity of the

staining pattern was reduced at the lower concentration of 1:200 (Figure 3.7 B). Similarly, the SRBI immunolabeled microglial cell bodies and processes only at the highest concentration (1:500); the intensity of the immunostaining pattern was reduced at the higher primary antibody concentrations (Figure 3.7 C).

In contrast, the UCHL staining pattern showed non-specific staining at the highest concentration, whereas no staining was observed at the lower concentrations, indicating unreliable markers for IHC (Figure 3.7 D).

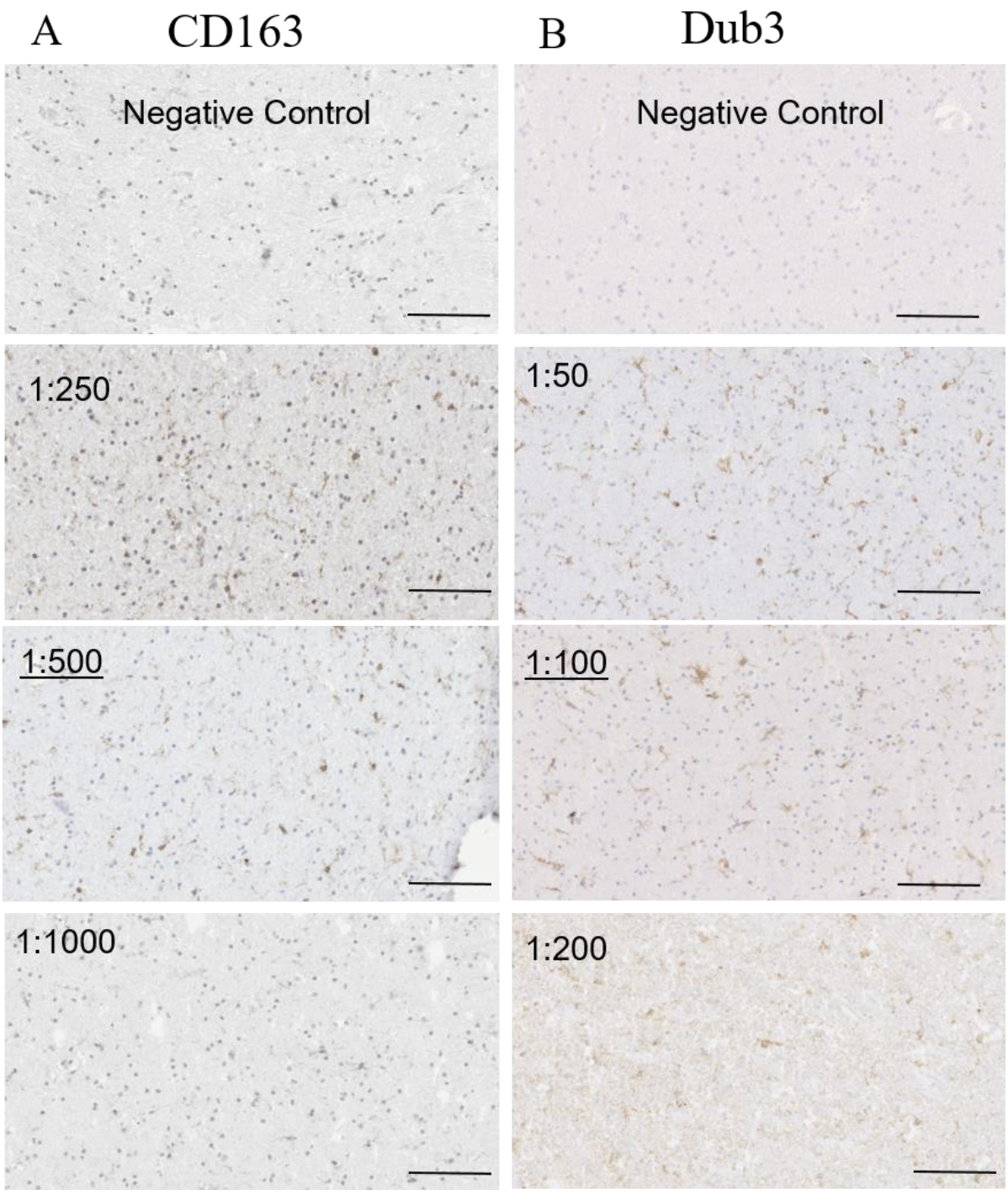
A
CD163
B
Dub3
Negative Control
Negative Control
1:250
1:50
1:500
1:100
1:1000
1:200

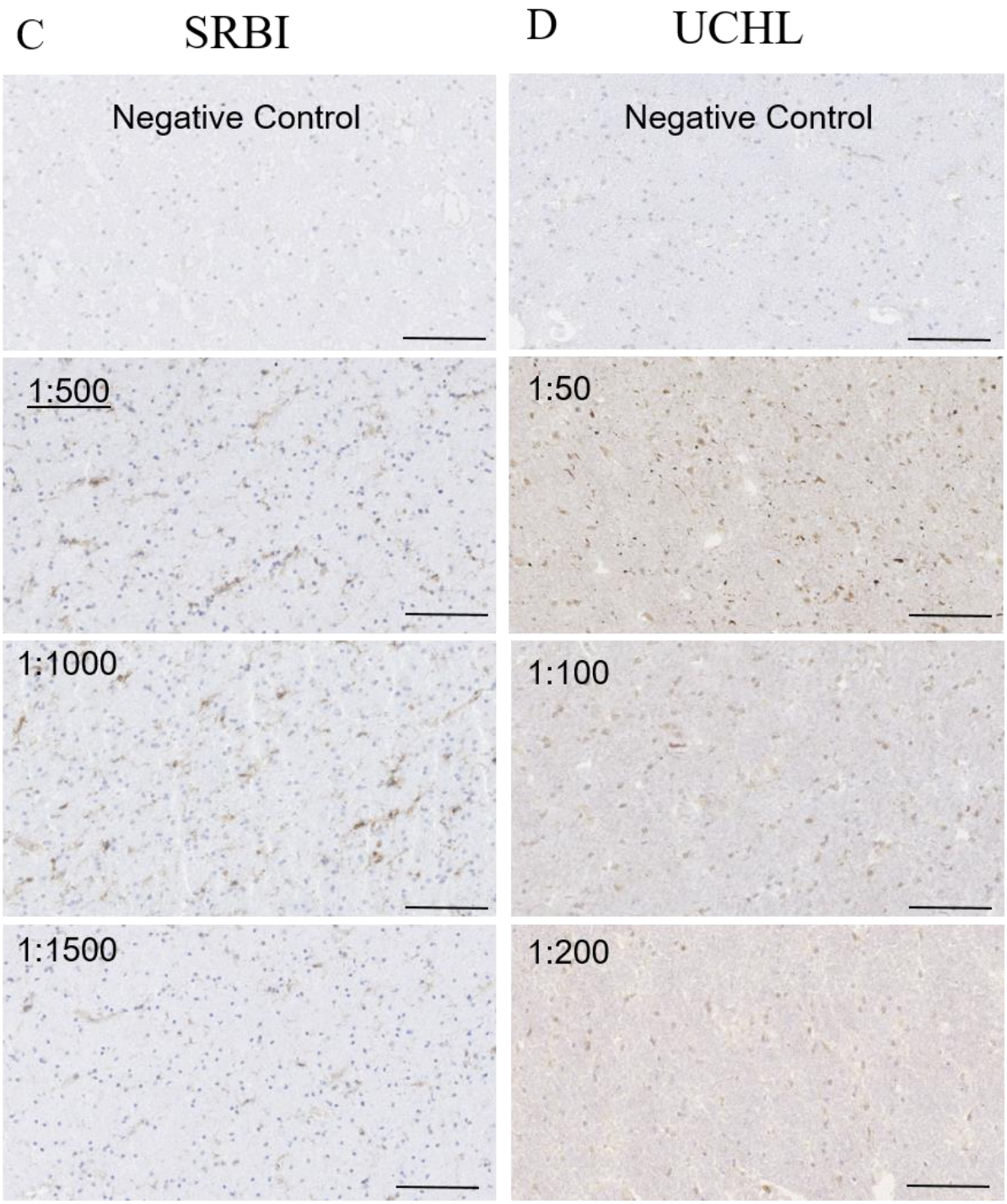

Figure 3.7 - Optimisation of antibodies to assess proteins encoded by the candidate genes. The expression of proteins encoded by four genes was assessed using IHC for four markers: CD163, Dub3, SRBI and UCHL. The optimum concentration chosen where the lowest concentration of the primary antibody gives a clear visualisation of specific binding markers to the microglial cell body and processes are underlined. The scale bar represents 100 µm.

3.3.8 The validation of microarray candidate gene expression using immunohistochemistry

The correlation between mRNA and proteomic levels in differentially expressed transcripts has a stronger association than mRNA and proteomic levels with insignificantly expressed transcripts (Koussounadis et al., 2015). Thus, the IHC validation was used to increase the microarray outcome reliability. The IHC method is preferable over the RT-qPCR as it enables the determination of the cellular localisation of the protein.

While other validation candidates were primarily selected due to their high fold change and association with microglial function, it should be noted that the haptoglobin-haemoglobin complex is dysregulated, rapidly recognised and degraded via the macrophage scavenger receptor CD163, is associated with M2 microglia (insert reference). The validation of candidate gene expression, identified by the microarray analysis, was evaluated using immunohistochemistry to assess the immunoreactive profile of the protein encoded by the candidate genes CD163, Dub3, and SRBI (Figure 3.8) and the immunoreactive area quantified (Table 3.).

Extensive CD163, Dub3 and SRBI immunoreactivity was a prominent feature of the DSCL compared to both the NAWM and control white matter from non-lesional cases. Within the DSCL, CD163, Dub3 and SRBI immunolabeled large, round microglia with an amoeboid phenotype, while in the control WM and NAWM, the immunoreactivity was associated with the cell body and processes of microglia with a ramified morphology. Quantification of the expression of Dub3 and SRBI identified significant differences in the

immunoreactive profile between DSCL and control WM groups; P= 0.018 and p=0.027, respectively. However, there was no significant difference in the immunoreactive profile of CD163 across the three groups, P>0.05; Figure 3.9 A-C.

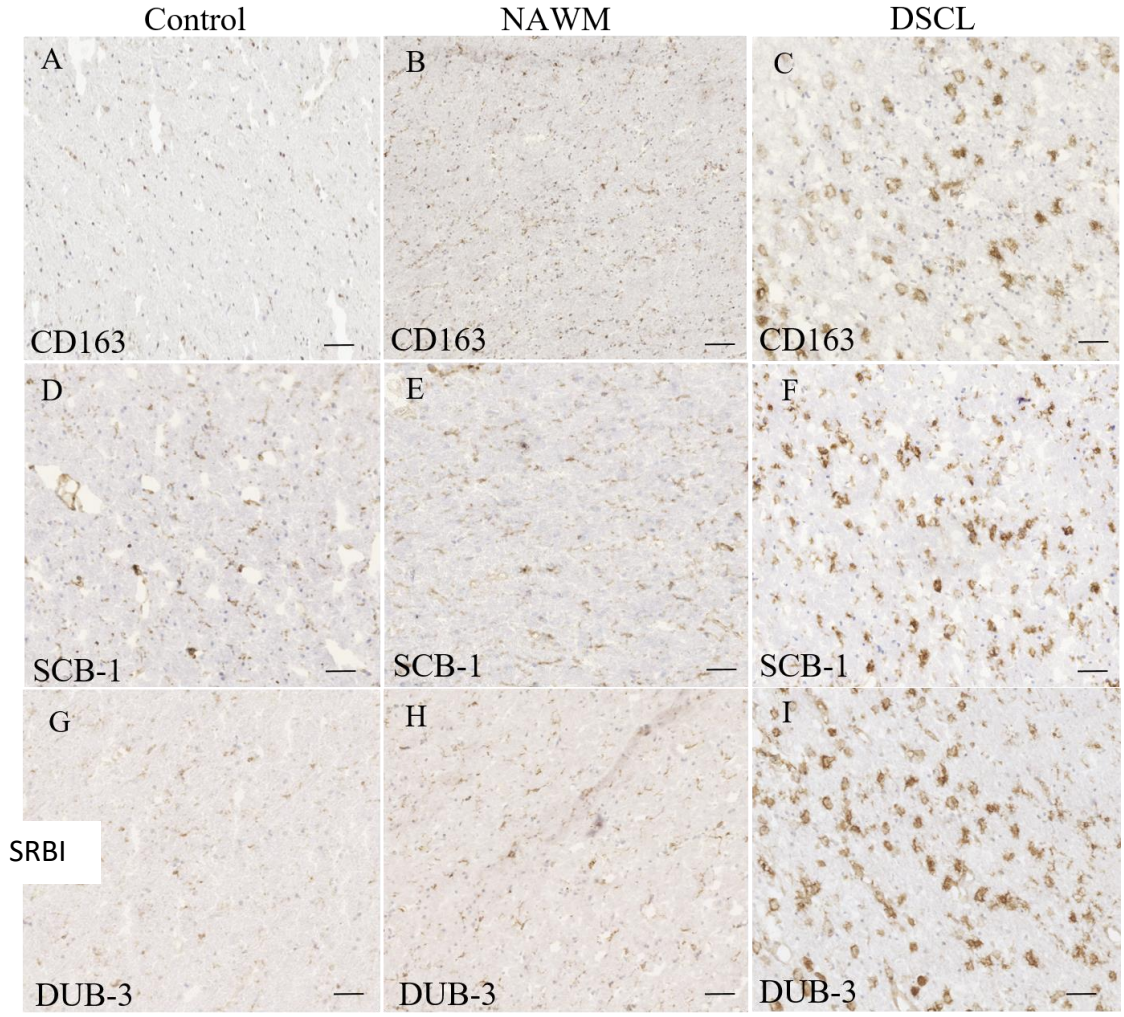

Figure 3.8 - Histological validation of proteins encoded by candidate genes identified from the microarray analysis. The positively immunolabeled microglia cell bodies and the processes are visualised with the markers (A-C) CD163, (D-F) SRBI, and (G-I) Dub3 in control, NAWM and DSCL groups. The scale bar represents 250 µm.

Table 3.9 - Expression of CD163, Dub3 and SRBI in age-associated deep subcortical white matter

WM group	Control	NAWM	DSCL
CD163	0.47 (0.29-0.85)	1.41 (0.43-3.24)	4.07 (2.12-6.41)
Dub3	0.25 (0.20-0.28)	0.44 (0.30-0.66)	4.44 (1.09-7.89)
SRBI	0.46 (0.22-0.70)	0.83 (0.74-0.93)	7.02 (1.85-15.09)

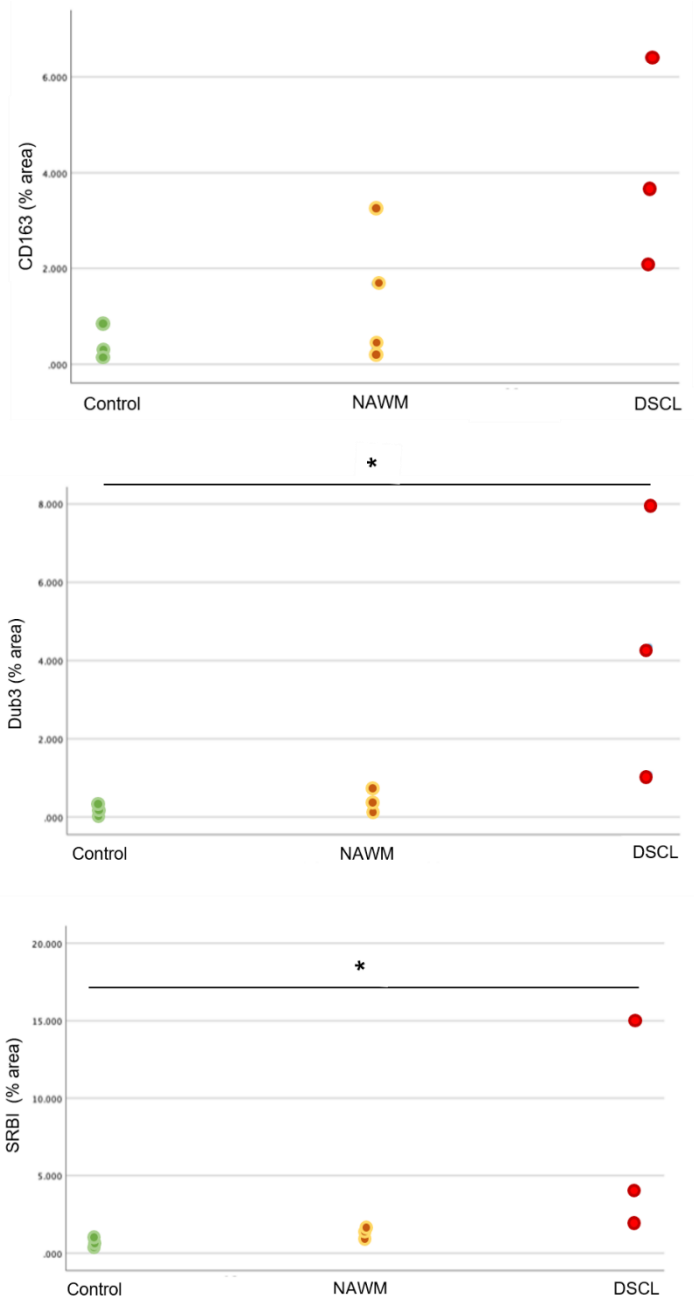

*Figure 3.9 - Quantitation of the protein encoded by the candidate genes in deep-subcortical white matter. Within the three deep subcortical white matter groups, the percentage area for the immunoreactivity of the protein encoded by a panel of candidate genes was evaluated. (A) The immunoreactive profile of CD163 is not significantly differentially expressed across the three groups (B) the expression of (B) Dub3 and (C) SRBI were significantly higher in DSCL compared to non-lesional control. Number of sample per group: Control n=3, NAWM n=4, DSCL n=3,*p<0.05.*

3.4 Discussion

Age-associated WML are a common feature of the ageing brain, with DSCL occurring in around 60% of the ageing population (Simpson et al., 2011). Age-associated WML are associated with cognitive decline (Fadul et al., 2020), are an independent risk factor for dementia (Fernando et al., 2004b, Hu et al., 2021), and are characterised by high levels of microglia with an amoeboid phenotype (Simpson et al., 2011). This chapter aimed to identify microglial-associated mechanisms underlying the pathogenesis of DSCL using a microarray transcriptomic profiling approach. A comparison transcriptomic analysis was performed to detect significantly differentially expressed genes between three WM groups, namely DSCL, NAWM from lesional cases and control WM from non-lesional cases. The microarray findings reveal complex roles for microglia within the DSCL. The present data imply a neuroprotective role for microglia within the DSCL, while the microglia in NAWM appear neurotoxic, as explained in the paragraphs below.

3.4.1 Upregulation of haptoglobin binding in the DSCL infers microglia adapt a neuroprotective profile within age-associated DSCL

Haptoglobin (Hp) is a plasma protein that immediately and irreversibly binds to haemoglobin (Hb) during haemolysis, forming the haemoglobin-haptoglobin complex (Hb-Hp). By forming this complex, Hp reduces the oxidative properties of the Hb, playing an antioxidant role (Sadrzadeh and Bozorgmehr, 2004). The plasma Hp level increases in inflammation, infection and tissue damage (Yang et al., 2000). Following dysfunction of

the BBB, for example following intracranial bleeding (Bulters et al., 2018), red blood cells (RBC) enter the CNS, where they are broken down and release Hb. The extravasation of RBC and the subsequent breakdown of Hb results in the accumulation of iron and reactive oxygen species, which can induce cell death via oxidation and inflammation (Sadrzadeh and Bozorgmehr, 2004).

Following cerebral ischemia, Hb has been detected in cerebral neurons, astrocytes and microglia (He et al., 2011). An increase in the haemoglobin β subunit (*HBB*) has also been reported in a range of neurodegenerative diseases. In a multiple sclerosis (MS) post-mortem proteomic analysis, HBB was found to be co-localised in neurons (Brown et al., 2016) and $CD68^{+}$ microglia (Brown, 2014). In an adult rat model of intracerebral haemorrhage (ICH), significantly increased mRNA levels of both the haemoglobin α subunit (*HBA*) and β subunit HBB in neurons and glia cells. Furthermore, rat neurons exposed to 50 or 100 μM hemin (containing iron, similar to an endogenous level resulting from vascular injury) significantly upregulate the expression of *HBA* and *HBB in vitro*. These *in vivo* and *in vitro* studies indicate that neurons and glia are associated with significantly increased expression of Hb following cerebrovascular damage (He et al., 2011).

Microglia become activated following a cerebrovascular event, such as a haemorrhage. In a post-mortem study of a patient who suffered from a subarachnoid haemorrhage, iron deposition was found and correlated with the cognitive outcome. In addition, the microglial activation and motility markers (CD68 and Iba1) were both significantly elevated following Intracerebral haemorrhage (ICH) (Shatya et al., 2021) and

subarachnoid haemorrhage (Galea et al., 2022). In the present study, microarray analysis revealed the significant upregulation of transcripts associated with Hp binding and the Hb-Hp complex by microglia in DSCL. These findings suggest that in response to Hb accumulation as a result of RBC extravasation due to BBB dysfunction in DSCL, microglia increase their haptoglobin binding, thereby protecting the brain from the damage induced by Hb.

The Hb-Hp complex is rapidly recognised and degraded via the macrophage scavenger receptor CD163 (Bicho et al., 2013). In human neurological disorders, the Hp levels elevated in the cerebrospinal fluid (CSF) following a haemorrhage paralleled a similar rise in Hb, forming the Hb-Hp complex (Bulters et al., 2018, Kristiansen et al., 2001). Tissues sampled around Intracerebral haemorrhage and haematomas display a significant increase in CD163-positive microglia (Bulters et al., 2018), and in patients with ICH, a significant increase in serum CD163 levels is associated with increased haematoma absorption and improved neurological recovery (Xie et al., 2016). In Alzheimer's disease (AD), microglia activation-associated markers, including the CD163, are significantly increased (Hopperton et al., 2018). In the current study, the significant increase in *CD163* expression is not reciprocated at the protein in DSCL, which likely reflects the low number of cases used in this validation study. Nevertheless, considering that the Hb-Hp complex has an antioxidant function and the upregulation of CD163 is one of the M2-associated microglial markers (Borda et al., 2008, Var and Byrd-Jacobs, 2020), the current data suggests microglia within DSCL may play a neuroprotective role.

3.4.2 Downregulation of protein ubiquitination and deubiquitination in the NAWM infers microglia adapt a neurotoxic profile in the regions surrounding DSCL

Although MRI and histological analyses suggest that the NAWM appears very similar to the non-lesional control WM, the transcriptomic profile of microglia is significantly different, including dysregulation of genes associated with protein ubiquitination and deubiquitination, and the scavenger receptor class B, member 1.

Protein ubiquitination is a post-translational modification where ubiquitin is attached to a substrate protein. The deubiquitinating enzymes (deubiquitinases, or DUBs) regulate ubiquitination levels of the target protein (Hu, 2012, Guo and Tadi, 2022) by removing ubiquitin from the target protein, hence maintaining the protein stability (Bousman et al., 2019, Yang et al., 2021). Maintaining a balance of ubiquitination and deubiquitination is essential in protein homeostasis (proteostasis), where the protein ubiquitination and deubiquitination regulate the degradation, transport, localization, and activity of proteins (Guo and Tadi, 2022, Yang et al., 2021) and play a role in maintaining neuronal function, growth and survival (Zajicek and Yao, 2021, Amer-Sarsour et al., 2021).

DUB is crucial for balancing the two reversible processes, ubiquitination and deubiquitination (Yang et al., 2021). The ubiquitin-proteasome system (UPS) is a direct protein degradation system (Zheng et al., 2016), and a primary regulator for neural biology (Caldeira et al., 2014). In the CNS, dysregulated/dysfunctional UPS is associated

with intracellular ubiquitin-positive inclusions formed by the accumulation of neurotoxic proteins that instigate neurodegeneration (Zheng et al., 2016). This common pathological feature is observed in many neurological disorders, including: schizophrenia, autism spectrum disorders (ASDs), Parkinson's disease (PD), and AD (Zajicek and Yao, 2021). During the ageing process, neurological disorders are associated with failure of the UPS (Lim et al., 2020). For example, in AD, the primary pathogenesis is the aggregation of neurotoxic proteins, including β-amyloid (Aβ) and ubiquitinated proteins, within vulnerable brain regions triggering a neurodegenerative cascade leading to neuronal death (Zheng et al., 2016).

The current study identified dysregulation in expression of genes associated with protein ubiquitination and deubiquitination dysregulation, including the ubiquitin-specific peptidase 17-like family member (USP17L), the ring finger protein 8 (*RNF8*), and the Toll interaction protein (*TOLLIP*).

USP17L subfamily, also referred to as DUB3, is a deubiquitinating enzyme. USP17L removes the conjugated ubiquitin from target proteins to regulate cellular processes, including progression through the cell cycle, apoptosis, cell migration, and cellular immune responses (Pontén et al., 2008). Within the CNS, USP17L regulates cell proliferation, neuronal autophagy and proteostasis (Das et al., 2020). The pro-inflammatory cytokines interleukin (IL-4) and IL-6 induce the release of USP17L (Yang et al., 2021) which impacts inflammation, cell motility, and carcinogenesis (Yang et al., 2021), and promotes apoptosis (Hanpude et al., 2015). The literature on *USP17L* in

neurological pathogenesis is limited; however, *USP17L* depletion is known to impact cell proliferation (Wang et al., 2015).

RNF8 encodes for the ubiquitin ligase RNF8 enzyme, which plays an essential role in the UPS system. In the CNS, RNF8 is essential to maintain neuronal integrity (Ouyang et al., 2015, Li et al., 2010), and is involved in neuronal-repair processes (Liu et al., 2013). Decreased expression of RNF8 is associated with neuronal pathology, cognitive decline, and neurodegeneration (Ouyang et al., 2015). In a *RNF8*$^{-/-}$ rodent model, knockout of *RNF8* results in neuronal degeneration, impaired behavioural performance (Ouyang et al., 2015), increased genomic instability and elevated risk of tumorigenesis (Li et al., 2010).

TOLLIP encodes a ubiquitous intracellular adaptor protein TOLLIP that interacts with the Toll-like receptor (TLR) (Capelluto, 2012) and plays a role in innate immunity, and providing neuronal support (Li et al., 2021). In neuroinflammation, TOLLIP plays a neuroprotective role (Humbert-Claude et al., 2016), and is involved in multiple intracellular signalling pathways (Li et al., 2021). *TOLLIP* expression decreases with ageing (Won et al., 2016), and reduced expression is associated with neurodegenerative diseases, including AD, PD (Chen et al., 2017, Humbert-Claude et al., 2016) and Amyotrophic Lateral Sclerosis (ALS) (Won et al., 2016). In an *ApoE*$^{-/-}$ mouse model, reduced expression of *TOLLIP* reduces autophagy, resulting in the excessive accumulation of cellular proteins that may result in neurodegeneration (Chen et al., 2017). Furthermore, in the *TOLLIP*$^{-/-}$ mouse injection of lipopolysaccharide increases susceptibility to neuroinflammation characterised by the significant elevation in

expression of pro-inflammatory cytokines including tumour necrosis factor alpha (*TNF-α*), interleukin *IL-1β* and *IL-6* (Humbert-Claude et al., 2016).

In addition to the dysregulation of protein ubiquitination and deubiquitination in the NAWM, the microglia were associated with an up-regulation of *SCARB1*, which encodes the Scavenger Receptor Class B type 1 (SR-B1) membrane-bound receptor (Lenahan et al., 2019). SR-B1 is a multifunctional protein, found on the surface of various cells, including microglia (Wilkinson and El Khoury, 2012), and plays a key role in maintaining homeostasis, pathogen recognition (Lenahan et al., 2019), and pathogen clearance (Yu et al., 2015). SR-B1 is also involved in many biological processes, including lipid transport: it participates in the selective transport and regulation of cholesterol and lipids, which correlates with a risk of stroke (Lenahan et al., 2019). In addition, SR-B1 expression impacts the activation of microglia and their contribution to neurodegeneration (Eugenin et al., 2016), particularly in AD, as the accumulation of Aβ plaques is cleared by activated microglia via the scavenger receptors (Eugenin et al., 2016) (Wilkinson and El Khoury, 2012). Binding to SR-B1 triggers a pro-inflammatory response which may also contributing to AD pathology (Yu et al., 2015). SR-B1 plays a role in maintaining homeostasis under physiological conditions, however under pathological conditions, SR-B1 plays a role in the recruitment and activation of cells that contribute to the development of pathology (Yamada et al., 1998, Yu et al., 2015).

Balancing protein expression and degradation through the UPS and DUBs is critical for proteostasis (Lim et al., 2020). In the present study, the significant downregulation of genes associated with protein ubiquitination and deubiquitination, suggest that microglia

in the NAWM are no longer able to perform their homeostatic function. Furthermore, since *RNF8* and *TOLLIP* have neuroprotective effects (Zhu et al., 2022), the downregulation of these gene in association with the upregulation of the *SCARB-1* suggest that within the NAWM microglia adopt a neurotoxic phenotype which may contribute to lesion spread. However, it should be acknowledged that immunohistochemistry did not validate these gene expression changes at the protein level, and further detailed and more extensive validation is required.

3.5 Summary of the major findings

1. The DSCL microglia appear to have a neuroprotective role for its antioxidant function and the upregulation of CD163. However, microglia within the lesion are unable to repair the neural wounds.

2. Within the NAWM, microglia appear to adopt a neurotoxic profile, which may contribute to the lesion spread.

Chapter 4 **Characterising hypoxia-associated Microglial Phenotypic Changes in *vhl*$^{-/-}$ Mutant Zebrafish**

4.1 Introduction

Microglia actively monitor their surrounding microenvironment, playing an essential role in maintaining homeostasis with the CNS (Hashemiaghdam and Mroczek, 2020). In responding to hypoxia, the human microglial distribution, activity, and phenotype are altered, where microglia migrate to the hypoxic site and become activated (Wang et al., 2008, Fumagalli et al., 2015). Hypoxic conditions may induce microglial activation directly through production of reactive oxygen species, thereby triggering a neuroinflammatory response (Guo et al., 2014). Microglia are also indirectly activated via the entry of pro-inflammatory molecules into the CNS causing neuroinflammation (Kiernan et al., 2016). The precise role of microglia under hypoxic conditions and within ischemic human brains has been proposed to be either neurotoxic or protective; currently their exact role is therefore undefined (Fumagalli et al., 2015).

Similar to the human brain, the zebrafish microglia are involved in homeostatic maintenance (Var and Byrd-Jacobs, 2020). They display a ramified morphology under normal conditions and can be transformed to activated state with amoeboid morphology (adopting either an M1 or M2 phenotype) under pathological conditions (Var and Byrd-Jacobs, 2020). Microglia in zebrafish are first formed in the embryonic stages, where primitive macrophages develop in the yolk sac and spread into the cephalic mesenchyme at about 24 hrs post-fertilization (hpf). Afterwards, around 60 hpf, when neural apoptosis

starts to occur, invasion of microglia to the brain is initiated (Herbomel et al., 2001, Mazzolini et al., 2020). Microglia are fully functional at 3 days post-fertilization (dpf), evidenced by clearing apoptotic neurons and directly interacting with neuronal injuries. Between the age of 3 dpf and 5 dpf, microglial morphology is characterised by rapidly transforming between phagocytic and ramified profiles. These morphing microglia finally settle into a typical mature ramified morphology by 5 dpf and become more processed by 7 dpf (Svahn et al., 2013). Notably, the mechanisms of microglial function in zebrafish are similar to humans, indicating a high degree of homology across species (Mazzolini et al., 2020).

Reduction of oxygen levels leads to activation of the hypoxic signalling pathway (Weidemann et al., 2008), many of the biological responses to hypoxia are orchestrated by this signalling pathway which results in stabilisation of the transcription factor hypoxia-inducible factor alpha (HIF-1α, HIF-2α and HIF-3α). VHL is a negative regulator of the pathway (Ang et al., 2002) (see below); therefore, the current project has utilised the *vhl*$^{-/-}$ line to investigate the effects of the sustained activity of the HIF pathway on the microglial phenotype.

The *vhl*$^{-/-}$ zebrafish carries a truncating mutation in exon 1 of VHL homolog, leading to a non-functional von Hippel-Lindau (VHL) protein, as detailed earlier in section 1.10. The VHL encoded normal protein function regulates an array of cellular and physiological processes. Most importantly, the VHL protein downregulates the main regulator of hypoxia adaptation, the HIF-α subunit, by targeting the protein for degradation (Ang et al., 2002). Therefore, a mutation of the VHL protein will eventually lead to permanent

activation of the HIF pathway within the *vhl*$^{-/-}$ mutant fish. The homozygous offspring display systemic responses to hypoxia, including polycythemia; pronephric defects with hyperventilation; and angiogenesis soon after maternal *vhl* mRNA and protein run out. However, the reactions of increased cardiac rate are demonstrated until later larval stages of 5 dpf (van Rooijen et al., 2009).

The optical clarity of the zebrafish during its development is one of the ultimate advantages of this model by allowing the *in-vivo* high-quality imaging of the internal structure. Thus, the *vhl*$^{-/-}$ zebrafish model enables the real-time characterisation of sustained HIF signalling activation inducing microglial changes. Activation of the HIF pathway can be visualised using a hypoxia reporter line of *Tg(phd3::EGFP)*$^{i144/i144}$, where up-regulation of the phd3 gene produces fluorescence from 28 hpf. In addition, the *Tg(mpeg1::mCherryCAAX)*^{sh378} can be used to visualise microglia within the live zebrafish (Ogryzko et al., 2019). Therefore, the double transgenic line *vhl* $^{hu2117/+}$ *(mpeg1::mCherryCAAX, phd3::GFP)* can be utilised for high-resolution confocal imaging of microglia in response to sustained HIF signalling in transgenic zebrafish.

In response to injury-dependent changes in neuronal activity, microglia alter their morphology, accumulate rapidly at injury sites, and perform their phagocytic function (Var and Byrd-Jacobs, 2020). At the site of the lesion, activated microglia clear away the damaged neurons while restoring the CNS homeostasis via secreting both types of functional cytokines of interleukin (IL) in the lesioned larvae: Pro-inflammatory (IL-1β, IL-6) and anti-inflammatory (IL-4, IL-10) interleukins (Gan et al., 2020).

Hypothesis, Aims and Objectives

The *vhl*$^{-/-}$ fish was first reported in 2009, but to date, no studies have examined the impact of sustained HIF signalling on microglia in this model. We hypothesise that in response to sustained activation of the HIF signalling pathway, microglia adopt an M1 phenotype, characterised by a change in their morphology and secretion of pro-inflammatory cytokines. Further, the inflammatory profile of microglia will be amplified in the *vhl*$^{-/-}$, which undergo additional stress (head injury) compared to their wildtype siblings. Therefore, this chapter aims to perform a detailed morphological assessment of microglia phenotypes and their inflammatory profile in the *vhl*$^{-/-}$ during development compared to their wildtype siblings.

The chapter objectives are:

1. Evaluate the microglial phenotype under the response of sustained activation of the HIF pathway within the *vhl*$^{-/-}$ larvae stage of 3, 5 and 7 dpf
2. Evaluate the inflammatory profile of the *vhl*$^{-/-}$ zebrafish larvae
3. Evaluate the immediate inflammatory response following additional stress (head injury), and after 24 hrs under the effects of the sustained activation of the HIF signalling pathway.

4.2 Materials and Methods

4.2.1 Ethics Statement

All zebrafish were raised in the Bateson Centre Aquaria. All protocols were performed according to the guidelines of the UK Animal (Scientific Procedures) Act 1986, under project licence PB2866ED0 issued to Dr Freek van Eeden and my personal licence IEDEC4510. Procedures were conducted as per the UK Home Office guidelines and approved by The University of Sheffield Review Ethics Panel.

4.2.2 The *vhl* zebrafish

The *vhl* $^{hu2117/+}$ (*phd3::eGFP*$^{i144/+}$*; mpeg1:mCherryCAAX*$^{sh378/+}$) transgenic breeding colony, was developed in the aquarium services facility at the University of Sheffield, Biomedical Science Department by Dr Fredericus van Eeden, and fish were selected as embryos by his laboratory technician Miss Eleanor Markham to identify *phd3::egfp*$^{/+}$; *mpeg1:: mCherryCAAX*$^{sh378/+}$ carriers.

For these studies, the fish were in-crossed to generate *vhl* $^{hu2117/\ hu2117;}$ *phd3::eGFP*$^{i144/\ i144}$*; mpeg1:mCherryCAAX*$^{sh378/+}$, here referred to as *vhl*$^{-/-}$, and *vhl* $^{hu2117/+}$; *phd3::eGFP*$^{i144/+}$*; mpeg1:mCherryCAAX*$^{sh378/+}$ embryos, their sibling, within Mendelian ratio. Within this thesis, 'sibling' refers to wildtype and heterozygous fish, +/+ or +/-; this classification is based on the knowledgethat *vhl* heterozygotes do not show any phenotype and are fully viable (van Rooijen et al., 2009). Hence, in the current project, a

mix of wt and heterozygous fish were used as a wt-sibling. It was impossible to distinguish these animals without genotyping, which is incompatible with practical experiments.

4.2.3 Zebrafish Husbandry and General Practice

4.2.3.1 Adult Zebrafish Maintenance

The adult zebrafish breeding stock was group-housed in a recirculating aquarium system. They were raised and maintained under the standard conditions of water temperature of 26-28°C, pH 7.5 and light cycles of 14:10 light:dark hours. Adult zebrafish were fed Artemia nauplius larvae and maintained at a maximum density of four fish per litre of aquarium water. The aquarium standards of zebrafish husbandry, breeding and mating were performed according to the appropriate guidelines (Nüsslein-Volhard & Dahm 2002, Westerfield, 1995).

4.2.3.2 Zebrafish Mating

As mentioned previously homozygous mutant zebrafish, *vhl*$^{-/-}$ die prematurely, around 10 dpf (van Rooijen et al., 2008). Therefore, heterozygous *vhl*$^{-/+}$ fish were in-crossed to produce the homozygous mutant (*vhl*$^{-/-}$) and wildtype zebrafish siblings (wt: *vhl*$^{-/+}$, *vhl* $^{+/+}$).

For mating, both heterozygous adult males and females were placed in a tank separated by a divider overnight. The following day the divider was removed, enabling breeding and egg production. The laid eggs passed through a protective mesh to the bottom of the breeding tank, preventing the eggs from being ingested by the parents.

After a couple of hours, the adult zebrafish were removed from the breeding tank and returned to the housing tank. Alternatively, to obtain large numbers of eggs, the tanks were placed into the adult stock tanks, thus, assisting multiple eggs lay from different females and fertilisation by other males. The embryos were collected by sieving the tank water and then placed in fresh aquarium water.

The embryos were sorted to remove any dead, unfertilised or anomalous developing eggs within one hour. The desired embryos were reared in a 90 mm petri dish (Sterilin, Newport, UK) filled with pre-prepared E3 medium at a maximum density of 60 embryos to maintain adequate water quality and aeration and incubated at 28°C. Petri dishes were checked daily to remove dead embryos or empty chorions; the E3 media was refreshed as required. For embryos raised beyond 5.2 dpf, the density was reduced to a maximum of 20 larvae per plate.

The embryo staging was defined according to the age in hours/days post fertilisation (hpf/dpf) (Kimmel et al., 1995). When required, 24 hpf embryos were treated with 0.00004 % of N-phenylthiourea (PTU- Sigma, Poole, UK), where 12.5 µl of a 2000x stock in DMSO was added to every 25 ml of E3 medium, to prevent embryo pigmentation and enhance transparency for imaging (Karlsson et al., 2001). In all experiments, unless raising larvae to 7 dpf was required, embryos were maintained to 5.2 dpf. To terminate larvae at 5.2 dpf, the fish were anaesthetised using pre-prepared tricaine before being placed in bleach.

4.2.3.3 Zebrafish anaesthesia

Zebrafish adults and larvae were anaesthetised using Tricaine (also known as MS222) (PharmaQ, Hampshire, UK); obtained and prepared via the University of Sheffield veterinary services department. Tricaine stock solution (4mg/ml in milliQH2O [Millipore MA, USA]) was adjusted to pH 7 using 1M Tris. For adult fish sedation and the fin clip procedure, the stock solution was further diluted to a final concentration of 0.168 mg/ml of aquarium water. For larvae anaesthetic and manipulation, the stock solution was added to 100 ml of E3 media instead. The final concentration was adjusted conditional to the required duration and depth of sedation required of embryo mounting for imaging purposes.

4.2.3.4 E3 Media

All zebrafish embryos used for the project experiments were reared in E3 media, diluted 10x stock by distilled water (dH_2O), including the following final concentrations of NaCl (5 mM); KCl (0.17 mM); CaCl (0.33 mM); $MgSO_4$ (190.33 mM) and Methylene Blue (0.00001% w/v; Sigma-Aldrich), as a fungicide and antibacterial agent, and stored at 28°C.

4.2.3.5 Larval Sorting

Prior to each experiment and at 3 dpf, the Leica microscope EL6000 with the Leica Application Suite X (LAS X) software was used to identify fluorescent reporters and sort the larval genotypes accordingly. For sorting, larvae were placed on a petri dish containing E3 media supplemented with tricaine. The fluorescent channels ET-GFP and ET-RFP were used to identify the positively expressed EGFP and mCherry larvae, respectively. Sorting

images presented in this thesis were taken using a Leica M165 FC dissection scope and a Leica DFC310 FX camera (Leica microsystems, Milton Keynes, UK). The scale bars were then added using LAS X software.

4.2.3.6 Zebrafish Genotyping Using PCR

Tail fin clip biopsies were used to determine the genetic status of the adult zebrafish. To collect the fin clip, fish were anaesthetised in a tricaine methanesulfonate solution (4.2 ml in 100 ml of aquarium water) until the gill movement was reduced. Afterwards, maximally one-quarter of the tail fin was collected from each fish using sterile scissors (rinsed with 70% ethanol then sterile dH_2O). Each clip was placed in an individual well of a standard 96 well plate while the fish were placed in individual tanks to allow later identification.

To extract the DNA from the fin tissue, the tissue was suspended in 25µl 20% Tween in TE, an extraction solution, and vortexed before it was heated at 95°C for 15 min. Following this, the tissue was digested by adding 2µl 25mg/ml of proteinase-k (Prot-k; Sigma-Aldrich) to the mixture and heated at 55°C for 3hours. This mixture was incubated at 98°C for 15 min to denature the digestion enzyme, 25µl of MilliQ-water added, and the plate vortexed for a few seconds. The samples were used in a polymerase chain reaction (PCR) mixture to amplify the *vhl* allele.

PCR amplification was performed on the genomic DNA using specific primers to amplify the mutated region of the *vhl* ortholog gene in zebrafish (Table 4.1) where the PCR primers Invitrogen(Paisley, UK) were diluted inMilliQ-water from a 10 mM stock to a final master mix concentration 5µM. The amplification protocol using the FIREPol®

master mix (Solis Biodyne, Tartu, Estonia) is summarised in Table 4.2and the thermal protocol issummarised in Table 4.3.

The amplified *vhl* PCR products (5µl) were incubated with the restriction enzyme *Bci*VI (10,000 units/ml, New England Biolabs, Hitchin, UK) to enable the digestion of the wildtype *vhl* gene, as summarised in Table 4.4, and incubated overnight at 37°C. The digest mixture was visualised by gel electrophoresis, where 20µl PCR product and Hyperladder IV DNA ladder 5µl of 100 base ladder ; (Bioline, London, UK)were loaded onto a 3% molecular grade agarose gel, run at 100V for 30 minutes, and imaged using UVdoc imager (UVItec Cambridge, UK).

The *Bci*VI enzyme digests the restriction site localised in the wildtype (WT) and cuts 6 nucleotides down from the site of the sequence (5-GTATCC$(N)_6$-3). Following agarose gel electrophoresis, homozygous $vhl^{-/-}$ present a single band at 412 bp, heterozygous $vhl^{-/+}$ present two bands (412 bp and 200 bp), whereas wt zebrafish genotypes present as one intense band at 200 bp, as shown in Figure 4.1.

Table 4.1 - Oligonucleotide primer sequence used to amplify the vhl ortholog gene

Gene	Primer Sequence
vhl	Forward 5’ TAAGGGCTTAGCGCATGTTC 3’
	Reverse 5’ CGAGTTAAACGCGTAGATAG 3’

Table 4.2 - PCR master mix components used for allele amplification

Component	Volume
genomic DNA	1.5µl
Firepol	4µl
Forward vhl primer	1µl
Reversed vhl primer	1µl
MilliQ (mQ) H2O	12.5µl

Table 4.3 - PCR program used for amplification process

Steps	Temperature	Duration
Initial denaturing	94°C	5 min
Denaturing	92°C	1 min
Annealing	56°C	30 sec
Extension	72°C	40 sec
Repetition of steps 2-4	92-72 °C	39 cycles
Final elongation	72°C	10 min
Hold	4°C	∞

Table 4.4- Restriction enzyme mixture that used to digest the vhl allele

Component	Volume
NEB buffer	1.8µl
*Bci*VI enzyme	0.4µl
mQH2O	12.8µl
vhl PCR product	5µl

A

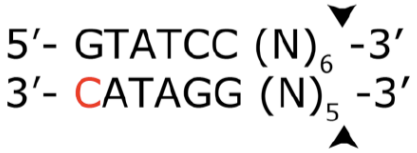

B

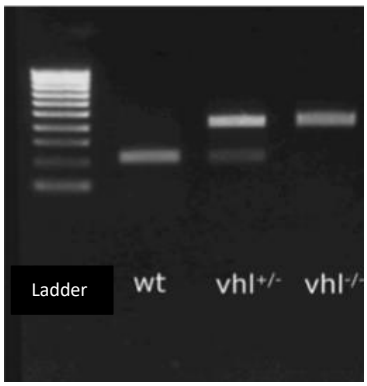

4.2.4 Figure 4.1 - Restriction enzyme digestion of the mutated region of the vhl allele in the vhl zebrafish. (A) The cleavage site of the enzyme BciVI, where the cytosine (highlighted in red) is mutated in the $vhl^{-/-}$ (C/T). (B) The BciVI enzyme digestion of vhl PCR products is preserved in the mutant $vhl^{-/-}$, PCR products, where the $vhl^{-/-}$lacks

the recognition site of the enzyme, but not at the heterozygotes and WT zebrafish. The HLIV ladder is 100 bp. Representative image are kindly provided by Dr van Eeden.Imaging: embryo preparation

This experiment assessed the microglia in live larvae at specific timepoints and across time-points using a time-lapse recording. The *mpeg1::mCherryCAAX*$^{sh378/+}$ transgenic line of *vhl* zebrafish enables the visualisation of microglia, as the mCherry positively expressed cells can be viewed under a fluorescent microscope with the excitement of ET-RFP laser wavelength of 525 nm emission and detection at 640 nm. For clarity purposes and to avoid interference with the melanin pigmentation during the imaging process, larvae were treated with N-phenylthiourea (PTU- Sigma, Poole, UK) at 24 hpf.

This study involved imaging microglia using two independent approaches: Light-Sheet microscopy and spinning-disk confocal microscopy. Following the preparation, larvae were embedded in an 8% low-melting gel (Sigma-Aldrich) in a chamber suitable for the specialised microscopic systems. The acquired images were analysed; the microglia phenotype changes were evaluated by exploratory comparison between the *vhl*$^{-/-}$ zebrafish and their wildtype sibling.

4.2.5 *In Vivo* time-lapse Imaging of Microglia using Zeiss Light-sheet Fluorescence Microscopy

4.2.5.1 Animals Used and Experimental protocol

Three pairs of PTU treated *vhl*$^{-/-}$ and wt were used at 3 dpf for 24 hrs recording. One *vhl*$^{-/-}$ mutant and one sibling larva for each recording were mounted in a 0.8% low melting point agarose gel using a capillary glass tube. Images were localised at the dorsal perspective to enable the best view of the brain. The laser channels of 488 nm and 561 nm were set to visualise EGFP and mCherry fluorescence, respectively. Using the Zeiss Zen Black software (ZEISS Germany), z-stack images for both *vhl*$^{-/-}$ mutant and wt sibling larva were taken at 10 min intervals throughout 24 hrs. At the end of each recording, the heartbeats were checked to ensure the larva survived during the recording period.

4.2.5.2 Data Collection and Analysis

For analysis, the z-stack recording was converted to Maximum Intensity Projections (MIP). Z-stack images with 1 µm thickness were produced for every 30 minutes of the recorded videos. Using Fiji software (Madison, USA), the Image type was switched to 8bit to enable automated counting. Next, via the selection tool of Fiji, the region of interest (ROI) was selected using bright-field; it covered the anatomical areas extending from the olfactory bulb to the base of the cerebellum, excluding the eyes and mouth. Using this approach ensured the ROI was consistent between fish. Then the automated cell counting was applied using the Fiji particles tool, where the minimum size range was restricted to 36 nm to eliminate any background noise. A visual illustration of the counting method is presented in Figure 4.2. The validity of the automatic cell counting method, which was used to carry out all the analysis, was confirmed by blinded manual counts (conducted by 2 independent observers) of the microglia. As both automated and

blinded manual counts gave similar results for total microglia counts, the less time-consuming automated method was applied to all subsequent analyses.

The quantitated microglia cells were further subdivided into those with active or ramified morphology, based on the spherical shape of the cell body. Due to the heterogeneity of microglial phenotypes, cells were assigned manually (conducted by 2 independent observers) using the Fiji cell counter plugin tool. The microglia represented a spectrum of microglial morphologies, including those with a 'resting' phenotype and other activated phenotypes either with shorter and thicker processes or amoeboid microglia with a rounder morphology and no visible processes. The counting process was applied for these two genotypes, with the three biological repeats.

To assess the microglial phenotype, range of parameters were measured using Prism 8 software (Graph Pad Software, La Jolla, USA). All the activity parameters were calculated per animal and averaged per genotype. Repeated Measures ANOVA were used to assess if there were significant genotype differences in the number of microglia in the zebrafish larva brain. All values for the statistical tests were reported as the mean ± SEM with the significance set at $P<0.05$.

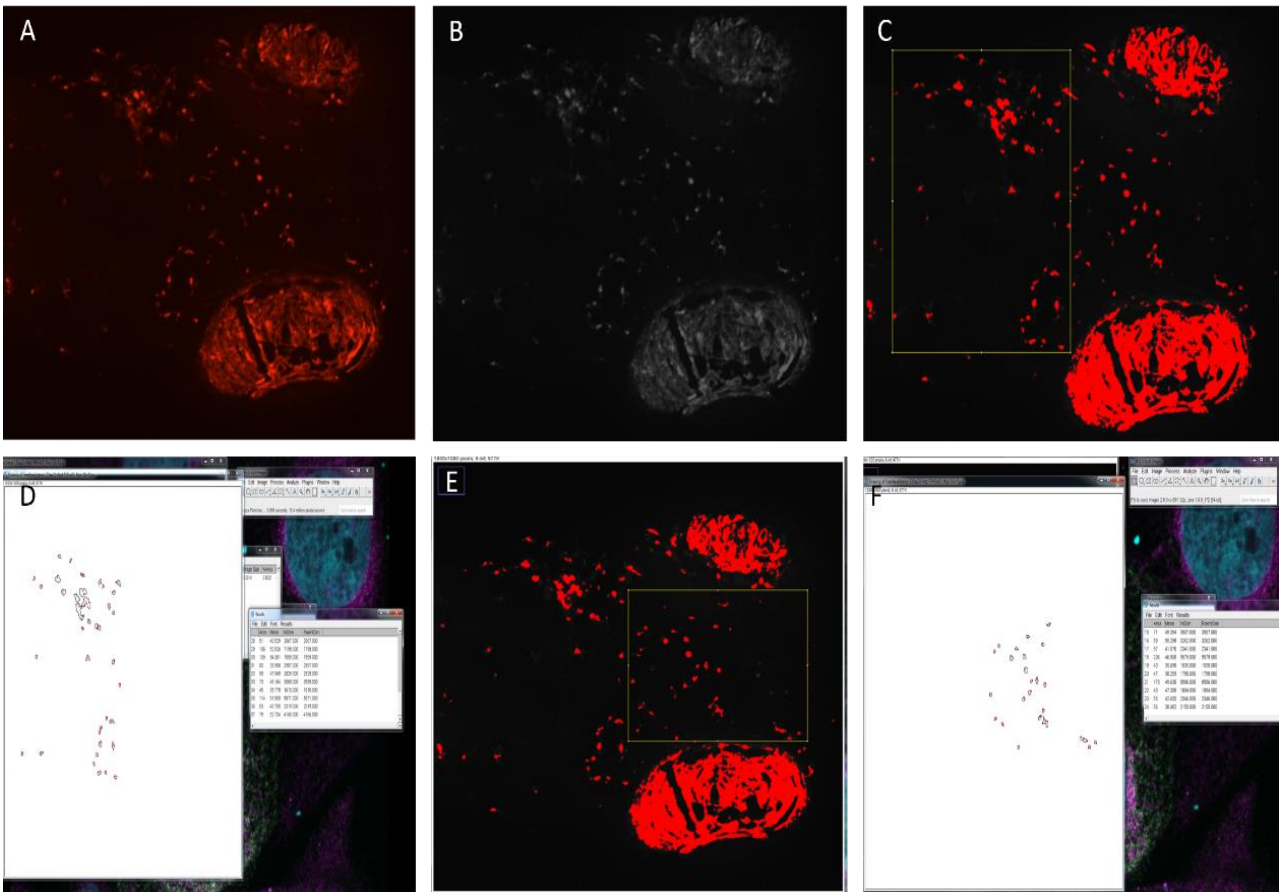

Figure 4.2 - The microglia automated counting method using MIP image and Fiji tools. To count the microglia, A: Image type was switched to 8bit in to enable the automated counting, B: The image threshold was adjusted to allow visualising the microglia and eliminate any background noise, C: The ROI was selected referring to the bright field, D: Using the A-Particular option, the size was set to 36 nm minimum, and the analysis was carried on, E: The remaining ROI is selected, and the exact steps are repeated. Eventually, the sum cell counts for both ROIs are calculated. The illustrated larvae image is for a wt sibling fish during its 6 hrs of microglia recording.

4.2.6 *In Vivo* Imaging of Microglia at 3 dpf: Using Zeiss Light-sheet Fluorescence Microscopy

4.2.6.1 Animals Used and Experimental Protocol

Nine pairs of PTU treated *vhl*$^{-/-}$ and wt siblings were used to take a single-time point between the age of 3.2 – 3.6 dpf, using the sample preparation and instrument set-up as described in section 2.4.1. The time point was selected to assess the impact of hypoxia on the microglial phenotype at an early stage.

4.2.6.2 Data Collection and Analysis

Data collection and cell counting methods are consistent with section 2.4.1.2. Independent t-tests were used to determine significant genotype-related differences in the microglia phenotype for analysis. The one-way ANOVA test was used to assess any significant genotype differences in the number of cells expressing a ramified or activated morphology. All statistical tests were shown as mean ± SEM, and a P value <0.05 was used to indicate statistical significance.

4.2.7 *In Vivo* Imaging of Microglia at 5 and 7 dpf: Using Spinning-disk Confocal Microscopy

4.2.7.1 Animals Used and Experimental Protocol

Nine *vhl*$^{-/-}$ and eleven wildtype (wt) siblings PTU treated larvae were used to image at two time- points of 5 dpf and 7 dpf. Zebrafish larvae were sedated in Tricaine and

embedded in a dorsal position for optimal visualisation of the brain area, in 0.8% low melting point agarose (Sigma-Aldrich) with 0.0168 mg/ml Tricaine for immediate imaging. Once the gel was set, it was covered with a Tricaine E3 media to prevent dehydration. High-resolution imaging was performed using 10x, 20x and 40x objectives on an UltraVIEWVoX spinning disc confocal laser imaging system (Perkin Elmer Life and Analytical Sciences). Fluorescence for GFP and mCherry was acquired using an excitation wavelength of 488 nm and 525 nm emission and detected at 510 nm and 640 nm, respectively. Z-stack images were acquired every 1 µm slice. Images were processed using Velocity™ software.

4.2.7.2 Data Collection and Analysis

For image analysis, the Z-stack with 1 µm thickness was used to create a maximum projection. The ROI was selected using bright-field and covered the anatomical areas extending from the olfactory bulb to the base of the cerebellum, excluding the eyes and mouths, referenced by referring to the bright-field image. Using this approach ensured the ROI was consistent between fish.

Quantifying the number of microglia was recognised by *Tg(mpeg1::mCherryCAAX)*^{sh378} labelled microglia and performed manually using Fiji counting tool on images taken under 10x objective of the spinning disk microscope. The counting approach was achieved by going within the ROI through the z-stack of the extended view images.

The microglia phenotypes were determined using Fiji circulatory measurement index, modified to the methods used in previously published articles (Hamilton et al.,

2020). For this, and via using Fiji tools, the image was adjusted for colour threshold. Next, the analyser particles were set as size (*Pixel$^{\wedge 2}$) of 36-infinity, and circulatory measurements were taken where 0-0.2 refers to the smallest (flat) cell body of ramified microglia, and 0.8-1 index for perfect circular microglia with amoeboid morphology. Indexes between 0.3 and 0.7 were considered for microglia with different morphology spectrums occurring between ramified and amoeboid, as illustrated in Figure 4.3.

The indication of the circulatory index was decided based on studying the detailed cell morphology under 40x, where cell body and process length enabled visualisation of ramified, amoeboid and active morphology within spectrum morphology, Figure 2-2: C-E. Hence, the classification of microglial morphology for images taken at ages of 5 and 7 dpf was based on the circular index, which was originally built on studying cell morphology under high magnifications lenses. This enabled more accurate explanations of changes occurring within the microglia. Notably, activated microglia were assigned based solely on their circulatory index measurement and morphology, and not their pro- or anti-inflammatory profile.

All statistical analysis was conducted using Prism 8 software (Graph Pad Software, La Jolla, USA). All values for the statistical tests were reported as the mean ± SEM with the significance set at $P<0.05$. All experiments were repeated three times, using three pairs of embryos from each different batch, where larvae were born on other dates. Both total microglia and morphology assessments were conducted by two individuals independently.

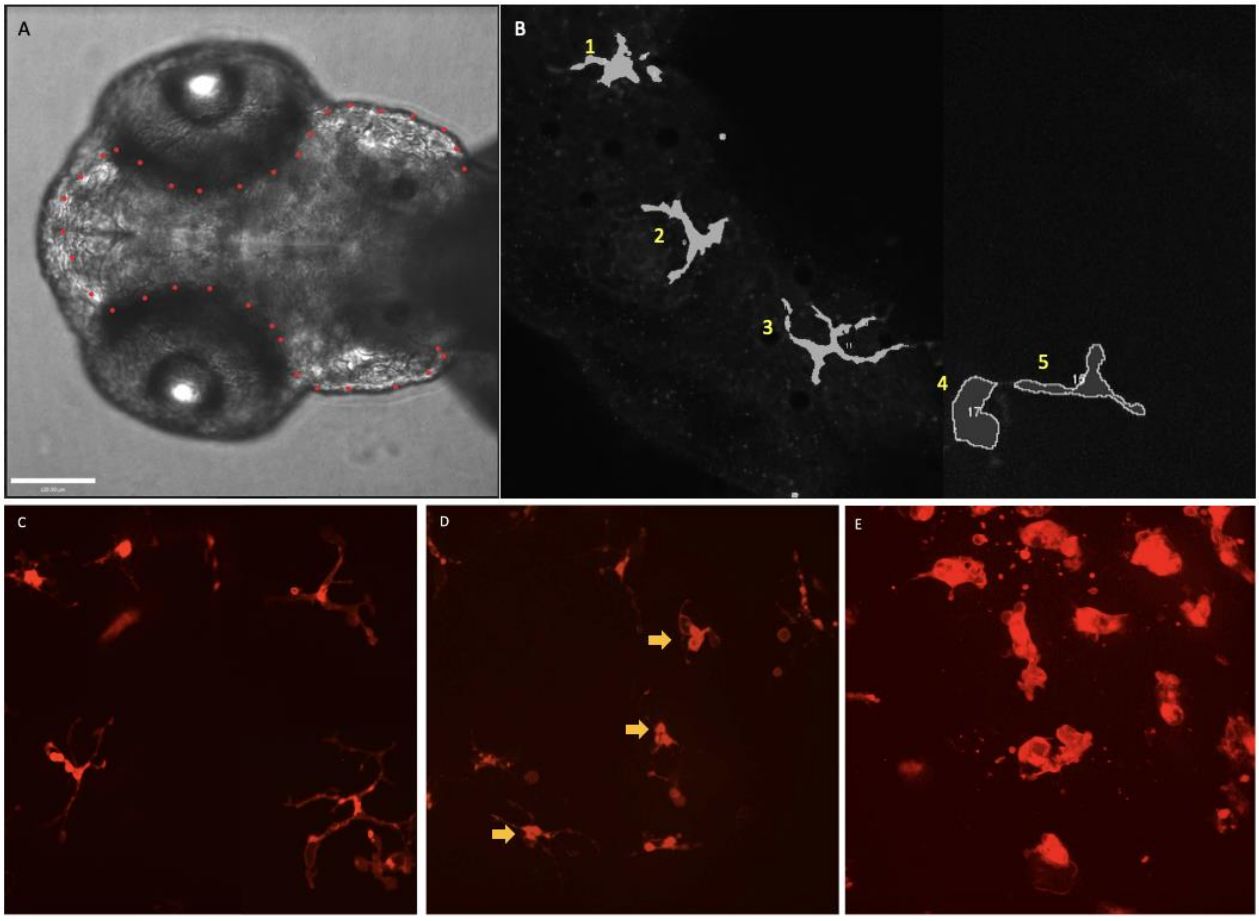

Figure 4.3 - The used approach of quantifying Microglia morphology. (A) The red dots identify the ROI, where the head area was considered, excluding the eyes and mouth (B) Examples of the circulatory index defining the microglia morphology; where the index indicators were 0.38, 0.12, 0.07, 0.81 and 0.1, for cells number 1-5, respectively, under the 20x magnifications (C) Representative image of microglia with ramified morphology (D) Microglia with within-spectrum morphology (arrowed) (E) representative image of amoeboid microglia, C-E images under 40x. Scale bar is 100 µm.

4.2.8 Evaluating TNF expression by microglia

Tumour Necrosis Factor- alpha subunit (TNF-α) is a cytokine involved in systemic inflammation during the acute phase reaction, produced by some glial and immune defence cells. The *(tnfα::GFP)* ^{pd1028} transgenic zebrafish line was used to assess *in vivo* readouts of the microglial activation profile.

4.2.8.1 Animal Used and Experimental Protocol

The double transgenic *vhl* $^{hu2117/+}$ *(mpeg1::mCherryCAAX, tnfα::GFP)* fish line used for the current project were obtained by outcrossing *vhl* $^{hu2117/+}$ *(phd3::eGFP*$^{i144/+}$*; mpeg1:mCherryCAAX*$^{sh378/+}$*)* into Tg*(tnfα::GFP)*^{pd1028} fish line (kindly provided by Dr Philip M. Elks and Dr Michael Bagnat; Bateson Centre, the University of Sheffield). The cross produced *vhl*$^{-/+}$ offspring carrying either one, or more of the three transgenic embryos at a mendelian ratio. Larvae were sorted for tnfα::GFP expression at 1-2 dpf, appearing as a reasonably bright GFP expression at the end of the gut, Figure 4.4. The larvae were further sorted for *mpeg1::mCherryCAAX*$^{sh378/+}$ microglia at 5 dpf. The *phd3::eGFP*$^{i144/+}$ expression was sorted at 3dpf; any larvae carrying this expression were excluded to avoid GFP overlap expressions at the experimental images. Under bright-field, *vhl*$^{-/+}$ siblings were selected. Hereafter, *vhl*$^{-/+}$ Larvae with the double transgenic *mpeg1::mCherryCAAX*$^{sh378/+}$*; tnfα::GFP* ^{pd1028} were raised under the standard husbandry procedures as described in section 4.2.3.1. At 2 months old, adult fish were genotyped for *vhl* mutation using the fin-clip samples and following the genotyping protocol, previously explained in section 4.2.3.6. The fish with the desired transgenic *(mpeg1::mCherryCAAX, tnfα::GFP)* were then raised and used for mating for the experimental purpose.

In preparation for the experiment, under fluorescent field larvae were sorted for double transgenic (*mpeg1::mCherryCAAX*$^{sh378/+}$*, tnfα::GFP* ^{pd1028}); *vhl*$^{-/-}$ and *vhl*$^{-/+}$ larvae were sorted under bright-field following the criteria mentioned previously at section1.11, and then reared in E3 medium supplemented with PTU at 24 hpf onward. The comparisons of tnfα::GFP expression among the two genotypes were achieved by acquiring live images using confocal spinning disk microscope (Leica) under 10x, 20x and 40x magnifications, every 24 hrs starting from 2 dpf until the age of 7 dpf. Image acquisitions were fixed through all images.

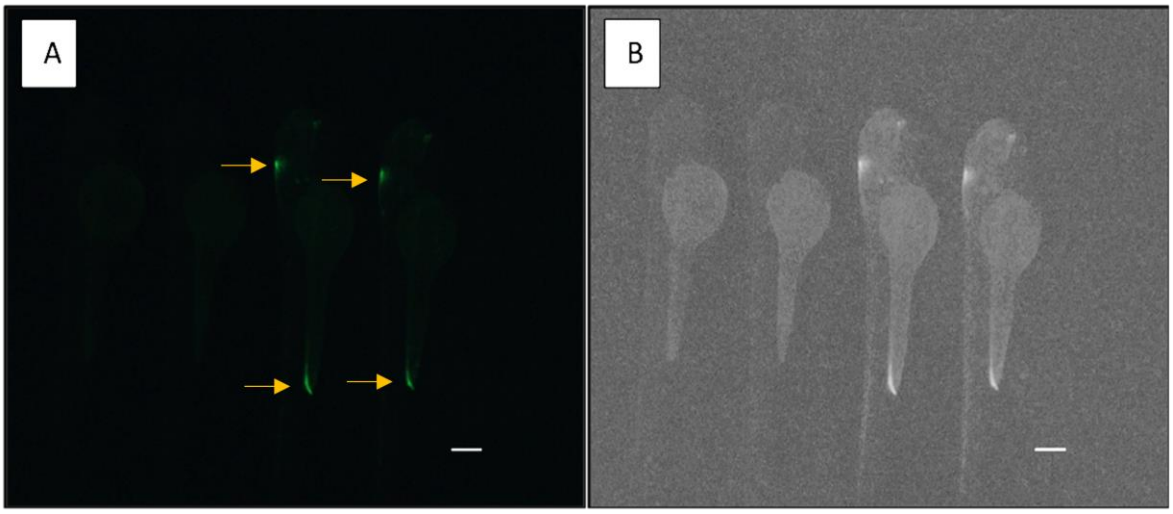

Figure 4.4 - tnfα::GFP pd1028 expression in larvae zebrafish. The tnfα::GFP transgenic larvae appear as (A) GFP positive expression at the gut and brain neural mass compared (yellow arrows), (B) Grayscale image illustrates both tnfα::GFP positive and negative expression at two larva lines. Larvae are 3 dpf old; the Scale bar is 200 µm in length.

4.2.8.2 Data Collection and Analysis

Over the period from 2 dpf to 7 dpf, Tnf-α expression in the brain was assessed in *vhl*$^{-/-}$ larva compared to their wt sibling (n=3 larvae per genotype). Microglial expression

of Tnf-α was observed as overlapping emission from mCherry and GFP positive cells producing a yellow emission.

4.2.9 Evaluating the Tnf-α expression in the *vhl* following head injury

4.2.9.1 Animals Used and Experimental Protocol

Briefly, the 4 dpf larvae were reared in E3 in Petri dishes, supplemented with PTU at 24 hrs onward. For stab injury operation, 12 larvae (*vhl*$^{-/-}$ n=6, wt n=6) were anaesthetised with 0.02% tricaine until the heartbeats became slow (for about 20 seconds). The anaesthetised larvae were placed on a groove agarose plate facing downwards (prone position). Using a micromanipulator, a 26 µm glass micro capillary needle was positioned at a 45^{o} angle to the horizontal plane of the optic tectum. The needle was inserted across the dorsal area of the hindbrain, reaching the jawline, illustrated in Figure 4.5. Once the head stab procedure was completed, larvae were returned to the Petri dishes and observed until complete recovery and a regular swimming pattern were obtained. Tnf-α expression was imaged every3 hours post-injury (hpi) for 24 hrs period, using the confocal spinning-disk microscopy under 10x, 20x or 40x objective lenses. All the induced injuries were done under the supervision of Dr Freek van Eeden to ensure procedure consistency.

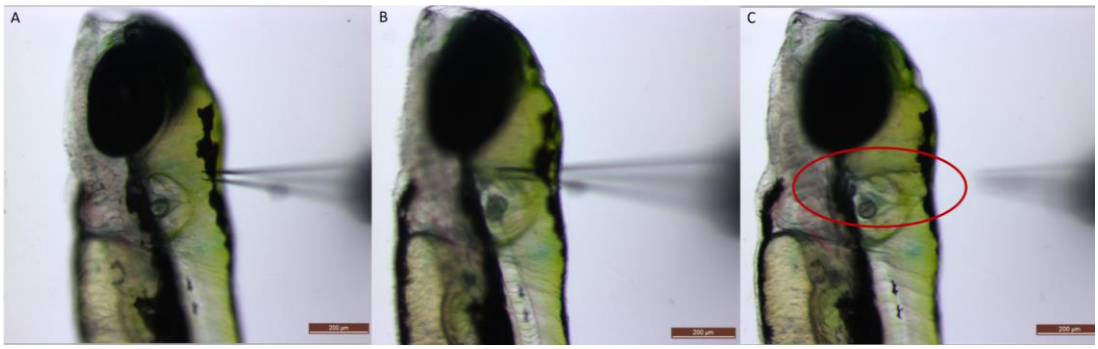

Figure 4.5 - Illustration of a head injury procedure of larvae. larvae are placed in agarose ridges in an appropriate orientation. A ~25 µm thickness glass needle was inserted vertically across the hindbrain. The red circle in (C) is surrounding the trace line left behind after needle retraction. The scale bar is 200 µm in length.

4.2.9.2 Evaluating expression of TNF-α in stimulated peripheral macrophages

Parallel to the head stab procedure, a tailfin injury was performed and utilised as a positive control. In this procedure, tail transection was performed to stimulate the peripheral macrophage immune response. Six PTU treated larvae (*vhl*$^{-/-}$ n=3, wt n=3) were raised and treated under the same conditions for larvae used in the head injury procedure. On the procedure day, anaesthetised larvae had their tailfin transected using a sterile scalpel blade under a stereo microscope. The tail *GFP* expression (under the control of Tnf-α) was imaged at 16 hpi using the same imaging acquisitions setting for head injuries.

To eliminate any cause of inflammation other than the procedures outlined above, non-injured control larvae were utilised (negative control). For this, both *vhl*$^{-/-}$ and wt larvae (n=3 for each genotype) were raised and imaged under the same conditions as the injured larvae. *tnf-α:GFP* expression within the heads and tails of the control larvae were considered a baseline.

4.2.9.3 Data Collection and Analysis

Post-procedure images were analysed for *GFP* expression (under the control of Tnf-α) expression and compared to *vhl*$^{-/-}$ and wt larvae. Microglial/macrophage expression of Tnf-α was observed as an overlapping emission of both mCherry and GFP and appeared yellow.

4.2.10 Evaluating the expression of interleukins using quantitative real-time polymerase chain reaction

4.2.10.1.1.1 Animals used and experimental protocol

A total of 300 larvae (*vhl*$^{-/-}$ n=150, wt n=150) were reared in E3 in Petri dishes. At 4 dpf, a head stab injury was induced, as described in section 4.2.9.1. At the time-points of 1 and 24 hpi, larvae heads were removed, and total RNA was extracted from 6 biological repeats per genotype, where each repeat contained 23 fish. Control non-lesioned wt siblings and *vhl*$^{-/-}$ larvae were treated parallel to the lesioned groups to assess the impact of hypoxia on cytokine expression.

4.2.10.2 Sample collection and RNA extraction

Larval heads were transected above the yolk-sac using sterile surgical micro-scissors under a stereomicroscope. Heads were collected in ice-cold Eppendorf tubes (4°C) containing E3 medium. The medium with replaced by 500 µl of TRIzoL and samples were subsequently homogenised by pipetting for 5 min. Then, 100 µl of chloroform was added, and the Eppendorf was shaken vigorously for 15 seconds, and left at room-temperature for 3 min before centrifugation at 12000xg at 4°C for 15 min. The upper aqueous layer containing the RNA was carefully removed and placed into a new sterile Eppendorf tube before being mixed with 250 µl of isopropanol. The mixture was left at room-temperature for 10 min, and centrifuged at 12000 xg for 10 min at 4°C. The supernatant was carefully removed, and the RNA pellet was washed in 1 ml of freshly prepared 75% ethanol. The solution was centrifuged at 7500 xg for 5 min at 4°C. The

supernatant was carefully removed, and the RNA pellet air-dried for 2 min before being resuspended in 15 µl of milliQ-water. The concentration of RNA was measured using the Nanodrop ND-1000 spectrophotometer. Extracted RNA was stored at -80°C until required.

4.2.10.3 cDNA synthesis

First strand-cDNA was synthesised from the extracted RNA at a concentration of 500ng/µl. Synthesis was carried out according to the manufacturer's instructions using the Protoscript II first-strand cDNA synthesis Kit (NEB). For this, the master mix was prepared including 1 µl d(T)23 VN/random hexamer, 5 µl ProtoScript II Reaction Mix (2X) and 1 µl ProtoScript II Enzyme Mix (10X), topped with nuclease-free water to a total volume of 10 µl. The mixture was incubated at 42°C for 1 hour, followed by enzyme deactivation via a second incubation at 80°C for 5 minutes. The cDNA was stored at -20°C until required.

4.2.10.4 qPCR

The reaction mix included 1 µl of 100ng/µl cDNA, 4 µl of EvaGreen Hot Start Firepol mix (5x), 1 µl of each forward and reverse primers (listed in table 4.5) and 13 µl of milliQ-water. The expression levels of the genes of interest were measured; the expression of the ribosomal protein- rsp29 gene as a housekeeping gene was also quantified to normalise gene expression. Three technical repeats were performed for each biological repetition. As a negative control, 1 µl MilliQ water replaced the cDNA for both target and housekeeping genes.

The reaction was carried out in optically clear 96 well plates (Bio-Rad). The assay was performed using CFX96 Touch Real-Time PCR Detection System (BioRad) paired with CFX Mastro Analysis Software and programmed for the cycles as follows: at 95°C for 15 minutes, 95°C for 5s, 60°C for 15s, 72°C for 10s. The incubation steps (2 to 5) were repeated for 40 cycles, followed by a Melt curve from 70°C to 95°C by 0.2ºC increment every 10s per step. The cycle threshold (ct) values were automatically calculated using ROX as passive references dye.

4.2.10.5 Target genes and primers used

qPCR analysis of *il-10, il-4, il-6,* and *il-1β* were performed using the Applied Biosystems Sequence Detection System (SDS) Software v2.4.1 in conjunction with 7900HT Fast Real-Time qPCR System. The primer sequences, provided by the integrated and technologies (IDT, USA) are listed in the Table 4.5 below.

Table 4.5 - Sequence of primers used in qPCR. The genes of interest are the key M1 / M2 phenotype genes.

Gene of interest	Primer sequences
il-10	Forward: 5'-ATAAAACATAACATAAACAGTCCC-3' Reverse: 5'-TGGCAGAATGGTCTCCAAGTA-3'
il-4	Forward: 5'-AATGGGAAAGGGGAAAAAATGGAT-3' Reverse: 5'-GTTTTCTTAGAGTAGTGTCC-3'
il-1β	Forward: 5'-AGCACATCAAACCCCAATCCACAGA-3' Reverse: 5'- TGTAAGACGGCACTGAATCCACCAC-3'
il-6	Forward: 5'-TGGAGACGAAGTTCAGGATGTGGA-3' Reverse: 5'- GTCAGGACGCTGTAGATTCGC-3'
rsp29	Forward: 5'-TTTGCTCAAACCGTCACGGA-3' Reverse: 5'- ACTCGTTTAATCCAGCTTGACG-3'

4.2.10.6 Data collection and analysis

The ΔΔCT method was used to calculate the fold change values as described in (Livak and Schmittgen, 2020). For this, the change in ΔCT value between the target (ΔCttar) and the reference housekeeping gene (ΔCtref) was calculated for both control wt sibling (ΔCT control) and the mutant (ΔCT mutant) samples. The differences between the average ΔCT of mutant and the average of ΔCT wt siblings were used as normalisation to obtain the ΔΔCT values. The fold change was calculated as 2^-ΔΔCT.

In summary, the following formulas were used to calculate the fold changes.

1. ΔCT(control)=ct (target gene) – ct (reference gene)
2. ΔCT(mutant)= average ct (target gene) – average ct (reference gene)
3. ΔΔCT = ΔCT (mutant) – ΔCT (control)
4. FC= $2^{-\Delta\Delta CT}$

The statistical analysis was based on the fold change (ΔΔCT values), using the two-way ANOVA test.

4.3 Results

Important note: Through the results, we presumed that all mpeg1+ cells within the zebrafish brain are microglia. However, there is a small chance that macrophage cells could also be included. Hence, the word microglia here refers to the mpeg1+ brain macrophages.

4.3.1 Sustained HIF signalling does not modulate microglial number or phenotype at 3 dpf

The transgenic *mpeg1::mCherryCAAX*^{sh378} enabled the visualisation of microglia in the *vhl*$^{-/-}$ zebrafish line. At 3dpf, the microglia were imaged at a single point and recorded for 24 hrs, to assess the differences of microglia in the *vhl*$^{-/-}$ zebrafish compared with its sibling.

Z-series analysis at a single time-point between 3.2 and 3.6 dpf did not detect a significant difference in the microglial number between the *vhl*$^{-/-}$ (59 ± 0.11) compared to their wt siblings (58.89 ± 2.02) P= 0.957, Figure 4.6 A-C. Furthermore, there was no significant difference in either the number of microglia with a ramified morphology in *vhl*$^{-/-}$ (12.50 ± 1.50) compared to their wt siblings (14 ± 1.30), P =0.263, or the number of microglia with an activated morphology in the *vhl*$^{-/-}$ (45.76 ± 0.22) compared to their wt (45.44 ± 1.86), P= 0.906, Figure 4.6 D.

As the initial studies were conducted at a one-time point, additional studies were performed to assess both microglial number and morphology over a 24 hr period using an MIP video created from the light-sheet microscope recording. An average time-line track is presented in Figure 4.7. An individual representative graph for the 24 hrs time-

recording is presented in Appendix III. Unfortunately, several larvae died during the recording, which restricted the n value to be n=2 for wt, and n=3 for *vhl*$^{-/-}$ fish.

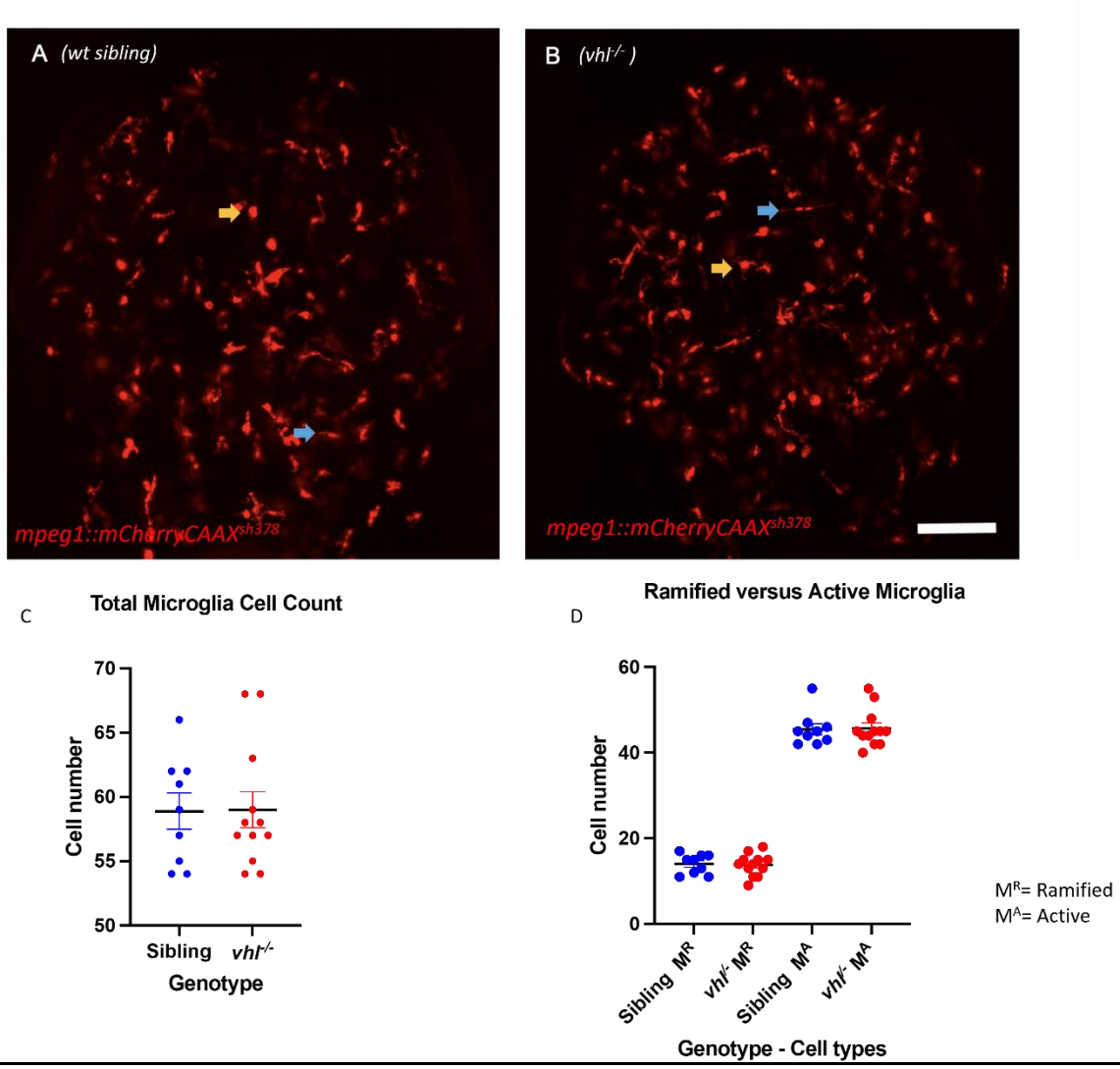

Figure 4.6 - There are no significant differences in either the number or morphology of microglia morphologies in the vhl$^{-/-}$ *zebrafish at 3 dpf. Representative z-stack image at 3 dpf for both (A) wildtype sibling and (B) vhl*$^{-/-}$ *zebrafish, enabling the visualisation of microglia with both ramified (blue arrows) and activated (yellow arrows) morphologies. (C) The vhl*$^{-/-}$ *contains similar microglia numbers compared to their siblings (unpaired t-test). (D) Levels of microglia with either a ramified or an activated morphology are similar*

compared in both vhl$^{-/-}$ and their siblings (two-way ANOVA). Data are presented as mean ± SEM, MR = ramified microglia, MA= activated microglia. The scale bar represents 100 µm

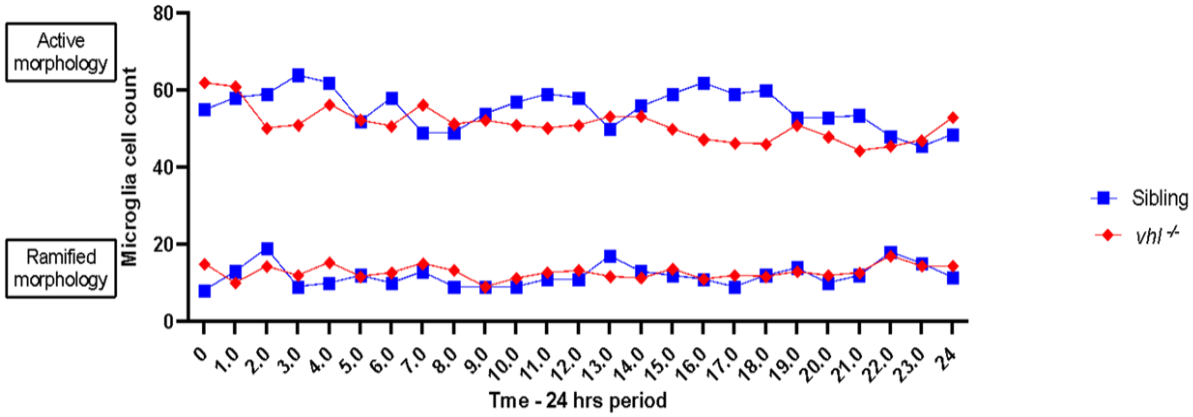

Figure 4.7- Representative timeline microglial morphologies in 3 dpf vhl$^{-/-}$ and their siblings over 24 hrs. The timeline graph represents the number of microglia with either a ramified or activated morphology, within both sibling (blue) and vhl$^{-/-}$ mutant (red), through 24 hrs of recording within 30 minutes intervals. While the cell number fluctuated over the recording period, no significant differences were observed between both genotypes, (repeated Measures ANOVA).

The number of ramified microglia ranged between 9- 17 cells and the number of active microglia ranged between 44-64 cells per time point over 24 hrs in both the *vhl*$^{-/-}$ and wt zebrafish, Figure 2-6. There was no significant difference in the number of microglia with either a ramified morphology (p=0.2689) or an activated morphology (p=0.4388) in *vhl*$^{-/-}$ compared to their siblings at any time point. At some time-points, during the 7th -13th hrs of recording, the number of activated microglia in the *vhl*$^{-/-}$ were higher when compared to wt sibling, while during the 3rd, 5th, 10th and 19th hrs of recording the number of microglia with an active morphology were higher in the wt sibling compared to the *vhl*$^{-/-}$; however, this was not statistically significant, P > 0.5.

4.3.2 Sustained HIF signalling does not modulate microglial number but impacts microglial activation at 5 dpf

The previous experiment showed no difference within the microglia phenotype at 3 dpf. The experiment was repeated at the advanced age of 5 dpf to evaluate the microglia profile following the morphing microglia phase.

Analysis of a single time-point between 5.2 and 5.6 dpf detected a large variation in the microglial morphology, where some *vhl*$^{-/-}$ zebrafish have comparable microglial profiles to their sibling, and others appear to have a marked different profile as illustrated in Figure 4.8 A-C. However, the Z-series analysis detected a similar total number of microglia in the *vhl*$^{-/-}$ (53.44 ± 3.08) compared to their wt (50.36 ±2.28), with no significant differences, P= 0.195.

While the total, and the ramified number of microglia did not significantly differ in the *vhl*$^{-/-}$ compared to their wt siblings, the *vhl*$^{-/-}$ larvae had significantly higher levels of activated microglia within spectrum (17.56 ± 12.46) compared to the wt (5.09 ± 5.12) (P= 0.03); Figure 4.8 D-E.

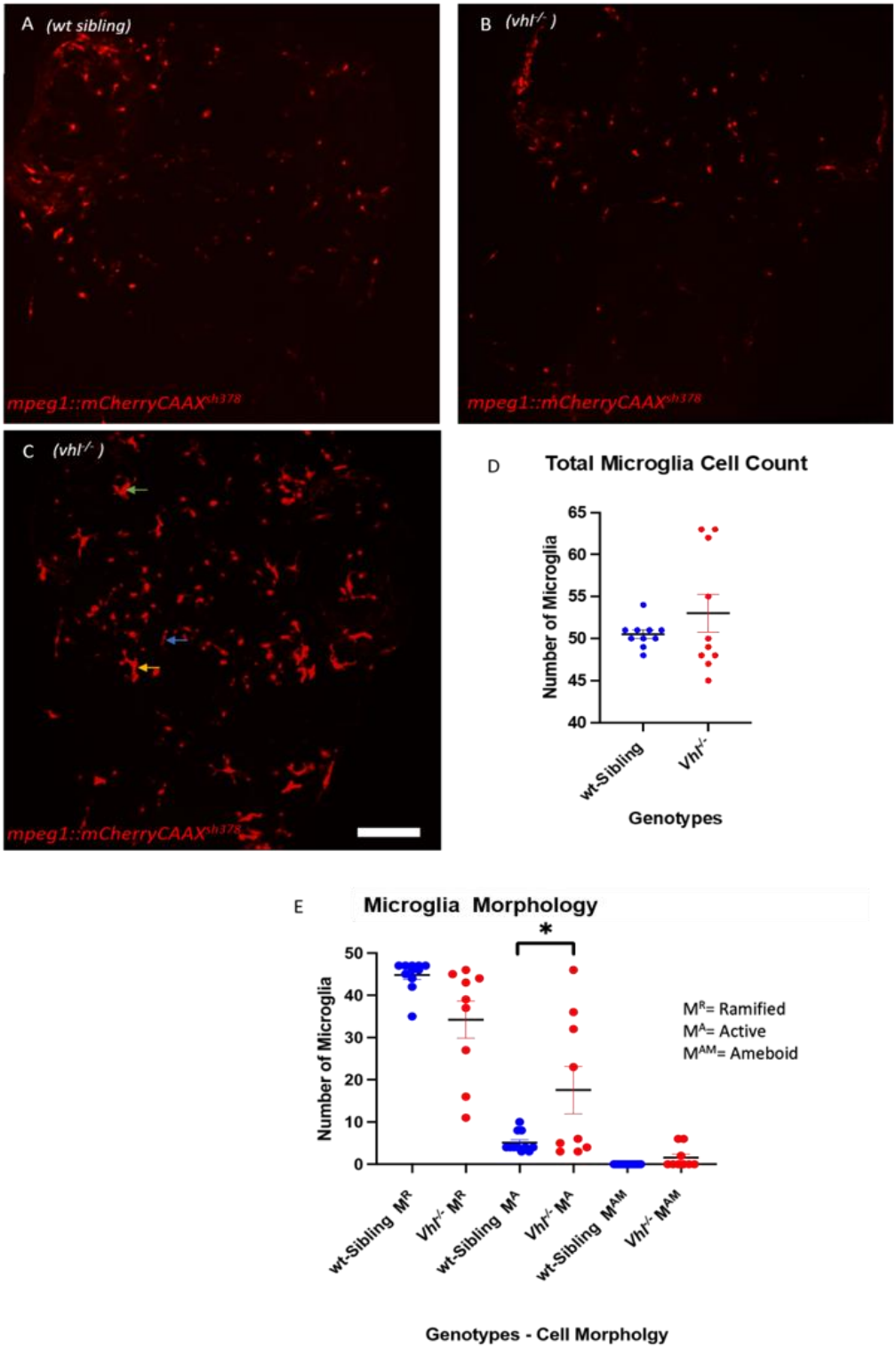

Figure 4.8 - The microglia morphologies in the vhl$^{-/-}$ zebrafish at 5 dpf suggest an increase of microglial number and activation in vhl$^{-/-}$ ZF. Representative z-stack image at 5 dpf for both (A) wt sibling, (B) vhl$^{-/-}$ zebrafish with a similar phenotype, and (C) vhl$^{-/-}$ zebrafish with

varied phenotype, enabling the visualisation of microglia with ramified (blue arrows), activated within the spectrum (yellow arrows), and amoeboid (green arrows) morphologies. (D) The vhl$^{-/-}$ contains similar microglia numbers compared to their siblings (unpaired t-test). (E) Levels of microglia with an activated morphology within the spectrum are significantly different between vhl$^{-/-}$ and their siblings (two-way ANOVA test). Data are presented as mean ± SEM, MR = ramified microglia, MA= activated microglia within the spectrum, and MAM= amoeboid microglia. The scale bar represents 100 µm

4.3.3 Sustained HIF signalling significantly impacts both microglial number and activation phenotype at 7 dpf

The spread of the *vhl*$^{-/-}$ data at 5 dpf suggests that microglia might still be switching from the morphing phase. Therefore, the microglia phenotype was revaluated at 7 dpf to confirm the changes noticed on 5 dpf data. To characterise microglial phenotypes at 7dpf single time-point images were acquired between 7.2 and 7.6 dpf using the spinning-disk confocal microscopy.

In contrast to earlier time points, *vhl*$^{-/-}$ larvae had significantly higher numbers of microglia (51.44 ± 2.54) compared to their sibling (48.90 ±0.76) (P = 0.003). Furthermore, analysis of the microglial morphologies indicated that *vhl*$^{-/-}$ larvae had significantly lower levels of ramified microglia (36.56 ± 6.75) compared to wt (43.31 ± 1.99), P= 0.0009, and significantly higher levels of active microglia (14.31 ± 9.24) compared to their siblings (5.08±1.95) (P< 0.0001).

The amoeboid morphology cells were half-cell (0.56 cells) on average in *vhl*$^{-/-}$ larvae compared to null within their sibling; The P value of 0.14 indicated no significant differences in amoeboid cells number; Figure 4.9: A-D.

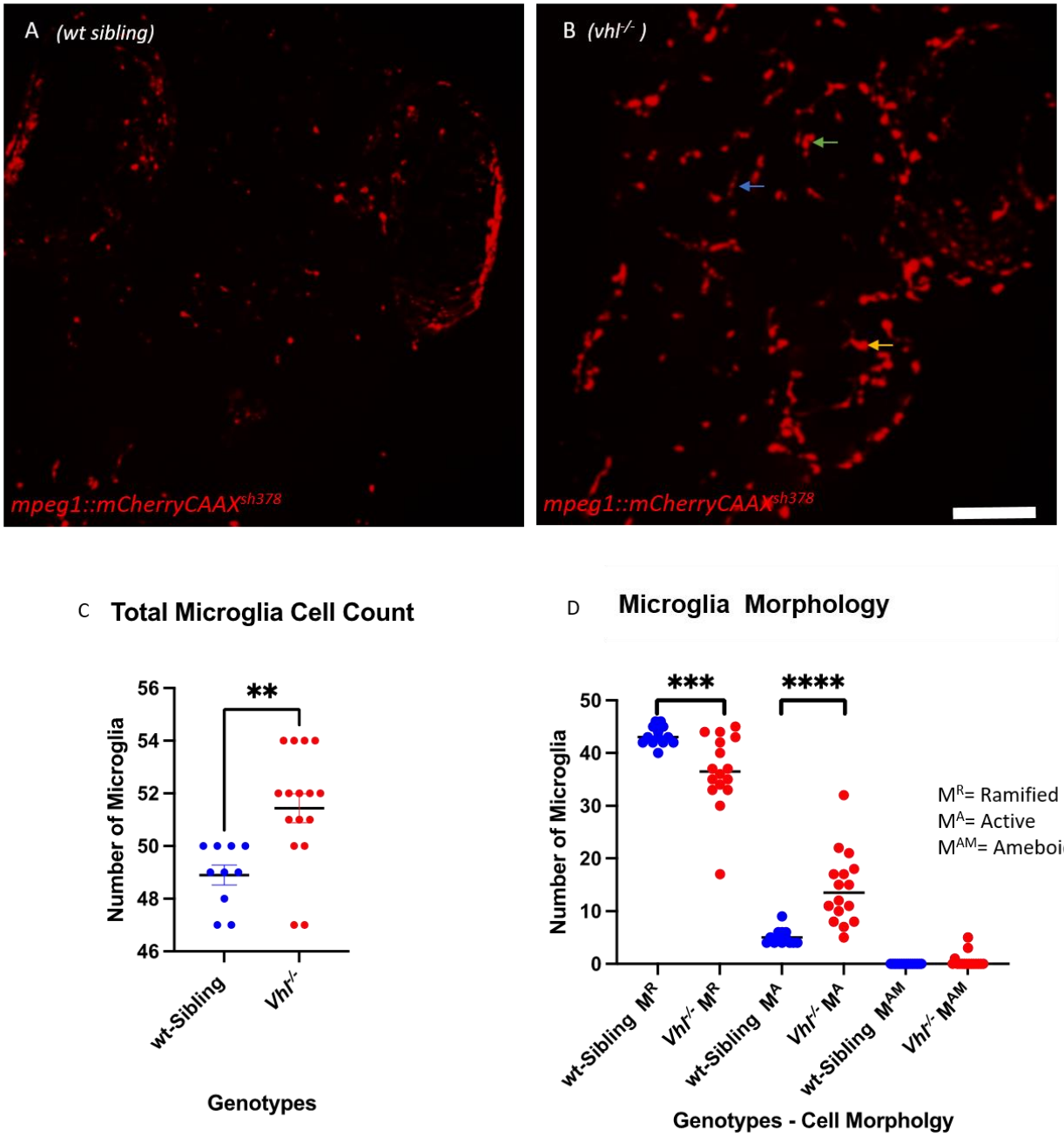

Figure 4.9 - The microglia morphologies in the vhl$^{-/-}$ zebrafish at 7 dpf implies sustained increase in the microglia numbers and activation. Representative z-stack image at 7 dpf for both (A) wt sibling, (B) vhl$^{-/-}$ zebrafish, enabling the visualisation of microglia with ramified (blue arrows), activated within the spectrum (yellow arrows), and amoeboid (green arrows) morphologies. (C) The vhl$^{-/-}$ contains significantly increased microglia numbers compared to their siblings (unpaired t-test). (D) Levels of microglia with either a ramified or an activated morphology are significantly different between vhl$^{-/-}$ and their

siblings (two-way ANOVA test). Data are presented as mean ± SEM, MR = ramified microglia, MA= activated microglia within the spectrum, and MAM= amoeboid microglia. The scale bar represents 100 µm.

4.3.4 Tnf-α expression is not associated with microglia in the *vhl*$^{-/-}$ larvae

TNF-α is a pro-inflammatory cytokine produced by macrophages/monocytes as part of the immune response. The current experiment tests whether the sustained activation of HIF pathways induces microglia to adopt an M1 phenotype and express Tnf-α, utilising the *tnfα::GFP* as an *in vivo* readout to assess the microglial activation profile.

The double transgenic (*mpeg1::mCherryCAAX*$^{sh378/+}$*, tnfα::GFP* ^{pd1028}*)* line enables the expression of Tnf-α by microglia in both *vhl*$^{-/-}$ and their wt sibling, from 2 dpf to 7 dpf. Microglia expressing Tnf-α can be identified by the colocalization of GFP (Tnf-α) with mCherry (microglia), producing a yellow signal. The merged images clearly show no overlap of tnf-α with microglia at any stage of development in either the *vhl*$^{-/-}$ or their wt sibling, Figure 4.10. It should be noted that Tnf-α was expressed in the zebrafish CNS, however as the current project focuses on microglial expression this was not assessed in more detail.

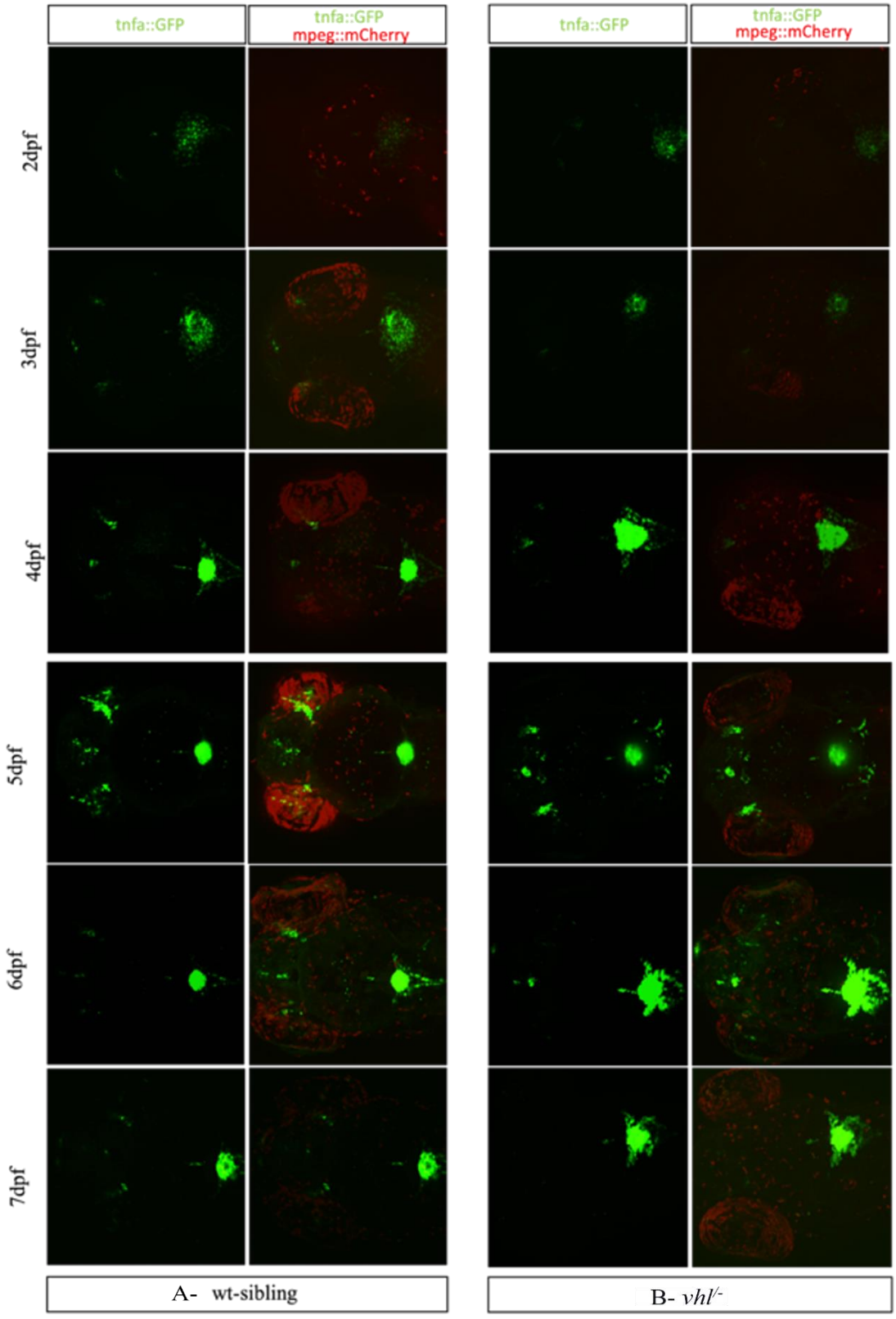
tnfa::GFP
tnfa::GFP
mpeg::mCherry
tnfa::GFP
tnfa::GFP
mpeg::mCherry
2dpf
3dpf
4dpf
5dpf
6dpf
7dpf
A- wt-sibling
B- vhl-/-

Figure 4.10- The daily observation of Tnf-α level within heads of vhl$^{-/-}$ and their sibling indicated no tnf-α expression. Representative confocal images for both (A) wt sibling and (B) vhl$^{-/-}$ zebrafish, during the age 2–7 dpf. The Tnf-α expression is localised as GFP expression, and microglia were recognised as mCherry positive cells.

4.3.5 Sustained activation of the HIF pathway does not alter microglial expression of Tnf-α following head injury

The baseline level of *tnf-α* expression as judged from *tnf-α:GFP* in the *vhl*$^{-/-}$ larvae was assessed. Next, the microglial expression of *tnf-α* was evaluated following a head injury to determine if additional stress was required to induce expression.

Sustained HIF signalling did not modulate microglial expression of Tnf-α; therefore, the zebrafish were exposed to an additional stress, namely a head injury. Within 24 hrs of injury microglia were recruited to the site of injury. The microglial profile at the lesion site was varied; with some larvae displaying high levels of microglia and others displaying lower levels at the injury site, as seen in Figure 4.11 A-B. The microglia migrated to the lesion site and mainly adopted amoeboid morphology, Figure 4.11 C. These variable responses were seen at both *vhl*$^{-/-}$ mutant and wt sibling larvae.

Following head injury, expression of Tnf-α was observed via serial confocal images of the head stabbed larvae for a total period of 24 hrs. Similar to the *vhl*$^{-/-}$ without head injury, expression of Tnf-α did not co-localise with mCherry microglia Figure 4.12. However, it should be noted that Tnf-*α* was associated with other neural cells.

Tailfin wounded larvae were included as a positive control. Unwounded tailfins displayed no accumulation of macrophages and no levels of Tnf-α expression. In contrast higher levels of mCherry macrophages were seen at the site of tailfin damage, and co-localised with higher levels of Tnf-α expression Figure 4.13.

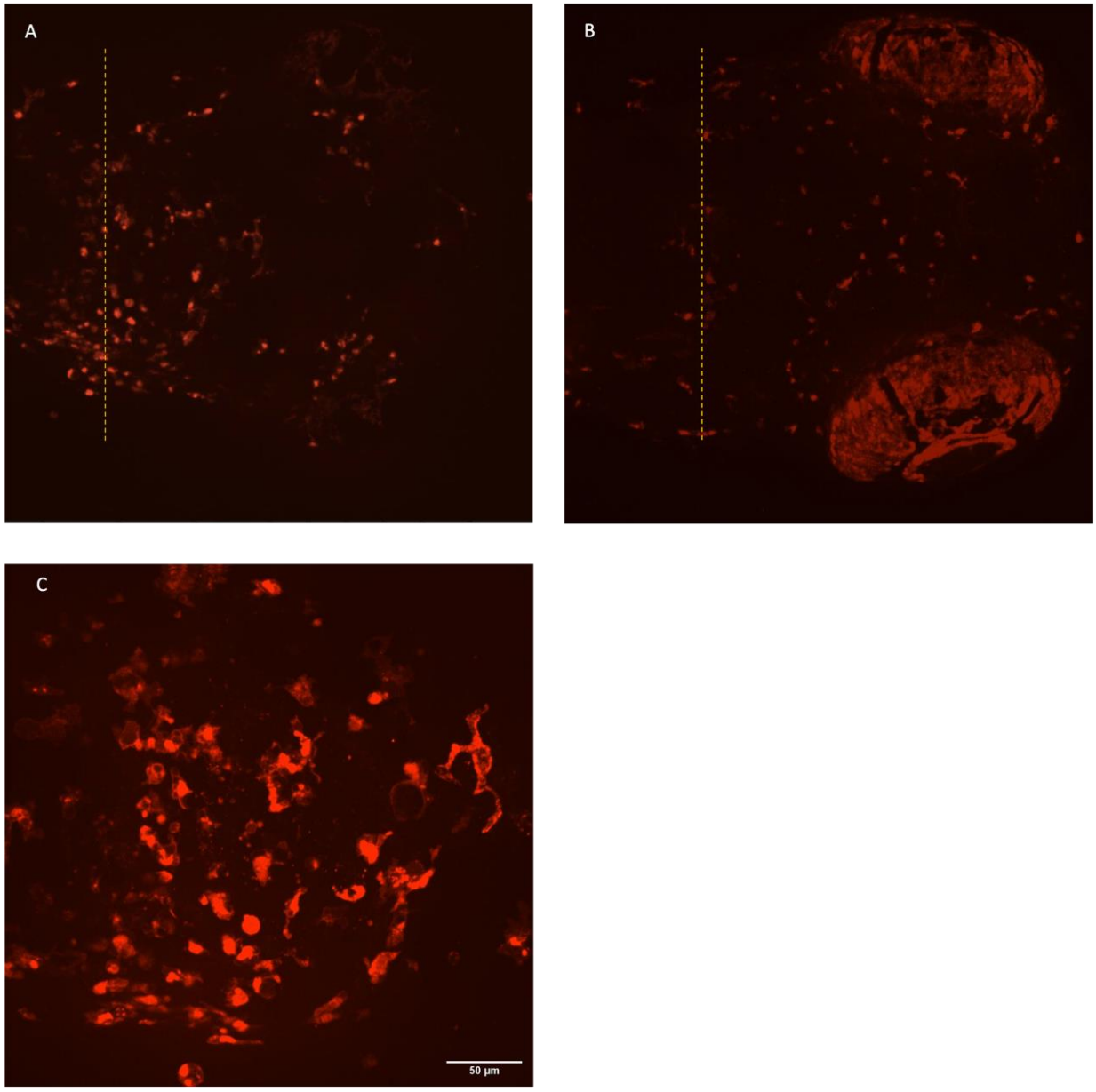

Figure 4.11 - Microglia responding to head injuries by migrating to the injured sites. Representative z-stack images at 4 dpf of vhl$^{-/-}$ head injured larvae show the microglia migration toward the injured site (indicated by a yellow line) at variable levels for (A) larva with vastly migrating cells to the wound site and (B) fewer microglia migrated to the injury site. (C) An injured site view under higher magnification.

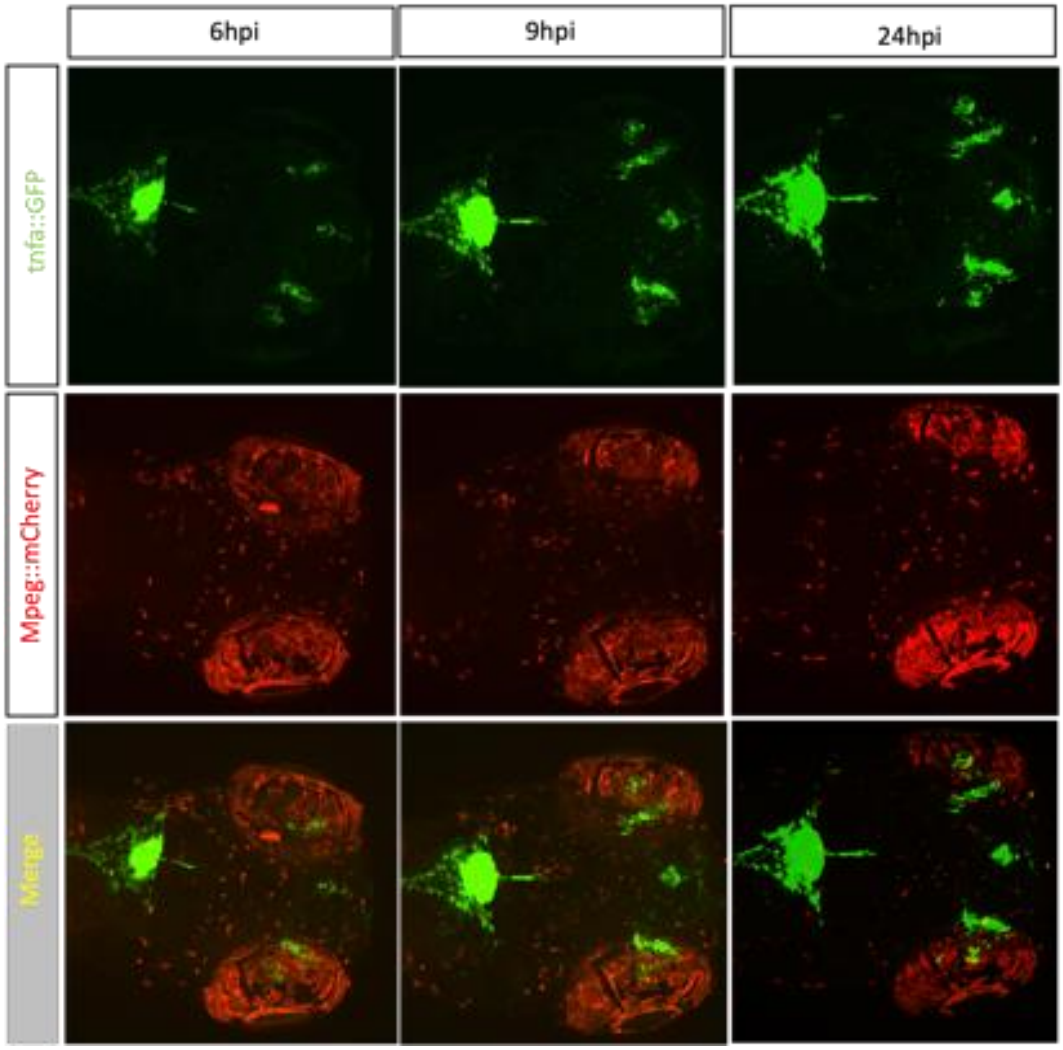

Figure 4.12 - Tnf-α does not colocalize with microglia in post head-injury larvae. Confocal serial images for 4 dpf double transgenic sibling larvae post-head stab procedure evidencing the absent expression of Tnf-α within evoked microglia in both vhl$^{-/-}$ mutant and wt larvae. The Tnf-a expression was detected as GFP expression, and microglia were recognised as mCherry positive cells.

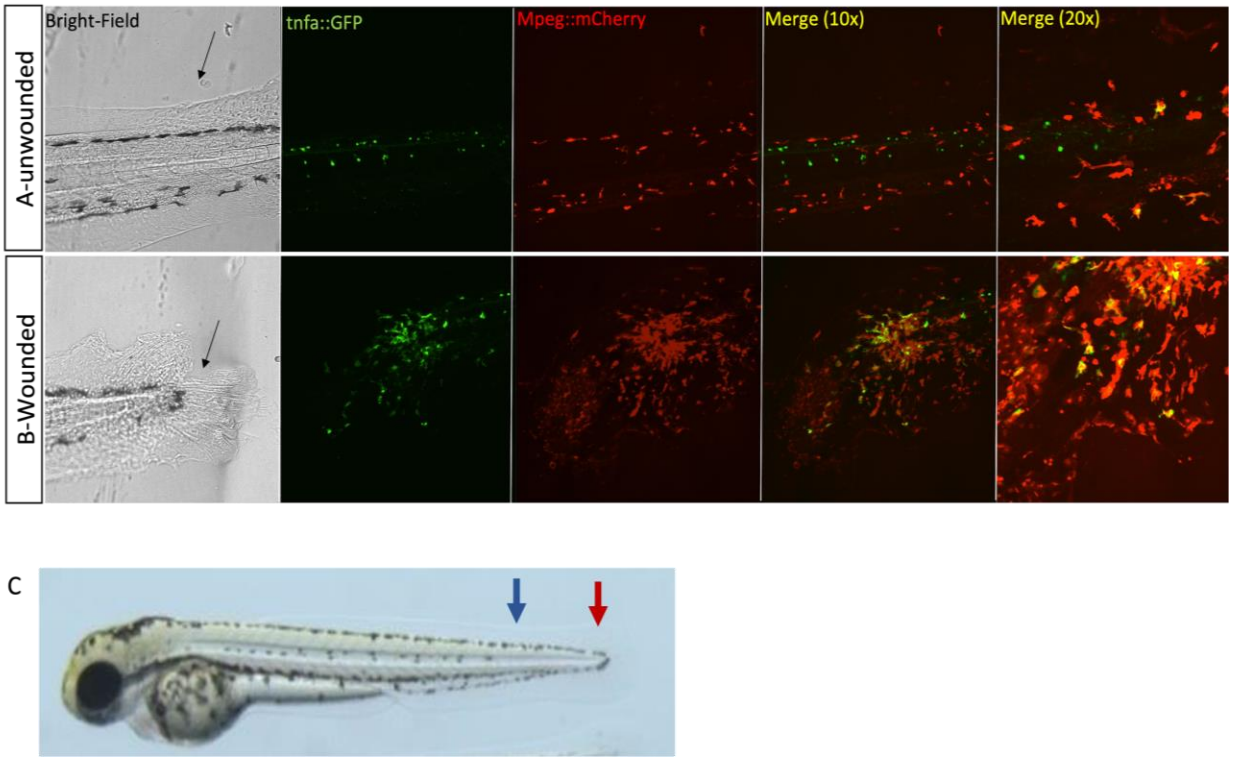

Figure 4.13 - A tail transection in zebrafish larvae showing upregulation of the tnfα::GFP localised within macrophages at 16 hpi. Representative confocal images at 4 dpf for (A) unwounded tail and (B) transaction wounded tail enables the visualising of macrophages' response to injuries. The Tnf-α activated within macrophages are expressed by yellow fluorescence (positive GFP expression is overlaid with mCherry positive cells) and were only seen at the tailfin injury site. (C) Zebrafish larvae locate the tailfin injury (red arrow) and unwounded area (blue arrow).

4.3.6 The interleukin levels assessed by qRT- PCR

The *Tnf-α* as a potential marker for the M1 phenotype was not suitable. Therefore, pro-and anti-inflammatory cytokines were also assessed using qPCR. The measurement levels were compared on larvae of both genotypes by measuring the gene expression of the pro-inflammatory (*il-1*β and *il-6)* and the anti-inflammatory (*il-4* and *il-10*) cytokines within the fish heads.

4.3.6.1 The sustained activation of the HIF pathway significantly increases expression of *il-10* at 4 dpf

Expression of a panel of pro- and anti-inflammatory interleukins were evaluated in both wt sibling and the *vhl*$^{-/-}$ mutant larvae heads at two age points, 4.1 and 5.1 dpf.

Mean levels of the pro-inflammatory (M1) *il-1β* were non-significantly different in the *vhl*$^{-/-}$ mutant larvae (Fold change=1.7 at 4.1 dpf and 1.4 at 5 dpf) compared to their wt siblings (Fold change= 1.0 at both ages 4.1 and 5.1 dpf). The M1 *il-6* were non-significantly different in the *vhl*$^{-/-}$ mutant larvae (Fold change= 1.2 at 4.1 dpf and 1.0 at 5.1 dpf) compared to their wt siblings (Fold change= 1.0 at 4.1 and 5.1 dpf); Figure 4.14 A-B.

Mean levels of the anti-inflammatory (M2) *il-4* were non-significantly different in the *vhl*$^{-/-}$ mutant larvae (Fold change= 2.8 at 4.1 dpf and 1.3 at 5.1 dpf) compared to their wt siblings (Fold change= 1.0 at 4.1 and 5.1 dpf); Figure 4.14C. *Il*-10 was significantly highly expressed at 4.1 dpf within the *vhl*$^{-/-}$ mutant larvae (Fold change= 4.3), comparable to the wt sibling (Fold change= 1.0), P value of 0.0347. The fold change value dropped

significantly over 24 hrs to reach 1.5 in the *vhl*$^{-/-}$ mutant larvae and 1.0 in the wt sibling at 5.1 dpf; Figure 4.14 D.

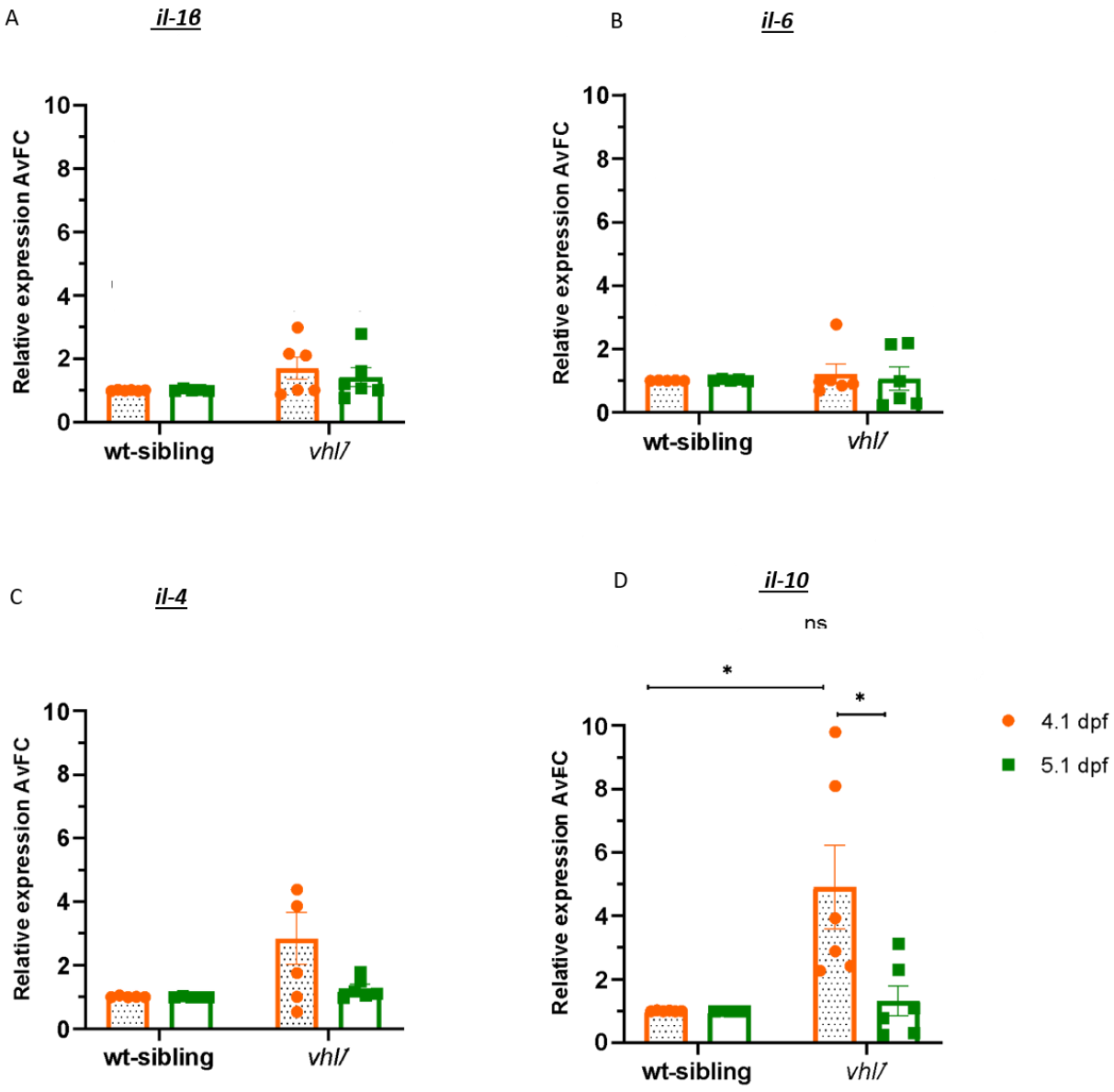

Figure 4.14 - The Sustained activation of the HIF pathway significantly increases expression of il-10 within the vhl$^{-/-}$ *heads at 4 dpf. The cytokines expression level at ages 4.1 (orange dots) and 5.1 (green squares) dpf for (A) il-1β, (B) il-6, (C) il-4, and (D) il-10*

*within both wt sibling and vhl$^{-/-}$ larvae. The anti-inflammatory cytokine, il-10, is up-regulated by the vhl$^{-/-}$ mutant larvae at the 4.1 dpf. Data presented are mean ± SEM; *p < 0.05; **p < 0.01, (two-way ANOVA test).*

4.3.6.2 Evaluation of interleukins levels and the immune response in post head injury

The following experiment was to measure how the sustained signalling of the HIF pathways has affected the immune response profile by assessing the pro and anti-inflammatory interleukin genes in head-injured *vhl$^{-/-}$* and wt larvae at 1 and 24 hpi.

Mean levels of the pro-inflammatory (M1) *il-1β at* 1 hpi were significantly higher in the injured *vhl$^{-/-}$* mutant larvae (Fold change= 2.9) compared to their injured wt siblings (Fold change= 1.1), P=0.0424. However, at 24 hpi, *il-1β* was not-significantly different in the *vhl$^{-/-}$* mutant larvae (Fold change= 1.2) compared to their injured wt siblings (Fold change= 1.4); Figure 4.15 A. Another M1 cytokine *il-6* was non-significantly different in the injured *vhl$^{-/-}$* mutant larvae (Fold change= 1.2 at 1 hpi and 1.1 at 24 hpi) compared to their injured wt siblings (Fold change= 1.9 at 1 hpi and 2.8 at 24 hpi); Figure 4.15 B.

Mean levels of the anti-inflammatory (M2) *il-4* were significantly higher in the injured *vhl$^{-/-}$* mutant larvae at 1 hpi (Fold change= 3.763) compared to their injured wt siblings (Fold change= 1.4), P= 0.0037. At 24 hpi, the M1 *il-4 level,* however, was non-significantly different in the injured *vhl$^{-/-}$* mutant larvae (Fold change= 0.8) compared to their injured wt siblings (Fold change= 1.5); Figure 4.15 C. Another M2 marker, *il-10,* was non-significantly different in the injured *vhl$^{-/-}$* mutant larvae (Fold change= 6.5 at 1 and 24

hpi) compared to their injured wt siblings (Fold change= 4.3 at 1 hpi and 1.0 at 24 hpi); Figure 4.15 D.

A

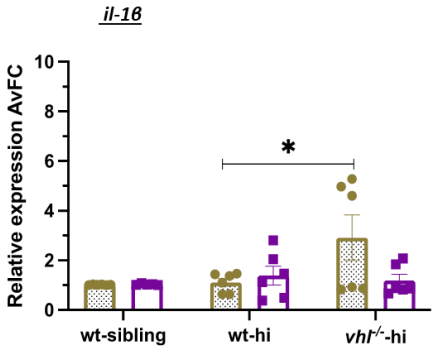
il-1β
Relative expression AvFC
10
8
6
4
2
0
*
wt-sibling
wt-hi
vhl-/--hi

B

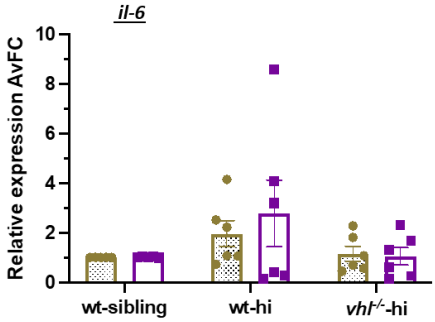
il-6
Relative expression AvFC
10
8
6
4
2
0
wt-sibling
wt-hi
vhl-/--hi

C

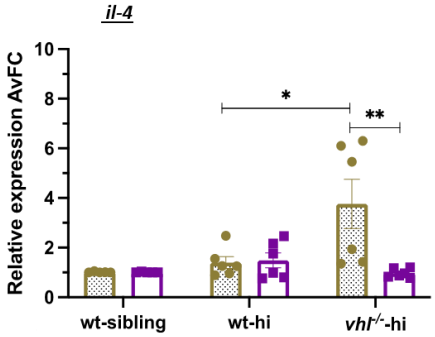
il-4
Relative expression AvFC
10
8
6
4
2
0
*
**
wt-sibling
wt-hi
vhl-/--hi

D

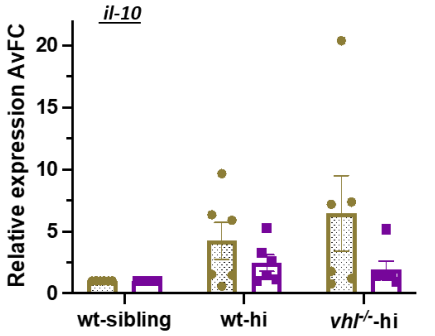
il-10
Relative expression AvFC
20
15
10
5
0
wt-sibling
wt-hi
vhl-/--hi


1 hpi
24 hpi

Figure 4.15 - Average fold changes of cytokines level within healthy and injured larva. The detection of the expression levels of (A) il-1β, (B) il-6, (C) il-4 and (D) il-10 within the zebrafish heads by q RT-PCR at 1 and 24 hpi. The pro-inflammatory il-1β, and the anti-inflammatory cytokine il-4, are being up-regulated by vhl/- injured at 1 hpi. Data presented are mean ± SEM, (two-way ANOVA test). Wt-hi: wt sibling with an induced head injury, vhl-hi: vhl$^{/-}$ with induced head injured.

4.4 Discussion

Hypoxia is a feature of several human neurodegenerative diseases, and it influences the microglial phenotype, driving them to adopt either a pro-inflammatory (M1) or an anti-inflammatory (M2) phenotype; the exact role of microglia is unclear as yet (Fumagalli et al., 2015). Employing the zebrafish can help investigate the microglial response to various stimuli. This chapter aimed to examine the effects of sustained hypoxia signalling on microglial morphology using a *vhl*$^{-/-}$ zebrafish model. The study also aimed to assess the microglial phenotype by assessing the secretion of pro-and anti-inflammatory cytokines at both the basal level and in post-head-injured *vhl*$^{-/-}$ and wildtype larvae.

4.4.1 Sustained activation of the HIF pathway is associated with the significant activation of microglia

In the current study, the membrane reporter line of *Tg*(*mpeg1*:*mCherryCAAX*)^{sh378} was utilised; both microglia and macrophages are labelled by an mCherry positive cell membrane (Hamilton et al., 2020, Herbomel et al., 2001). Utilising the transgenic *vhl* $^{hu2117/+}$ mutant carrier line has enabled changes in live fish to be observed in response to sustained activation of the HIF pathway; and demonstrated that both control and *vhl*$^{-/-}$ mutant larvae have a similar microglial phenotype at 3 dpf whilst at 5 and 7 dpf *vhl*$^{-/-}$ mutant larvae contain significantly higher levels of microglia with an activated morphology.

At 3 dpf microglia develop as highly motile amoeboid cells involved in the phagocytosis of apoptotic cells in the developing brain (Svahn et al., 2013). In the current study the number of microglia with an activated morphology was similar in the *vhl*$^{-/-}$ zebrafish compared with its wildtype siblings over a 24 hr period. However, any effect of sustained activation of the HIF pathway on the microglial phenotype may be masked by the remodelling occurring in the developing brain at this stage. The microglial number and distribution in the brain are based on the level, rate, and pattern of the neural apoptosis (Svahn et al., 2013).

Therefore, microglia imaging experiments were repeated at a later larval stage to examine whether the microglia of the *vhl*$^{-/-}$ fish would respond similarly to the sibling ones. At 5 dpf, the total number of microglia in the *vhl*$^{-/-}$ larvae was similar to their siblings while showing more active morphology; a prolonged morphing stage might mask significant differences (if they exist) at this stage (Svahn et al., 2013). At 7 dpf, sustained activation of the HIF signalling pathway was associated with a significant increase in microglia number and activation; the finding might be due to increased phagocytic activity in the *vhl*$^{-/-}$ mutant larva.

Hypoxia resulting in microglial activation has been reported in several studies on other species suggesting that the change in microglial morphology could be associated with activation of the HIF pathway. In a severe/chronic perinatal hypoxia-ischemia human study, microglia adopt a very active morphology. Activation of the microglia facilitates cell migration and phagocytosis (Panayotacopoulou et al., 2022, Ohsawa et al., 2004). The hypoxia effects on microglia were also studied in a mouse model, where 6 months old

mice were exposed to a single acute hypoxic condition (7% oxygen in a hypoxic chamber). Mice were sacrificed immediately after the experiments, and the microglia evaluation showed M1 microglia activity recognised by elevated M1 markers, including CD86, TNF-α and IL-6, compared to the control mice group, which were kept under normoxic conditions within a similar chamber (Zhang et al., 2017).

In zebrafish, the neural apoptosis rate affects the number of microglia. In a study where hemispheres of 3 dpf embryos were irradiated via a low-power UV laser, the microglial number was compared between the irradiated and the non-irradiated hemisphere (internal control). The number of apoptotic nuclei and microglia was higher within the irradiated hemispheres, suggesting that neuronal apoptosis provides a mechanism for controlling the number of microglia in the zebrafish brains (Casano et al., 2016). Increased microglial numbers could be due to migration or proliferation of the microglia. Microglial proliferation is suggested to occur locally as an acute response to an extensive neural death (Oosterhof et al., 2017).

In a bacterial nitroreductase-expressing transgenic (NTR) zebrafish, the addition of metronidazole (MTZ) induces neural apoptosis and cell loss (Mathias et al., 2014). In a study that involved a single dose administration of the MTZ to the zebrafish hindbrain, the microglia number was observed for 7 days after admission. Interestingly, the microglia colonised at the hindbrain 24 hrs after the addition, and the microglial number remained elevated up to 1-week post-treatment. In contrast, the microglia number and distribution pattern were unaltered in the non-treated brain area (Casano et al., 2016). The findings together suggest that the pattern and the level of neuronal apoptosis were found to have

an intense and prolonged influence on the microglial number and distribution in the zebrafish brains (Casano et al., 2016).

An increased immune response can evoke stress signals, resulting in recruiting more immune cells to the brain. In a leukoencephalopathy zebrafish model (RNAseT2-deficient), the number of mCherry positive cells was higher in the *vhl*$^{-/-}$ mutant than in their control wildtype (Hamilton et al., 2020). This study concluded that increasing apoptosis will recruit entry of circulating macrophages, explaining the increased number of mCherry cells (microglia and macrophages) in the brain (Hamilton et al., 2020, Casano et al., 2016, Xu et al., 2016). Another zebrafish study investigating glioma in the zebrafish brain has supported the microglia/macrophage interaction and migration toward the glioma (Hamilton et al., 2016, Var and Byrd-Jacobs, 2020).

By reflecting on the elevated microglia number in the *vhl*$^{-/-}$ larvae at 7 dpf, it is suggested that either activated microglia secrete stress factors which recruit circulating macrophages into the brain and/or neural death has occurred, triggering microglial proliferation. A further test using a microglial specific marker, for example, immunostaining using 4C4 monoclonal antibody (Mazzolini et al., 2018), can help distinguish between resident microglia and infiltrating macrophages and clarify if increasing the microglia number is caused by macrophage infiltration.

4.4.2 Spinning disc confocal microscopy is a more robust approach to analyses microglial morphology in ZF larvae

The current project employed two imaging systems: Light-Sheet microscopy (LSM) and Spinning-Disk Confocal microscopy. The advantage of LSM is that it can record the zebrafish larva for extended periods (Kaufmann et al., 2012, Bassi, 2015), enabling observation of microglia *in vivo* for over 24 hrs. However, several limitations of this approach should be acknowledged, including the highest magnification available is 20x, which impedes analysis of the detailed microglia morphology. Therefore, when this approach was used, the microglia were only classified as either ramified or activated morphology due to the low-level magnification of images taken by LSM, preventing accurate identification of the different morphologies. Another limitation is the low throughput; only two embryos can be imaged at the same time. The sample embedding technique is also a limitation, where it is difficult to get the correct orientation of the fish.

From the literature, the spinning disk confocal fluorescence microscope is commonly used to image microglia within zebrafish for quantitation and more detailed analysis of glial morphology in zebrafish larvae (Hamilton et al., 2020, Hamilton et al., 2016). The disk confocal microscope has several advantages; the most important is allowing confocal imaging at a higher magnification (x40). The higher magnification more readily enables the classification of the microglia morphologies, enabling measurement of the circulatory index range of each cell. Another advantage is its high throughput (Jemielita et al., 2013), where many embryos can be embedded together and imaged within a shorter time. Also, it is easier to embed embryos in the correct orientation, unlike the LSM.

4.4.3 Tnf-α is not expressed by microglia in zebrafish

TNF-α is a multifunctional pro-inflammatory cytokine, which is secreted by inflammatory cells and plays an essential role in cellular survival, proliferation, cellular homeostasis and immune protection against neurological insult (Sriram and O'Callaghan, 2007, Wang and Lin, 2008). In the human CNS, activated microglia are the major source of this cytokine. In the brain, TNF-α levels are elevated and contribute to neurodegeneration following injuries including ischemia and infection. Human research reveals that microglia mediate hypoxia-induced inflammation by producing the pro-inflammatory cytokines IL-1β, IL-6 and TNF-α (Guo et al., 2014, Sriram and O'Callaghan, 2007), where TNF-α is induced very early in the process within the affected region (Sriram and O'Callaghan, 2007).

Mouse studies have also demonstrated hypoxia-induced upregulation of the expression of TNF-α by microglia (Clausen et al., 2008). One study that focused on hypoxic effects involved incubating cells in an anaerobic chamber (O2 tension<0.2%) for 8 hrs (mild hypoxia condition) before being reoxygenated in a regular normoxic incubator (95% air, 5% CO2) for 24 hrs. This resulted in the production of Nitric oxide and TNF-α, suggesting that the hypoxic conditions could lead to the inflammatory activation of microglia (Park et al., 2002). The study implied that hypoxia directly damages neurons during cerebral ischemia and indirectly promotes neuronal injury via microglial activation.

Previous studies have demonstrated TNF-α is co-expressed with mammalian glial cells and zebrafish macrophages under pro-inflammatory conditions (Lewis and Elks, 2019). Thus, the current study assessed microglial expression of Tnf-α during sustained

activation of HIF signalling in zebrafish. However, while peripheral macrophages were shown to express Tnf-α following tailfin injury, the current study failed to detect microglial Tnf-α expression in the CNS as judged by the *tnfα::GFP* transgene, either as a response to HIF activation, head injury, or both.

Surprisingly, despite the aforementioned reports in mammals, in the zebrafish larvae, we found that Tnf-α was not expressed within the activated microglia. This was consistent with reports that Tnf-α is expressed almost exclusively in L-plastin-positive macrophages cells (Tsarouchas et al., 2018). Nevertheless, there has been an instance where microglial expression of L-plastin has been shown to co-localize with Tnf-α expression (Tsarouchas et al., 2018). Additionally, the microglial gene signature might be changed at the incident of neural death. In 3 dpf zebrafish larvae treated with MTZ, microglial proliferation is activated, combined with the increased expression of L-plastin (Oosterhof et al., 2017). In zebrafish with a chronic seizure-like condition (induced by the pilocarpine), the brain Tnf-α was measured using the qPCR and compared with control wildtype adult zebrafish. The Tnf-α mRNA expression level was elevated in the treated group compared to the control wildtype (Paudel et al., 2020).

While the current study initially hypothesised that Tnf-α would co-express within microglia due to sustained activation of the HIF signalling pathway and/or induced after insult by the activated microglia, Tnf-α expression was not associated with microglia in either condition.

4.4.4 Sustained activation of the HIF pathway significantly increases expression of *il-10* at 4 dpf

The myeloid cells of microglia and macrophages are considered the principal source of interleukins (Hasegawa et al., 2017, Gan et al., 2020). In a traumatic brain injury (TBI) zebrafish model, the heads interleukin secretions were associated with activated microglia (Gan et al., 2020). In parallel, in the current study, the interleukin measurements represented the entire head's tissue response to the sustained activation of the HIF pathway and were not limited to the microglial responses. However, based on previous reports, results are considered to mainly reflect the secretion of interleukins by microglia (Gan et al., 2020). Of the panel of cytokines investigated, only *il-10* showed a significant increase in the *vhl*$^{-/-}$ mutant fish affected by the sustained activation of the HIF pathway.

Within the human CNS IL-10 is the most critical anti-inflammatory cytokine (Glocker et al., 2011). It is secreted by M2 activated microglia and maintains the immune system balance by limiting the secretion of pro-inflammatory cytokines, such as TNF-α, IL-6 and IL-1 (Royle et al., 2009, Laffer et al., 2019); hence, IL-10 protects against excessive immune responses and tissue damage (Glocker et al., 2011, Wu et al., 2010). In an *in vitro* lipopolysaccharide (LPS) stimulation study, the deficiency of IL-10 resulted in the elevation of the M1-like phenotype. The microglial phenotype was analysed by the flow cytometry and demonstrated elevated expression of the phagocytic marker (CD66), associated with increased IL-6, and TNF-α. Meanwhile, the M2 microglial profile was attenuated, influenced by the absence of the IL-10 (Laffer et al., 2019). Another *in vitro*

human study using the tumour cell-released autophagosomes (TRAPs) line has shown that under hypoxic conditions, the TRAPs induced more IL-10-producing B cells with suppressive activities on T cells (Zhang et al., 2019b); thus, interestingly, suggesting that HIF-1α regulates the *IL-1*0 expression level (Wu et al., 2010) and contributes to its production at least in B cells (Meng et al., 2018).

Similarly, in a mouse study and under hypoxic conditions, expression of HIF-1α was elevated within activated B cells, which regulate the production and function of IL-10 (Meng et al., 2018). In contrast, HIF-1α deficiency was found to limit the expansion of the B cells and reduce their intracellular IL-10 production (Meng et al., 2018). Further, when splenic B cells were cultured under hypoxic conditions, IL-*10* mRNA expression was significantly elevated compared to B cells cultured in normoxic conditions (Meng et al., 2018). In rats with a hypoxic-ischemic condition, the level of neural apoptosis negatively correlated with IL-10, indicating the neuroprotective role of IL-10 when hypoxia occurs, causing neural damage (Li et al., 2014a).

Taken together from the mentioned studies, within the *vhl*$^{-/-}$ *heads*, *il-10* expression increases with the microglial-M2 inflammatory profile and under hypoxic conditions, providing a neuroprotective role. Zebrafish *IL-10* is an essential anti-inflammatory and critical for gill homeostasis (Bottiglione et al., 2020). We speculate that the elevation of *il-10* at the *vhl*$^{-/-}$ *head's* model at 4 dpf is under the effects of sustained activation of the HIF pathway and has a neuroprotective role that might be related to the apoptotic neurons.

4.4.5 After injury, the sustained activation of the HIF pathway significantly increases the expression of *il-1β* and *il-4* at 4 dpf

The zebrafish microglial response to injury is recognised as having both pro-and anti-inflammatory effects, demonstrated by cytokine levels regulated by injuries (Gan et al., 2020). Activated microglia have been shown to secrete both pro-inflammatory (M1) cytokines such as IL-6 and IL-1β and anti-inflammatory (M2) cytokines such as IL-4 and IL-10.

In the current study the microglial immune response was measured when additional stress was induced to evaluate if sustained HIF signalling might exacerbate or reduce the microglial response. The interleukin levels were assessed in post-injured zebrafish's heads within the *vhl*$^{-/-}$ and sibling wildtype larvae. At 1 hpi, the *vhl*$^{-/-}$ larvae showed elevations of the pro-inflammatory (M1) *il-1β* and the anti-inflammatory (M2) *il-4*; both dropped to a normal level within 24 hpi.

In humans, IL-1β is mainly produced by microglia (Zhu et al., 2019). The elevation level of human CNS IL-1β is usually combined with altered microglial morphology, a hallmark for CNS inflammation (Liu and Quan, 2018). The integration of activated microglia and IL-1β within their pro-inflammatory role causes brain hyper-inflammation, neural damage and excessive oxidative stress; eventually leading to neural pathology progression and CNS disease. Significantly increased expression of IL-1β has been reported in several neurological diseases, including Alzheimer's disease, Parkinson's

disease, autoimmunity, chronic depression and bacterial/viral infections (Liu and Quan, 2018).

In the human CNS, the anti-inflammatory cytokine IL-4 is essential in brain memory and learning functions (Sachin et al., 2012). It is also an essential regulator for M1/M2 polarisation by switching microglia away from the pro-inflammatory subtype, promoting the neuroprotective effects (He et al., 2020, Yi et al., 2020). *In vitro* administration of IL-4 revealed a reduction of M1 markers, pro-inflammatory cytokines and neuroapoptosis markers while significantly raising M2 markers and anti-inflammatory cytokines (Yi et al., 2020, Sachin et al., 2012). In addition to antagonising the production of IL-1β (Bottiglione et al., 2020), IL-4 can directly induce proliferative and neurogenic ability in human neural stem cells (Cosacak et al., 2019).

In zebrafish, il-1β is a classical pro-inflammatory cytokine produced primarily by myeloid (macrophage and microglia) cells to recruit immune cells to the lesion site (de Abreu et al., 2018). Similar to the human studies, the elevation of il-*1β* in zebrafish was associated with physiological inflammatory responses (Zhang et al., 2019a). This was evidenced by a study utilising adult zebrafish with chronic seizure-like conditions caused by Pilocarpine treatment. The treatment group was found to express an elevated *il-1* level compared to the control untreated group (Paudel et al., 2020).

Zebrafish il-4 cytokines suppress the M1 immunity response and enhance the M2 type (Bottiglione et al., 2020). An additional role of il-4 in the zebrafish brain is to enhance neural progenitor, cell proliferation, and neurogenesis via initiation in neural stem cells, similarly to their role in humans (Cosacak et al., 2019).

Our current data imply that the heads elevation of *il-1β* in the present study resulted from the inflammatory response induced via the head injury. The secretion of *il-4* is likely a homeostatic response to suppress the production of *il-1β*, which eventually suppresses inflammation (Bottiglione et al., 2020). Within 24 hpi, the *il-4* level dropped parallel to the *il-1β* level, suggesting a balance in the inflammatory response within the injured heads. Noteworthy, at 1 hpi, the *il-1β* and *il-4* expression levels in *vhl*$^{-/-}$ larvae were higher than wildtype siblings, suggesting that sustained activation of the HIF pathway amplifies the immune responses following inducing the injury.

Our findings conflict with studies where the interleukin profile was measured in a traumatic brain injury model of zebrafish (Gan et al., 2020). In a double transgenic zebrafish Tg(*coro1a:EGFP*) ^{hkz04t} and Tg(*HuC:EGFP*)^{as8} , at 3 dpf, a head-wound injury was induced at the hindbrain. The total heads RNA was extracted from 3 dpf (25 larvae per group). Then the pro-and anti-inflammatory expression of *il-1β*, *il-6* and *il-4, and il-10* genes was measured using the real-time quantitative reverse transcription-polymerase chain reaction (qRT-PCR) assays at different time-points following the wound induction. In contrast to the current data, the published results show a significant up-regulation across all the measured inflammatory interleukins, which drop gradually over the next 48 hpi (Gan et al., 2020). In the current study, it was expected that the wildtype sibling would reflect the published results, enabling the evaluation of whether the *vhl*$^{-/-}$ mutant responses are greater or less than the healthy larvae.

The experiments performed in this study mirrored those used for the published data, with two minor changes: the needle size was increased from 22 µm to ~25 µm, and

the published experiment was performed on 3 dpf larvae rather than 4 dpf. While these two factors may seem irrelevant to the conflicting results, the other variation between the two datasets is the sample size; the published data was for one sample per group, where each sample was pooled of 25 larvae heads. In comparison, the current data is representative of 6 samples per group, where each sample is pooled from 23 larvae heads. The initial experiment included 3 samples per group, and the qPCR measurements were repeated on different 3 samples to draw conclusive results. Yet, no trend of up-regulation or similarity between the two studies was confirmed.

Our experiment aimed to investigate the differences in the immune response between the genotypes at the basal level and when head injuries were induced to recognise if the sustained activation of HIF signalling affects the immune response within the *vhl*$^{-/-}$ zebrafish. It could be that microglial gene expression changes are lost in the large amount of RNA originating from all the cells in the ZF head rather than measuring the microglia profile only. Hence, an affirmative approach to studying the microglial specific profile within the two larval groups would be extremely helpful by isolating the microglia for RNA-sequencing transcriptomic studies.

4.5 Summary of the major findings

1- Sustained activation of the HIF pathway in the *vhl*$^{-/-}$ larvae causes the microglia to adopt an activated morphology at 5 and 7 dpf.

2- The immediate inflammatory response following additional stress (head injury), is amplified in the *vhl*$^{-/-}$ larvae, thought to be driven by the sustained activation of the HIF signalling pathway.

3- Studying the transcriptomic profile of isolated microglia is critical to confirm the microglial inflammatory profile in response to the sustained activation of the HIF pathway.

Chapter 5 **Optimisation of zebrafish microglial cell sorting**

5.1 Introduction

The popularity of zebrafish (ZF) as an *in vivo* model for the study of human diseases has increased significantly since the 1980s (Bradford et al., 2017). The zebrafish genome has been characterised in detail and now, a high quality and precisely mapped reference genome has become available with approximately 70% of the protein-coding genes between zebrafish and humans being conserved (Li et al., 2022), hence offering exciting prospects for functional genomic analyses (Loontiens et al., 2019).

The development of transgenic fluorescent reporter zebrafish lines, where a fluorescent tag enables the visualisation of the cells of interest, has facilitated the gene expression analysis of fluorescence-activated cell sorting (FACS) sorted cell populations (Liao et al., 2016). FACS is a technique which enables the isolation of specific cell populations according to their fluorescent phenotype and the specific light scattering detected by flow cytometry, enabling further analyses of a single cell type, without the influence of unwanted cells (Liao et al., 2016). The advantage of FACS is the accurate isolation of cells of interest from a heterogeneous population. However, the FACS recovery rate of ~70% may be an issue when dealing with a low number of cells (Liao et al., 2016). After sorting, downstream applications, including RNA-sequencing (RNA-seq) and microarray experiments have enabled the investigation of the transcriptomic profile

of specific cell types, and the identification of altered gene expression under specific genetic mutations or chemical perturbation (Maurer and Quimby, 2015).

Nowadays, and based on the currently available genome sequences, databases can immediately characterise orthology between species (Loontiens et al., 2019, Maurer and Quimby, 2015). Studying the ZF orthologs of human genes, which are implicated in human disease aetiology, provides an understanding of the molecular basis underlying the pathogenesis of the disease (Maurer and Quimby, 2015). The transcriptomic analysis of zebrafish sorted cells using RNA-seq approaches has been successfully employed to characterise the role of neurons/glial cells in brain disease (Mazzolini et al., 2018), retinal regeneration (Sun et al., 2018), as well several immune cells' roles in the progression pathologies (Fei et al., 2021, Burroughs-Garcia et al., 2019).

Hypothesis, Aims and Objectives

RNA-sequencing is an excellent tool for studying the gene expression profile of specific cell populations in zebrafish disease models. Extracting RNA from a specific cell type requires a robust protocol to sort cells from the cell suspension. The number of microglia is very low in the early stages of brain development (Mazzolini et al., 2018). From the previous chapter, the microglia are scattered through the fish brain in a small number (~60 cells) compared to other neural and glial cells, making sorting a challenge.

The current project hypothesised that the microglia of *vhl* $^{-/-}$ fish, which display a sustained activation of the HIF pathway, have a similar transcriptomic profile to those isolated from a chronic hypoxic condition of post-mortem deep-subcortical lesions (PM-DSCL). The optimisation experiments in this chapter aimed to provide a workflow that

successfully produced a sufficient amount of high-quality RNA extracted from sorted cells using the FACS system that was available at the University of Sheffield. The main aim for this chapter was to isolate RNA samples from mCherry^{+} microglia from the ZF head of both *vhl* $^{-/-}$ and wildtype siblings, and then compare the transcriptomic profiles with the PM-DSCL transcriptomic profile findings (detailed in chapter 3). Unfortunately, due to the impact of COVID-19, it was not possible to complete all the main aims within the project timeframe.

The chapter objectives were to conduct a survey for the robust approach to isolate microglia from zebrafish samples. The optimisation strategy involved many different conditions with limited repeats and included:

1- Evaluation and optimisation of the liberase homogenising protocol.

2- Evaluation and optimisation of the cold homogenising protocol.

3- Evaluation and assessment of three extraction kits, several sorting media, and collection tube options.

4- Identification of the optimal collection media, collection tube, and sorting period to be used for the sample preparation protocol.

5- Preliminary transcriptomic profiling of microglia in *vhl* $^{-/-}$ and wildtype siblings fish samples using RNA-seq.

6- Bioinformatic analysis of the datasets generated by RNA-seq to identify significantly differentially expressed genes, dysregulated pathways, and functional groups.

7- Comparison of the microglial transcriptomic profiles from the PM-DSCL and *vhl* $^{-/-}$ fish.

5.2 Material and Methods

5.2.1 General practice

Zebrafish husbandry, general practice and anaesthesia were performed as previously detailed in sections 4.2.3. The samples used for were a mix of wt-sibling and *vhl*$^{-/-}$ larvae, with the double transgenic line *vhl* $^{hu2117/+}$ *(mpeg1::mCherryCAAX, phd3::GFP)* used at 5 dpf. Both mCherry^{+} microglia and mCherry^{+} macrophages will have been isolated during these optimising experiments.

5.2.2 Optimisation of the sorting protocol for the isolation of microglia from zebrafish using fluorescent activated cell sorting

All steps were performed at 4°C unless otherwise stated, including cooled instruments, reagents, and tubes. Solutions were made with diethylpyrocarbonate (DEPC)-treated water under RNase-free conditions. For sorting, the FACS-Melody, which is previously reported for its accurate isolation of mCherry^{+} cells (BD Science, UK), was used with a 100 µm nozzle. The flow rate was set at 5, with 75-80% efficiency.

5.2.3 Evaluating the accuracy of the FACS sorting

FACS sorting is an accurate and sensitive sorting method (Yang et al., 2016). Following the sample homogenizing, the accuracy of FACS sorting the mCherry^{+} cells was tested.

For sample homogenisation, a protocol adopted from (Mazzolini et al., 2018) was used. Brefiely, 400 *mpeg1::mCherry* transgenic larvae were anaesthetised in tricaine and then transferred with a minimal amount of the E3 medium into a cold glass homogeniser containing 1 mL ice-cold media-A, composed of 15 mM Hepes and 25 mM D-Glucose dissolved in Hank's Balanced Salt Solution (HBSS). The larvae were dissociated by 40 turns of the homogeniser. Afterwards, 2 ml of media-A was added to the cell suspension; this helps reduce the cell agglutination and facilitates separation at a later step. The cell suspension was passed 3 times through a 40 µm cell strainer placed over an ice-cold 50 mL falcon tube to reduce further agglutination. Next, 1 ml of the cell suspension was transferred into cold 2 mL Eppendorf tubes and centrifuged at 300 g for 10 min. Afterwards, the supernatant was removed using a 10-mL syringe and 23G x 1" needle. The cell pellet was resuspended in 0.5 ml of a density gradient medium, composed of 9 volumes of Percoll solution mixed with 1 volume of HBSS (10x). A top layer of ice-cold DPBS was then gently added. The separation step was performed using a slow acceleration centrifuge (without a break) at 950 g for 30 min. This caused the cells to form a pellet at the bottom of the tube, while the myelin was sequestered at the interphase of DPBS and the density gradient medium. After discarding the supernatant, the cells were washed in 0.5 ml media-A supplemented with 2% normal goat serum (NGS: a supplement

advised by the protocol to keep the cells nourished and alive) and centrifuged at 300 g for 10 min.

Afterword, the accuracy of FACS sorting the mCherry$^+$ cells was tested using two approaches. In the first approach a total of 10,000 mCherry$^+$ cells were sorted into cold media-A with 2% NGS buffer. The cell suspension was then resorted and the percentage of mCherry$^+$ cells within both the first and second sorts were compared.

In the second approach, the sorting accuracy was tested via visualising the sorted mCherry$^+$ cells under a fluorescent microscope. The cells were centrifuged in the cytospin and fixed after FACS sorting, using a protocol developed by Dr Catarina Henriques's group. For this, 10,000 mCherry$^+$ cells were sorted in cold media-A with 2% NGS buffer. The cell suspension was centrifuged at 4 °C at 600 g for 10 min. Immediately, the supernatant was removed, and the cells were fixed in 200 µl cold neutral buffered formalin and incubated on ice for 10 min. Afterwards, the cell suspension was centrifuged in a cytospin at 900 g for 7 min; the cells were collected on a dry superfrost charged slide and left in the dark to dry overnight. On the following day, 100 µl DAPI was gently added to the slide at 1:10,000 in DMS (5 mg/ml), and incubated for 10 min. The excess was gently removed by wiping, and the slide was immediately mounted with a Vectashield mounting medium for fluorescence (Vector, Burlingame, CA), to prevent any cell loss. The slide was stored in the dark at 4^{o}C and imaged within two days to quantitate the proportion of mCherry$^+$ cells. A negative control sample of non-mCherry cells was also prepared and imaged.

5.2.3.1 Image acquisition and data analysis

Using the Nikon widefield microscope, the cells were viewed and imaged under 40x magnification, within 30 fields across the cytospin stained slides. Identification of the cells was done using both DAPI and mCherry fluorescent excitation, where DAPI aided in the localisation of the cells, and a DsRed filter was used to detect the mCherry fluorescent status. Fluorescence for DAPI and mCherry was acquired using an excitation wavelength of 395 nm and 455 nm emission and detected at 510 nm and 640 nm, respectively. The cells were visualised using overlapping fluorescence: Figure 5.1, any dead cells, recognised by auto-fluorescence across the entire cell, were excluded from the analysis.

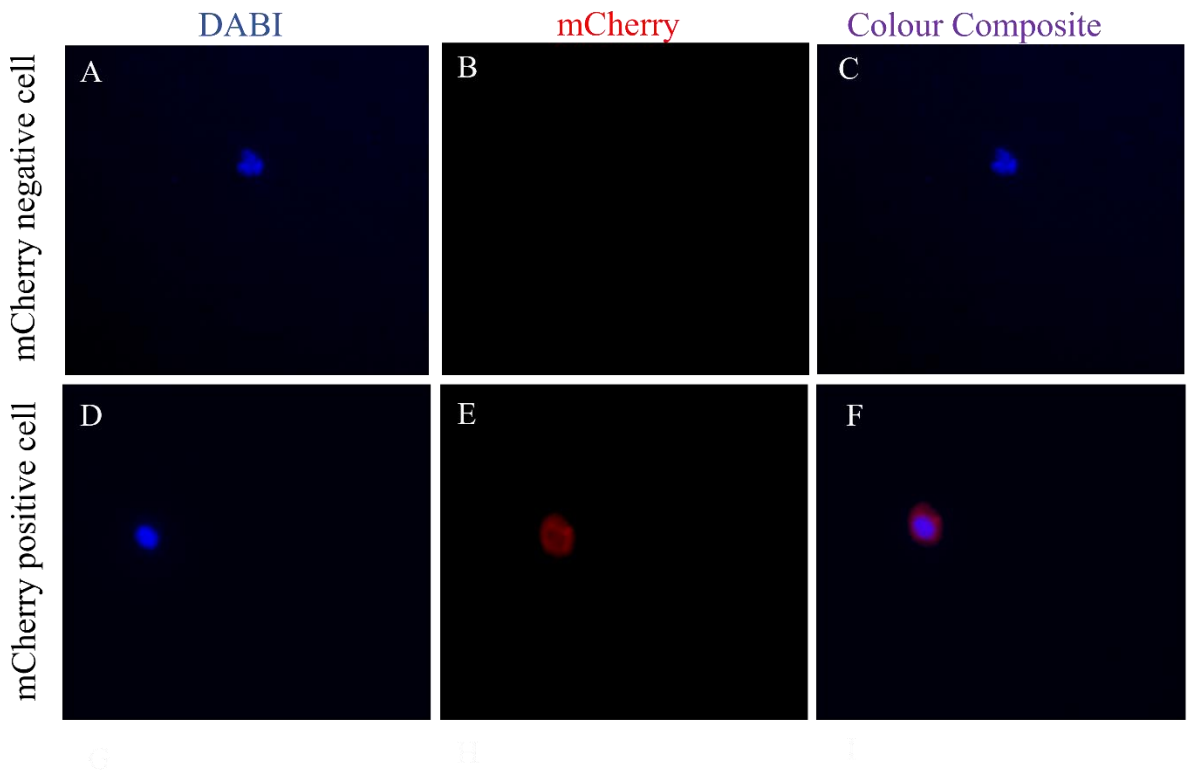

Figure 5.1- Detection of the proportion of mCherry cells. DAPI labels the nuclei of cells (A, D). Negative mCherry cell, where the nucleus is labelled by DAPI (A) but there is no mCherry expression (B). (E) Positive mCherry cell, where the nucleus is more prominent in mCherry cell, (F) and the cell wall labelled by mCherry.

5.2.4 Optimisation of the liberase homogenising protocol

For embryo dissociation, larvae were anaesthetised in tricaine and transferred to a cold surface (4^{o}C), and all E3 media was removed. The larvae were finely chopped with a sterile scalpel blade before being suspended in 3 ml of phosphate-buffered saline (PBS). Subsequently, Liberase™ TL (Thermolysin Low) diluted in PBS (1:65; with a final concentration of 46.15 µl for 3 ml PBS) was added, and the larvae incubated at 37^{o}C in a shaker (Innova 44, 200 RPM) for 40 min, while being gently mixed by pipetting every 10 min to enable clump dissociation. Next, the sample was transferred to cold Eppendorf tubes (4^{o}C), and centrifuged for 6 min at 300 g, 4^{o}C. The sample was resuspended in 1 ml cold live sorting buffer composed of L15 media, 20% FBS and 5mM EDTA, and placed on ice. It was then transferred to the Flow Cytometry Core Services at the University of Sheffield, where it was passed through a 40 µm filter before being analysed on the FACS Cell Sorter.

At the FACS unit, the cell viability was assessed using Propidium iodide (PI, Thermofisher, UK), where 3 µl was added to the cell suspension and mixed by pipetting. It was then incubated for 5 min on ice, before the cell viability was measured for a total of 100,000 events.

Afterwards, variable cell numbers of 500, 1000, 2000, 2500, 5000, 10000, 50000 and 100000 cells, harvested from 100 whole embryo, were sorted directly in two solutions: cold live sorting buffer and RNAse free lysis RLT (composition unknown, provided within the Qiagen RNAeasy micro kit). The samples were mixed thoroughly. The solution volume was amended to avoid exceeding the maximum dilution point caused by

the sorting; it aimed to keep the final concentration of less than 1:10 of the sorted cells per solution volume. This was important because a small amount of cold live sorting buffer is involved with each sorted cell. A summary of the samples collected is displayed in Table 5.1 below.

Table 5.1- The sorted plan included sorted cells number and collecting media to assess the liberase preparation protocol for cell isolation. Cells are obtained from 100 whole embryo. RLT: RNAse free lysis RLT buffer solutions, SB: cold live sorting buffer

Sample number	Number of mCherry+ sorted cells	Volume	Media
1	500	75 µl	RLT
2	500	75 µl	SB
3	1000	100 µl	RLT
4	1000	100 µl	SB
5	2000	125 µl	RLT
6	2000	125 µl	SB
7	2500	150 µl	RLT
8	2500	150 µl	SB
9	5000	250 µl	RLT
10	5000	250 µl	SB
11	10,000	275 ml	RLT
12	10,000	275 ml	SB
13	50,000	1 ml	RLT
14	50,000	1 ml	SB
15	100,000	1 ml	RLT
16	100,000	1 ml	SB

The RNA was extracted immediately after sorting, using the Qiagen RNAeasy micro kit according to the manufacturer's instructions (Qiagen, Hilden, Germany). The samples sorted into the cold live sorting buffer were first centrifuged at 300 g for 1 min; the supernatant was discarded and replaced with 350 µl of the kit's RLT buffer. Samples with

a cell sorted count of fewer than 1000 cells were replaced with a 75 µl RLT buffer (following the manufacturer's instructions). All samples were vortexed for 30 sec, then mixed with 5 µl of freshly prepared RNA carrier (poly-A), which improved the recovery of the RNA extraction and purification (Jewkes et al., 2011).

For cell homogenisation, the lysate mixture was passed through a blunt 10-gauge needle (0.9 mm diameter) fitted to an RNase-free syringe, before 1 volume of 70% ethanol was added to the lysate and mixed by pipetting. Next, the mixture was transferred to a new RNeasy spin column placed in a 2 ml of collection tube and centrifuged at 8000 g for 15 sec. The mixture was washed by 350 µl of buffer RW1 and centrifuged at 8000 g for 15 sec. Following this, 80 µl of freshly prepared DNase in the RDD buffer (with a ratio 1:7) was added to the spin column and incubated for 15 min at RT. This step was followed by another wash with 350 µl of buffer RW1 and centrifuged at 8000 g for 15 sec. Next, 500 µl of buffer RPE was added, and the total mixture was centrifuged at 8000 g for 15 sec to wash the spin column membrane. Another 500 µl of buffer RPE was added and centrifuged at 8000 g for 2 min. Afterwards, the RNA was eluted by adding 14 µl RNase-free water and centrifuged at 14,000 g for 1 min.

5.2.4.1 Evaluation of sample RNA quality and quantity

The quantity and quality of the extracted RNA, from samples prepared using the enzymatic homogenising protocol, were measured using both the 1000 spectrophotometer (Labtech International, Uckfield, UK) and the 2100 Bioanalyzer

(Agilent, UK), respectively. After evaluating the RNA profiles, all RNA samples were stored under sterile conditions at −80°C for future downstream applications.

5.2.4.2 Optimisation of the extraction protocol when omitting the RNA carrier:

The same experimental conditions were repeated to isolate mCherry^{+} cells using the liberase homogenising protocol and the Qiagen RNAeasy micro extraction kit; however, for this extraction, the RNA carrier step was omitted from the extraction protocol due to its potential interference with the amplification protocol using oligo-dT primers.

In an attempt to enhance the RNA quality, and as recommended in the extraction kit handbook, the supplementary DTT was added to the lysing buffer to prevent RNase effects (that may degrade RNA); and hence, yield higher levels of RNA (Guardado et al., 2020). The optimising conditions used for these experiments is summarised in Table 5.2; where two sorting media were used.

Table 5.2- Summary of the collection media used to assess the liberase preparation protocol for microglia isolation and extraction using the Qiagen RNeasy micro kit, omitting the adding of the carrier to the samples. Cells were obtained from 100 whole embryo.

Sample ID	5000 mCherry+ Sorted cells collected in
A	250 µl lysis RLT buffer
B	250 µl lysis RLT buffer supplemented with freshly prepared 2M of DL-Dithiothreitol (DTT)

5.2.5 Optimisation of the cold homogenising protocol using the Qiagen RNeasy Plus Micro kit

A cold homogenising protocol has been developed concerning the sorting and isolation of microglia from zebrafish heads (Mazzolini et al., 2018).

For sample homogenisation, larvae were anaesthetised in tricaine and then transferred with a minimal amount of the E3 medium into a cold glass homogeniser containing 1 mL ice-cold media-A, composed of 15 mM Hepes and 25 mM D-Glucose dissolved in Hank's Balanced Salt Solution (HBSS). The larvae were dissociated by 40 turns of the homogeniser. Afterwards, 2 ml of media-A was added to the cell suspension; this helps reduce the cell agglutination and facilitates separation at a later step. The cell suspension was passed 3 times through a 40 μm cell strainer placed over an ice-cold 50 mL falcon tube to reduce further agglutination. Next, 1 ml of the cell suspension was transferred into cold 2 mL Eppendorf tubes and centrifuged at 300 g for 10 min. Afterwards, the supernatant was removed using a 10-mL syringe and 23G x 1" needle. The cell pellet was resuspended in 0.5 ml of a density gradient medium, composed of 9 volumes of Percoll solution mixed with 1 volume of HBSS (10x). A top layer of ice-cold DPBS was then gently added. The separation step was performed using a slow acceleration centrifuge (without a break) at 950 g for 30 min. This caused the cells to form a pellet at the bottom of the tube, while the myelin was sequestered at the interphase of DPBS and the density gradient medium. After discarding the supernatant, the cells were washed in 0.5 ml media-A supplemented with 2% normal goat serum (NGS: a supplement

advised by the protocol to keep the cells nourished and alive) and centrifuged at 300 g for 10 min. The samples were transferred on ice to the Flow Cytometry Core Services at the University of Sheffield, where they were passed through a 40 µm filter before being analysed using the FACS Cell Sorter. At the FACS unit, the cell viability was assessed using TO-PRO-3. Next, 10,000 mCherry+ cells were collected into either (1) cold media-A supplemented with 2% NGS, (2) lysing buffer supplemented with β-mercaptoethanol (BME) (10 µl in 1 ml lysis buffer or (3) pure lysing buffer (no supplements). For cells collected in media-A with NGS, the sorted cells were centrifuged at 300 g for 10 min, and the supernatant discarded. Afterwards, the cells were washed with 1 ml media-A, and the supernatant discarded. Next, cell pellets were lysed with (option 1) either the lysing buffer, (option 2) lysing buffer supplemented with β-mercaptoethanol (BME), or (option 3) lysing buffer supplemented with DTT. Note that all lysis buffers with supplementary material were freshly prepared immediately before use (Graham et al., 2021). The conditions are summarised in Table 5.3.

Table 5.3 - Summary of the collection media and lysis buffers options used to optimise the cold homogenising protocol using the Qiagen RNeasy Plus Micro kit. Where the lysing buffer used is the one provided from the extraction kit. Each 10,000 mCherry+ cells were obtained from 100 whole embryo.

Sample ID	mCherry+ Sorted cells collected in	Lysing solution
1	cold media-A with 2% NGS	lysing buffer + BME
2	cold media-A with 2% NGS	lysing buffer + DTT
3	cold media-A with 2% NGS	lysing buffer
4	lysing buffer supplemented with BME	
5	Lysing buffer	

Immediately after sorting, RNA was extracted using the Qiagen RNeasy plus Micro kit (Qiagen, Hilden, Germany), according to the manufacturer's protocol. The cells were homogenised with their corresponding lysing buffer and supplements by vortexing for 1 min. The lysate mixtures were pipetted directly onto a Qiashredder column, placed in a 2 ml collection tube, and centrifuged at 14,000 g for 2 min. The lysate mixtures were transferred to the 'gDNA eliminator' spin column, placed in a 2 ml collection tube, and centrifuged at 8,000 g for 30 sec. 1 volume of freshly prepared 70% ethanol was added to the flow-through mixture and mixed by pipetting. Next, samples were transferred to an RNeasy MinElute spin column, placed in a 2 ml collection tube, and centrifuged at 8,000 g for 15 sec. A 700 µl of buffer RW1 was added to the spin column and centrifuged at 8,000 g for 15 sec. The columns were washed with 500 µl of 80% ethanol and centrifuged at 8,000 g for 2 min, followed by full-speed centrifugation (14,000 g) for 5 min to dry the membrane. The RNA was eluted in 14 µl of RNase-free water by full-speed spin for 1 min.

The RNA quantity and quality were evaluated with the bioanalyzer assays only. All RNA samples were stored under sterile conditions at −80°C for future downstream applications.

5.2.5.1 Optimisation of the sorting time

The experimental condition for sample sorted in cold media-A supplemented with 2% NGS then lysed by lysing buffer supplemented with BME (as sample 1 from Table 5.3 above) was repeated three times, where variable cell numbers were sorted during the sorting period. The experiment details are summarised in Table 5.4.

Table 5.4 - Summary of the sorted plan used to test the effects of prolonged sorting period on RNA quality. Each 10,000 mCherry+ cells were obtained from 200 whole embryo.

Sample ID	Number of mCherry+ Sorted cells	Time required for sorting
1	25,000	over an hour
2	13,000	45 min
3	8,000	30 min

5.2.5.2 Measuring cell viability

Cell viability was measured using the TO-PRO-3 (Thermofisher, UK), as previously detailed in section 5.2.4. The mixture was incubated for 5 min on ice before the cell viability was measured for a total of 100,000 events.

To evaluate the media-A supplemented with 2% NGS's ability of preserving cells, the TO-RPO-3 positive cells were re-measured after incubating the samples on ice for 15 min.

5.2.6 Optimisation of the cold homogenising protocol using the Norgen single cell RNA purification kit

Sample preparation was conducted using the protocol outlined in section 5.2.5.1. In this experiment, a new extraction kit was optimised by testing a variety of collection media and collecting tubes, where mCherry^{+} sorted cells were collected in one of the options summarised in Table 5.5.

Table 5.5 - Summary of the collection media and tube options used to optimise the cold homogenising protocol using the Norgen single cell kit. Where the lysing buffer used is the one provided from the extraction kit. The mCherry+ cells were obtained from 100 whole embryo.

Sample ID	Number of mCherry+ cells sorted and media	Collection tubes/plates
1	50 cells into Lysing buffer	1.5 ml Eppendorf tubes
2	50 cells into Lysing buffer	96 flat bottomed well plate
3	50 cells into Lysing buffer supplemented with BME	1.5 ml Eppendorf tubes
4	50 cells into Lysing buffer supplemented with BME	96 flat bottomed well plate
5	50 cells into cold media-A + NGS then lysed with freshly prepared lysing buffer supplemented with BME	96 flat bottomed well plate
6	500 cells into cold media-A + NGS then lysed with freshly prepared lysing buffer supplemented with BME	1.5 ml Eppendorf tubes

For cells collected in media-A with NGS (before proceeding with the extraction steps), they were centrifuged at 300 g for 10 min, and the supernatants were discarded. Afterwards, the cells were washed with 1 ml media-A, and the supernatant was discarded, before 100 µl of lysing buffer supplemented with BME was added. Sorted cells in 96 well

plates were first lysed by pipetting up and down 10x, then transferred to 1.5 ml Eppendorf tubes to proceed with the extraction.

For extraction, the Norgen single-cell RNA purification kit (Norgen Biotek, Canada) was used, according to the manufacturer's guidelines. Briefly, cell lysis was performed by pipetting up and down for 10 times before adding 100 µl of freshly prepared 70% ethanol. The mixture was vortexed for 30 sec and transferred to a micro spin-column for a 1 min centrifugation at 3,500 g. A 400 µl of wash solution A was added, and the column was centrifuged at 14,000g for 1 min. The washing step was repeated 3 times before the RNA was eluted in 11 µl of the elution solution A. The RNA quantity and quality were assessed with the bioanalyzer assays; all RNA samples were stored under sterile conditions at −80°C for future downstream applications.

5.2.6.1 Comparing the effects of time on the RNA profile

Once the optimal sorting condition was identified of sorting cells into cold media-A + NGS in 1.5 ml Eppendorf tube, the experiment was duplicated. In this experiment, the sorting duration was varied to test the effects of sorting time on the RNA quality. The sorting period for sample one was 15 min, where 1700 cells were sorted, and the second sorting period was 25 min, where 5000 cells were sorted. The sorted cells were collected in 1 ml of media-A supplemented with NGS and placed in a sterile 1.5ml Eppendorf tube. The RNA was extracted using the Norgen single cell extraction kit.

5.3 Results

In the current project, two different sorting protocols were optimised and evaluated. Sorting directly into a lysing buffer was compared with collecting into sorting media. Further, the additions of two co-extracters into the lysing buffer were compared to confirm similar functions for both products under our experimental conditions. The current project also tested the ability of either BME or DTT to reduce RNA degradation by using the lysing buffer only without any supplement. An outline of the different optimisation steps is shown in Figure 5.2.

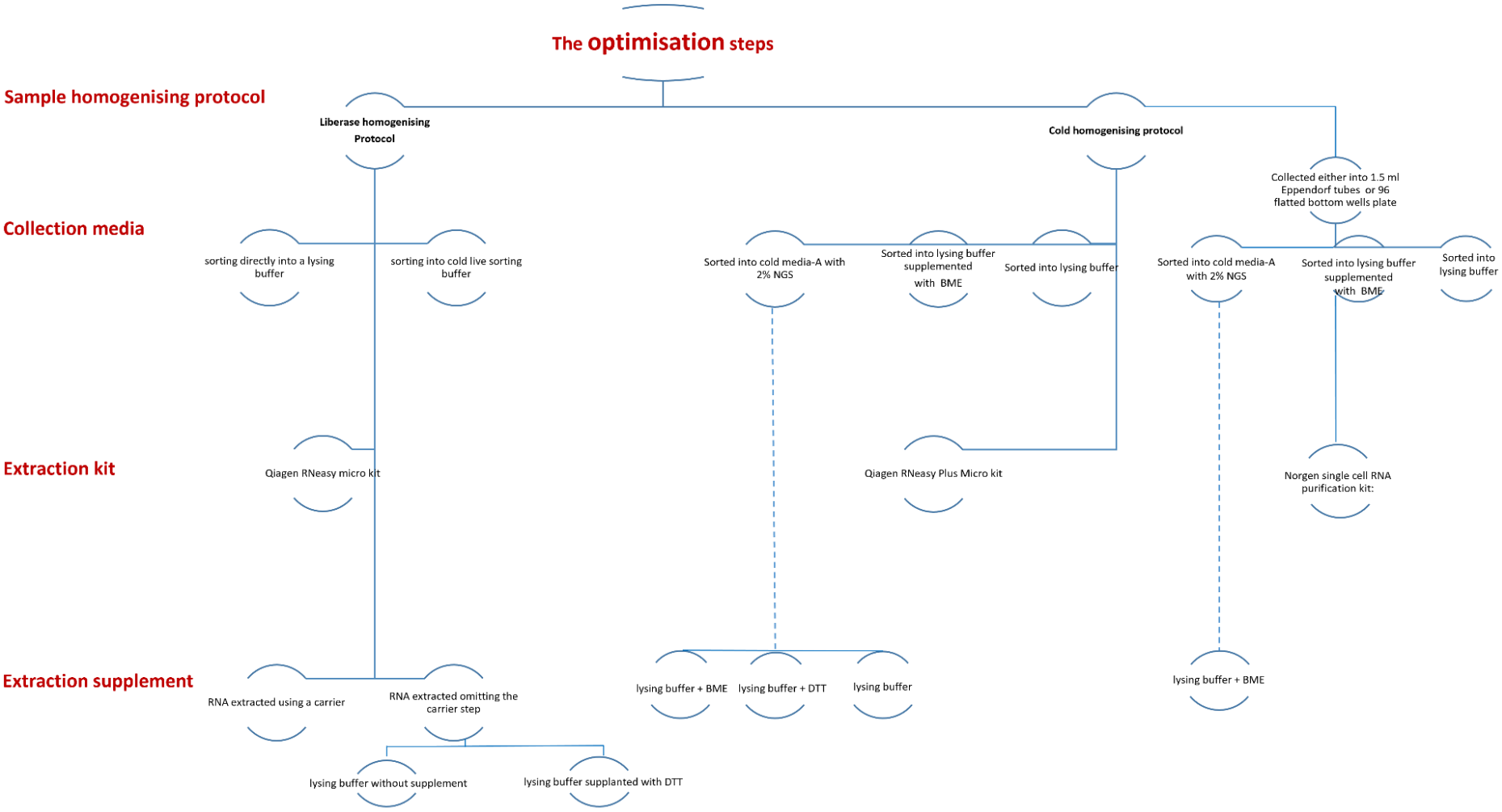
The optimisation steps
Sample homogenising protocol
Collection media
Extraction kit
Extraction supplement
Liberase homogenising Protocol
Cold homogenising protocol
Collected either into 1.5 ml Eppendorf tubes or 96 flatted bottom wells plate
sorting directly into a lysing buffer
sorting into cold live sorting buffer
Sorted into cold media-A with 2% NGS
Sorted into lysing buffer supplemented with BME
Sorted into lysing buffer
Sorted into cold media-A with 2% NGS
Sorted into lysing buffer supplemented with BME
Sorted into lysing buffer
Qiagen RNeasy micro kit
Qiagen RNeasy Plus Micro kit
Norgen single cell RNA purification kit:
RNA extracted using a carrier
RNA extracted omitting the carrier step
lysing buffer + BME
lysing buffer + DTT
lysing buffer
lysing buffer + BME
lysing buffer without supplement
lysing buffer supplanted with DTT

Figure 5.2- Flow-chart summarises the different optimising steps involved in sample preparation, sorting and extraction. BME: Beta-Mercaptoethanol, DTT: Dithiothreitol

5.3.1 The cold homogeniser protocol preserves cell viability within the sample suspensions more than the liberase homogenising protocol

Following the sample dissociating processes using the liberase homogenising protocol, cell viability was assessed using PI dye which binds to dead cells. Figure 5.3 A presents the viability of cells within 100,000 collected events, where approximately 74.18 % of cells were alive at the sorting stage

In contrast, more cell viability was detected for samples prepared using the cold homogeniser protocol using TOPRO-3, where 91.43 % of cells were viable at the sorting stage, and only 8.57% of cells were TOPRO-3 positive. When cell viability was measured 15 min later, dead cells number was elevated to 17.48% of TOPRO-3 positive cells: Figure 5.3 B-C.

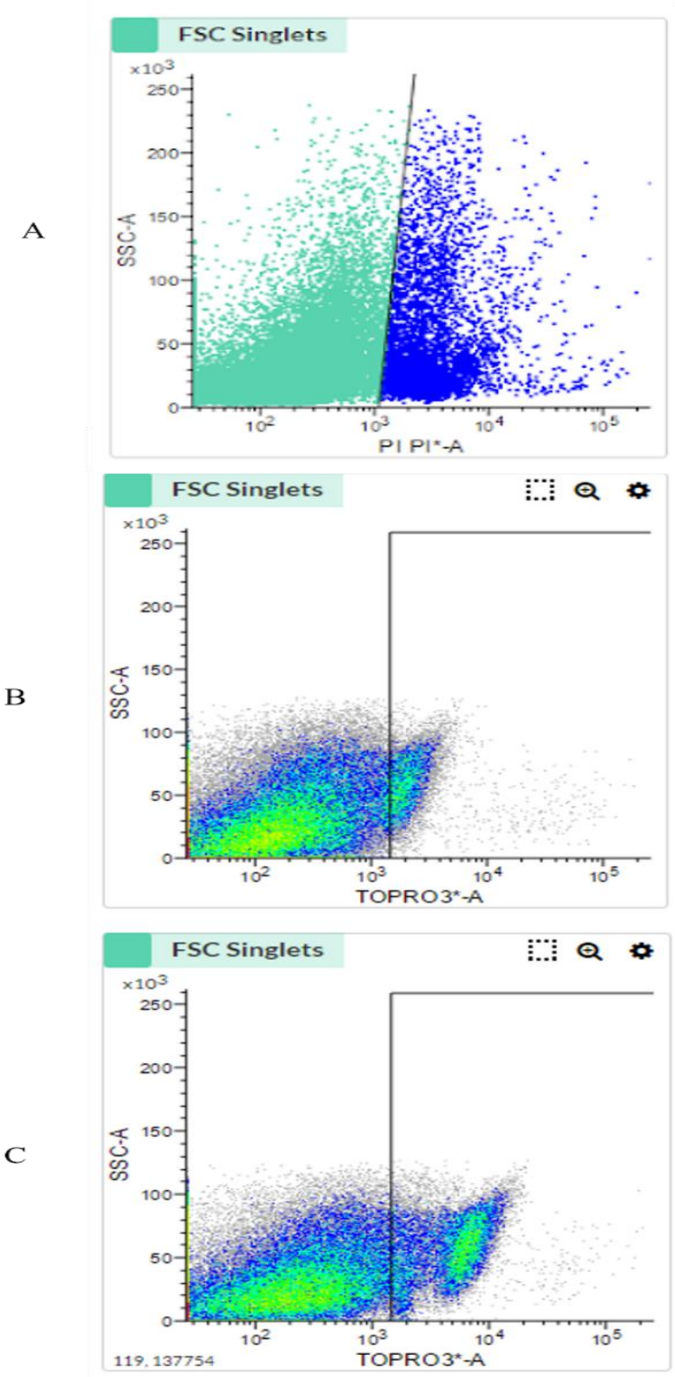

Figure 5.3 - Assessing cell viability of samples prepared using the Liberase homogenising protocol, and the cold homogenising protocol. (A) Using the liberase homogenising protocol, the PI positive cells, where FACS detected 74.18% viable (green) and 25.82% dead cells (blue). Using the cold homogenising protocol: (B) TOPRO-3 positive cells incubated for 5 min before assessing cells availability, where FACS detected 91.43 % viable

(green) and 8.57% dead cells (blue), (C) TOPRO-3 positive cell incubated for 15 min before analysis, where 17.48% cells were dead (blue).

5.3.2 FACS is a robust approach to accurately sort cells of interest

It is critical to evidence the accuracy of the FACS sorting machine that has been used for this project, where only mCherry$^+$ positive cells are to be isolated. The sorting accuracy confirms the specificity of the cell origin of the RNA harvested. The FACS sorting accuracy was evaluated by assessing mCherry$^+$ sorted cells versus non-mCherry$^+$ cells using the FACS instrument. The proportion of mCherry$^+$ cells was 94.28%, while 5.82% of the sorted cells were non-mCherry$^+$: Figure 5.4

In addition, when sorted mCherry$^+$ labelled cells were viewed under the DsRed fluorescent field, a total of 59 cells were seen within 30 fields; 48 cells were mCherry$^+$ labelled cells, while 11 cells were dead. No non-mCherry labelled cells were seen within the live mCherry$^+$ sorted sample, giving an accuracy of the sorted live cells of 100%, Figure 5.5.

The differences between the two percentages of the accuracy statistics are due to the variable cell number involved, where observation of the live mCherry$^+$ cytospinned cells was performed on a low cell number, compared to the higher number of sorted mCherry$^+$ cells.

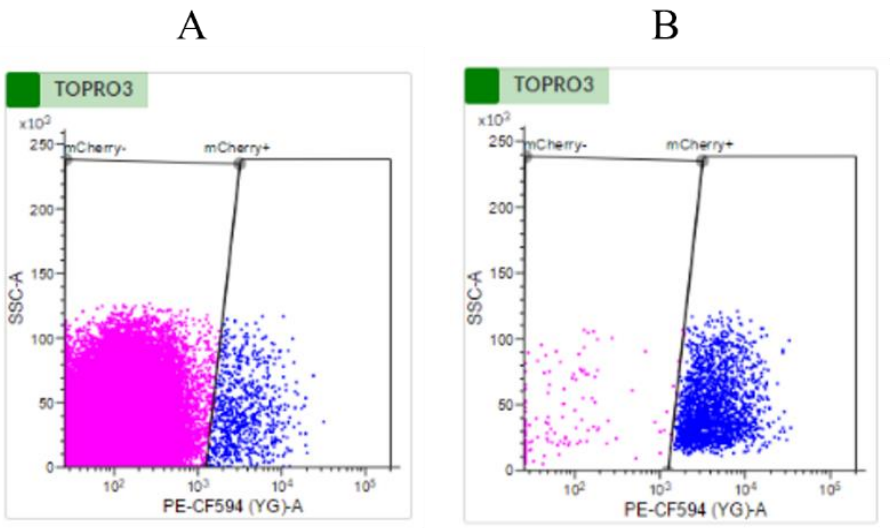

Figure 5.4 - Evaluating the FACS sorting accuracy via resorting mCherry⁺ sorted cells. (A) The mCherry⁺ cells (blue dots) were sorted from the cell suspension. Afterwards, (B) mCherry⁺ cells were resorted, where the majority of the resorted cells were mCherry⁺ positive (blue dots), while a small portion were non-mCherry cells (pink dots).

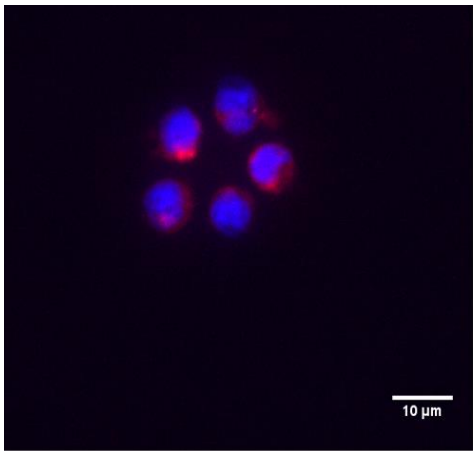

Figure 5.5 - Evaluating the accuracy of mCherry⁺ sorted cells using visualised cytospinned mCherry⁺ cells. A representative field for mCherry⁺ labelled cells. The scale bar represents 10 µm

5.3.3 Using the liberase homogenising protocol, a sample with an adequate RNA profile can be obtained using a carrier during the extraction process

The liberase homogenising protocol was in the process of being developed by a collaborative effort between Dr Noemie Hamilton, Amy Lewis (Elks Group) and Pamela Ellis (Henriques Group), combining their experience with the RNAeasy extraction kit and cell sorting (using FACS) directly into the kit buffer. My role in optimising the liberase homogenising protocol was a collaboration with Dr Noemie Hamilton; my task was to identify the optimum number of cells sorted and choice of the collecting solution, which would produce suitable RNA quantity and quality for down-stream applications.

5.3.3.1 A higher yield of intact RNA is obtained from samples collected directly in the lysing buffer

RNA was extracted from a range of microglial cell numbers and collecting media; the impact of the different methods on the isolation of RNA was assessed. Firstly, the RNA quantity was evaluated using the NanoDrop; a summary of results on RNA concentration (ng/µl) is presented in Table 5.6. Samples collected in the RLT buffer had a higher average RNA concentration of 11.03 ± 9.16 ng/µl than those sorted into the cold live sorting buffer, with an average of 2.18 ± 1.7 ng/µl.

The samples were further assessed using the bioanalyzer to assess the RNA profile, identified by the RIN numbers and rRNA ratio: A summary of results is presented in Table

5.7. A representative figure for the bioanalyzer results, involving samples with high, low, and unidentified RIN values is presented in Figure 5.6 A-E.

For RNA profile assessments, the RIN values and the rRNA were taken into consideration. Combining those two assessment criteria, it appears that sample ID 9 (Figure 5.6 C), is a preferable choice.

It is, however, noticeable that there is the extreme variation between the results obtained. The concentration of yielded RNA measured by the NanoDrop and the bioanalyzer is mismatched, which suggests avoiding relying on NanoDrop measurements. It was also noted that sorting high cell numbers did not result in a higher yield of RNA, possibly caused by the lysis buffer exceeding its maximum dilution point by the collection volume.

Table 5.6 - NanoDrop 1000 spectrophotometer assessment of RNA quantity. Cells were obtained from 100 whole embryo.

Sample 9 is highlighted in blue. RLT: RNAse free lysis RLT buffer solutions, SB: cold live sorting buffer

Sample ID	Number of mCherry+ sorted cells	Collecting Media	RNA (ng/ µl)
1	500	RLT	1.13
2	500	SB	4.91
3	1000	RLT	8.38
4	1000	SB	2.1
5	2000	RLT	22.78
6	2000	SB	3.06
7	2500	RLT	14.41
8	2500	SB	1.74
9	5000	RLT	14.47
10	5000	SB	0.35
11	10,000	RLT	2.33
12	10,000	SB	0.59
13	50,000	RLT	1.36
14	50,000	SB	0.54
15	100,000	RLT	23.37
16	100,000	SB	4.18
Average concentration ± SD for samples collected in RLT			11.03 ± 9.16
Average concentration ± SD for samples collected in SB			2.18 ± 1.7

Table 5.7 - Bioanalyzer assessment of the RNA quality of samples sorted directly into the lysing buffer. Sample 9 is highlighted in blue. The samples ID is equivalent to the one mentioned in Table 5.6 above.

Sample ID	Number of cells sorted in RLT	RNA con. pg/µl	RIN values	rRNA ratio
1	500	637	4.5	0.2
3	1000	1,471	6.3	1.4
5	2000	76	2.8	0
7	2500	68	n/a	0.4
9	**5000**	**9,925**	**3.4**	**2**
11	10,000	1,598	2.60	0.1
13	50,000	237,662	n/a	378.9
15	100,000	896	n/a	1.1

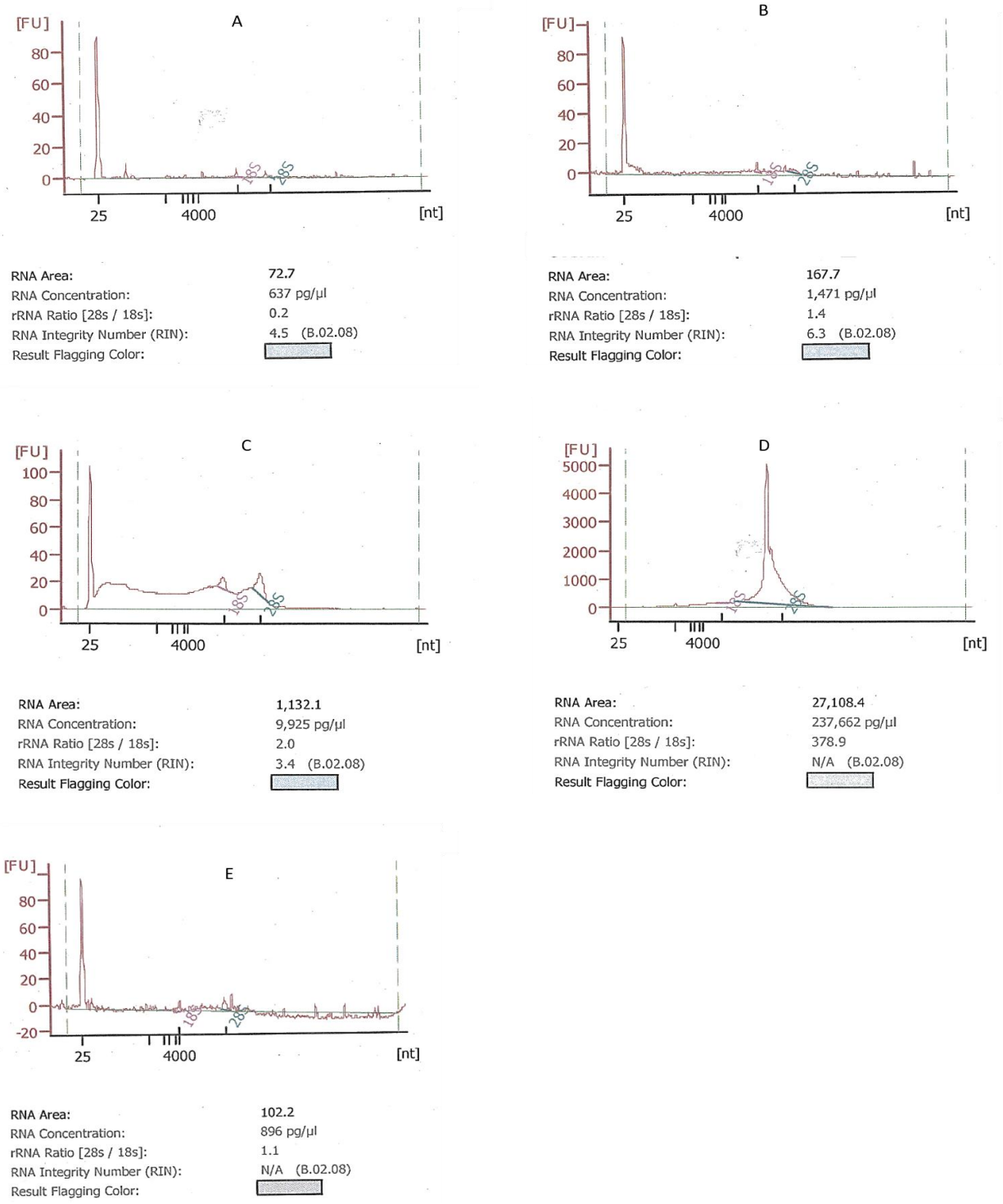

Figure 5.6 - RNA quality assessment using the bioanalyzer. RNA profiles obtained from sample numbers (A) 1, (B) 3, (C) 9, (D) 13, and (E) 15; where the expected RNA ribosomal peaks are visualised in figure (C), with good RNA quantity, RIN value is 3.4 and rRNA ratio is 2. Sample ID details are mentioned in Tables 5.6 and 5.7 above.

5.3.3.2 Confirmation of protocol reproducibility with liberase homogenising, using the Qiagen RNAeasy micro extraction kit including the carrier step

Once the optimal condition of sorting 5000 mCherry^{+} cells into 250 µl lysis RLT buffer cells was identified, the experiment was duplicated to confirm the protocol reproducibility.

RNA assessments were performed using the NanoDrop spectrometer and the bioanalyzer assays for the two replicates. The NanoDrop reads for RNA concentrations are presented in Table 5.8. Despite the same cell numbers being collected, different RNA concentrations were obtained from the replicates. The RNA quality profiles indicate RIN values of 8.6 and 7.8, and a 28S:18S rRNA ratio of 2.4 and 3.1 for replicates 1 and 2, respectively: Figure 5.7. The RNA yield and quality of the two replicates are superior to the initial experiment (sample 9 from Table 5.6 above).

Table 5.8 - RNA quantity measurements using the NanoDrop for replicate samples homogenised using the liberase homogenising protocol and extracted using a carrier of Qiagen RNAeasy micro extraction kit

Sample ID	RNA conc. (ng/ µl)
Replicate 1	24.98
Replicate 2	37.91

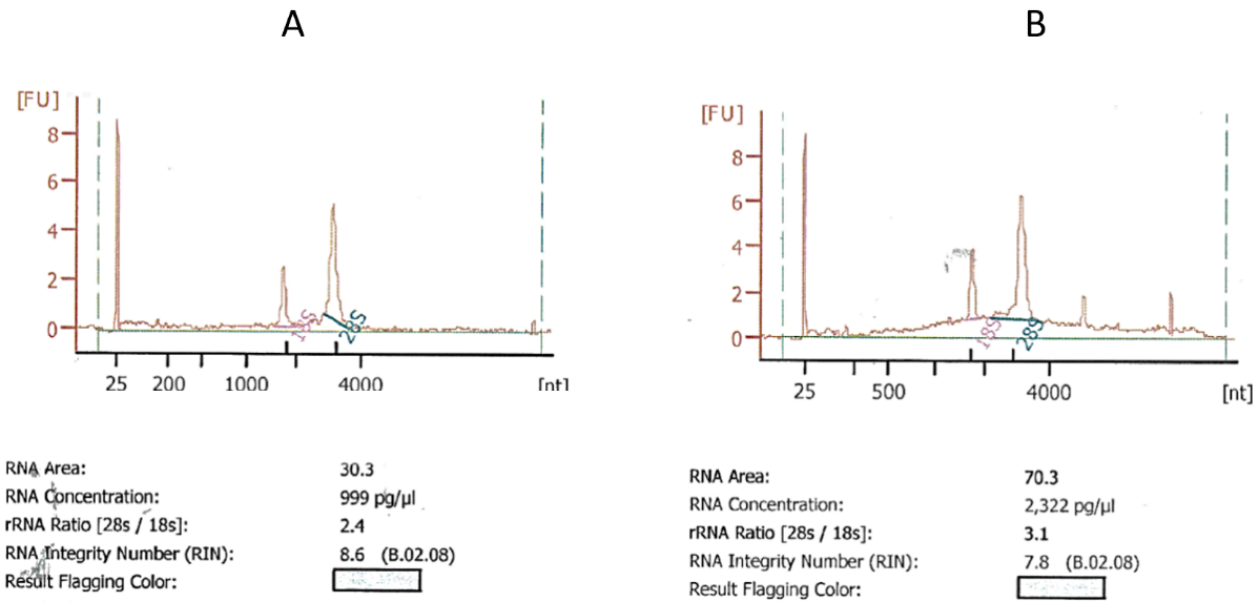

Figure 5.7 - The graphs are representative RNA profiles using the bioanalyzer for samples homogenised using the liberase homogenising protocol and extracted using a carrier of Qiagen RNAeasy micro extraction kit. The data shows the profiles of RNA extracted from 5000 mCherry+ cells from (A) replicate 1, and (B) replicate 2. For both samples, RNA is of sufficient quantity and quality for further downstream applications.

5.3.3.3 The optimum RNA profile is not reproducible when omitting the carrier step

The optimal sorting condition using the liberase homogenising protocol and the Qiagen RNAeasy micro extraction kit was repeated, where this time the carrier step was omitted from the extraction process, as it was found to be interfering with the RT-PCR using oligo-dT primers. Thus, the aim was to assess if the liberase homogenising protocol can produce a suitable RNA sample without interfering with the PCR primers.

Whether the DTT was supplemented into the lysing buffer or not, the bioanalyzer profile indicated a poor RNA profile, with a high degradation level, and low or undetectable RIN values, Figure 5.8.

A summary of the findings, utilising the liberase homogenising protocol and Qiagen RNAeasy micro extraction kit, by either adding or omitting the carrier from the extraction process, is presented in Table 5.9.

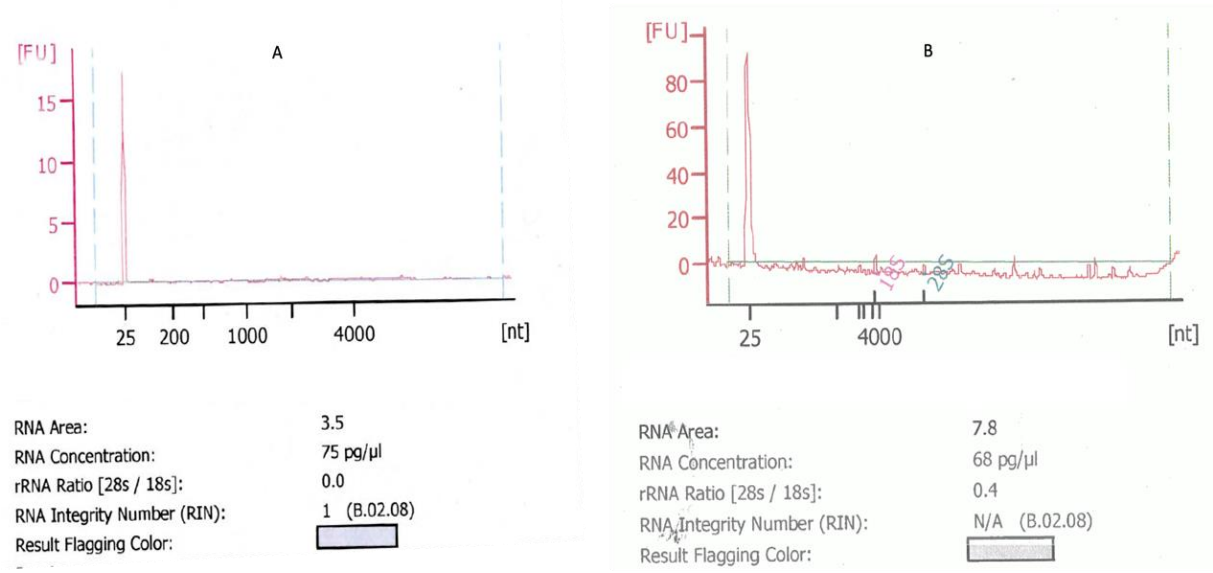

Figure 5.8 - RNA quality assessment for samples homogenised using the liberase homogenising protocol and extracted without the usage of a carrier in the Qiagen RNAeasy micro extraction kit. The graph is representative of the RNA profile extracted from 5000 mCherry+ sorted cells into (A) lysing buffer, (B) lysing buffer supplemented with DTT. Both profiles indicate that the RNA quantity is very low with a high degradation level.

Table 5.9 - Summary of findings using the liberase homogenising protocol and Qiagen RNAeasy micro extraction kit, either adding or omitting the carrier from the extraction process. Overall, using the carrier provides good RNA profiles that are suitable FOR for downstream applications. Each 10,000 mCherry+ cells were obtained from 200 whole embryo. RLT: lysing buffer

Sample ID	Description	RNA con. pg/µl	RIN	rRNA ratio
Replicate 1	5000 mCherry$^+$ cells sorted in RLT and extracted with a carrier	999	8.6	2.4
Replicate 2		2,322	7.8	3.1
Sample A	5000 mCherry$^+$ cells sorted in RLT and extracted without a carrier	75	1	0
Sample B	5000 mCherry$^+$ cells sorted in RLT + DTT and extracted without a carrier	68	n/a	0.4

5.3.4 Using the cold homogenising protocol and Qiagen kit, the yield RNA profile is unsuitable for downstream applications

RNA is a thermodynamically unstable molecule, and temperature can directly impact both the quality and quantity of the RNA obtained. It has been suggested that temperature affects the microglial phenotype (Mazzolini et al., 2020), which may directly impact the transcriptomic profile of these cells. Therefore, to avoid microglial activation due to increasing the temperature, a cold homogenising protocol was been developed to sort and isolate microglia from zebrafish heads (Mazzolini et al., 2018).

5.3.4.1 RNA profile of microglia isolated using a cold homogenising protocol

The sorted samples were collected in different media (cold media-A with 2% NGS, lysing buffer supplemented with BME, and lysing buffer: Table 5.3 from material and methods) then RNA extraction was performed via Qiagen RNeasy Plus Micro kit. The RNA profiles were assessed using the picochip bioanalyzer, Figure 5.9. Overall, and despite several collection and lysing media being used the RNA was degraded with undetectable RIN values and rRNA ratios under all conditions. It was noticeable, however, that samples collected in media-A plus NGS, then lysed with a supplementary lysing buffer, presented a double peak of RNA in comparison to the remaining samples. Another noticeable point was that sample processes involving the presence of BME, either lysed with a BME solution (Figure 5.9 A) or directly sorted into BME media (Figure 5.9 D), yielded higher RNA quantities than samples without.

Summary of findings using the cold homogenising protocol and Qiagen RNAeasy plus micro extraction kit is presented in Table 5.10

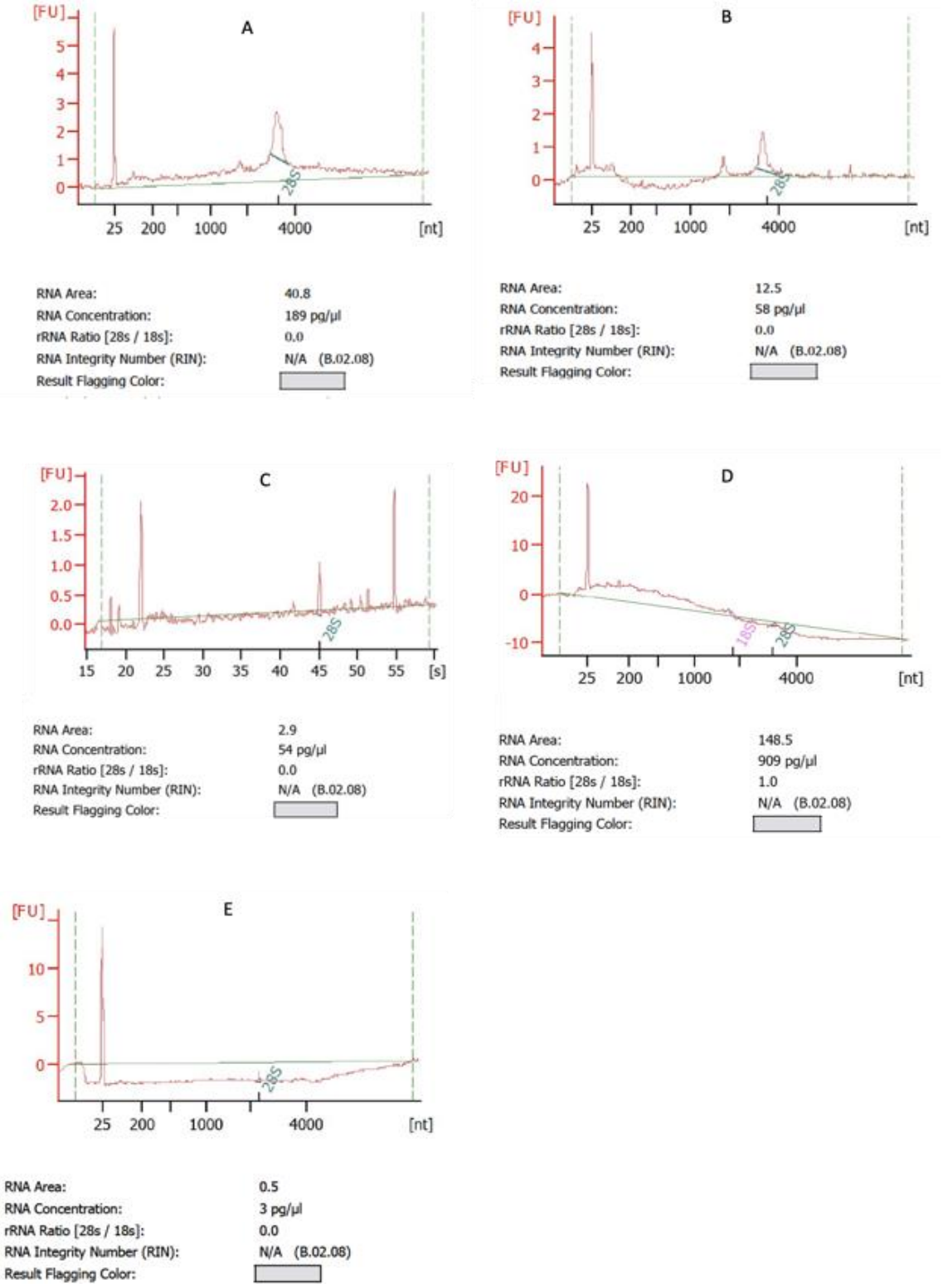

Figure 5.9- RNA quality assessment for samples homogenised using the cold homogenising protocol and Qiagen RNAeasy plus micro extraction kit. The graphs are representative of the RNA profiles for 10,000 cells sorted in (A) Media-A+NGS then lysed with a lysing buffer

supplemented with BME, (B) Media-A+NGS then lysed with a lysing buffer supplemented with DTT, (C) Media-A+NGS then lysed with a lysing buffer, (D) immediately into the lysing buffer supplemented with BME, (E) lysing buffer with no supplementary. A results overview suggested that sorting in media-A is better than sorting directly into the lysing buffer, as RNA ribosomal peaks were clearly observed. Also, the usage of BME preserved RNA over the DTT. Despite several collection media having been used, RNA degradation was a prominent feature of all samples, with undetectable RINs (n/a).

Table 5.10 - Summary of findings using the cold homogenising protocol and Qiagen RNAeasy plus micro extraction kit. Overall, no sample has suitable RNA for downstream applications; however, the usage of BME within the process helps in preserving RNA quantity. Each 10,000 mCherry+ cells were obtained from 200 whole embryo. RLT: Lysing buffer.

Sample ID	**Description** **10,000 cells sorted in**	**RNA con.** **pg/µl**	**RIN** **values**	**rRNA** **ratio**
A	Media-A+NGS then lysed with a RLT + BME	189	n/a	0
B	Media-A+NGS then lysed with RLT + DTT	58	n/a	0
C	Media-A+NGS then lysed with a RLT	54	n/a	0
D	immediately into the RLT + BME	909	n/a	1
E	RLT with no supplementary	3	n/a	0

5.3.4.2 Prolonged sorting periods negatively affect the yield of RNA

As demonstrated in Figure 5.10, the prolonged sorting period appeared to negatively affect the yield of RNA samples. Despite having the highest sorted number of cells (25,000), sample (A) produced the lowest yield of RNA (66 pg/µl). In contrast, sample (C) contained the lowest number of sorted cells (8,000) yet produced the highest RNA yield of 189 pg/µl. A summary of the findings is presented in Table 5.11.

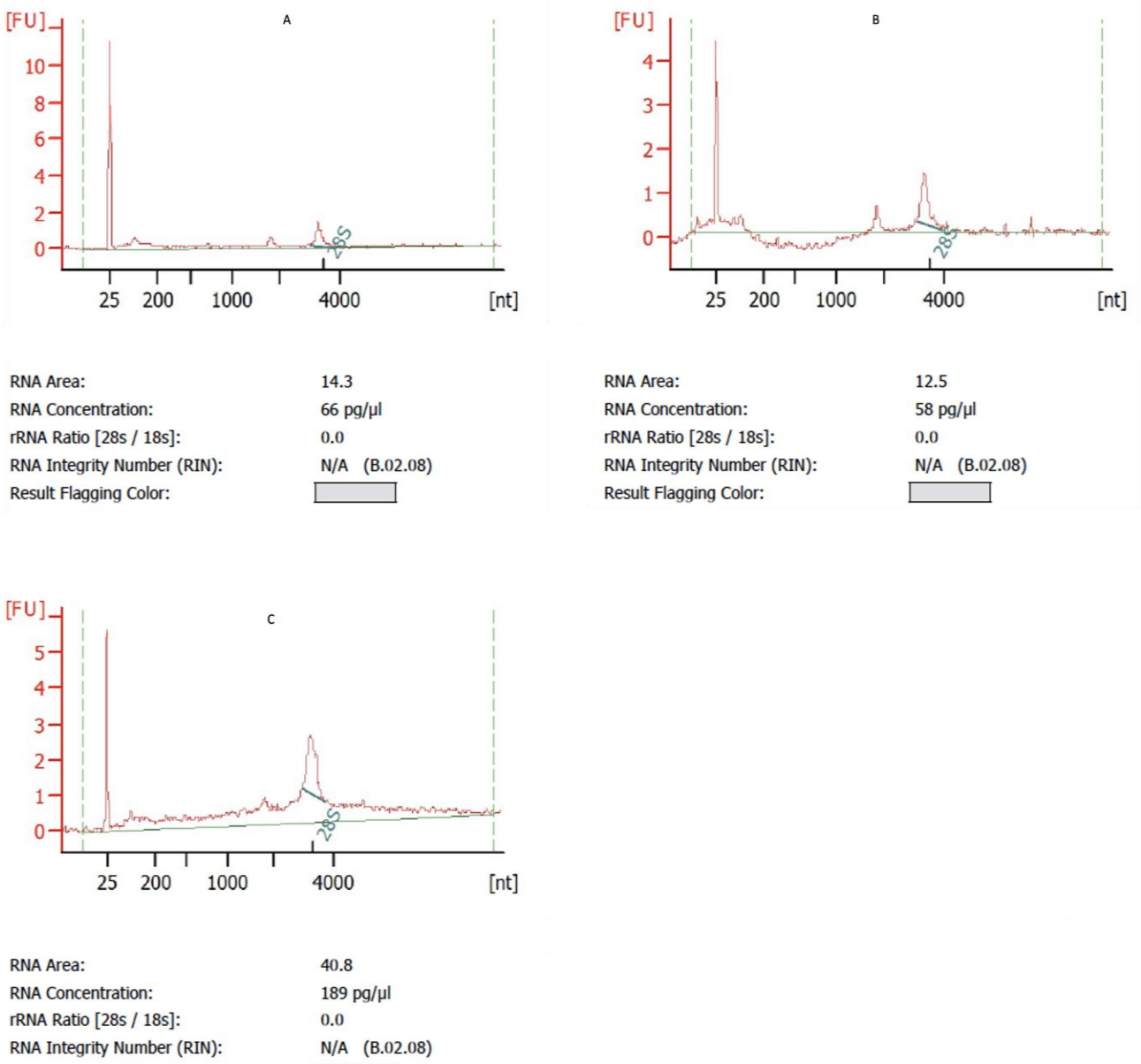

Figure 5.10 - RNA quality assessment for a prolonged sorting period. The graphs are representative of the RNA profiles for a variable number of sorted cells that were collected in a variable period: (A) 25,000 cells sorted within over an hour, (B) 13,000 cells sorted within 45 min, and (C) 8,000 cells sorted in 30 min. The shorter sorting period has yielded samples with the highest RNA quantity.

Table 5.11 - The effects of prolonged sorting period on RNA quality using the cold homogenising protocol and Qiagen RNAeasy plus micro extraction kit. Overall, a longer sorting period negatively affects the yield RNA.

Sample ID	Sorting period	Number of sorted cells	Cells collection media	RNA con. pg/µl	RIN values	rRNA ratio
1	over an hour	25,000	0.5 ml cold media-A supplemented with 2% NGS	66	n/a	0
2	45 min	13,000		58	n/a	0
3	30 min	7,000		189	n/a	0

5.3.5 The combination of the cold homogenising protocol with the Norgen extraction kit produces RNA suitable for downstream applications

Although RNA-seq can be done from a single-cell, our experiments of sorting up to 5,000 cells have failed to provide a sufficient amount or quality of RNA suitable for RNA-seq analysis. It was then suggested that perhaps the kits used for single-cell RNA-seq applications have a higher capability of preserving RNA. Unfortunately, the kits' reagents have proprietary components, and the differences between each component of the kit were not able to be obtained; however, in the next stage of the protocol development it was decided to test a single-cell kit to investigate its capability to preserve RNA from our FACS-sorted samples. Therefore, sample extraction using the Norgen single cell RNA purification kit followed the cold homogeniser protocol.

5.3.5.1 RNA profile assessment

In this experiment, samples were collected in several media choices within variable collection tubes/plates and the RNA profile for each was assessed, as shown in Figure 5.11.

Figure 5.11 A-B indicates that sample collection in the 96 well plate yielded a higher RNA concentration of 214 pg/µl with a RIN of 2.4, compared to sample collection in an Eppendorf tube sample which produced a yield of 167 pg/µl and undefined RIN value. Conversely, sorting into freshly prepared lysing buffers supplemented with BME within an Eppendorf tube produced a yield of 169 pg/µl, and RIN value of 2.5, compared

to a yield of 110 pg/µl and RIN of 1 for the sample sorted in the same media within a 96 well plate: Figure 5.11 C-D.

Cells sorted into media-A supplemented with NGS, either into a 96 well plate or an Eppendorf tube, displayed a higher RIN value of 4.4 appearing with double ribosomal peaks for the Eppendorf tube, compared to a RIN value of 1.6 for the 96 wells plate: Figure 5.11 E-F. However, the Eppendorf tube had a lower RNA concentration (393 pg/µl) extracted from 500 sorted cells, whereas the 96 well plate sample had an RNA concentration of 411 pg/µl, extracted from only 50 sorted cells.

Interestingly, the effect on RIN values of collecting into the lysing buffer in a 96 well plate has a similar effect to collecting in the lysing buffer plus BME within an Eppendorf tube; however, the second choice has a preferable rRNA ratio of 3.6.

As shown in Table 5.12 E-F: the sample (E) sorted into the media-A plus NGS from a lower cell number had a slightly higher RNA concentration, higher rRNA ratio, and lower RIN values, in comparison with sorting 10x more cells using the same approach.

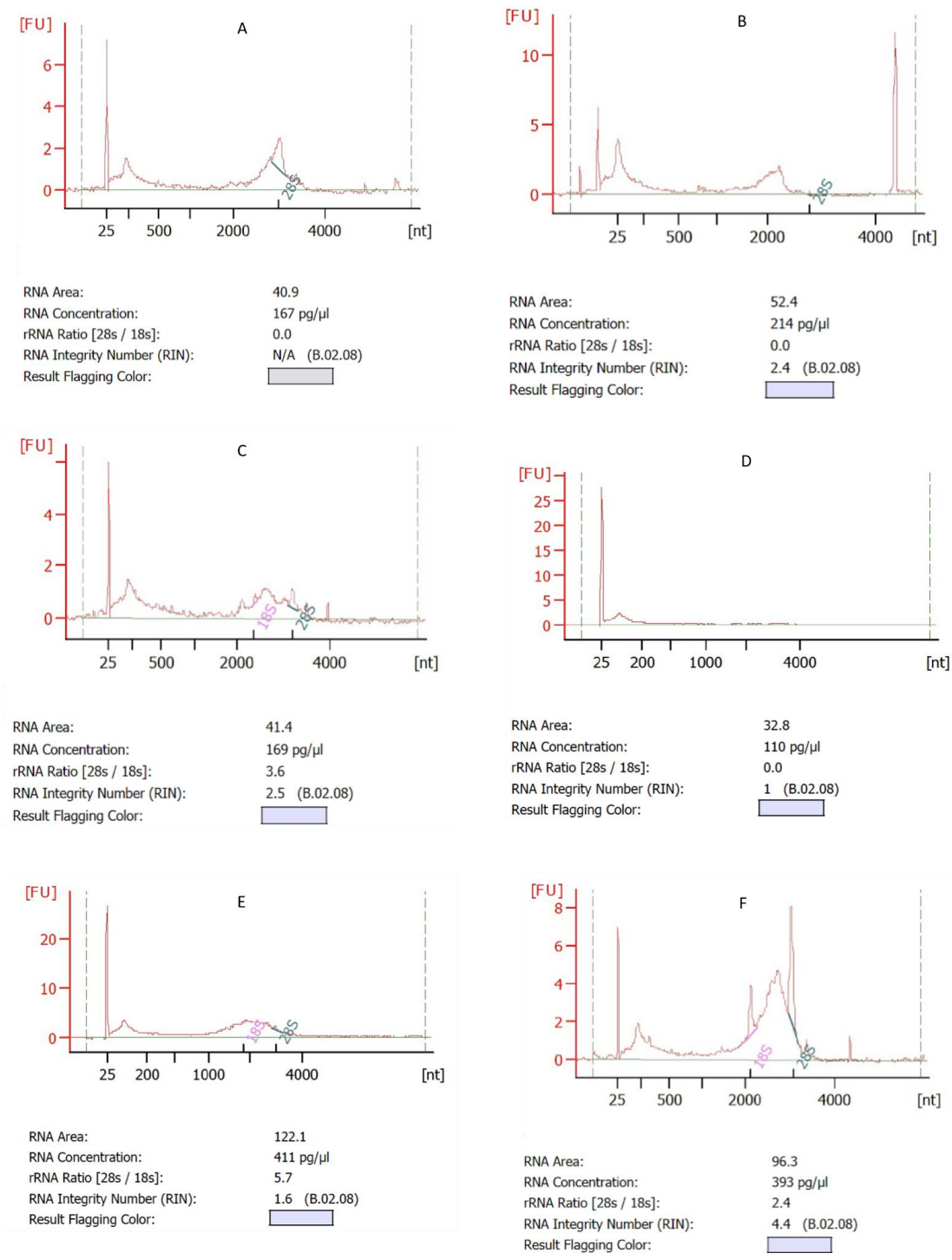

Figure 5.11 - RNA quality assessment for samples homogenised using the cold homogenising protocol and Norgen extraction kit. The graphs are representative of the RNA profiles for cells sorted into (A) lysing buffer within an Eppendorf tube, (B) lysing buffer within a 96 well plate, (C) Lysing buffer supplemented with BME within an

Eppendorf tube, (D) Lysing buffer supplemented with BME within a 96 well plate, (E) cold media-A + NGS within a 96 well plate, (F) cold media-A + NGS within an Eppendorf tube. Among all samples, Sample F has the best RNA profile identified by RIN and rRNA ratio measurements.

Table 5.12 - Summary of findings using the cold homogenising protocol and Norgen extraction kit. Overall, the best results were from collecting samples in cold media-A+NGS in an Eppendorf tube. The mCherry+ cells were obtained from 100 whole embryo. RLT: Lysing buffer

Sample ID	**Number of sorted cells**	**Description**	**RNA con. pg/µl**	**RIN value**	**rRNA ratio**
A	50	RLT within an Eppendorf tube	167	n/a	0
B	50	RLT within a 96 well plate	214	2.4	0
C	50	RLT + BME in an Eppendorf tube	169	2.5	3.6
D	50	RLT + BME in a 96 well plate	110	n/a	0
E	50	cold media-A + NGS in a 96 well plate	411	1.6	5.7
F	500	cold media-A + NGS in an Eppendorf tube	393	4.4	2.4

5.3.5.2 Confirmation of the protocol reliability within a reasonable sorting period

The identified optimal sorting conditions (Sorting 500 cells into 1.5 ml Eppendorf tube containing media-A supplemented with NGS) were then repeated twice to confirm the reproducibility of the sorting protocol, using variable sorting periods. For sample 1 (Figure 5.12 A) with a shorter sorting time, 576 pg/µl RNA was obtained from 1,700 cells and had a RIN of 6.1, where the double ribosomal peaks were clearly seen. Sample 2 had a 10 min longer sorting time and higher sorting cell number (5,000 cells), producing a yield of 1,465 pg/µl RNA, with a similar RIN value of 5.9: (Figure 5.12 B and Table 5.13).

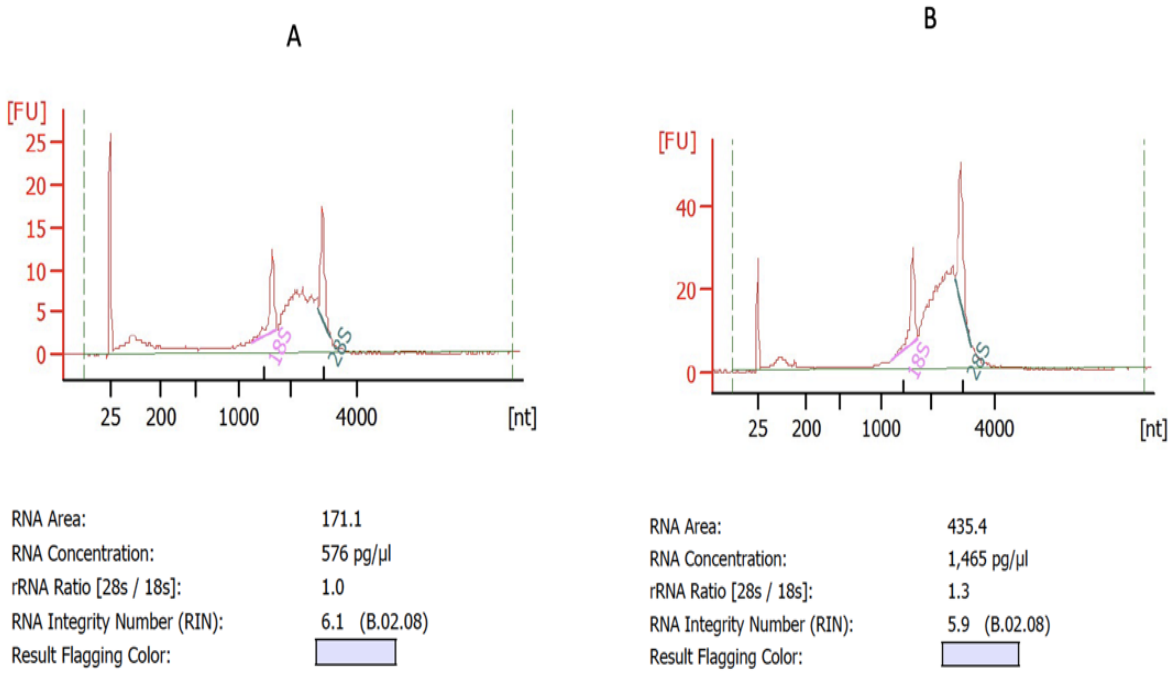

Figure 5.12 - RNA quality assessment for samples homogenised using the cold homogenising protocol and extracted with Norgen kit. The graphs are representative of the RNA profiles for cells sorted into cold media-A + NGS in an Eppendorf tube for total sorted cell counts of (A) 1700 cells and (B) 5000 cells, within 15- and 25-min sorting periods, respectively. The RNA quality recognised by the RIN values and picochip profiles are similar between the two samples.

Table 5.13 - Summary of two replicated samples sorted using the cold homogenising protocol and Norgen extraction kit where the RNA quality and quantity are suitable to proceed with the downstream applications.

Sample number	Description	RNA con. pg/µl	RIN values	rRNA ratio
A	1700 sorted cells within 15 min	576	6.1	1
B	5000 sorted cells within 25 min	1,465	5.9	1.3

5.4 Discussion

It is widely acknowledged that gene expression profiling enables the detailed characterisation of cells/region of interest and enables the non-hypothesis driven identification of key transcriptomic changes which may contribute to disease pathogenesis (Mazzolini et al., 2018, Wali et al., 2022). The popularity of RNA-seq has increased due to its sensitivity and insights into novel transcribed regions, but gene expression profiling in specific CNS populations in zebrafish remains challenging (Loontiens et al., 2019). In this chapter, a robust protocol for isolating mCherry cells from zebrafish was established, which enabled sufficient high-quality RNA to be obtained which is suitable for downstream transcriptomic analysis. Various parameters were optimised to achieve this goal, including experimental temperature, number of sorted cells, collection media/collection tubes, and RNA extraction kits. The optimal protocol identified involved preparing the samples using a cold homogeniser protocol, sorting cells into media-A supplemented with NGS, and extracting RNA using a lysing buffer supplemented with BME. Furthermore, the optimal duration of the sorting period was 25 minutes, with the extraction carried out immediately using the Norgen single-cell extraction kit.

5.4.1 For microglial gene expression, it is recommended to obtain the samples using the cold protocol over the liberase homogenising protocol

The gene expression profile of microglia and macrophages is highly dependent on their microenvironment (Mazzolini et al., 2018). The dissociation step of the liberase homogenising protocol is performed at 37°C, which likely influences the gene expression profile in response to the experimental conditions (Mazzolini et al., 2018) as normal fish temperature is 28.5°C. Therefore, the current study employed the cold homogenising protocol which aimed to keep the sample at 4°C during the entire process up to the RNA extraction step, thus slowing down the cellular processes and metabolic activities, and minimising potential impacts on gene expression profiles that might occur during the process (Mazzolini et al., 2018). Hence, the transcriptomic analysis of the sorted cells is more likely to accurately reflect the pathological condition rather than changes that have occurred during the preparation process.

Another advantage of the cold homogenising protocol over the liberase procedure is its ability to preserve cell viability within the sample suspension. In the current study, around one quarter of the cells were lost during the enzymatic homogenising process in which larvae were dissociated using the liberase enzyme that required incubation at temperatures up to 37°C, as opposed to less than one-tenth of cells that were lost during the cold homogenising preparation that was conducted at 4°C. It also suggests the remaining cells may be less “stressed”.

5.4.2 How the optimised protocol compares to other studies

The media used to collect sorted cells is crucial in obtaining adequate high-quality RNA for downstream applications such as RNA-seq; however, the choice of the collection media is controversial. Some studies suggest that sorting-based isolation of fluorescent cells induces a stress response and cells need time to recover; therefore, sorting the cells directly into lysis buffer is not recommended (Rosental, 2017). In contrast other studies suggest collecting a small number of cells directly into the lysing buffer ensures cell lysis, protects the RNA from being degraded, and has been shown to result in a yield of high-quality RNA (Loontiens et al., 2019). In a transgenic zebrafish study, sorting fluorescent reporter cells directly into the RNeasy plus micro kit lysing buffer has successfully yielded high quality RNA. Furthermore, sorting directly into the RNeasy Micro Kit lysis buffer has been employed to extract RNA from up to 75,000 sorted cells (Loontiens et al., 2019). In our hands, however, sorting a high number of cells has not improved the yield RNA.

Subsequent optimisation steps focused on the usage of the co-extracters in the lysis buffer, including BME and DTT, to aid the extraction of high-quality RNA material (Mommaerts, 2015). The effectiveness of BME in the extraction process of zebrafish samples has been verified in several successful studies (Mazzolini et al., 2018, Wali et al., 2022, Cosacak et al., 2020, Peterson, 2009, Mazzolini, 2020). BME serves as a reduction agent and is used in the RNA isolation process to prevent the degradation of RNA. BME acts by eliminating the ribonucleases released during cell lysis and reduces the disulfide bonds that stabilise the ribonucleases enzymes and denature the proteins (Yee, 2018).

Both BME and DTT preserve RNA quality by reducing its degradation (Yee, 2018); however, DTT is often more preferable due to the high volatility of BME, which has severe health risks for researchers (Mommaerts, 2015, He, 2017). In an RNA extraction comparison study, the effectiveness of using DTT over BME was tested (Mommaerts, 2015). The study was conducted using two approaches; firstly, evaluating the yield and quality of RNA, and secondly running an assay to measure the RNase activity after using each reducing reagent. The study concluded that DTT is more effective in deactivating the RNases activity than BME (Mommaerts, 2015), conflicting with the current study which indicates that increased yields of RNA are obtained when BME is added to the lysis buffer compared to DTT.

In the current project, it was noticed that cells sorted directly into the NGS supplemented media-A produced acceptable RNA profile samples for downstream application, compared to the cells sorting directly into a lysis buffer, either solely or supplemented with co-extractors.

In addition to optimising the collection media, the impact of collecting the cells into either the traditional choice 1.5 ml Eppendorf tube or a 96 well flat-bottomed plate was also compared. From the literature, the 96 well flat-bottomed plate has been successfully employed in cell sorting experiments for either single cells or a low number of sorted cells (Wineberg, 2020, Gao, 2021). From the literature also, the 1.5 ml Eppendorf tubes were used in successful sorting experiments (Mazzolini et al., 2018). From the current study, sorting in 1.5 ml Eppendorf tubes appears to improve the quality and the yield of RNA.

Both the temperature and duration of sorting impacts on the quality and quantity of the RNA obtained, where a shorter sorting period preserves higher yield and quality (Tsinkalovsky, 2005, Yamada, 2010). The current study is consistent with this, as when the sorting period is increased to collect a greater number of cells, the RNA quantity decreases, and recommends a maximum sorting period of 25 mins.

Having optimised several aspects of the original cold homogenising protocol the next step was to compare RNA extraction kits. The Qiagen RNAeasy plus micro extraction kit has been shown to provide high-quality RNA from low numbers of FACS sorted transgenic zebrafish cells (Loontiens et al., 2019, Mazzolini et al., 2018). One main difference between the two Qiagen extraction kits used in the present study (Qiagen RNAeasy plus micro kit and the Qiagen RNAeasy micro kit) was that the RNeasy Plus kit contains gDNA eliminator columns as a replacement for the DNase I (lyophilised) step, aiming to preserve RNA quality while avoiding digestion of the DNA. This was found to improve the RNA quality for RNA-seq (Loontiens et al., 2019). Despite multiple studies supporting the Qiagen RNAeasy plus micro extraction kit, in the current study the kit resulted in a degradation profile of the yield RNA. As a further alternative, a kit used for single-cell experiments was tested, as kits used for single cell sequencing where material is even more limited might improve the yields and quality. The Norgen single-cell extraction kit was chosen, as it has been reported to be commonly used to extract RNA from small cell numbers which is suitable for transcriptomic profiling (Ogawa, 2021, Biagini, 2022, Crilly, 2021, Potter, 2019, Voigt, 2021). In the current study, utilising the

Norgen single-cell extraction appears to improve the yield and the quality of the obtained RNA samples.

A summary of the media choices used in the current project and their justifications are outlined in Table 5.14.

Table 5.14 - Summary of media choices (and the usage justifications) used for optimising the two-homogeniser protocol. Successful protocol is written in green.

<table>
<tr><th>Sample homogenising protocol</th><th>mCherry+ cells sorted into</th><th>Lysing solution</th><th>Reason</th><th>Extraction kit</th></tr>
<tr><td>liberase homogenising protocol</td><td colspan="2">cold live sorting buffer</td><td>Sorting-based isolation of fluorescent cells induces a stress response that negatively affects the quantity & quality of RNA. Therefore, it is advised to sort into media prior to the lysing step</td><td>Qiagen RNAeasy micro kit</td></tr>
<tr><td rowspan="4">cold homogenising protocol</td><td colspan="2">RLT

L RLT +BME/DTT</td><td>sorting directly into the lysing buffer preserves RNA better than the sorting media

Supplementing the lysing buffer with co-extracters yields good-quality RNA</td><td>Qiagen RNAeasy micro kit</td></tr>
<tr><td rowspan="3">cold media-A supplemented with 2%NGS</td><td>RLT +BME</td><td>The approach was used successfully in isolating high-profile RNA samples from sorted microglia (Mazzolini et al., 2018)</td><td rowspan="3">Qiagen RNeasy plus micro kit
And
Norgen single cell RNA purification kit</td></tr>
<tr><td>RLT +DTT</td><td>To compare the use of the co-extracter DTT rather than BME under the current experimental conditions</td></tr>
<tr><td>RLT</td><td>To test if adding co-extracter supplements makes any serious difference to the extracted RNA samples</td></tr>
</table>

5.4.3 The challenges and benefits of RNA-seq

Zebrafish are an important animal model for studying a range of human diseases. In order to understand the molecular characteristics of certain cell types within the model, the cells of interest first need to be isolated (Cosacak et al., 2020, Bates et al., 2016). FACS enables the isolation of specific cell populations from transgenic zebrafish lines according to their fluorescent phenotype (Mazzolini et al., 2018, Liao et al., 2016). RNA can then be extracted from the sorted cells and used for downstream applications, including gene expression analysis.

The major challenges of performing RNA-seq on samples isolated from zebrafish are the cell isolation process and RNA extraction (Shi et al., 2021). The challenge is increased when sorting a low number of cells within a heterogeneous population, as the FACS recovery rate of ~70% may result in losing a large proportion of the cells of interest (Liao et al., 2016). Despite the challenges faced during the isolation and sequencing of zebrafish samples, the benefits of RNA-seq are numerous. Due to the high orthology between human and zebrafish (Loontiens et al., 2019), the comparative transcriptomics studies between the two species adds to our understanding of the pathogenesis of a variety of diseases (Mazzolini et al., 2018).

5.5 Summary of the major findings

The current study details an optimised procedure to isolate mCherry cells from zebrafish and extract RNA of suitable quality for RNA-seq analysis. It is, however,

unfortunate that while this study developed an optimal protocol for the isolation and mRNA extraction from mCherry^{+} cells, no actual experiment comparing the gene profile expression between the *vhl*$^{-/-}$ mutant and wildtype sibling was conducted. The project was not completed within the study period due to delays resulting from the COVID pandemic that have affected progress and access to FACS facilities.

Chapter 6 **General Discussion**

6.1 Major findings and future work

Age-associated WML are a common feature of the ageing brain, which appear as hyperintensities on MRI scans. Depending on their anatomical location, WML can be classified as either periventricular or deep subcortical WML with PVL occurring in around 90% of the individuals over the age of 65 and DSCL occurring in around 60% of the ageing population (Fernando et al., 2004a, Simpson et al., 2007). Large-scale population-based studies have shown that DSCL are associated with cognitive decline and depression, and may be a risk factor for the progression of mild cognitive impairment to dementia (Fernando et al., 2004b, Hu et al., 2021). Based on previous histological studies, DSCL are associated with chronic cerebral hypoperfusion and hypoxia, and the microglia within the DSCL have a phagocytic profile characterised by their large amoeboid morphology and positive immunoreactivity for CD68 (Simpson et al., 2007, Waller et al., 2019). However, detailed characterization of the microglia is lacking in the literature. Therefore, the current study tested the hypothesis that, and under the effect of chronic hypoxia, microglia adopt an M1 phenotype in both age-associated DSCL and the surrounding NAWM. This hypothesis was tested in post-mortem tissue and the *vhl*$^{-/-}$mutant zebrafish, which display sustained activation of the HIF pathway.

In support of previous studies, DSCL were histologically characterized by demyelination and high levels of CD68^{+} amoeboid microglia, while in contrast control and NAWM cases displayed intact myelin and low levels of CD68^{+} cells with a smaller, ramified

morphology (Waller et al., 2012, Simpson et al., 2007). Interestingly, the histological evaluation of three cases did not agree with the consultant radiologists Schelten's rating for the contralateral hemisphere; evidencing the asymmetry of the DSCL, and highlighting the need for detailed histological evaluation of the cases before experimental interrogation.

Similar to the microglial profile observed in DSCL, the microglial morphology observed in the *vhl*$^{-/-}$ zebrafish suggest that sustained activation of the HIF pathway drives microglia to adopt an amoeboid phenotype. Interestingly, at 7 dpf, and in addition to the microglia adopting an activated morphology, the total number of microglia was significantly elevated, similar to the microglia profile seen within the post-mortem DSCL. These initial findings suggest that the *vhl*$^{-/-}$ zebrafish may be a biologically relevant model to investigate the impact of sustained activation of the HIF pathway on the microglial phenotype. However, it should be emphasized that this is not a model of age-associated WML and any extrapolation of the findings should always be interpreted with caution and validated rigorously.

Transcriptomic profiling enables the gene expression profile of samples to be assessed, potentially identifying novel biologically relevant mechanisms associated with disease pathogenesis. In the current study, the transcriptomic profile of LCM-ed microglia from age-associated DSCL, NAWM and control WM cases were assessed using RNA-seq and microarray. In our hands, RNA-seq was found to be incompatible with the immuno-LCM-ed post-mortem material.

Bioinformatic analysis of the microarray data revealed a neuroprotective antioxidant role for microglia within the DSCL, while microglia within the surrounding NAWM adopt a neurotoxic profile, likely contributing to the progression of lesion pathology. While the limited validation studies support the array findings, further work is required to explore the candidates identified in this study in more detail. In addition to the antibody panel used for the validation, a comprehensive study using an extensive panel of microglial markers should be employed to enable a detailed characterisation of the M1/M2 immunoreactive profile. In particular future work should aim confirm the neuroprotective profile associated with DSCL focussing on assessing the immunoreactive profile of the M2 markers CCL22 and the Mannose receptor expression. Furthermore, the M1 profile of microglia in the NAWM should be validated by extending the study to include the M1-associated markers CD74, CD40, and CCR7. Furthermore, dual labelling IHC could be performed with these markers to better examine understand the association of microglial phenotype with cerebral hypoxia and BBB dysfunction.While the post-mortem study identified a potential role for the microglia in the pathogenesis of DSCL, the data are focused on established WML and do not identify the mechanism(s) by which the lesions arise. Visualising real-time changes in human microglial phenotypes is challenging, necessitating the use of appropriate animal models for earlier stages of investigation. The zebrafish larva is a robust and reliable model employed to study the microglial response to various stimuli. The model's popularity is based on the optical transparency of the fish's body, its genetic accessibility, and ease of pharmacological manipulation (Bradford et al., 2017, Chakraborty et al., 2009).

To determine whether the *vhl*$^{-/-}$ microglia adapt a neurotoxic or neuroprotective phenotype in response to sustained HIF signalling, we planned to optimize a robust protocol to isolate microglia from zebrafish and assess their transcriptomic profile. While the current study established a reproducible sorting protocol that provides a suitable yield and quality of RNA, sufficient for downstream applications such as RNAseq, unfortunately transcriptomic profiling could not be performed due to the labs closing and then restricted access during the COVID-19 pandemic.

It should also be noted that the *mpeg1::mCherry* transgenic line labels both microglia and macrophages, therefore future studies should be undertaken using microglial-specific antibodies, such as 4C4. This would enable the specific isolation of microglia as opposed to the isolation of a mixed population of mCherry-positive macrophages and microglia. Future studies comparing the transcriptomic profile of *vhl*$^{-/-}$ microglia to those isolated from DSCL could potentially determine if the *vhl*$^{-/-}$ zebrafish is a potential biologically relevant model to study the microglial response to hypoxia. If the microglial response to hypoxia across the two species is found to be similar, future studies should aim to utilise the *vhl*$^{-/-}$ zebrafish to identify potential therapeutic targets to manipulate microglia to adapt a neuroprotective phenotype within NAWM in response to chronic hypoxia.

6.2 Study Limitations

While the post-mortem study has added to our understanding of the role of microglia in the pathogenesis of DSCL several limitations of this study should be acknowledged.

The histological characterisation and the transcriptomic profile were conducted on twelve samples, four cases per study group. It is widely recognized that transcriptomic profiling should be conducted using a minimum of twelve samples per group (Schurch et al., 2016).

In addition to assessing the immunoreactive profile of CD68, the current study would benefit from characterizing a more extensive panel of microglial markers including the M1 associated markers CD74, CD40, and CCR7 (Peferoen et al., 2015); and the M2 associated markers CCL22 and Mannose receptor (Peferoen et al., 2015).

The initial study design was to compare the gene expression profile of microglia across the three WM groups using RNA-seq. RNA-seq is sensitive to RNA quality, and in the current study was an unsuitable approach to assess the transcriptome of microglia isolated by immuno-LCM. In contrast, microarray analysis did enable the transcriptomic profile of immuno-LCM isolated microglia to be successfully assessed. Nevertheless, it should be acknowledged that microarrays have their own limitations. Microarrays require probes for gene expression detection; hence, they only detect known sequences. Furthermore, this high-throughput, low-cost approach is less accurate and has a lower sensitivity compared to RNA-seq (Rao et al., 2019).

The candidate gene expression changes identified in the microarray analysis were validated using IHC. It should be acknowledged that the same blocks are used for both

the microarray analysis and validation. A more robust validation study on an extended cohort is required to increase confidence in the differential expression of the candidates.

With the numerous factors supporting the usage of the *vhl*$^{-/-}$ zebrafish as a model to study the impact of sustained HIF signalling on the microglial phenotype, there are limitations to using this model, which should be acknowledged. Firstly, zebrafish are able to regenerate complex tissue structures, including neural tissue within the CNS (Kanagaraj et al., 2020, Ghosh and Hui, 2016). Secondly, the *vhl*$^{-/-}$ zebrafish model used in the current study only models one aspect of DSCL, the sustained activation of the HIF pathway.

Further, the neural damages associated with ischemia generate reactive astrogliosis processes within higher vertebrates. This process is activation of astrocytes responding to CNS damage, leading to accumulating and proliferating astrocytes in the injured region (Sofroniew, 2009), whether this is beneficial or can be maladaptive, is debated. The astrocyte accumulation leads to glial scar, which barricades the proliferation, migration and survival of neural and glial progenitor cells. The process will, eventually, prevent the repair of white matter and neurogenesis and contribute to the occurrence of diseases (Sofroniew, 2015). Lower vertebrates, however, have different responses to neural death and axonal damage. In zebrafish, it was found that neural inflammation triggers the production of the inflammatory mediating leukotriene molecules (Kyritsis et al., 2012). These molecules, in turn, activate the radial glial cell proliferation, instead of producing a glial scar, which allows neurogenesis to follow, which can lead to true regeneration. Both reactive astrocyte and astrogliosis are common features observed in WML but are not clearly seen in zebrafish (Fernando et al., 2006,

Scheltens et al., 1995). Accordingly, zebrafish might lack the ability to represent the full range of pathology observed in WML. It might be beneficial to study the effect of chronic exposure to hypoxic signalling on astrocyte phenotype in zebrafish by utilising labelled astrocytes in similar experiments to the current research. However, while there are limitations, the current findings suggest that this is a valuable model which could greatly benefit future research into the microglial response to hypoxia/sustained HIF activation.

Appendix

Appendix I

CFAS
Cognitive Function & Ageing Study

FOR CFAS OFFICE USE

Tissue request no.

AUTHORISATION TO USE TISSUE FROM THE COGNITIVE FUNCTION AND AGEING STUDY (CFAS) BIOLOGICAL RESOURCE

FOLLOWING CONSIDERATION BY THE CFAS MANAGEMENT COMMITTEE (CMC) AND BIOLOGICAL RESOURCE ADVISORY COMMITTEE (BRAC):

Study Title: Hypoxia-induced changes in astrocytes and their role in the formation of age-associated white matter lesions

Head of proposed study

Title: Dr

Name: Julie Simpson

Investigators: Ms Taghreed Almansouri, Prof Steve Wharton, Dr Freek van Eeden, Dr Paul Heath

Organisation: University of Sheffield
Address: Sheffield Institute for Translational Neuroscience, 385A Glossop Road, Sheffield, S10 2HQ

Telephone No: 0114 222 2242 Fax No: 0114 222 2290

Email: Julie.simpson@sheffield.ac.uk

CFAS TISSUE REQUEST NUMBER: **16/11**

This project was reviewed by both CMC and BRAC committees and approval was given to release the requested tissue under the following REC approval:

Title of Ethical application: Cognitive Function and Ageing Studies: Diabetes, Defective Nutrient Signalling and Dementia: an Epidemiological Neuropathology approach.

REC No: 15/SW/0246
IRAS No: 184134

Professor Carol Brayne
Chief Investigator CFAS

Date: 09/11/2018

CFAS Tissue Approval / Version1.0, February 2017

Appendix II

Differentially expressed genes identified using DAVID analysis

These tables represent the differentially expressed genes identified in the transcriptomic profile of deep subcortical white matter.

DSCL compared to Control

Gene Symbol	Description	Fold Change	P-val
RNF185	Transcript Identified by AceView, Entrez Gene ID(s) 91445	-2.24	0.0007
CFAP70	cilia and flagella associated protein 70	-2.68	0.0016
MFSD1	major facilitator superfamily domain containing 1	1.85	0.0016
SPDYE5	speedy/RINGO cell cycle regulator family member E5	-2.35	0.0045
ITGA5	integrin alpha 5	1.85	0.0046
SLC22A3	solute carrier family 22 (organic cation transporter), member 3	2.87	0.0054
HBB	hemoglobin, beta	9.26	0.0056
KMT5B	lysine (K)-specific methyltransferase 5B	-2.33	0.0064
TMEM2	transmembrane protein 2	1.8	0.0075
MARVELD2	MARVEL domain containing 2	2.23	0.0076
MIR6809; TNS1	microRNA 6809; tensin 1	2.72	0.0079
INTS5	integrator complex subunit 5	-2.04	0.008
SEL1L	sel-1 suppressor of lin-12-like (C. elegans)	-2.12	0.0083
DDX1	DEAD (Asp-Glu-Ala-Asp) box helicase 1	2.38	0.0088
PRKY	protein kinase, Y-linked, pseudogene	1.84	0.0092
GPC6	glypican 6	-1.7	0.0093
C6orf183	chromosome 6 open reading frame 183	-2.54	0.0095
EPN3	Transcript Identified by AceView, Entrez Gene ID(s) 55040	-3.03	0.0098
SPG7	spastic paraplegia 7 (pure and complicated autosomal recessive)	-1.96	0.01
GINM1	glycoprotein integral membrane 1	2.71	0.01
OMP	olfactory marker protein	-1.89	0.0101
CTNNA1	catenin (cadherin-associated protein), alpha 1	2.9	0.0107
GNPAT	glyceronephosphate O-acyltransferase	1.67	0.0117
SGEF	Transcript Identified by AceView, Entrez Gene ID(s) 26084	-2.34	0.0118
PMP2	peripheral myelin protein 2	2.08	0.0122
TRIM66	tripartite motif containing 66	-1.71	0.0126
E2F4	E2F transcription factor 4, p107/p130-binding	2.58	0.0129
SLC38A5	solute carrier family 38, member 5	2.4	0.0132
KLHL7	kelch-like family member 7	2.2	0.0142
CXorf40A	chromosome X open reading frame 40A	-1.62	0.0143
TAF15	Transcript Identified by AceView, Entrez Gene ID(s) 8148	-2.24	0.0147
HECTD2	Transcript Identified by AceView, Entrez Gene ID(s) 143279	-1.74	0.0148
TMCC2	transmembrane and coiled-coil domain family 2	2.25	0.0152
CFLAR	CASP8 and FADD like apoptosis regulator	2.53	0.0154
STXBP3	syntaxin binding protein 3	1.73	0.0155
BBOF1	basal body orientation factor 1	-1.84	0.0157
HBA2	hemoglobin, alpha 2	2.76	0.0164
ZNF516	zinc finger protein 516	-2.47	0.0164
FKBP7	FK506 binding protein 7	1.62	0.0165
ZNF587	zinc finger protein 587	-1.86	0.0165
RGMB	repulsive guidance molecule family member b	-1.45	0.0168
CLASP2	Transcript Identified by AceView, Entrez Gene ID(s) 23122	2.14	0.0179
PRTG	protogenin	1.51	0.0189
SERPINF1	serpin peptidase inhibitor, clade F (alpha-2 antiplasmin, pigment epithel	2.09	0.019
SHC4	SHC (Src homology 2 domain containing) family, member 4	1.9	0.019
ABCC9	Transcript Identified by AceView, Entrez Gene ID(s) 10060	-2.48	0.0192
FXYD7	FXYD domain containing ion transport regulator 7	-1.67	0.0192

COBLL1	cordon-bleu WH2 repeat protein like 1	1.89	0.0194
ELMOD2	ELMO/CED-12 domain containing 2	2.84	0.0202
TRMT1L	tRNA methyltransferase 1 like	1.62	0.0203
PSMC4	proteasome 26S subunit, ATPase 4 [Source:HGNC Symbol;Acc:HGNC:9551]	-1.45	0.0205
CYFIP2	cytoplasmic FMR1 interacting protein 2	-2.2	0.0206
ISY1	ISY1 splicing factor homolog	-1.63	0.0212
TBC1D3B; TBC1D3	TBC1 domain family, member 3B; TBC1 domain family, member 3H; TBC1 domain family, member 3I; TBC1 domain family, member 3F	-1.97	0.0213
TRAF3	TNF receptor-associated factor 3	1.72	0.0219
SLC38A11	solute carrier family 38, member 11	3.13	0.0221
HSD17B2	hydroxysteroid (17-beta) dehydrogenase 2	-1.66	0.0222
CYP2C8	cytochrome P450, family 2, subfamily C, polypeptide 8	-1.51	0.023
FBXO6	F-box protein 6	-1.6	0.0233
C1GALT1C1	C1GALT1 specific chaperone 1	1.91	0.0236
NIPSNAP3A; NIPSN	nipsnap homolog 3A (C. elegans); nipsnap homolog 3B (C. elegans)	1.59	0.0239
TRGJ1; TRGC2; TRC	T cell receptor gamma joining 1; T cell receptor gamma constant 2; T cell receptor gamma joining 2; T cell receptor gamma variable 9	2.83	0.0248
CEP95	centrosomal protein 95kDa	-1.43	0.025
TRIM16	tripartite motif containing 16	1.76	0.0252
ME2	malic enzyme 2, NAD(+)-dependent, mitochondrial	2.81	0.0252
EIF2D	eukaryotic translation initiation factor 2D	1.86	0.0256
SMARCD1	SWI/SNF related, matrix associated, actin dependent regulator of chromatin, subfamily d, member 1	-1.77	0.0257
CROCC	ciliary rootlet coiled-coil, rootletin	-1.66	0.0258
NET1	neuroepithelial cell transforming 1	2.08	0.0259
GRK4	G protein-coupled receptor kinase 4	-1.34	0.0262
FBXO48	F-box protein 48	-1.5	0.0264
SFXN4	sideroflexin 4	-1.49	0.0265
RPL7A; SNORD36C	ribosomal protein L7a; small nucleolar RNA, C/D box 36C; small nucleolar RNA, C/D box 36B; small nucleolar RNA, C/D box 24; small nucleol	1.63	0.0267
FHL5	four and a half LIM domains 5	2.06	0.0267
DSTYK	dual serine/threonine and tyrosine protein kinase	-1.58	0.0269
ZC3H7B	zinc finger CCCH-type containing 7B	1.64	0.0272
CASP3	caspase 3	-1.94	0.0278
TET3	tet methylcytosine dioxygenase 3	-1.79	0.0284
ZNF607	zinc finger protein 607	-2.1	0.0284
LY75-CD302; CD30	LY75-CD302 readthrough; CD302 molecule; lymphocyte antigen 75	1.7	0.0286
STRADB	STE20-related kinase adaptor beta	1.89	0.0287
GOLGA6L9	golgin A6 family-like 9	-1.67	0.0288
EEPD1	endonuclease/exonuclease/phosphatase family domain containing 1	1.86	0.0291
SEC11A	SEC11 homolog A, signal peptidase complex subunit	1.62	0.0293
RAI2	retinoic acid induced 2	-1.95	0.0294
FAM196A	family with sequence similarity 196, member A	-2.15	0.0303
SLC25A26	solute carrier family 25 (S-adenosylmethionine carrier), member 26	-1.57	0.0307
FGF17	fibroblast growth factor 17	-1.59	0.0308
DUS1L	dihydrouridine synthase 1-like	-1.61	0.0309
PKD2	polycystic kidney disease 2 (autosomal dominant)	2.01	0.0314
PRKD3	protein kinase D3	1.94	0.0315
YTHDF1	YTH N(6)-methyladenosine RNA binding protein 1	-1.46	0.032
SF3A2	splicing factor 3a subunit 2	-1.75	0.032
ACP6	acid phosphatase 6, lysophosphatidic	1.59	0.0322
THTPA	thiamine triphosphatase	2.54	0.0325

FOXN3	forkhead box N3	1.74	0.0327
FAM134B	family with sequence similarity 134, member B	1.67	0.0327
APIP	APAF1 interacting protein	2.01	0.0327
CREM	cAMP responsive element modulator	2.78	0.0335
PNPLA8	patatin-like phospholipase domain containing 8	3.09	0.0336
CMTM3	CKLF-like MARVEL transmembrane domain containing 3	-1.4	0.0338
CASP8AP2	caspase 8 associated protein 2	3.21	0.034
NKX6-2	NK6 homeobox 2	1.76	0.034
DHX38	DEAH (Asp-Glu-Ala-His) box polypeptide 38	1.71	0.0341
CFL2	cofilin 2 (muscle)	2.23	0.0341
TNFSF13	tumor necrosis factor (ligand) superfamily, member 13	-1.35	0.0342
LOC389834; AL354	ankyrin repeat domain 57 pseudogene	-1.55	0.0343
SLC16A1	solute carrier family 16 (monocarboxylate transporter), member 1	1.96	0.0345
PYY	peptide YY	-1.49	0.0348
OS9	osteosarcoma amplified 9, endoplasmic reticulum lectin	1.88	0.035
ZACN	zinc activated ligand-gated ion channel	-1.56	0.0351
PTPN13	Transcript Identified by AceView, Entrez Gene ID(s) 5783	1.8	0.0351
MYL9	myosin light chain 9	1.96	0.0352
SPDYE1	speedy/RINGO cell cycle regulator family member E1	-1.67	0.0357
CC2D2B	coiled-coil and C2 domain containing 2B	-2.98	0.0358
TNFRSF25	tumor necrosis factor receptor superfamily, member 25	-2.28	0.0362
PDSS2	prenyl (decaprenyl) diphosphate synthase, subunit 2	-1.84	0.0366
DSCC1	DNA replication and sister chromatid cohesion 1	1.41	0.0368
ZNF334	zinc finger protein 334	-2.13	0.0368
TBC1D3L; TBC1D3E	TBC1 domain family, member 3L; TBC1 domain family, member 3E	-1.85	0.037
CMKLR1	chemerin chemokine-like receptor 1	1.77	0.0373
CFAP47	cilia and flagella associated protein 47	-2.02	0.0374
GALR1	galanin receptor 1	1.89	0.0376
SOX9	SRY box 9	-1.79	0.0377
PDCD2L	programmed cell death 2-like	-2.03	0.0383
SLC6A8	solute carrier family 6 (neurotransmitter transporter), member 8	1.55	0.0391
LRRC17	leucine rich repeat containing 17	-1.71	0.0396
CHMP7	charged multivesicular body protein 7	-1.48	0.0402
TMLHE	trimethyllysine hydroxylase, epsilon	1.99	0.0404
TMEM59	transmembrane protein 59	1.99	0.0409
DYNLRB2	dynein, light chain, roadblock-type 2	-1.48	0.041
NVL	nuclear VCP-like	-1.65	0.0412
ALOXE3	arachidonate lipoxygenase 3	-1.62	0.0412
PFN2	profilin 2	2.31	0.0414
TMPRSS5	transmembrane protease, serine 5	2.35	0.0416
XRN1	5-3 exoribonuclease 1	1.69	0.0417
MUL1	mitochondrial E3 ubiquitin protein ligase 1	-1.32	0.0419
PCSK7	proprotein convertase subtilisin/kexin type 7	-1.57	0.042
OPRK1	opioid receptor, kappa 1	-1.67	0.042
ARHGAP17	Memczak2013 ALT_ACCEPTOR, ALT_DONOR, coding, INTERNAL, intronic bes	2.61	0.0421
RUNX1	runt-related transcription factor 1	-1.68	0.0422
ZNF503	zinc finger protein 503	1.41	0.0424
ANKRD46	ankyrin repeat domain 46	1.82	0.0424

MCAM; MIR6756	melanoma cell adhesion molecule; microRNA 6756	1.27	0.0426
DHFR	dihydrofolate reductase	1.41	0.0433
ACAA2	acetyl-CoA acyltransferase 2	1.66	0.0433
SALL1	spalt-like transcription factor 1	1.65	0.0436
HBA1	hemoglobin, alpha 1	2.48	0.044
SLC12A8	solute carrier family 12, member 8	-2.1	0.0441
SERTAD4	SERTA domain containing 4	2.24	0.0441
GTPBP1	GTP binding protein 1	-1.59	0.0446
TTC28	Jeck2013 ALT_ACCEPTOR, ALT_DONOR, coding, INTERNAL, intronic best tra	-1.68	0.0447
CATSPER3	cation channel, sperm associated 3	-2.08	0.045
TSSK3	testis-specific serine kinase 3	-1.9	0.0452
DRC3	dynein regulatory complex subunit 3	-1.79	0.0453
TMEM135	transmembrane protein 135	1.97	0.0454
MRPL49	mitochondrial ribosomal protein L49	-1.41	0.0456
FCHSD1	FCH and double SH3 domains 1	-1.9	0.0456
NDUFV3	NADH dehydrogenase (ubiquinone) flavoprotein 3, 10kDa	-2.05	0.0461
LRRC39	leucine rich repeat containing 39	-1.49	0.0462
AKR1E2	aldo-keto reductase family 1, member E2	2.67	0.0463
KIF1C	kinesin family member 1C	1.42	0.0464
B4GALT4	UDP-Gal:betaGlcNAc beta 1,4- galactosyltransferase, polypeptide 4	-2.05	0.0466
AZIN2	antizyme inhibitor 2	2.02	0.047
GANC	glucosidase, alpha; neutral C	2.27	0.047
CLASRP	CLK4-associating serine/arginine rich protein	-2.13	0.0471
LIMS2	LIM and senescent cell antigen-like domains 2	1.74	0.0471
MRPS33	mitochondrial ribosomal protein S33	1.83	0.0478
ERMP1	endoplasmic reticulum metallopeptidase 1	1.57	0.0479
CALD1	caldesmon 1	3.34	0.0479
FOXP2	forkhead box P2	-1.73	0.0481
ZNF32	zinc finger protein 32	1.56	0.0483
PIGP	phosphatidylinositol glycan anchor biosynthesis class P	1.91	0.0484
HDLBP	Transcript Identified by AceView, Entrez Gene ID(s) 3069	-1.52	0.0487
CAST	calpastatin	1.59	0.0489
CRB1	crumbs family member 1, photoreceptor morphogenesis associated	-1.71	0.0493
MLLT6	myeloid/lymphoid or mixed-lineage leukemia; translocated to, 6	-1.51	0.0494
FPR1	formyl peptide receptor 1	-2.39	0.0495
NKIRAS2	NFKB inhibitor interacting Ras-like 2	-1.86	0.0496
NUP54	nucleoporin 54kDa	1.68	0.0498
SAV1	salvador family WW domain containing protein 1	1.59	0.05

NAWM compared to Control

Gene Symbol	Description	Fold Change	P-val
SLC38A6	solute carrier family 38, member 6	2.37	0.0012
CFLAR	CASP8 and FADD like apoptosis regulator	2.66	0.0024
FUT9	fucosyltransferase 9 (alpha (1,3) fucosyltransferase)	2.39	0.0024
CHRM4	cholinergic receptor, muscarinic 4	2.4	0.0025
ZNF32	zinc finger protein 32	2.36	0.0029
FLOT2	Memczak2013 ANTISENSE, coding, INTERNAL, UTR3 best transcript NM_004475	-3.83	0.003
P2RX6	purinergic receptor P2X, ligand gated ion channel, 6	-2.21	0.003
ZNF623	zinc finger protein 623	2.1	0.0031
SLC38A5	solute carrier family 38, member 5	2.64	0.0035
TOR1AIP2	torsin A interacting protein 2	1.77	0.0035
SLA	Src-like-adaptor	2.12	0.0043
SPDYE5	speedy/RINGO cell cycle regulator family member E5	-2.2	0.0046
PAIP2; CTB-43	poly(A) binding protein interacting protein 2 [Source:EntrezGene;Acc:51247]; novel transcript	-2	0.0047
EIF2D	eukaryotic translation initiation factor 2D	2.17	0.0047
KMT5B	lysine (K)-specific methyltransferase 5B	-2.41	0.0048
SALL3	spalt-like transcription factor 3	-1.68	0.0048
CLVS1	clavesin 1	3.76	0.0052
CCL14; CCL15	chemokine (C-C motif) ligand 14; chemokine (C-C motif) ligand 15; CCL15-CCL14 readthrough (NMD candidate)	2.45	0.0054
RESP18	regulated endocrine-specific protein 18	2.18	0.0056
TTC12	tetratricopeptide repeat domain 12	-1.93	0.0057
TSSK3	testis-specific serine kinase 3	-2.08	0.0057
KLHL7	kelch-like family member 7	2.06	0.0061
PLEK	pleckstrin	9.25	0.0066
RUNX1T1	runt-related transcription factor 1; translocated to, 1 (cyclin D-related)	1.92	0.0068
PAQR3	progestin and adipoQ receptor family member III	1.88	0.0073
ANP32C	acidic nuclear phosphoprotein 32 family member C	1.53	0.0073
UBE2J2	ubiquitin-conjugating enzyme E2, J2	1.69	0.0075
GNAS	GNAS complex locus	-3.81	0.0078
HOOK3	hook microtubule-tethering protein 3	-2.32	0.0078
SAV1	salvador family WW domain containing protein 1	1.97	0.0079
ICE1	interactor of little elongation complex ELL subunit 1	-3.42	0.0084
HOMER3	homer scaffolding protein 3	-1.71	0.0086
TMLHE	trimethyllysine hydroxylase, epsilon	2.08	0.0087
KCNJ1	potassium channel, inwardly rectifying subfamily J, member 1	2.24	0.0089
TMEM2	transmembrane protein 2	1.68	0.0089
DTX3	deltex 3, E3 ubiquitin ligase	1.78	0.0091
MEIOC	meiosis specific with coiled-coil domain	-2.52	0.0092
SPATS2L	spermatogenesis associated, serine-rich 2-like	-2.7	0.0092
RNF185	Transcript Identified by AceView, Entrez Gene ID(s) 91445	-1.68	0.0092
KMT5A	lysine (K)-specific methyltransferase 5A	-2.35	0.0093
NIF3L1	NIF3 NGG1 interacting factor 3-like 1	1.76	0.0094
LRFN2	leucine rich repeat and fibronectin type III domain containing 2	-2.19	0.0102
LOXHD1	lipoxygenase homology domains 1	2.66	0.0109
IDH1	isocitrate dehydrogenase 1 (NADP+)	-2.11	0.0109
SERTAD4	SERTA domain containing 4	2.18	0.0109
RAB39A	RAB39A, member RAS oncogene family	-1.63	0.0112
ATP11C	ATPase, class VI, type 11C	2.34	0.0115

C11orf58	chromosome 11 open reading frame 58	-1.62	0.0122
ZNF512	Memczak2013 ANTISENSE, coding, INTERNAL, UTR3 best transcript NM_03243	-5.39	0.0123
TMEM108	transmembrane protein 108	-4.32	0.0124
ISCA1	iron-sulfur cluster assembly 1	-1.58	0.0125
FAM161B	family with sequence similarity 161, member B	-1.6	0.013
IGSF21	immunoglobin superfamily, member 21	-2.68	0.0131
WDR35	WD repeat domain 35	2.35	0.0134
SYNGR3	synaptogyrin 3	-1.85	0.0135
PACRG	PARK2 co-regulated	7.37	0.0137
PAQR7	progestin and adipoQ receptor family member VII	1.75	0.0138
DDX27	DEAD (Asp-Glu-Ala-Asp) box polypeptide 27	-2.51	0.0139
TATDN2; GHR	TatD DNase domain containing 2; ghrelin opposite strand/antisense RNA	2.32	0.0142
GINM1	glycoprotein integral membrane 1	2.56	0.0147
RAB40C	RAB40C, member RAS oncogene family	1.47	0.0148
FNBP1L	formin binding protein 1-like	20.89	0.0149
ZACN	zinc activated ligand-gated ion channel	-1.73	0.0151
VGLL3	vestigial-like family member 3	1.68	0.0154
ONECUT2	one cut homeobox 2	2.24	0.0156
UBXN1	UBX domain protein 1	-1.5	0.0157
FRMPD1	FERM and PDZ domain containing 1	3.33	0.0157
CMPK2	cytidine monophosphate (UMP-CMP) kinase 2, mitochondrial	2.67	0.0158
MLH1	mutL homolog 1	6.06	0.016
NIPSNAP3A; N	nipsnap homolog 3A (C. elegans); nipsnap homolog 3B (C. elegans)	1.64	0.0161
CCDC125	coiled-coil domain containing 125	-2.3	0.0161
MFSD9	major facilitator superfamily domain containing 9	2.06	0.0162
OR2D2	olfactory receptor, family 2, subfamily D, member 2	2.02	0.0162
C14orf159	chromosome 14 open reading frame 159	1.49	0.0162
ADAMTS17	ADAM metallopeptidase with thrombospondin type 1 motif 17	-1.91	0.0163
SPDYE2; SPDY	speedy/RINGO cell cycle regulator family member E2; speedy/RINGO cell	-2.33	0.0164
SPDYE2B	speedy/RINGO cell cycle regulator family member E2B	-2.33	0.0164
LIMK1	Memczak2013 ANTISENSE, CDS, coding, INTERNAL best transcript NM_001204	-3.26	0.0164
CCDC110	coiled-coil domain containing 110	1.94	0.0165
FAM168A	family with sequence similarity 168, member A	1.85	0.0165
TMEM38A	transmembrane protein 38A	2.02	0.0171
DNASE2	deoxyribonuclease II, lysosomal	1.63	0.0173
BLMH	bleomycin hydrolase	3.32	0.0185
EML5	Transcript Identified by AceView, Entrez Gene ID(s) 161436	1.83	0.0186
SLC25A28	solute carrier family 25 (mitochondrial iron transporter), member 28	1.5	0.0187
SPDYE1	speedy/RINGO cell cycle regulator family member E1	-1.88	0.0189
ING3	Transcript Identified by AceView, Entrez Gene ID(s) 54556	-1.73	0.019
KIAA1683	Memczak2013 ANTISENSE, CDS, coding, INTERNAL best transcript NM_001145	-2	0.0191
CRB1	crumbs family member 1, photoreceptor morphogenesis associated	-1.76	0.0191
ANKRD50	ankyrin repeat domain 50	1.7	0.0193
CAMKMT	calmodulin-lysine N-methyltransferase	4.65	0.0194
FAM118B	family with sequence similarity 118, member B	1.77	0.0194
PSMC3IP	PSMC3 interacting protein	-1.61	0.0198
MYADM	Memczak2013 ANTISENSE, CDS, coding, INTERNAL best transcript NM_001020	-1.89	0.0202
PUS10	pseudouridylate synthase 10	1.91	0.0203

PEBP1	Memczak2013 ANTISENSE, coding, INTERNAL, UTR3 best transcript NM_002567	-4.87	0.0203
USP17L19	ubiquitin specific peptidase 17-like family member 19	-2.09	0.0204
CDH6	cadherin 6, type 2, K-cadherin (fetal kidney)	3.47	0.0204
TRIM16	tripartite motif containing 16	1.81	0.0204
INTS5	integrator complex subunit 5	-1.72	0.0211
NAV3	neuron navigator 3	-1.61	0.0213
ALG3	ALG3, alpha-1,3- mannosyltransferase	1.6	0.0215
APAF1	apoptotic peptidase activating factor 1	-1.99	0.0217
FAM53B	Memczak2013 ALT_ACCEPTOR, ALT_DONOR, coding, INTERNAL, intronic best transcript NM_0146	-2.08	0.0218
YLPM1	YLP motif containing 1	2.15	0.0218
ZFPL1	zinc finger protein-like 1	1.74	0.0222
SERTAD4	SERTA domain containing 4	1.8	0.0223
DGKZ	diacylglycerol kinase, zeta	1.51	0.0223
ZNF569	zinc finger protein 569	2.05	0.0224
TMTC1	transmembrane and tetratricopeptide repeat containing 1	2.34	0.0226
CCDC14	coiled-coil domain containing 14	1.62	0.0232
CXorf36	chromosome X open reading frame 36	1.69	0.0235
CTNNB1	catenin (cadherin-associated protein), beta 1	2.78	0.0235
KNDC1	kinase non-catalytic C-lobe domain (KIND) containing 1	-1.68	0.0236
EFHC1	EF-hand domain (C-terminal) containing 1	4.34	0.0237
CLEC17A	C-type lectin domain family 17, member A	1.53	0.0241
SPDYE16	speedy/RINGO cell cycle regulator family member E16	-2.54	0.0242
PCDH9	Memczak2013 ALT_ACCEPTOR, ALT_DONOR, coding, INTERNAL, intronic best transcript NM_2034	-1.75	0.0243
KCNQ5	potassium channel, voltage gated KQT-like subfamily Q, member 5	8.09	0.0244
ATP5L2	ATP synthase, H+ transporting, mitochondrial Fo complex subunit G2	-1.96	0.0244
STK19	Homo sapiens serine/threonine kinase 19 (STK19), transcript variant 1, mRNA.; Homo sapiens s	1.64	0.0244
SLC35F3	solute carrier family 35, member F3	17.96	0.0245
NUP210L; MI	nucleoporin 210kDa like; microRNA 5698	-1.88	0.0247
RHOXF2B; RH	Rhox homeobox family, member 2B; Rhox homeobox family, member 2	-2.57	0.0248
LOC1019283	uncharacterized LOC101928327; novel transcript	4.34	0.0249
DENND4A	DENN/MADD domain containing 4A	2.27	0.0261
RSPH10B2	radial spoke head 10 homolog B2 (Chlamydomonas)	-2.25	0.0262
DPP3	dipeptidyl-peptidase 3	-1.4	0.0262
RUFY1	RUN and FYVE domain containing 1	-2.15	0.0263
USF1	upstream transcription factor 1	1.46	0.0263
FMN1	formin 1	-2.42	0.0264
TMEM167A	Transcript Identified by AceView, Entrez Gene ID(s) 153339	-3.37	0.0264
WDR77	WD repeat domain 77	1.4	0.0266
ZNF93	zinc finger protein 93	1.41	0.0266
SMPD3	sphingomyelin phosphodiesterase 3, neutral membrane (neutral sphingomyelinase II)	4.67	0.0266
FAM189B	family with sequence similarity 189, member B	1.64	0.0268
AES	amino-terminal enhancer of split	-1.39	0.0268
RRP15	ribosomal RNA processing 15 homolog	-2.22	0.0268
MLLT3	Jeck2013 ALT_ACCEPTOR, ALT_DONOR, coding, INTERNAL, intronic transcript NM_004529	4.55	0.0269
MVD	mevalonate (diphospho) decarboxylase	1.47	0.027
FAM78A	family with sequence similarity 78, member A	1.6	0.0273
TGDS	TDP-glucose 4,6-dehydratase	1.68	0.0274
SCAP	Memczak2013 ANTISENSE, CDS, coding, INTERNAL best transcript NM_012235	-1.85	0.0274

FOXN3	forkhead box N3	1.89	0.0275
DUSP22	dual specificity phosphatase 22	1.81	0.0275
MAK	male germ cell-associated kinase	-1.86	0.0275
AFF4	Memczak2013 ANTISENSE, CDS, coding, INTERNAL best transcript NM_014423	-2.45	0.0275
CLUAP1	clusterin associated protein 1	-2.03	0.0276
MKNK1	MAP kinase interacting serine/threonine kinase 1	1.66	0.0276
LMAN2L	lectin, mannose-binding 2-like	1.7	0.0277
FAM200A	family with sequence similarity 200, member A	2.39	0.0277
SLC38A11	solute carrier family 38, member 11	2.93	0.0277
BCO2; RPS12I	beta-carotene oxygenase 2; ribosomal protein S12 pseudogene 21	1.83	0.0278
AASS	aminoadipate-semialdehyde synthase	1.62	0.0279
RNF8	ring finger protein 8, E3 ubiquitin protein ligase	-1.95	0.0281
PTBP3	polypyrimidine tract binding protein 3	1.86	0.0282
REV3L	REV3 like, DNA directed polymerase zeta catalytic subunit	1.49	0.0283
USP17L27; US	ubiquitin specific peptidase 17-like family member 27; ubiquitin specific peptidase 17-like family membe	-1.84	0.0284
USP17L28; US	ubiquitin specific peptidase 17-like family member 28; ubiquitin specific peptidase 17-like family membe	-1.84	0.0284
USP17L29; US	ubiquitin specific peptidase 17-like family member 29; ubiquitin specific peptidase 17-like family membe	-1.84	0.0284
USP17L25; US	ubiquitin specific peptidase 17-like family member 25; ubiquitin specific peptidase 17-like family membe	-1.84	0.0284
BCL2	B-cell CLL/lymphoma 2	1.5	0.0284
RNF212	ring finger protein 212	2.16	0.0285
FAM50B	family with sequence similarity 50, member B	1.55	0.0285
HIST1H2BF	histone cluster 1, H2bf	1.57	0.0286
SH3RF2	SH3 domain containing ring finger 2	1.6	0.0291
LYG1	lysozyme G-like 1	1.49	0.0292
LACTB2	lactamase, beta 2	2.29	0.0293
POLE3	polymerase (DNA directed), epsilon 3, accessory subunit	-1.85	0.0294
DMKN	dermokine	5.92	0.0294
PRPH2	peripherin 2 (retinal degeneration, slow)	-1.73	0.0295
INTS7	integrator complex subunit 7	1.59	0.0296
GRIPAP1	GRIP1 associated protein 1	-1.51	0.0296
LHFP	lipoma HMGIC fusion partner	1.89	0.0296
COL24A1	collagen, type XXIV, alpha 1	2.85	0.0296
PLGRKT	plasminogen receptor, C-terminal lysine transmembrane protein	2.11	0.0298
MSH2	mutS homolog 2	2.62	0.0301
PRKY	protein kinase, Y-linked, pseudogene	1.73	0.0301
FGFR1OP	FGFR1 oncogene partner	2.46	0.0303
HDLBP	Transcript Identified by AceView, Entrez Gene ID(s) 3069	-1.57	0.0303
TET3	tet methylcytosine dioxygenase 3	-1.67	0.0304
USP31	ubiquitin specific peptidase 31	1.77	0.0305
SAP30L	SAP30-like	-1.53	0.0306
ZNF131	zinc finger protein 131	3.71	0.0308
SVBP	small vasohibin binding protein	-2.57	0.0308
ZNF286B; FOX	zinc finger protein 286B; forkhead box O3B pseudogene	1.46	0.0309
MMP23B; MM	matrix metallopeptidase 23B; matrix metallopeptidase 23A (pseudogene)	1.47	0.0309
PEX19	peroxisomal biogenesis factor 19	1.66	0.0309
CLASRP	CLK4-associating serine/arginine rich protein	-1.97	0.0312
SMAD3	SMAD family member 3	2.95	0.0314
ZNF229	zinc finger protein 229	1.44	0.0319

ZNF780B	zinc finger protein 780B	3.53	0.0319
ZNF780B	zinc finger protein 780B	3.53	0.0319
OGG1	8-oxoguanine DNA glycosylase	2.51	0.0319
ST5	Transcript Identified by AceView, Entrez Gene ID(s) 6764	-3.44	0.0326
HMGN2	high mobility group nucleosomal binding domain 2	-1.57	0.0327
MAP3K1	mitogen-activated protein kinase kinase kinase 1, E3 ubiquitin protein ligase	1.84	0.033
SLC25A26	solute carrier family 25 (S-adenosylmethionine carrier), member 26	-1.53	0.033
NFXL1	nuclear transcription factor, X-box binding-like 1	1.75	0.0331
SNCG	synuclein gamma	-4.36	0.0334
NYAP2	neuronal tyrosine-phosphorylated phosphoinositide-3-kinase adaptor 2	1.92	0.0336
GAN; MIR472	gigaxonin; microRNA 4720	-1.74	0.0338
SPATA13; C1C	spermatogenesis associated 13; C1q and tumor necrosis factor related protein	1.73	0.0339
SETD3	Transcript Identified by AceView, Entrez Gene ID(s) 84193	1.62	0.034
HSP90B1; MII	heat shock protein 90kDa beta (Grp94), member 1; microRNA 3652	1.74	0.0344
FXYD7	FXYD domain containing ion transport regulator 7	-1.96	0.0344
ATP5H	ATP synthase, H+ transporting, mitochondrial Fo complex subunit D	-1.69	0.0345
SCAMP4; ADA	secretory carrier membrane protein 4; adenosine deaminase, tRNA-specific 3	1.43	0.0348
ZFP64	ZFP64 zinc finger protein	1.79	0.0352
PTH	parathyroid hormone	-4.08	0.0355
Mar-11	membrane associated ring finger 11	-2.68	0.0355
TLR1	toll-like receptor 1	1.57	0.0355
CECR1	cat eye syndrome chromosome region, candidate 1	-1.98	0.0356
CROCC	ciliary rootlet coiled-coil, rootletin	-1.59	0.0361
NKIRAS2	Memczak2013 ANTISENSE, coding, INTERNAL, UTR3 best transcript NM_0010013	-2.35	0.0361
UCP3	uncoupling protein 3 (mitochondrial, proton carrier)	-1.46	0.0362
EBF1	early B-cell factor 1	2.66	0.0362
GRIA4	glutamate receptor, ionotropic, AMPA 4	-2.57	0.0364
MPDU1	mannose-P-dolichol utilization defect 1	1.67	0.0365
IFNAR2	interferon (alpha, beta and omega) receptor 2	2.1	0.0365
ZNF503	zinc finger protein 503	1.49	0.0365
BCL11A	B-cell CLL/lymphoma 11A (zinc finger protein)	2.59	0.0367
TBC1D4	TBC1 domain family, member 4	2.59	0.0369
PHKA2	phosphorylase kinase, alpha 2 (liver)	1.96	0.0369
CDK11B	cyclin-dependent kinase 11B	-2.51	0.0369
AKAP8	A kinase (PRKA) anchor protein 8	-1.65	0.0371
GAS8	growth arrest-specific 8	-1.77	0.0371
CDH8	cadherin 8, type 2	1.51	0.0371
EPHA6	EPH receptor A6	1.72	0.0371
SLC22A3	solute carrier family 22 (organic cation transporter), member 3	2.16	0.0374
OTOF	otoferlin	2.61	0.0375
ZFHX3	zinc finger homeobox 3	1.43	0.0376
INPP5D	inositol polyphosphate-5-phosphatase D	1.28	0.0378
DDX5	Memczak2013 ANTISENSE, CDS, coding, INTERNAL best transcript NM_004396	-2.31	0.0379
FZD3	frizzled class receptor 3	1.44	0.0382
NWD2	NACHT and WD repeat domain containing 2	-1.82	0.0382
EXTL2	exostosin-like glycosyltransferase 2	2.55	0.0382
DYRK1B	dual specificity tyrosine-(Y)-phosphorylation regulated kinase 1B	1.42	0.0383
TSEN2	TSEN2 tRNA splicing endonuclease subunit	1.46	0.0384

FAAP24	Fanconi anemia core complex associated protein 24	-1.56	0.0385
CNR1	cannabinoid receptor 1 (brain)	6.14	0.0385
ARFRP1	ADP-ribosylation factor related protein 1	-1.4	0.0388
CNOT3	CCR4-NOT transcription complex subunit 3	1.63	0.0393
RACGAP1	Rac GTPase activating protein 1	1.99	0.0393
ATXN3	ataxin 3	1.63	0.0393
XRN1	5-3 exoribonuclease 1	1.5	0.0394
BCL7B	B-cell CLL/lymphoma 7B	1.62	0.0394
DIRAS1	DIRAS family, GTP-binding RAS-like 1	-2.55	0.0398
WDR26	Transcript Identified by AceView, Entrez Gene ID(s) 80232	-1.61	0.0401
WDFY2	WD repeat and FYVE domain containing 2	-1.39	0.0401
USP17L28; US	ubiquitin specific peptidase 17-like family member 28; ubiquitin specific peptidase 17	-1.56	0.0403
C14orf177	chromosome 14 open reading frame 177	-2.44	0.0403
TRANK1	tetratricopeptide repeat and ankyrin repeat containing 1	2.52	0.0403
ABCB8	ATP binding cassette subfamily B member 8	1.58	0.0405
CES1P1; CES1	carboxylesterase 1 pseudogene 1; carboxylesterase 1	1.45	0.0405
CXorf40B	chromosome X open reading frame 40B	-1.45	0.0405
LOC1019275	uncharacterized LOC101927572; Memczak2013 ANTISENSE, CDS intronic transcript NM_015526; novel tra	-1.65	0.0405
C19orf44	chromosome 19 open reading frame 44	1.41	0.0406
HABP2	hyaluronan binding protein 2	-1.94	0.0407
C7orf55-LUC7	C7orf55-LUC7L2 readthrough; LUC7-like 2 pre-mRNA splicing factor; chromosome 7 open reading frame 55	-1.36	0.0409
GCNT4	glucosaminyl (N-acetyl) transferase 4, core 2	2.18	0.0409
LTBR	lymphotoxin beta receptor (TNFR superfamily, member 3)	1.78	0.041
ROPN1	rhophilin associated tail protein 1	-1.42	0.0411
ZDHHC1	zinc finger, DHHC-type containing 1	1.5	0.0412
ARHGAP18	Rho GTPase activating protein 18	-1.6	0.0412
PPP1R1A	protein phosphatase 1, regulatory (inhibitor) subunit 1A	3.14	0.0412
OMP	olfactory marker protein	-1.57	0.0413
TIMP4	TIMP metallopeptidase inhibitor 4	-1.79	0.0414
DDX1	DEAD (Asp-Glu-Ala-Asp) box helicase 1	1.52	0.0414
SNRPG	small nuclear ribonucleoprotein polypeptide G	-1.33	0.0415
CRBN	cereblon	-1.93	0.0416
CDHR3	cadherin-related family member 3	2.18	0.0417
CCNI2	cyclin I family, member 2	-2.07	0.0418
PROSER3	proline and serine rich 3	1.7	0.0418
SH3YL1	SH3 and SYLF domain containing 1	1.33	0.0418
GPR87	G protein-coupled receptor 87	-1.78	0.0419
LRP6	LDL receptor related protein 6	1.44	0.0419
MICAL1	Jeck2013 ANTISENSE, coding, INTERNAL, intronic best transcript NM_022765	-3.29	0.042
HMBS	hydroxymethylbilane synthase	-2	0.0423
LINC00092	long intergenic non-protein coding RNA 92	-1.66	0.0424
KCNK2	potassium channel, two pore domain subfamily K, member 2	1.87	0.0426
VSIG1	V-set and immunoglobulin domain containing 1	3.07	0.0427
F11R	F11 receptor	2.28	0.0428
SLC39A13	solute carrier family 39 (zinc transporter), member 13	-1.33	0.0429
NCBP3	nuclear cap binding subunit 3	-1.85	0.043
MDGA2	MAM domain containing glycosylphosphatidylinositol anchor 2	2.65	0.043
EDEM3	ER degradation enhancer, mannosidase alpha-like 3	1.39	0.0431

TAF1C	TATA box binding protein (TBP)-associated factor, RNA polymerase I, C, 110kDa	1.65	0.0432
TSC2	tuberous sclerosis 2	1.76	0.0435
PCLO	piccolo presynaptic cytomatrix protein	2.09	0.0435
PDSS2	prenyl (decaprenyl) diphosphate synthase, subunit 2	-1.82	0.0435
NUDT7	nudix hydrolase 7	1.49	0.0436
NHSL2	NHS-like 2	2.36	0.0437
METTL20	methyltransferase like 20	-1.72	0.0438
SKAP2	src kinase associated phosphoprotein 2	1.94	0.044
LTV1	LTV1 ribosome biogenesis factor	1.41	0.044
PLCB2	phospholipase C, beta 2	1.72	0.0441
PDE3B	phosphodiesterase 3B, cGMP-inhibited	2.05	0.0441
TUBB	tubulin, beta class I	-1.74	0.0442
ZNF732	zinc finger protein 732	2.2	0.0442
USP17L26; US	ubiquitin specific peptidase 17-like family member 26; ubiquitin specific peptic	-1.62	0.0445
TP63	tumor protein p63	-2.25	0.0445
DDX20	DEAD (Asp-Glu-Ala-Asp) box polypeptide 20	1.8	0.0446
MFSD1	major facilitator superfamily domain containing 1	1.49	0.0447
TOLLIP	toll interacting protein	-1.38	0.045
SALL2	spalt-like transcription factor 2	2.04	0.0451
SCLY	selenocysteine lyase	1.46	0.0452
CEP72	centrosomal protein 72kDa	-1.96	0.0452
CTHRC1	collagen triple helix repeat containing 1	-2.43	0.0453
HPR	haptoglobin-related protein	-2.46	0.0454
DGKD	diacylglycerol kinase, delta 130kDa	1.9	0.0456
NUPL2	nucleoporin like 2	-1.45	0.0457
SYNE2	spectrin repeat containing, nuclear envelope 2	1.87	0.046
ZDHHC8	zinc finger, DHHC-type containing 8	2.52	0.0461
SLC30A7	solute carrier family 30 (zinc transporter), member 7	1.74	0.0465
ATG13	autophagy related 13	1.28	0.0465
ZNF273	zinc finger protein 273	2.56	0.0466
ARFIP1	ADP-ribosylation factor interacting protein 1	1.28	0.047
DOC2A	double C2-like domains, alpha	-1.64	0.047
ELMOD1	ELMO/CED-12 domain containing 1	2.79	0.047
HSPB11	heat shock protein family B (small), member 11	-1.92	0.0471
THSD4	thrombospondin type 1 domain containing 4	1.98	0.0471
HMBS	hydroxymethylbilane synthase	-2.28	0.0471
SRMS	src-related kinase lacking C-terminal regulatory tyrosine and N-terminal myrist	-1.76	0.0473
FOXO1	forkhead box O1	3.45	0.0475
LRRC3	leucine rich repeat containing 3	-1.57	0.0475
RAB21	RAB21, member RAS oncogene family	-1.83	0.0476
ZNF318	zinc finger protein 318	2.3	0.0476
EXOSC6	exosome component 6	-1.71	0.0476
MEIS1	Transcript Identified by AceView, Entrez Gene ID(s) 4211	2.07	0.0478
LGI1	leucine-rich, glioma inactivated 1	3.19	0.0479
TMEM173	transmembrane protein 173	5.22	0.0481
RHO	rhodopsin	1.3	0.0482
ASPHD2	aspartate beta-hydroxylase domain containing 2	6.29	0.0482
BTN2A2	butyrophilin, subfamily 2, member A2	1.89	0.0485

SCARB1	scavenger receptor class B, member 1	9.13	0.0486
TMEM44	transmembrane protein 44	1.7	0.0487
TUT1	terminal uridylyl transferase 1, U6 snRNA-specific	-1.67	0.0487
KDM4C	Transcript Identified by AceView, Entrez Gene ID(s) 23081	-2.06	0.0491
SPIN3	spindlin family, member 3	2.84	0.0493
ZNF134	zinc finger protein 134	1.46	0.0494
ACTR3C	ARP3 actin-related protein 3 homolog C (yeast)	2.17	0.0494
USP32	ubiquitin specific peptidase 32	2.22	0.0496
EQTN	equatorin, sperm acrosome associated	2.22	0.0497
C4orf50	chromosome 4 open reading frame 50	2.89	0.0497
NUP107	nucleoporin 107kDa	1.37	0.0498
FAM153A	family with sequence similarity 153, member A	1.85	0.0498

DSCL compared to NAWM

Gene Symbol	Description	Fold Change	P-val
ZNF516	zinc finger protein 516	-4.6	0.0007
ALG3	ALG3, alpha-1,3- mannosyltransferase	-1.96	0.0012
OSCP1	organic solute carrier partner 1	-1.85	0.0019
KCNJ1	potassium channel, inwardly rectifying subfamily J, member 1	-3.06	0.002
SMARCD1	SWI/SNF related, matrix associated, actin dependent regulator of chromatin, subfamily d, membe	-2.11	0.0026
DTX3	deltex 3, E3 ubiquitin ligase	-1.97	0.0031
SLC12A8	solute carrier family 12, member 8	-2.55	0.0033
ELMOD1	ELMO/CED-12 domain containing 1	-4.21	0.0035
CHRM4	cholinergic receptor, muscarinic 4	-2.09	0.0041
CAST	calpastatin	1.94	0.0044
DGKZ	diacylglycerol kinase, zeta	-1.89	0.0044
GTDC1	glycosyltransferase like domain containing 1	3.71	0.0051
PCDH9	Memczak2013 ALT_ACCEPTOR, ALT_DONOR, coding, INTERNAL, intronic best transcript NM_203487	2.14	0.0054
ASIC3	acid sensing ion channel 3	-1.89	0.0058
CCNI	cyclin I	2.6	0.0059
C14orf159	chromosome 14 open reading frame 159	-1.6	0.0061
SLA	Src-like-adaptor	-2.16	0.0062
CES1P1; CES1	carboxylesterase 1 pseudogene 1; carboxylesterase 1	-1.76	0.0063
PAIP2; CTB-43	poly(A) binding protein interacting protein 2 [Source:EntrezGene;Acc:51247]; novel transcript	2.09	0.0064
CD151	CD151 molecule (Raph blood group)	1.61	0.0065
MIS12	MIS12 kinetochore complex component	-2.83	0.0065
TATDN2; GHR	TatD DNase domain containing 2; ghrelin opposite strand/antisense RNA	-2.57	0.0066
TOR1AIP2	torsin A interacting protein 2	-1.6	0.0075
PLEK	pleckstrin	-5.59	0.0077
GSAP	gamma-secretase activating protein	1.81	0.0078
FAM198B	family with sequence similarity 198, member B	-2.41	0.0079
DSCC1	DNA replication and sister chromatid cohesion 1	1.58	0.0079
DYRK1B	dual specificity tyrosine-(Y)-phosphorylation regulated kinase 1B	-1.76	0.0082
YLPM1	YLP motif containing 1	-2.4	0.0087
LOXHD1	lipoxygenase homology domains 1	-2.7	0.0095
MOGS	mannosyl-oligosaccharide glucosidase	-1.8	0.0096
AVIL	advillin	-2.13	0.0098
TRIM66	tripartite motif containing 66	-1.73	0.01
AOC2	amine oxidase, copper containing 2 (retina-specific)	-2.59	0.01
NKX6-2	NK6 homeobox 2	2.14	0.0104
SERPINF1	serpin peptidase inhibitor, clade F (alpha-2 antiplasmin, pigment epithelium derived factor)	2.56	0.0108
CALD1	caldesmon 1	4.49	0.0109
NAV3	neuron navigator 3	1.75	0.0111
VSIG1	V-set and immunoglobulin domain containing 1	-4.38	0.012
ACER3	alkaline ceramidase 3	2.74	0.0121
ST20-MTHFS	ST20-MTHFS readthrough	-1.9	0.0127
RUNX1T1	runt-related transcription factor 1; translocated to, 1 (cyclin D-related)	-1.76	0.0128
ZNF737	zinc finger protein 737	-1.8	0.013
SHISA9	shisa family member 9	-1.65	0.0135
CHAD	chondroadherin	-1.74	0.0136
PROSER3	proline and serine rich 3	-1.53	0.0136
EPCAM	epithelial cell adhesion molecule	-2.17	0.0137

FAM189B	family with sequence similarity 189, member B	-1.9	0.014
CFAP70	cilia and flagella associated protein 70	-2.32	0.0144
PTBP3	polypyrimidine tract binding protein 3	-2.16	0.0147
ANO3	anoctamin 3	-3.77	0.0148
SPATS2L	spermatogenesis associated, serine-rich 2-like	2.02	0.0151
MUC20; SDHA	mucin 20, cell surface associated; succinate dehydrogenase complex subunit A, flavoprotein pseudogene 2; microRNA 570	-2.07	0.0151
PLEKHA6	pleckstrin homology domain containing, family A member 6	-4.29	0.0156
CCL14; CCL15	chemokine (C-C motif) ligand 14; chemokine (C-C motif) ligand 15; CCL15-CCL14 readthrough (NMD candidate)	-1.82	0.0157
BRICD5	BRICHOS domain containing 5	-1.51	0.0158
PRTG	protogenin	1.55	0.0161
ZNF512	Memczak2013 ANTISENSE, coding, INTERNAL, UTR3 best transcript NM_032434	4.65	0.0161
EML5	Transcript Identified by AceView, Entrez Gene ID(s) 161436	-1.74	0.0164
PELI1	pellino E3 ubiquitin protein ligase 1	-2.3	0.0168
UBE2J2	ubiquitin-conjugating enzyme E2, J2	-1.61	0.0169
RAB28	RAB28, member RAS oncogene family	1.93	0.017
LOC1019283	uncharacterized LOC101928327; novel transcript	-3.16	0.0171
RGS20	regulator of G-protein signaling 20	-2.69	0.0173
GAB2	GRB2-associated binding protein 2	1.83	0.0179
PYY	peptide YY	-1.4	0.0179
CLVS1	clavesin 1	-2.73	0.0182
NPY	neuropeptide Y	-3.05	0.0182
SLC38A6	solute carrier family 38, member 6	-1.68	0.0186
ZNF587	zinc finger protein 587	-1.82	0.0193
ZMYM1	zinc finger, MYM-type 1	1.53	0.0195
ONECUT2	one cut homeobox 2	-1.88	0.0196
GRIP1	glutamate receptor interacting protein 1	-2.53	0.0197
XXYLT1	xyloside xylosyltransferase 1	-2.15	0.0198
FAM134B	family with sequence similarity 134, member B	1.71	0.0198
PITPNB	phosphatidylinositol transfer protein, beta	1.36	0.0199
LIMS2	LIM and senescent cell antigen-like domains 2	1.83	0.0199
ETS1	v-ets avian erythroblastosis virus E26 oncogene homolog 1	2.17	0.0202
APITD1-CORT	APITD1-CORT readthrough; cortistatin; apoptosis-inducing, TAF9-like domain 1	-1.78	0.0202
LINC00173	long intergenic non-protein coding RNA 173	-3.3	0.0203
GKAP1	G kinase anchoring protein 1	3.15	0.0205
FEZF2	FEZ family zinc finger 2	1.94	0.0205
FOXD4L6	forkhead box D4-like 6	-1.61	0.0206
CCDC81	coiled-coil domain containing 81	2.34	0.0206
FAM13C	family with sequence similarity 13, member C	2.41	0.0207
ATP7B	ATPase, Cu++ transporting, beta polypeptide	-1.79	0.0208
FRMPD1	FERM and PDZ domain containing 1	-2.16	0.0208
KIF1C	kinesin family member 1C	1.75	0.0208
ZSWIM5	zinc finger, SWIM-type containing 5	-1.83	0.0213
NUP107	nucleoporin 107kDa	-1.54	0.0214
CENPW	centromere protein W	-1.71	0.0214
MTHFS	5,10-methenyltetrahydrofolate synthetase (5-formyltetrahydrofolate cyclo-ligase)	-1.78	0.0217
ART4	ADP-ribosyltransferase 4 (Dombrock blood group)	1.33	0.0222
DNASE1	deoxyribonuclease I	-1.6	0.0223
TMSB4Y	thymosin beta 4, Y-linked	1.78	0.0223

RHO	rhodopsin	-1.41	0.0224
ESPN	espin	-1.81	0.0228
IGSF5	immunoglobulin superfamily, member 5	-2.5	0.0229
MYADM	Memczak2013 ANTISENSE, CDS, coding, INTERNAL best transcript NM_001020819	1.89	0.0229
MEIS1	Transcript Identified by AceView, Entrez Gene ID(s) 4211	-2.1	0.0231
AIF1L	allograft inflammatory factor 1-like	1.62	0.0232
PRKCH	protein kinase C, eta	-1.87	0.0232
APAF1	apoptotic peptidase activating factor 1	1.53	0.0234
CHKB-CPT1B	CHKB-CPT1B readthrough (NMD candidate)	-1.71	0.0235
DYNLL2	Memczak2013 ANTISENSE, coding, INTERNAL, UTR3 best transcript NM_080677	1.56	0.0236
PHKA2	phosphorylase kinase, alpha 2 (liver)	-2.31	0.0236
SYTL5	synaptotagmin-like 5	-6.05	0.0239
TRDMT1	tRNA aspartic acid methyltransferase 1	-2.74	0.0239
ZNF175	zinc finger protein 175	-1.99	0.0241
C4orf47	chromosome 4 open reading frame 47	-1.93	0.0243
MYCBPAP	MYCBP associated protein	-2.12	0.0244
ROPN1	rhophilin associated tail protein 1	1.71	0.0245
ECE2	endothelin converting enzyme 2	-1.75	0.0248
DSTYK	dual serine/threonine and tyrosine protein kinase	-1.62	0.0248
DPY19L1	dpy-19-like 1 (C. elegans)	2.05	0.0249
PITPNC1	phosphatidylinositol transfer protein, cytoplasmic 1	-2.11	0.0249
FILIP1	filamin A interacting protein 1	-1.71	0.0249
UBXN1	UBX domain protein 1	1.46	0.025
PLBD1	phospholipase B domain containing 1	-1.88	0.0253
CCDC110	coiled-coil domain containing 110	-1.81	0.0255
PLCB2	phospholipase C, beta 2	-1.88	0.0256
CTPS1	CTP synthase 1	-1.88	0.0257
CBARP	calcium channel, voltage-dependent, beta subunit associated regulatory protein	-1.58	0.0257
RPA4	replication protein A4	-1.74	0.0261
RERG	RAS-like, estrogen-regulated, growth inhibitor	-2.46	0.0263
FTCD	formimidoyltransferase cyclodeaminase	-1.92	0.0264
TPD52	tumor protein D52	1.55	0.0265
CPB2	carboxypeptidase B2 (plasma)	1.91	0.0265
EML5	echinoderm microtubule associated protein like 5	-2.21	0.0267
LMAN2L	lectin, mannose-binding 2-like	-1.83	0.0267
CFTR	cystic fibrosis transmembrane conductance regulator	-2.03	0.0268
SYNGR3	synaptogyrin 3	1.71	0.0269
LRRCC1	leucine rich repeat and coiled-coil centrosomal protein 1	1.7	0.027
LINGO1	leucine rich repeat and Ig domain containing 1	1.84	0.0271
MLPH	melanophilin	2.27	0.0271
PPP1R1A	protein phosphatase 1, regulatory (inhibitor) subunit 1A	-2.34	0.0272
WDSUB1	WD repeat, sterile alpha motif and U-box domain containing 1	-1.76	0.0274
SYN3	synapsin III	-2.42	0.0275
C9orf147; HSI	Transcript Identified by AceView, Entrez Gene ID(s) 100133204	-1.49	0.0275
SMPD3	sphingomyelin phosphodiesterase 3, neutral membrane (neutral sphingomyelinase	-4.27	0.028
ZNF91	zinc finger protein 91	-2.29	0.028
PNLDC1	poly(A)-specific ribonuclease (PARN)-like domain containing 1	-1.48	0.0283
NXPE3	neurexophilin and PC-esterase domain family, member 3	1.76	0.0284

CCDC88C	coiled-coil domain containing 88C	-6.16	0.0285
C11orf58	chromosome 11 open reading frame 58	1.69	0.0286
NFRKB	nuclear factor related to kappaB binding protein	-2	0.0287
PRRT2	proline-rich transmembrane protein 2	-1.56	0.029
PMP2	peripheral myelin protein 2	1.97	0.0291
EFHC1	EF-hand domain (C-terminal) containing 1	-3.8	0.0294
SPATA13; C1C	spermatogenesis associated 13; C1q and tumor necrosis factor related protein 9	-1.75	0.0299
TMCC2	transmembrane and coiled-coil domain family 2	2.08	0.03
ACTR3C	ARP3 actin-related protein 3 homolog C (yeast)	-2.1	0.0301
POLR2F; MIR4	polymerase (RNA) II (DNA directed) polypeptide F; microRNA 4534; microRNA 6820	1.56	0.0301
ATXN3	ataxin 3	-1.66	0.0301
HMGB1	high mobility group box 1	1.38	0.0302
MRPS25	mitochondrial ribosomal protein S25	-1.75	0.0303
NRIP1	nuclear receptor interacting protein 1	1.89	0.0303
CAMK1D	Memczak2013 ALT_ACCEPTOR, ALT_DONOR, coding, INTERNAL, intronic best transcr	-1.55	0.0304
GPR88	G protein-coupled receptor 88	-4.55	0.0304
NIF3L1	NIF3 NGG1 interacting factor 3-like 1	-1.62	0.0306
GRIA1	glutamate receptor, ionotropic, AMPA 1	-1.87	0.0307
ANKRD34B	ankyrin repeat domain 34B	-4.83	0.0308
ABCC9	Transcript Identified by AceView, Entrez Gene ID(s) 10060	-1.98	0.0309
PRB2	proline-rich protein BstNI subfamily 2	-1.46	0.0309
PCNP	PEST proteolytic signal containing nuclear protein	1.63	0.031
TRIM73	tripartite motif containing 73	-1.66	0.0313
ZFPL1	zinc finger protein-like 1	-1.55	0.0314
QRICH2	Jeck2013 ALT_DONOR, coding, INTERNAL, intronic best transcript NM_032134	-1.92	0.0315
DYRK1B	dual specificity tyrosine-(Y)-phosphorylation regulated kinase 1B	-1.71	0.0315
PRPF39	pre-mRNA processing factor 39	-1.76	0.0315
CNR1	cannabinoid receptor 1 (brain)	-4.25	0.0319
ABRACL	ABRA C-terminal like	1.67	0.0321
NYAP2	neuronal tyrosine-phosphorylated phosphoinositide-3-kinase adaptor 2	-1.74	0.0325
SLFN11	schlafen family member 11	-1.71	0.0328
TMEM44	transmembrane protein 44	-1.77	0.0329
NUPL2	nucleoporin like 2	1.45	0.033
AATK	apoptosis-associated tyrosine kinase	1.85	0.033
SEC23B	Sec23 homolog B, COPII coat complex component	-1.58	0.033
FMN1	formin 1	2.78	0.0331
TAGLN	transgelin	2.11	0.0332
BBOF1	basal body orientation factor 1	-1.53	0.0332
GRAMD1C	GRAM domain containing 1C	-1.64	0.0333
FAM196A	family with sequence similarity 196, member A	-1.46	0.0337
MTMR1	myotubularin related protein 1	-1.72	0.0337
OTOF	otoferlin	-1.68	0.0337
SMIM15	small integral membrane protein 15	1.85	0.0338
SPATC1L	spermatogenesis and centriole associated 1-like	-1.75	0.0339
RAB39A	RAB39A, member RAS oncogene family	1.39	0.034
PKD1L1	polycystic kidney disease 1 like 1	-1.66	0.034
PAQR3	progestin and adipoQ receptor family member III	-2.16	0.0344
DYRK1B	dual specificity tyrosine-(Y)-phosphorylation regulated kinase 1B	-1.77	0.0344

WSB2	WD repeat and SOCS box containing 2	1.68	0.0346
MDFI	MyoD family inhibitor	1.42	0.0348
SULT1A2	sulfotransferase family 1A member 2	-1.39	0.0349
ALOXE3	arachidonate lipoxygenase 3	-1.68	0.035
ATPAF2	ATP synthase mitochondrial F1 complex assembly factor 2	2.06	0.0351
ZNF658B	zinc finger protein 658B, pseudogene	-2.05	0.0352
ATP6V1E2	ATPase, H+ transporting, lysosomal 31kDa, V1 subunit E2	-1.58	0.0352
GPR149	G protein-coupled receptor 149	-7.77	0.0353
GPC6	glypican 6	-1.44	0.0357
FAM53B	Memczak2013 ALT_ACCEPTOR, ALT_DONOR, coding, INTERNAL, intronic best transcript NM_01466	2.04	0.0358
DOC2A	double C2-like domains, alpha	1.8	0.036
DCLK3	doublecortin-like kinase 3	-1.95	0.0362
RLBP1	retinaldehyde binding protein 1	-1.65	0.0362
BCO2; RPS12I	beta-carotene oxygenase 2; ribosomal protein S12 pseudogene 21	-1.92	0.0363
MIR6809; TNS	microRNA 6809; tensin 1	2.58	0.0364
LRCH4	leucine-rich repeats and calponin homology (CH) domain containing 4	-1.85	0.0366
EGR1	early growth response 1	-1.74	0.0369
SALL3	spalt-like transcription factor 3	1.29	0.037
IL17RE	interleukin 17 receptor E	-1.79	0.037
HDAC11	histone deacetylase 11	1.98	0.0371
ARHGAP33	Rho GTPase activating protein 33	-1.84	0.0372
HRNR	hornerin	1.62	0.0374
TMEM39B	transmembrane protein 39B	-1.91	0.0376
RAB11FIP5	RAB11 family interacting protein 5 (class I)	-1.33	0.0379
SFXN2	sideroflexin 2	-2.53	0.0386
CYB5D1	cytochrome b5 domain containing 1	-2.07	0.0386
ADAMTSL5	ADAMTS like 5	-1.42	0.0387
HRH2	histamine receptor H2	-6.38	0.0387
C14orf119	chromosome 14 open reading frame 119	1.37	0.0388
RESP18	regulated endocrine-specific protein 18	-1.71	0.0388
STMN1; MIR3	stathmin 1; microRNA 3917	3.44	0.0388
KCTD1	potassium channel tetramerization domain containing 1	-2.68	0.0389
CXorf36	chromosome X open reading frame 36	-1.47	0.039
GTF2H1	general transcription factor IIH subunit 1	-1.79	0.0391
CNTNAP3	contactin associated protein-like 3	-1.89	0.0391
CCL28	chemokine (C-C motif) ligand 28	1.94	0.0392
SLC39A13	solute carrier family 39 (zinc transporter), member 13	1.35	0.0392
MYL9	myosin light chain 9	1.91	0.0395
SNN	stannin	-1.49	0.0398
FAM153A	family with sequence similarity 153, member A	-2.16	0.0399
GNAS	GNAS complex locus	1.93	0.04
ACAN	aggrecan	1.85	0.04
LMCD1; LINC(	LIM and cysteine-rich domains 1; long intergenic non-protein coding RNA 312	-1.57	0.0401
HS3ST2	heparan sulfate (glucosamine) 3-O-sulfotransferase 2	2.23	0.0401
CDH6	cadherin 6, type 2, K-cadherin (fetal kidney)	-4.06	0.0402
SLC16A9	solute carrier family 16, member 9	-1.58	0.0404
PHLDB2; PLC)	pleckstrin homology-like domain, family B, member 2; phosphatidylinositol-specific phospholipa	2.25	0.0406
SALL2	spalt-like transcription factor 2	-1.79	0.0408

KDM4B	lysine (K)-specific demethylase 4B	-1.42	0.0408
PAK6; BUB1B	p21 protein (Cdc42/Rac)-activated kinase 6; BUB1 mitotic checkpoint serine/threonine kin	-1.7	0.0408
OMA1	OMA1 zinc metallopeptidase	1.82	0.0409
FUT9	fucosyltransferase 9 (alpha (1,3) fucosyltransferase)	-1.72	0.0416
CENPC	centromere protein C	-1.7	0.0417
PEF1	penta-EF-hand domain containing 1	-1.62	0.042
TNFRSF21	tumor necrosis factor receptor superfamily, member 21	2.8	0.042
BMP6	bone morphogenetic protein 6	-1.35	0.042
ADAMTS3	ADAM metallopeptidase with thrombospondin type 1 motif 3	-2.21	0.0421
PPP1R14B	protein phosphatase 1, regulatory (inhibitor) subunit 14B	2.07	0.0421
Sep-07	septin 7	1.72	0.0423
GPR176	G protein-coupled receptor 176	1.84	0.0424
MORF4L2	mortality factor 4 like 2	1.45	0.0431
FILIP1L	filamin A interacting protein 1-like	2.2	0.0431
CDH8	cadherin 8, type 2	-1.79	0.0434
ZNF740	zinc finger protein 740	-1.72	0.0434
TMEM168	transmembrane protein 168	-2.01	0.0435
UAP1	UDP-N-acetylglucosamine pyrophosphorylase 1	1.75	0.0438
CAMKMT	calmodulin-lysine N-methyltransferase	-2.9	0.044
IGSF21	immunoglobin superfamily, member 21	1.84	0.0442
CHURC1	churchill domain containing 1	1.61	0.0445
STK36	serine/threonine kinase 36	-1.77	0.0446
GALNT11	polypeptide N-acetylgalactosaminyltransferase 11	-1.57	0.0446
ADGRA2	adhesion G protein-coupled receptor A2	1.57	0.0448
LRRC3	leucine rich repeat containing 3	1.49	0.0451
ZFP64	ZFP64 zinc finger protein	-1.83	0.0454
SEC23IP	SEC23 interacting protein	-1.62	0.0454
HUS1	HUS1 checkpoint clamp component	-2.14	0.0455
HIPK4	homeodomain interacting protein kinase 4	-1.31	0.0455
ZKSCAN7	zinc finger with KRAB and SCAN domains 7	-1.76	0.0456
FMN1	formin 1	2.25	0.0463
MYCN	v-myc avian myelocytomatosis viral oncogene neuroblastoma derived homolog	1.49	0.0464
DGKH	diacylglycerol kinase, eta	-11.93	0.0464
TXNDC11	thioredoxin domain containing 11	-2.29	0.0465
GPRIN1	G protein regulated inducer of neurite outgrowth 1	1.62	0.0467
ASXL3	additional sex combs like transcriptional regulator 3	2.2	0.0473
MTX1	metaxin 1	1.48	0.0473
FBN1	fibrillin 1	1.97	0.0474
OR1F1	olfactory receptor, family 1, subfamily F, member 1	-1.55	0.0475
SERTAD4	SERTA domain containing 4	-1.52	0.0475
VWA7	von Willebrand factor A domain containing 7	-1.32	0.0476
WFDC2	WAP four-disulfide core domain 2	-2.38	0.0476
AP1B1	Zhang2013 ALT_ACCEPTOR, ALT_DONOR, coding, INTERNAL, intronic best transcript NM_001	-1.28	0.0478
TCFL5	transcription factor-like 5 (basic helix-loop-helix)	1.68	0.0479
ISCA1	iron-sulfur cluster assembly 1	1.42	0.0479
DMKN	dermokine	-3.15	0.0482
CPVL	carboxypeptidase, vitellogenic-like	-1.24	0.0484
DCDC5; DCDC	doublecortin domain containing 5; doublecortin domain containing 1	-1.68	0.0485

INO80D	INO80 complex subunit D	-2	0.0486
ZNF480	zinc finger protein 480	1.42	0.0488
MKNK1	MAP kinase interacting serine/threonine kinase 1	-1.52	0.0488
HTR1D	5-hydroxytryptamine (serotonin) receptor 1D, G protein-coupled	-3.28	0.049
TBC1D3B; TBC	TBC1 domain family, member 3B; TBC1 domain family, member 3H; TBC1 domain family, member 3I; TBC1 domain family, member 3F	-1.39	0.049
SLC16A10	solute carrier family 16 (aromatic amino acid transporter), member 10	-1.41	0.049
LRTM2	leucine-rich repeats and transmembrane domains 2	-1.8	0.0493
DENND5B	DENN/MADD domain containing 5B	-2.3	0.0493
SLC25A28	solute carrier family 25 (mitochondrial iron transporter), member 28	-1.53	0.0496
ST6GALNAC6	ST6 (alpha-N-acetyl-neuraminyl-2,3-beta-galactosyl-1,3)-N-acetylgalactosaminide alpha-2,6-sialyltransferase 6	-1.46	0.0497
CTTNBP2	cortactin binding protein 2	-1.82	0.0497
TMEM120B	transmembrane protein 120B	-3.17	0.0499

Appendix III

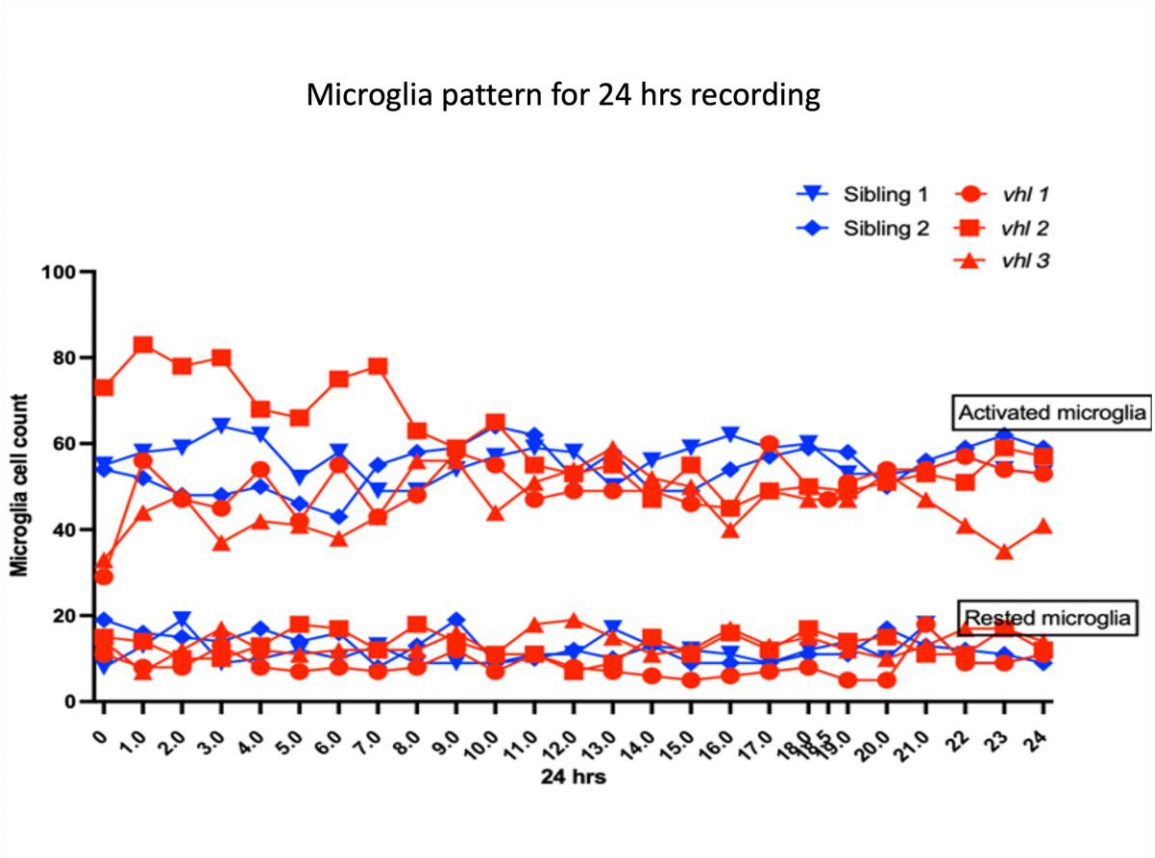

Individual characterisation of microglial morphologies in *vhl*$^{-/-}$ and sibling zebrafish over 24 hrs recording.

References

Affymetrix. 2009. GeneChip Human Genome U133 Plus 2.0 Array. Product Description: Affymetrix.

AHN, K., LEE, S.-J. & MOOK-JUNG, I. 2022. White matter-associated microglia: New players in brain aging and neurodegenerative diseases. *Ageing Research Reviews,* 75**,** 101574.

AL-MASHHADI, S., SIMPSON, J. E., HEATH, P. R., DICKMAN, M., FORSTER, G., MATTHEWS, F. E., BRAYNE, C., INCE, P. G., WHARTON, S. B., FUNCTION, M. R. C. C. & PATHOLOGY, A. S. J. B. 2015. Oxidative glial cell damage associated with white matter lesions in the aging human brain. 25**,** 565-574.

ALOISI, F. J. G. 2001. Immune function of microglia. 36**,** 165-179.

AMER-SARSOUR, F., KORDONSKY, A., BERDICHEVSKY, Y., PRAG, G. & ASHKENAZI, A. 2021. Deubiquitylating enzymes in neuronal health and disease. *Cell death & disease,* 12**,** 1-11.

ANG, S. O., CHEN, H., GORDEUK, V. R., SERGUEEVA, A. I., POLYAKOVA, L. A., MIASNIKOVA, G. Y., KRALOVICS, R., STOCKTON, D. W. & PRCHAL, J. T. 2002. Endemic polycythemia in Russia: mutation in the VHL gene. *Blood Cells, Molecules, and Diseases,* 28**,** 57-62.

AURIEL, E., CSIBA, L., BERENYI, E., VARKONYI, I., MEHES, G., KARDOS, L., KARNI, A. & BORNSTEIN, N. M. J. N. 2012. Leukoaraiosis is associated with arterial wall thickness: a quantitative analysis. 32**,** 227-233.

AZAD, P. & HADDAD, G. G. 2013. Genetic animal models of preconditioning. *Translational stroke research,* 4**,** 51-55.

BAEZNER, H., BLAHAK, C., POGGESI, A., PANTONI, L., INZITARI, D., CHABRIAT, H., ERKINJUNTTI, T., FAZEKAS, F., FERRO, J. & LANGHORNE, P. 2008. Association of gait and balance disorders with age-related white matter changes: the LADIS study. *Neurology,* 70**,** 935-942.

BAI, Y., ZHANG, Y., HAN, B., YANG, L., CHEN, X., HUANG, R., WU, F., CHAO, J., LIU, P. & HU, G. 2018. Circular RNA DLGAP4 ameliorates ischemic stroke outcomes by targeting miR-143 to regulate endothelial-mesenchymal transition associated with blood–brain barrier integrity. *Journal of Neuroscience,* 38**,** 32-50.

BAILEY, C., CLARKE, C. L., GIBB, C., HAINING, S., WILKINSON, H., TIPLADY, S. J. H., RISK & SOCIETY 2013. Risky and resilient life with dementia: Review of and reflections on the literature. 15**,** 390-401.

BANCROFT, J. D. & GAMBLE, M. 2008. *Theory and practice of histological techniques*, Elsevier health sciences.

BANG, J., SPINA, S. & MILLER, B. L. J. T. L. 2015. Frontotemporal dementia. 386**,** 1672-1682.

BARKHOF, F., SCHELTENS, P. J. J. O. N., NEUROSURGERY & PSYCHIATRY 2006. Is the whole brain periventricular? 77**,** 143-144.

BASSI, A., SCHMID, B. AND HUISKEN, J. 2015. Optical tomography complements light sheet microscopy for in toto imaging of zebrafish development. *Development,* 142(5)**,** 1016-1020.

BATES, T. J., NAUMANN, U. & ENGLERT, C. 2016. Fluorescence-Activated Cell Sorting (FACS) Protocol for Podocyte Isolation in Adult Zebrafish. *The Wilms' Tumor (WT1) Gene.* Springer.

BELTRÁN-CASTILLO, S., VON BERNHARDI, R. & EUGENÍN, J. 2021. The impact of aged microglia on d-serine-regulated glutamatergic transmission. *Factors Affecting Neurological Aging.* Elsevier.

BHARGAVA, V., HEAD, S. R., ORDOUKHANIAN, P., MERCOLA, M. & SUBRAMANIAM, S. 2014. Technical variations in low-input RNA-seq methodologies. *Scientific reports,* 4**,** 1-10.

BIAGINI, V., BUSI, F., ANELLI, V., KERSCHBAMER, E., BAGHINI, M., GURRIERI, E., NOTARANGELO, M., PESCE, I., VAN NIEL, G., D'AGOSTINO, V.G. AND MIONE, M. 2022. Zebrafish Melanoma-Derived Interstitial EVs Are Carriers of ncRNAs That Induce Inflammation. *International Journal of Molecular Sciences***,** 5510.

BICHO, M. C., DA SILVA, A. P., MEDEIROS, R. & BICHO, M. 2013. The role of haptoglobin and its genetic polymorphism in cancer: a review. *Acute phase proteins*.

BIRDSILL, A. C., WALKER, D. G., LUE, L., SUE, L. I. & BEACH, T. G. 2011. Postmortem interval effect on RNA and gene expression in human brain tissue. *Cell and tissue banking,* 12**,** 311-318.

BOCHE, D., PERRY, V. & NICOLL, J. 2013. Activation patterns of microglia and their identification in the human brain. *Neuropathology and applied neurobiology,* 39**,** 3-18.

BORDA, J. T., ALVAREZ, X., MOHAN, M., HASEGAWA, A., BERNARDINO, A., JEAN, S., AYE, P. & LACKNER, A. A. 2008. CD163, a marker of perivascular macrophages, is up-regulated by microglia in simian immunodeficiency virus encephalitis after haptoglobin-hemoglobin complex stimulation and is suggestive of breakdown of the blood-brain barrier. *The American journal of pathology,* 172**,** 725-737.

BOTTERO, V., ALRAFATI, F., SANTIAGO, J. A. & POTASHKIN, J. A. 2021. Transcriptomic and Network Meta-Analysis of Frontotemporal Dementias. *Frontiers in Molecular Neuroscience,* 14**,** 747798.

BOTTIGLIONE, F., DEE, C. T., LEA, R., ZEEF, L. A., BADROCK, A. P., WANE, M., BUGEON, L., DALLMAN, M. J., ALLEN, J. E. & HURLSTONE, A. F. 2020. Zebrafish IL-4–like cytokines and IL-10 suppress inflammation but only IL-10 is essential for gill homeostasis. *The Journal of Immunology,* 205**,** 994-1008.

BOUSMAN, C. A., LUZA, S., MANCUSO, S. G., KANG, D., OPAZO, C. M., MOSTAID, M., CROPLEY, V., MCGORRY, P., SHANNON WEICKERT, C. & PANTELIS, C. 2019. Elevated ubiquitinated proteins in brain and blood of individuals with schizophrenia. *Scientific reports,* 9**,** 1-8.

BOVEN, L. A., VAN MEURS, M., VAN ZWAM, M., WIERENGA-WOLF, A., HINTZEN, R. Q., BOOT, R. G., AERTS, J. M., AMOR, S., NIEUWENHUIS, E. E. & LAMAN, J. D. 2006. Myelin-laden macrophages are anti-inflammatory, consistent with foam cells in multiple sclerosis. *Brain,* 129**,** 517-526.

BOZZALI, M., FALINI, A., FRANCESCHI, M., CERCIGNANI, M., ZUFFI, M., SCOTTI, G., COMI, G., FILIPPI, M. J. J. O. N., NEUROSURGERY & PSYCHIATRY 2002. White matter damage in Alzheimer's disease assessed in vivo using diffusion tensor magnetic resonance imaging. 72**,** 742-746.

BRADFORD, Y. M., TORO, S., RAMACHANDRAN, S., RUZICKA, L., HOWE, D. G., EAGLE, A., KALITA, P., MARTIN, R., TAYLOR MOXON, S. A. & SCHAPER, K. 2017. Zebrafish models of human disease: gaining insight into human disease at ZFIN. *ILAR journal,* 58**,** 4-16.

BRAYNE, C., MCCRACKEN, C. & MATTHEWS, F. E. 2006. Cohort profile: the Medical Research Council cognitive function and ageing study (CFAS). *International Journal of Epidemiology,* 35**,** 1140-1145.

BRIEN, J. T. & THOMAS, A. 2015. Non-Alzheimer's dementia 3 Vascular dementia.

BROWN, N., ALKHAYER, K., CLEMENTS, R., SINGHAL, N., GREGORY, R., AZZAM, S., LI, S., FREEMAN, E. & MCDONOUGH, J. 2016. Neuronal hemoglobin expression and its relevance to multiple sclerosis neuropathology. *Journal of molecular neuroscience,* 59**,** 1-17.

BROWN, N. J. 2014. *Localization of hemoglobin in MS cortex and its relevance to MS neuropathology.* Kent State University.

BROWN, W. R., MOODY, D. M., THORE, C. R., ANSTROM, J. A. & CHALLA, V. R. J. J. O. T. N. S. 2009. Microvascular changes in the white mater in dementia. 283**,** 28-31.

BRUN, A., ENGLUND, E. J. A. D. & DISORDERS, A. 1987. A white matter disorder in dementia of the Alzheimer type: a pathoanatomical study. 1**,** 51.

BULTERS, D., GAASTRA, B., ZOLNOURIAN, A., ALEXANDER, S., REN, D., BLACKBURN, S. L., BORSODY, M., DORÉ, S., GALEA, J. & IIHARA, K. 2018. Haemoglobin scavenging in intracranial bleeding: biology and clinical implications. *Nature Reviews Neurology,* 14**,** 416-432.

BURROUGHS-GARCIA, J., HASAN, A., PARK, G., BORGA, C. & FRAZER, J. K. 2019. Isolating Malignant and Non-Malignant B Cells from lck: eGFP Zebrafish. *JoVE (Journal of Visualized Experiments)***,** e59191.

CAI, M., LEE, J. H. & YANG, E. J. J. M. N. 2017. Bee venom ameliorates cognitive dysfunction caused by neuroinflammation in an animal model of vascular dementia. 54**,** 5952-5960.

CALDEIRA, M. V., SALAZAR, I. L., CURCIO, M., CANZONIERO, L. M. & DUARTE, C. B. 2014. Role of the ubiquitin–proteasome system in brain ischemia: Friend or foe? *Progress in neurobiology,* 112**,** 50-69.

CAPELLUTO, D. G. 2012. Tollip: a multitasking protein in innate immunity and protein trafficking. *Microbes and infection,* 14**,** 140-147.

CAROLINE BRENNAN 2014. Five reasons why zebrafish make excellent research models. *The national centre for the replacement, refinement, and reduction of animals in research.*

CASAMASSIMI, A., FEDERICO, A., RIENZO, M., ESPOSITO, S. & CICCODICOLA, A. 2017. Transcriptome profiling in human diseases: new advances and perspectives. *International journal of molecular sciences,* 18**,** 1652.

CASANO, A. M., ALBERT, M. & PERI, F. 2016. Developmental apoptosis mediates entry and positioning of microglia in the zebrafish brain. *Cell Reports,* 16**,** 897-906.

CHAKRABORTY, C., HSU, C. H., WEN, Z. H., LIN, C. S. & AGORAMOORTHY, G. J. C. D. M. 2009. Zebrafish: a complete animal model for in vivo drug discovery and development. 10**,** 116-124.

CHEN, K., YUAN, R., GENG, S., ZHANG, Y., RAN, T., KOWALSKI, E., LIU, J. & LI, L. 2017. Toll-interacting protein deficiency promotes neurodegeneration via impeding autophagy completion in high-fat diet-fed ApoE−/− mouse model. *Brain, behavior, and immunity,* 59**,** 200-210.

CHO, K. O., LA, H. O., CHO, Y. J., SUNG, K. W. & KIM, S. Y. J. J. O. N. R. 2006. Minocycline attenuates white matter damage in a rat model of chronic cerebral hypoperfusion. 83**,** 285-291.

CHUI, H. C., RAMIREZ-GOMEZ, L. J. N.-A. S. & DEMENTIA, A. 2016. Vascular cognitive impairment: Diagnosis and treatment. 30.

CLAUSEN, B. H., LAMBERTSEN, K. L., BABCOCK, A. A., HOLM, T. H., DAGNAES-HANSEN, F. & FINSEN, B. 2008. Interleukin-1beta and tumor necrosis factor-alpha are expressed by different subsets of microglia and macrophages after ischemic stroke in mice. *Journal of neuroinflammation,* 5**,** 1-18.

COSACAK, M. I., BHATTARAI, P. & KIZIL, C. 2020. Protocol for Dissection and Dissociation of Zebrafish Telencephalon for Single-Cell Sequencing. *STAR protocols,* 1**,** 100042.

COSACAK, M. I., BHATTARAI, P., REINHARDT, S., PETZOLD, A., DAHL, A., ZHANG, Y. & KIZIL, C. 2019. Single-cell transcriptomics analyses of neural stem cell heterogeneity and contextual plasticity in a zebrafish brain model of amyloid toxicity. *Cell Reports,* 27**,** 1307-1318. e3.

COWAN, M. N., SETHI, I. & HARRIS, T. H. 2022. Microglia in CNS infections: insights from Toxoplasma gondii and other pathogens. *Trends in Parasitology*.

CREWS, F. T. & VETRENO, R. P. J. P. 2016. Mechanisms of neuroimmune gene induction in alcoholism. 233**,** 1543-1557.

CRILLY, S., COOPER, J., BRADFORD, L., PRISE, I.E., KRISHNAN, S. AND KASHER, P.R. 2021. RNA-Seq Dataset From Isolated Leukocytes Following Spontaneous Intracerebral Hemorrhage in Zebrafish Larvae. *Frontiers in cellular neuroscience,* 15**,** 660732.

CUNNEA, P., MHÁILLE, A. N., MCQUAID, S., FARRELL, M., MCMAHON, J. & FITZGERALD, U. 2011. Expression profiles of endoplasmic reticulum stress-related molecules in demyelinating lesions and multiple sclerosis. *Multiple Sclerosis Journal,* 17**,** 808-818.

DAMANI, M. R., ZHAO, L., FONTAINHAS, A. M., AMARAL, J., FARISS, R. N. & WONG, W. T. 2011. Age-related alterations in the dynamic behavior of microglia. *Aging cell,* 10**,** 263-276.

DAS, S., RAMAKRISHNA, S. & KIM, K.-S. 2020. Critical roles of deubiquitinating enzymes in the nervous system and neurodegenerative disorders. *Molecules and Cells,* 43**,** 203.

DAVIES, D. S., MA, J., JEGATHEES, T. & GOLDSBURY, C. 2017. Microglia show altered morphology and reduced arborization in human brain during aging and A lzheimer's disease. *Brain Pathology,* 27**,** 795-808.

DE ABREU, M. S., GIACOMINI, A. C., ZANANDREA, R., DOS SANTOS, B. E., GENARIO, R., DE OLIVEIRA, G. G., FRIEND, A. J., AMSTISLAVSKAYA, T. G. & KALUEFF, A. V. 2018. Psychoneuroimmunology and immunopsychiatry of zebrafish. *Psychoneuroendocrinology,* 92**,** 1-12.

DE GROOT, J. C., DE LEEUW, F. E., OUDKERK, M., VAN GIJN, J., HOFMAN, A., JOLLES, J. & BRETELER, M. M. J. A. O. N. 2002. Periventricular cerebral white matter lesions predict rate of cognitive decline. 52**,** 335-341.

DE LAAT, K. F., TULADHAR, A. M., VAN NORDEN, A. G., NORRIS, D. G., ZWIERS, M. P. & DE LEEUW, F.-E. J. B. 2010. Loss of white matter integrity is associated with gait disorders in cerebral small vessel disease. 134**,** 73-83.

DING, C. & CANTOR, C. R. 2004. Quantitative analysis of nucleic acids-the last few years of progress. *BMB Reports,* 37**,** 1-10.

DING, R., HASE, Y., AMEEN-ALI, K. E., NDUNG'U, M., STEVENSON, W., BARSBY, J., GOURLAY, R., AKINYEMI, T., AKINYEMI, R. & UEMURA, M. T. 2020. Loss of capillary pericytes and the blood–brain barrier in white matter in poststroke and vascular dementias and Alzheimer's disease. *Brain Pathology,* 30**,** 1087-1101.

DUNCOMBE, J., KITAMURA, A., HASE, Y., IHARA, M., KALARIA, R. N. & HORSBURGH, K. 2017. Chronic cerebral hypoperfusion: a key mechanism leading to vascular cognitive impairment and dementia. Closing the translational gap between rodent models and human vascular cognitive impairment and dementia. *Clinical Science,* 131**,** 2451-2468.

ELKS, P. M., RENSHAW, S. A., MEIJER, A. H., WALMSLEY, S. R. & VAN EEDEN, F. J. 2015. Exploring the HIFs, buts and maybes of hypoxia signalling in disease: lessons from zebrafish models. *Disease models & mechanisms,* 8**,** 1349-1360.

ELLETT, F., PASE, L., HAYMAN, J. W., ANDRIANOPOULOS, A. & LIESCHKE, G. J. 2011. mpeg1 promoter transgenes direct macrophage-lineage expression in zebrafish. *Blood,* 117**,** e49-e56.

EMMERT-BUCK, M. R., BONNER, R. F., SMITH, P. D., CHUAQUI, R. F., ZHUANG, Z., GOLDSTEIN, S. R., WEISS, R. A. & LIOTTA, L. A. 1996. Laser capture microdissection. *Science,* 274**,** 998-1001.

ESIRI, M., MATTHEWS, F., BRAYNE, C., INCE, P., MATTHEWS, F., XUEREB, J., BROOME, J., MCKENZIE, J., ROSSI, M. & MCKEITH, I. 2001. Pathological correlates of late-onset dementia in a multicentre, community-based population in England and Wales. *Lancet*.

EUGENIN, J., VECCHIOLA, A., MURGAS, P., ARROYO, P., CORNEJO, F. & VON BERNHARDI, R. 2016. Expression pattern of scavenger receptors and amyloid-β phagocytosis of astrocytes and

microglia in culture are modified by acidosis: implications for alzheimer's disease. *Journal of Alzheimer's Disease,* 53**,** 857-873.

FADUL, M. M., HEATH, P. R., COOPER-KNOCK, J., KURZ, J. M., AL-AZZAWI, H. A., ALI, Z., SMITH, T., MATTHEWS, F. E., BRAYNE, C. & WHARTON, S. B. 2020. Transcriptomic analysis of age-associated periventricular lesions reveals dysregulation of the immune response. *International journal of molecular sciences,* 21**,** 7924.

FAN, C., IACOBAS, D. A., ZHOU, D., CHEN, Q., LAI, J. K., GAVRIALOV, O. & HADDAD, G. G. 2005. Gene expression and phenotypic characterization of mouse heart after chronic constant or intermittent hypoxia. *Physiological genomics,* 22**,** 292-307.

FARKAS, E., DONKA, G., DE VOS, R. A., MIHÁLY, A., BARI, F. & LUITEN, P. G. 2004. Experimental cerebral hypoperfusion induces white matter injury and microglial activation in the rat brain. *Acta Neuropathologica,* 108**,** 57-64.

FARRALL, A. J. & WARDLAW, J. M. J. N. O. A. 2009. Blood–brain barrier: ageing and microvascular disease–systematic review and meta-analysis. 30**,** 337-352.

FAZEKAS, F., CHAWLUK, J. B., ALAVI, A., HURTIG, H. I. & ZIMMERMAN, R. A. J. A. J. O. R. 1987. MR signal abnormalities at 1.5 T in Alzheimer's dementia and normal aging. 149**,** 351-356.

FEI, C., NIE, L., ZHANG, J. & CHEN, J. 2021. Potential Applications of Fluorescence-Activated Cell Sorting (FACS) and Droplet-Based Microfluidics in Promoting the Discovery of Specific Antibodies for Characterizations of Fish Immune Cells. *Frontiers in Immunology,* 12.

FERNANDO, M., O'BRIEN, J., PERRY, R., ENGLISH, P., FORSTER, G., MCMEEKIN, W., SLADE, J., GOLKHAR, A., MATTHEWS, F. & BARBER, R. 2004a. Comparison of the pathology of cerebral white matter with post-mortem magnetic resonance imaging (MRI) in the elderly brain. *Neuropathology and applied neurobiology,* 30**,** 385-395.

FERNANDO, M., O'BRIEN, J., PERRY, R., ENGLISH, P., FORSTER, G., MCMEEKIN, W., SLADE, J., GOLKHAR, A., MATTHEWS, F., BARBER, R. J. N. & NEUROBIOLOGY, A. 2004b. Comparison of the pathology of cerebral white matter with post-mortem magnetic resonance imaging (MRI) in the elderly brain. 30**,** 385-395.

FERNANDO, M. S., SIMPSON, J. E., MATTHEWS, F., BRAYNE, C., LEWIS, C. E., BARBER, R., KALARIA, R. N., FORSTER, G., ESTEVES, F. & WHARTON, S. B. J. S. 2006. White matter lesions in an unselected cohort of the elderly: molecular pathology suggests origin from chronic hypoperfusion injury. 37**,** 1391-1398.

FERREIRA, P. G., MUÑOZ-AGUIRRE, M., REVERTER, F., SA GODINHO, C. P., SOUSA, A., AMADOZ, A., SODAEI, R., HIDALGO, M. R., PERVOUCHINE, D. & CARBONELL-CABALLERO, J. 2018. The effects of death and post-mortem cold ischemia on human tissue transcriptomes. *Nature communications,* 9**,** 1-15.

FLODEN, A. M. & COMBS, C. K. J. J. O. A. S. D. 2011. Microglia demonstrate age-dependent interaction with amyloid-β fibrils. 25**,** 279-293.

FOWLER, J. H., MCQUEEN, J., HOLLAND, P. R., MANSO, Y., MARANGONI, M., SCOTT, F., CHISHOLM, E., SCANNEVIN, R. H., HARDINGHAM, G. E., HORSBURGH, K. J. J. O. C. B. F. & METABOLISM 2018. Dimethyl fumarate improves white matter function following severe hypoperfusion: Involvement of microglia/macrophages and inflammatory mediators. 38**,** 1354-1370.

FREEZE, W. M., JACOBS, H. I., DE JONG, J. J., VERHEGGEN, I. C., GRONENSCHILD, E. H., PALM, W. M., HOFF, E. I., WARDLAW, J. M., JANSEN, J. F. & VERHEY, F. R. 2020. White matter hyperintensities mediate the association between blood-brain barrier leakage and information processing speed. *Neurobiology of Aging,* 85**,** 113-122.

FUMAGALLI, S., PEREGO, C., PISCHIUTTA, F., ZANIER, E. R. & DE SIMONI, M.-G. 2015. The ischemic environment drives microglia and macrophage function. *Frontiers in neurology,* 6**,** 81.

GALEA, I., DURNFORD, A., GLAZIER, J., MITCHELL, S., KOHLI, S., FOULKES, L., NORMAN, J., DAREKAR, A., LOVE, S. & BULTERS, D. O. 2022. Iron deposition in the brain after aneurysmal subarachnoid hemorrhage. *Stroke,* 53**,** 1633-1642.

GALLEGO ROMERO, I., PAI, A. A., TUNG, J. & GILAD, Y. 2014. RNA-seq: impact of RNA degradation on transcript quantification. *BMC biology,* 12**,** 1-13.

GAN, D., WU, S., CHEN, B. & ZHANG, J. 2020. Application of the zebrafish traumatic brain injury model in assessing cerebral inflammation. *Zebrafish,* 17**,** 73-82.

GAO, F., SÁ, M., CABANELAS, I.T.D., WIJFFELS, R.H. AND BARBOSA, M.J. 2021. Improved fucoxanthin and docosahexaenoic acid productivities of a sorted self-settling Tisochrysis lutea phenotype at pilot scale. . *Bioresource Technology***,** 124725.

GARNIER-CRUSSARD, A., BOUGACHA, S., WIRTH, M., ANDRÉ, C., DELARUE, M., LANDEAU, B., MÉZENGE, F., KUHN, E., GONNEAUD, J. & CHOCAT, A. 2020. White matter hyperintensities across the adult lifespan: relation to age, Aβ load, and cognition. *Alzheimer's research & therapy,* 12**,** 1-11.

GHOSH, S. & HUI, S. P. 2016. Regeneration of zebrafish CNS: adult neurogenesis. *Neural plasticity,* 2016.

GIBSON, G. E. & HUANG, H.-M. 1992. Animal Models of Brain Hypoxia. *In:* BOULTON, A. A., BAKER, G. B. & BUTTERWORTH, R. F. (eds.) *Animal Models of Neurological Disease, II: Metabolic Encephalopathies and the Epilepsies.* Totowa, NJ: Humana Press.

GINHOUX, F., LIM, S., HOEFFEL, G., LOW, D. & HUBER, T. J. F. I. C. N. 2013. Origin and differentiation of microglia. 7**,** 45.

GLOCKER, E. O., KOTLARZ, D., KLEIN, C., SHAH, N. & GRIMBACHER, B. 2011. IL-10 and IL-10 receptor defects in humans. *Annals of the New York Academy of Sciences,* 1246**,** 102-107.

GOODALL, E. F., LEACH, V., WANG, C., COOPER-KNOCK, J., HEATH, P. R., BAKER, D., DREW, D. R., SAFFREY, M. J., SIMPSON, J. E. & ROMERO, I. A. 2019. Age-associated mRNA and miRNA expression changes in the blood-brain barrier. *International journal of molecular sciences,* 20**,** 3097.

GRAHAM, T. G., DUGAST-DARZACQ, C., DAILEY, G. M., DARZACQ, X. & TJIAN, R. 2021. Simple, inexpensive RNA isolation and one-step RT-qPCR methods for SARS-CoV-2 detection and general use. *Current protocols,* 1**,** e130.

GRIFFANTI, L., ZAMBONI, G., KHAN, A., LI, L., BONIFACIO, G., SUNDARESAN, V., SCHULZ, U. G., KUKER, W., BATTAGLINI, M. & ROTHWELL, P. M. 2016. BIANCA (Brain Intensity AbNormality Classification Algorithm): a new tool for automated segmentation of white matter hyperintensities. *NeuroImage,* 141**,** 191-205.

GUARDADO, A. L. P., SWEENEY, C. L., HAYES, E., TRUEMAN, B. F., HUANG, Y., JAMIESON, R. C., RAND, J. L., GAGNON, G. A. & STODDART, A. K. 2020. Development and optimization of a new method for direct extraction of SARS-CoV-2 RNA from municipal wastewater using magnetic beads. *medRxiv*.

GUO, H. J. & TADI, P. 2022. Biochemistry, Ubiquitination. *StatPearls [Internet].* StatPearls Publishing.

GUO, K., MOU, X., HUANG, J., XIONG, N. & LI, H. 2014. Trans-caryophyllene suppresses hypoxia-induced neuroinflammatory responses by inhibiting NF-κB activation in microglia. *Journal of molecular neuroscience,* 54**,** 41-48.

HACHINSKI, V., POTTER, P. & MERSKEY, H. 1986. Leuko-araiosis: an ancient term for a new problem. *Canadian Journal of Neurological Sciences,* 13**,** 533-534.

HAMILTON, L., ASTELL, K. R., VELIKOVA, G. & SIEGER, D. 2016. A zebrafish live imaging model reveals differential responses of microglia toward glioblastoma cells in vivo. *Zebrafish,* 13**,** 523-534.

HAMILTON, N., RUTHERFORD, H. A., PETTS, J. J., ISLES, H. M., WEBER, T., HENNEKE, M., GÄRTNER, J., DUNNING, M. J. & RENSHAW, S. A. 2020. The failure of microglia to digest developmental apoptotic cells contributes to the pathology of RNASET2-deficient leukoencephalopathy. *Glia,* 68**,** 1531-1545.

HANPUDE, P., BHATTACHARYA, S., DEY, A. K. & MAITI, T. K. 2015. Deubiquitinating enzymes in cellular signaling and disease regulation. *IUBMB life,* 67**,** 544-555.

HARRIS, A. L. J. N. R. C. 2002. Hypoxia—a key regulatory factor in tumour growth. 2**,** 38.

HARRY, G. J. J. P. & THERAPEUTICS 2013. Microglia during development and aging. 139**,** 313-326.

HASE, Y., HORSBURGH, K., IHARA, M. & KALARIA, R. N. J. J. O. N. 2018. White matter degeneration in vascular and other ageing-related dementias. 144**,** 617-633.

HASEGAWA, T., HALL, C. J., CROSIER, P. S., ABE, G., KAWAKAMI, K., KUDO, A. & KAWAKAMI, A. 2017. Transient inflammatory response mediated by interleukin-1β is required for proper regeneration in zebrafish fin fold. *Elife,* 6.

HASHEMIAGHDAM, A. & MROCZEK, M. 2020. Microglia heterogeneity and neurodegeneration: The emerging paradigm of the role of immunity in Alzheimer's disease. *Journal of neuroimmunology,* 341**,** 577185.

HE, H., LI, R., CHEN, Y., PAN, P., TONG, W., DONG, X., CHEN, Y. AND YU, D. 2017. Integrated DNA and RNA extraction using magnetic beads from viral pathogens causing acute respiratory infections. . *Scientific reports***,** 1-8.

HE, Y., GAO, Y., ZHANG, Q., ZHOU, G., CAO, F. & YAO, S. 2020. IL-4 switches microglia/macrophage M1/M2 polarization and alleviates neurological damage by modulating the JAK1/STAT6 pathway following ICH. *Neuroscience,* 437**,** 161-171.

HE, Y., HUA, Y., KEEP, R. F., LIU, W., WANG, M. M. & XI, G. 2011. Hemoglobin expression in neurons and glia after intracerebral hemorrhage. *Intracerebral Hemorrhage Research.* Springer.

HEFENDEHL, J. K., NEHER, J. J., SÜHS, R. B., KOHSAKA, S., SKODRAS, A. & JUCKER, M. 2014. Homeostatic and injury-induced microglia behavior in the aging brain. *Aging cell,* 13**,** 60-69.

HERBOMEL, P., THISSE, B. & THISSE, C. 2001. Zebrafish early macrophages colonize cephalic mesenchyme and developing brain, retina, and epidermis through a M-CSF receptor-dependent invasive process. *Developmental biology,* 238**,** 274-288.

HOPPERTON, K., MOHAMMAD, D., TRÉPANIER, M., GIULIANO, V. & BAZINET, R. 2018. Markers of microglia in post-mortem brain samples from patients with Alzheimer's disease: a systematic review. *Molecular psychiatry,* 23**,** 177-198.

HORSBURGH, K., WARDLAW, J. M., VAN AGTMAEL, T., ALLAN, S. M., ASHFORD, M. L., BATH, P. M., BROWN, R., BERWICK, J., CADER, M. Z. & CARARE, R. O. J. C. S. 2018. Small vessels, dementia and chronic diseases–molecular mechanisms and pathophysiology. 132**,** 851-868.

HOWE, K., CLARK, M. D., TORROJA, C. F., TORRANCE, J., BERTHELOT, C., MUFFATO, M., COLLINS, J. E., HUMPHRAY, S., MCLAREN, K. & MATTHEWS, L. J. N. 2013. The zebrafish reference genome sequence and its relationship to the human genome. 496**,** 498.

HRDLICKOVA, R., TOLOUE, M. & TIAN, B. 2017. RNA-Seq methods for transcriptome analysis. *Wiley Interdisciplinary Reviews: RNA,* 8**,** e1364.

HU, H.-Y. 2012. protein ubiquitination and deubiquitination. *Current Protein and Peptide Science,* 13**,** 413-413.

HU, H.-Y., OU, Y.-N., SHEN, X.-N., QU, Y., MA, Y.-H., WANG, Z.-T., DONG, Q., TAN, L. & YU, J.-T. 2021. White matter hyperintensities and risks of cognitive impairment and dementia: a systematic review and meta-analysis of 36 prospective studies. *Neuroscience & Biobehavioral Reviews,* 120**,** 16-27.

HUANG, J., FRIEDLAND, R. & AUCHUS, A. 2007. Diffusion tensor imaging of normal-appearing white matter in mild cognitive impairment and early Alzheimer disease: preliminary evidence of axonal degeneration in the temporal lobe. *American journal of neuroradiology,* 28**,** 1943-1948.

HUMBERT-CLAUDE, M., DUC, D., DWIR, D., THIEREN, L., SANDSTRÖM VON TOBEL, J., BEGKA, C., LEGUEUX, F., VELIN, D., MAILLARD, M. & DO, K. 2016. Tollip, an early regulator of the acute inflammatory response in the substantia nigra. *Journal of neuroinflammation,* 13**,** 1-15.

JALAL, F. Y., YANG, Y., THOMPSON, J. F., ROITBAK, T. & ROSENBERG, G. A. 2015. Hypoxia-induced neuroinflammatory white-matter injury reduced by minocycline in SHR/SP. *Journal of Cerebral Blood Flow & Metabolism,* 35**,** 1145-1153.

JEMIELITA, M., TAORMINA, M. J., DELAURIER, A., KIMMEL, C. B. & PARTHASARATHY, R. 2013. Comparing phototoxicity during the development of a zebrafish craniofacial bone using confocal and light sheet fluorescence microscopy techniques. *Journal of biophotonics,* 6**,** 920-928.

JEWKES, R., SIKWEYIYA, Y., MORRELL, R. & DUNKLE, K. 2011. Gender inequitable masculinity and sexual entitlement in rape perpetration South Africa: findings of a cross-sectional study. *PloS one,* 6**,** e29590.

JI, X., WANG, M., LI, L., CHEN, F., ZHANG, Y., LI, Q. & ZHOU, J. 2017. The impact of repeated freeze–thaw cycles on the quality of biomolecules in four different tissues. *Biopreservation and biobanking,* 15**,** 475-483.

JIAO, C., GAO, F., OU, L., YU, J., LI, M., WEI, P. & MIU, F. 2018. Tetrahydroxystilbene glycoside antagonizes β-amyloid-induced inflammatory injury in microglia cells by regulating PU. 1 expression. *Neuroreport,* 29**,** 787.

JOHNSTON, N. L., CEREVNAK, J., SHORE, A. D., TORREY, E. F., YOLKEN, R. H. & CONSORTIUM, S. N. 1997. Multivariate analysis of RNA levels from postmortem human brains as measured by three different methods of RT-PCR. *Journal of neuroscience methods,* 77**,** 83-92.

KAELIN JR, W. G. J. N. R. C. 2008. The von Hippel–Lindau tumour suppressor protein: O 2 sensing and cancer. 8**,** 865.

KALARIA, R. N. 2018. The pathology and pathophysiology of vascular dementia. *Neuropharmacology,* 134**,** 226-239.

KALARIA, R. N., AKINYEMI, R. & IHARA, M. 2016. Stroke injury, cognitive impairment and vascular dementia. *Biochimica et Biophysica Acta (BBA)-Molecular Basis of Disease,* 1862**,** 915-925.

KANAGARAJ, P., CHEN, J. Y., SKAGGS, K., QADEER, Y., CONNER, M., CUTLER, N., RICHMOND, J., KOMMIDI, V., POLES, A. & AFFRUNTI, D. 2020. Microglia stimulate zebrafish brain repair via a specific inflammatory cascade. *BioRXiv*.

KARLSSON, J., VON HOFSTEN, J. & OLSSON, P.-E. 2001. Generating transparent zebrafish: a refined method to improve detection of gene expression during embryonic development. *Marine biotechnology,* 3**,** 522-527.

KARVE, I. P., TAYLOR, J. M. & CRACK, P. J. 2016. The contribution of astrocytes and microglia to traumatic brain injury. *British journal of pharmacology,* 173**,** 692-702.

KAUFMANN, A., MICKOLEIT, M., WEBER, M. & HUISKEN, J. 2012. Multilayer mounting enables long-term imaging of zebrafish development in a light sheet microscope. *Development,* 139**,** 3242-3247.

KIERNAN, E. A., SMITH, S. M., MITCHELL, G. S. & WATTERS, J. J. 2016. Mechanisms of microglial activation in models of inflammation and hypoxia: Implications for chronic intermittent hypoxia. *The Journal of physiology,* 594**,** 1563-1577.

KIM, T., LIM, C.-S. & KAANG, B.-K. 2015. Cell type-specific gene expression profiling in brain tissue: comparison between TRAP, LCM and RNA-seq. *BMB reports,* 48**,** 388.

KINGSBURY, A. E., FOSTER, O. J., NISBET, A. P., CAIRNS, N., BRAY, L., EVE, D. J., LEES, A. J. & MARSDEN, C. D. 1995. Tissue pH as an indicator of mRNA preservation in human post-mortem brain. *Molecular brain research,* 28**,** 311-318.

KIRSHNER, H. S. 2012. Memory Loss: A Practical Guide for Clinicians. LWW.

KOBAYASHI, K., HAYASHI, M., NAKANO, H., FUKUTANI, Y., SASAKI, K., SHIMAZAKI, M., KOSHINO, Y. J. N. & NEUROBIOLOGY, A. 2002. Apoptosis of astrocytes with enhanced lysosomal activity and oligodendrocytes in white matter lesions in Alzheimer's disease. 28**,** 238-251.

KOPP, R., SCHWERTE, T. & PELSTER, B. 2005. Cardiac performance in the zebrafish breakdance mutant. *Journal of experimental biology,* 208**,** 2123-2134.

KOUSSOUNADIS, A., LANGDON, S. P., UM, I. H., HARRISON, D. J. & SMITH, V. A. 2015. Relationship between differentially expressed mRNA and mRNA-protein correlations in a xenograft model system. *Scientific reports,* 5**,** 1-9.

KRISTIANSEN, M., GRAVERSEN, J. H., JACOBSEN, C., SONNE, O., HOFFMAN, H.-J., LAW, S. & MOESTRUP, S. K. 2001. Identification of the haemoglobin scavenger receptor. *Nature,* 409**,** 198-201.

KRUG, R. II, Poshusta TL, Skuster KJ, Berg MR, Gardner SL and Clark KJA (2014). *A transgenic zebrafish model for monitoring glucocorticoid receptor activity. Genes Brain Behav,* 13**,** 478-487.

LAFFER, B., BAUER, D., WASMUTH, S., BUSCH, M., JALILVAND, T. V., THANOS, S., MEYER ZU HÖRSTE, G., LOSER, K., LANGMANN, T. & HEILIGENHAUS, A. 2019. Loss of IL-10 promotes differentiation of microglia to a M1 phenotype. *Frontiers in cellular neuroscience,* 13**,** 430.

LAPPIN, T. R. & LEE, F. S. 2019. Update on mutations in the HIF: EPO pathway and their role in erythrocytosis. *Blood reviews,* 37**,** 100590.

LEE, J. J., LEE, E. Y., LEE, S. B., PARK, J. H., KIM, T. H., JEONG, H.-G., KIM, J. H., HAN, J. W. & KIM, K. W. 2015. Impact of White Matter Lesions on Depression in the Patients with Alzheimer's Disease. *Psychiatry Investigation,* 12**,** 516-522.

LEE, S., VIQAR, F., ZIMMERMAN, M. E., NARKHEDE, A., TOSTO, G., BENZINGER, T. L., MARCUS, D. S., FAGAN, A. M., GOATE, A. & FOX, N. C. 2016. White matter hyperintensities are a core feature of Alzheimer's disease: evidence from the dominantly inherited Alzheimer network. *Annals of neurology,* 79**,** 929-939.

LENAHAN, C., HUANG, L., TRAVIS, Z. D. & ZHANG, J. H. 2019. Scavenger Receptor Class B type 1 (SR-B1) and the modifiable risk factors of stroke. *Chinese Neurosurgical Journal,* 5**,** 1-10.

LEWIS, A. & ELKS, P. M. 2019. Hypoxia induces macrophage tnfa expression via cyclooxygenase and prostaglandin E2 in vivo. *Frontiers in immunology***,** 2321.

LEYS, D., PRUVO, J.-P., PARENT, M., VERMERSCH, P., SOETAERT, G., STEINLING, M., DELACOURTE, A., DEFOSSEZ, A., RAPOPORT, A. & CLARISSE, J. 1991. Could Wallerian degeneration contribute to" leuko-araiosis" in subjects free of any vascular disorder? *Journal of Neurology, Neurosurgery & Psychiatry,* 54**,** 46-50.

LI, L., HALABY, M.-J., HAKEM, A., CARDOSO, R., EL GHAMRASNI, S., HARDING, S., CHAN, N., BRISTOW, R., SANCHEZ, O. & DUROCHER, D. 2010. Rnf8 deficiency impairs class switch recombination, spermatogenesis, and genomic integrity and predisposes for cancer. *Journal of Experimental Medicine,* 207**,** 983-997.

LI, S., LIU, W., WANG, J., ZHANG, Y., ZHAO, D., WANG, T. & LI, Y. 2014a. The role of TNF-α, IL-6, IL-10, and GDNF in neuronal apoptosis in neonatal rat with hypoxic-ischemic encephalopathy. *European review for medical and pharmacological sciences,* 18**,** 905-909.

LI, S., TIGHE, S. W., NICOLET, C. M., GROVE, D., LEVY, S., FARMERIE, W., VIALE, A., WRIGHT, C., SCHWEITZER, P. A. & GAO, Y. 2014b. Multi-platform assessment of transcriptome profiling using RNA-seq in the ABRF next-generation sequencing study. *Nature biotechnology,* 32**,** 915-925.

LI, W., LI, X., MA, X., XIAO, W. & ZHANG, J. 2022. Mapping the m1A, m5C, m6A and m7G methylation atlas in zebrafish brain under hypoxic conditions by MeRIP-seq. *BMC genomics,* 23**,** 1-19.

LI, X., GOOBIE, G. C. & ZHANG, Y. 2021. Toll-interacting protein impacts on inflammation, autophagy, and vacuole trafficking in human disease. *Journal of molecular medicine,* 99**,** 21-31.

LIAO, X., MAKRIS, M. & LUO, X. M. 2016. Fluorescence-activated cell sorting for purification of plasmacytoid dendritic cells from the mouse bone marrow. *JoVE (Journal of Visualized Experiments)***,** e54641.

LIESCHKE, G. J. & CURRIE, P. D. J. N. R. G. 2007. Animal models of human disease: zebrafish swim into view. 8**,** 353.

LIM, K.-H., JOO, J.-Y. & BAEK, K.-H. 2020. The potential roles of deubiquitinating enzymes in brain diseases. *Ageing Research Reviews,* 61**,** 101088.

LIN, J., WANG, D., LAN, L. & FAN, Y. J. B. R. I. 2017. Multiple factors involved in the pathogenesis of white matter lesions. 2017.

LIU, C., WANG, D., WU, J., KELLER, J., MA, T. & YU, X. 2013. RNF168 forms a functional complex with RAD6 during the DNA damage response. *Journal of cell science,* 126**,** 2042-2051.

LIU, W., WANG, C.-H., CUI, Y., MO, L.-Q., ZHI, J.-L., SUN, S.-N., WANG, Y.-L., YU, H.-M., ZHAO, C.-M. & FENG, J.-Q. J. N. L. 2006. Inhibition of neuronal nitric oxide synthase antagonizes morphine antinociceptive tolerance by decreasing activation of p38 MAPK in the spinal microglia. 410**,** 174-177.

LIU, X. & QUAN, N. 2018. Microglia and CNS interleukin-1: beyond immunological concepts. *Frontiers in neurology,* 9**,** 8.

LIVAK, K. & SCHMITTGEN, T. 2020. Analysis of relative gene expression data using real-time quantitative PCR and the 2 (-Delta Delta C (T)) method. methods. 25: 402–408. 2001. *View Article: Google Scholar: PubMed/NCBI*.

LONERGAN, W., WHISTLER, T. & VERNON, S. D. 2007. Comparison of target labeling methods for use with Affymetrix GeneChips. *BMC biotechnology,* 7**,** 1-11.

LOONTIENS, S., DEPESTEL, L., VANHAUWAERT, S., DEWYN, G., GISTELINCK, C., VERBOOM, K., VAN LOOCKE, W., MATTHIJSSENS, F., WILLAERT, A. & VANDESOMPELE, J. 2019. Purification of high-quality RNA from a small number of fluorescence activated cell sorted zebrafish cells for RNA sequencing purposes. *BMC genomics,* 20**,** 1-16.

MARGUERAT, S. & BÄHLER, J. 2010. RNA-seq: from technology to biology. *Cellular and molecular life sciences,* 67**,** 569-579.

MASOTTI, A. & PRECKEL, T. 2006. Analysis of small RNAs with the Agilent 2100 Bioanalyzer. *Nature Methods,* 3**,** 658-658.

MATHIAS, J. R., ZHANG, Z., SAXENA, M. T. & MUMM, J. S. 2014. Enhanced cell-specific ablation in zebrafish using a triple mutant of Escherichia coli nitroreductase. *Zebrafish,* 11**,** 85-97.

MATTHEWS, F. E., BRAYNE, C., LOWE, J., MCKEITH, I., WHARTON, S. B. & INCE, P. 2009. Epidemiological pathology of dementia: attributable-risks at death in the Medical Research Council Cognitive Function and Ageing Study. *PLoS medicine,* 6**,** e1000180.

MAURER, K. J. & QUIMBY, F. W. 2015. Animal models in biomedical research. *Laboratory Animal Medicine.* Elsevier.

MAZZOLINI, J., CHIA, K. & SIEGER, D. 2018. Isolation and RNA extraction of neurons, macrophages and microglia from larval zebrafish brains. *JoVE (Journal of Visualized Experiments)***,** e57431.

MAZZOLINI, J., LE CLERC, S., MORISSE, G., COULONGES, C., KUIL, L. E., VAN HAM, T. J., ZAGURY, J. F. & SIEGER, D. 2020. Gene expression profiling reveals a conserved microglia signature in larval zebrafish. *Glia,* 68**,** 298-315.

MAZZOLINI, J., LE CLERC, S., MORISSE, G., COULONGES, C., KUIL, L.E., VAN HAM, T.J., ZAGURY, J.F. AND SIEGER, D. 2020. Gene expression profiling reveals a conserved microglia signature in larval zebrafish. *Glia***,** 298-315.

MCALEESE, K. E., WALKER, L., GRAHAM, S., MOYA, E. L., JOHNSON, M., ERSKINE, D., COLLOBY, S. J., DEY, M., MARTIN-RUIZ, C. & TAYLOR, J.-P. 2017. Parietal white matter lesions in Alzheimer's disease are associated with cortical neurodegenerative pathology, but not with small vessel disease. *Acta neuropathologica,* 134**,** 459-473.

MENG, X., GRÖTSCH, B., LUO, Y., KNAUP, K. X., WIESENER, M. S., CHEN, X.-X., JANTSCH, J., FILLATREAU, S., SCHETT, G. & BOZEC, A. 2018. Hypoxia-inducible factor-1α is a critical transcription factor for IL-10-producing B cells in autoimmune disease. *Nature communications,* 9**,** 1-17.

MICHAUD, M., BALARDY, L., MOULIS, G., GAUDIN, C., PEYROT, C., VELLAS, B., CESARI, M. & NOURHASHEMI, F. J. J. O. T. A. M. D. A. 2013. Proinflammatory cytokines, aging, and age-related diseases. 14**,** 877-882.

MOMMAERTS, K., SANCHEZ, I., BETSOU, F. AND MATHIESON, W. 2015. Replacing β-mercaptoethanol in RNA extractions. . *Analytical biochemistry***,** 51-53.

MOSCOSO, A., REY-BRETAL, D., SILVA-RODRÍGUEZ, J., ALDREY, J. M., CORTES, J., PIAS-PELETEIRO, J., RUIBAL, A., AGUIAR, P. & INITIATIVE, A. S. D. N. 2020. White matter hyperintensities are associated with subthreshold amyloid accumulation. *Neuroimage,* 218**,** 116944.

NELSON, N. J. 2001. Microarrays have arrived: gene expression tool matures. *Journal of the National Cancer Institute,* 93**,** 492-494.

NELSON, P. T., BRAYNE, C., FLANAGAN, M. E., ABNER, E. L., AGRAWAL, S., ATTEMS, J., CASTELLANI, R. J., CORRADA, M. M., CYKOWSKI, M. D. & DI, J. 2022. Frequency of LATE neuropathologic change across the spectrum of Alzheimer's disease neuropathology: combined data from 13 community-based or population-based autopsy cohorts. *Acta neuropathologica,* 144**,** 27-44.

NICHTERWITZ, S., BENITEZ, J. A., HOOGSTRAATEN, R., DENG, Q. & HEDLUND, E. 2018. LCM-Seq: a method for spatial transcriptomic profiling using laser capture microdissection coupled with PolyA-based RNA sequencing. *RNA Detection.* Springer.

NUSSLEIN-VOLHARD, C. & DAHM, R. 2002. *Zebrafish*, Oxford University Press.

O'BRIEN, J., DESMOND, P., AMES, D., SCHWEITZER, I., HARRIGAN, S. & TRESS, B. J. T. B. J. O. P. 1996. A magnetic resonance imaging study of white matter lesions in depression and Alzheimer's disease. 168**,** 477-485.

OGAWA, Y. A. C., J.C. 2021. Partitioning of gene expression among zebrafish photoreceptor subtypes. . *Scientific reports***,** 1-13.

OGRYZKO, N. V., LEWIS, A., WILSON, H. L., MEIJER, A. H., RENSHAW, S. A. & ELKS, P. M. 2019. Hif-1α–induced expression of Il-1β protects against mycobacterial infection in zebrafish. *The Journal of Immunology,* 202**,** 494-502.

OHSAWA, K., IMAI, Y., SASAKI, Y. & KOHSAKA, S. 2004. Microglia/macrophage-specific protein Iba1 binds to fimbrin and enhances its actin-bundling activity. *Journal of neurochemistry,* 88**,** 844-856.

OLAH, M., BIBER, K., VINET, J., WGM BODDEKE, H. J. C. & TARGETS, N. D.-D. 2011. Microglia phenotype diversity. 10**,** 108-118.

OOSTERHOF, N., HOLTMAN, I. R., KUIL, L. E., VAN DER LINDE, H. C., BODDEKE, E. W., EGGEN, B. J. & VAN HAM, T. J. 2017. Identification of a conserved and acute neurodegeneration-specific microglial transcriptome in the zebrafish. *Glia,* 65**,** 138-149.

OUYANG, S., SONG, Y., TIAN, Y., CHEN, Y., YU, X. & WANG, D. 2015. RNF8 deficiency results in neurodegeneration in mice. *Neurobiology of aging,* 36**,** 2850-2860.

OZSOLAK, F. & MILOS, P. M. 2011. RNA sequencing: advances, challenges and opportunities. *Nature reviews genetics,* 12**,** 87-98.

PANAYOTACOPOULOU, M. T., PAPAGEORGIOU, I., PAGIDA, M., KATSOGRIDAKI, A. E., CHRYSANTHOU-PITEROU, M., VALOUS, N. A., HALAMA, N., PATSOURIS, E. & KONSTANTINIDOU, A. E. 2022. Microglia Activation in the Midbrain of the Human Neonate: The Effect of Perinatal Hypoxic-Ischemic Injury. *Journal of Neuropathology & Experimental Neurology,* 81**,** 208-224.

PANTONI, L. 2010. Cerebral small vessel disease: from pathogenesis and clinical characteristics to therapeutic challenges. *The Lancet Neurology,* 9**,** 689-701.

PARAKALAN, R., JIANG, B., NIMMI, B., JANANI, M., JAYAPAL, M., LU, J., TAY, S. S., LING, E.-A. & DHEEN, S. T. 2012. Transcriptome analysis of amoeboid and ramified microglia isolated from the corpus callosum of rat brain. *BMC neuroscience,* 13**,** 1-20.

PARK, S. Y., LEE, H., HUR, J., KIM, S. Y., KIM, H., PARK, J.-H., CHA, S., KANG, S. S., CHO, G. J. & CHOI, W. S. 2002. Hypoxia induces nitric oxide production in mouse microglia via p38 mitogen-activated protein kinase pathway. *Molecular brain research,* 107**,** 9-16.

PAUDEL, Y. N., KUMARI, Y., ABIDIN, S. A. Z., OTHMAN, I. & SHAIKH, M. F. 2020. Pilocarpine induced behavioral and biochemical alterations in chronic seizure-like condition in adult zebrafish. *International journal of molecular sciences,* 21**,** 2492.

PEARSON, W. R. 2013. An introduction to sequence similarity ("homology") searching. *Current protocols in bioinformatics,* 42**,** 3.1. 1-3.1. 8.

PEFEROEN, L. A., VOGEL, D. Y., UMMENTHUM, K., BREUR, M., HEIJNEN, P. D., GERRITSEN, W. H., PEFEROEN-BAERT, R. M., VAN DER VALK, P., DIJKSTRA, C. D. & AMOR, S. 2015. Activation status of human microglia is dependent on lesion formation stage and remyelination in multiple sclerosis. *Journal of Neuropathology & Experimental Neurology,* 74**,** 48-63.

PERNECZKY, R., TENE, O., ATTEMS, J., GIANNAKOPOULOS, P., IKRAM, M. A., FEDERICO, A., SARAZIN, M. & MIDDLETON, L. T. J. B. M. 2016. Is the time ripe for new diagnostic criteria of cognitive impairment due to cerebrovascular disease? Consensus report of the International Congress on Vascular Dementia working group. 14**,** 162.

PERRY, V. H. & HOLMES, C. J. N. R. N. 2014. Microglial priming in neurodegenerative disease. 10**,** 217.

PETERSON, S. M. A. F., J.L. 2009. RNA isolation from embryonic zebrafish and cDNA synthesis for gene expression analysis. *JoVE (Journal of Visualized Experiments)***,** 1470.

PISOSCHI, A. M. & POP, A. J. E. J. O. M. C. 2015. The role of antioxidants in the chemistry of oxidative stress: A review. 97**,** 55-74.

PONTÉN, F., JIRSTRÖM, K. & UHLEN, M. 2008. The Human Protein Atlas—a tool for pathology. *The Journal of Pathology: A Journal of the Pathological Society of Great Britain and Ireland,* 216**,** 387-393.

POTTER, A. S., DRAKE, K., BRUNSKILL, E.W. AND POTTER, S.S. 2019. A bigenic mouse model of FSGS reveals perturbed pathways in podocytes, mesangial cells and endothelial cells. . *PloS one***,** 0216261.

POTTER, G. M., DOUBAL, F. N., JACKSON, C. A., SUDLOW, C. L., DENNIS, M. S. & WARDLAW, J. M. 2012. Lack of association of white matter lesions with ipsilateral carotid artery stenosis. *Cerebrovascular diseases,* 33**,** 378-384.

PRASAD, S., KATTA, M. R., ABHISHEK, S., SRIDHAR, R., VALISEKKA, S. S., HAMEED, M., KAUR, J. & WALIA, N. 2022. Recent advances in Lewy body dementia: A comprehensive review. *Disease-a-Month***,** 101441.

PRINS, N. D. & SCHELTENS, P. 2015. White matter hyperintensities, cognitive impairment and dementia: an update. *Nature Reviews Neurology,* 11**,** 157.

PRINS, N. D., VAN DIJK, E. J., DEN HEIJER, T., VERMEER, S. E., KOUDSTAAL, P. J., OUDKERK, M., HOFMAN, A. & BRETELER, M. M. 2004. Cerebral white matter lesions and the risk of dementia. *Archives of neurology,* 61**,** 1531-1534.

QIU, S., LUO, S., EVGRAFOV, O., LI, R., SCHROTH, G. P., LEVITT, P., KNOWLES, J. A. & WANG, K. 2012. Single-neuron RNA-Seq: technical feasibility and reproducibility. *Frontiers in genetics,* 3**,** 124.

RAMAKRISHNAN, S. K., SHAH, Y. M. J. N. & AGING, H. 2017. A central role for hypoxia-inducible factor (HIF)-2α in hepatic glucose homeostasis. 4**,** 207-216.

RANSOHOFF, R. M. 2016. A polarizing question: do M1 and M2 microglia exist? *Nature neuroscience,* 19**,** 987-991.

RAO, M. S., VAN VLEET, T. R., CIURLIONIS, R., BUCK, W. R., MITTELSTADT, S. W., BLOMME, E. A. & LIGUORI, M. J. 2019. Comparison of RNA-Seq and microarray gene expression platforms for the toxicogenomic evaluation of liver from short-term rat toxicity studies. *Frontiers in genetics,* 9**,** 636.

RASTOGI, A., WEISSERT, R. & BHASKAR, S. M. M. 2021. Emerging role of white matter lesions in cerebrovascular disease. *European Journal of Neuroscience,* 54**,** 5531-5559.

ROHAN WALKER, F., NILSSON, M. & JONES, K. J. C. D. T. 2013. Acute and chronic stress-induced disturbances of microglial plasticity, phenotype and function. 14**,** 1262-1276.

ROSARIO, B. L., ROSSO, A. L., AIZENSTEIN, H. J., HARRIS, T., NEWMAN, A. B., SATTERFIELD, S., STUDENSKI, S. A., YAFFE, K., ROSANO, C. & STUDY, H. A. 2016. Cerebral white matter and slow gait: contribution of hyperintensities and normal-appearing parenchyma. *The Journals of Gerontology: Series A,* 71**,** 968-973.

ROSENTAL, B., KOZHEKBAEVA, Z., FERNHOFF, N., TSAI, J.M. AND TRAYLOR-KNOWLES, N. 2017. Coral cell separation and isolation by fluorescence-activated cell sorting (FACS). *BMC cell biology,* 18(1)**,** 1-12.

ROYLE, C., LIM, S., XU, B., TOOHER, J., OGLE, R. & HENNESSY, A. 2009. Effect of hypoxia and exogenous IL-10 on the pro-inflammatory cytokine TNF-α and the anti-angiogenic molecule soluble Flt-1 in placental villous explants. *Cytokine,* 47**,** 56-60.

SACHIN, P., GADANI, S., CRONK, J., NORRIS, G. & KIPNIS, J. 2012. Interleukin-4: a cytokine to remember. *J Immunol,* 189**,** 4213-4421.

SADRZADEH, S. H. & BOZORGMEHR, J. 2004. Haptoglobin phenotypes in health and disorders. *Pathology Patterns Reviews,* 121**,** S97-S104.

SAFAIYAN, S., KANNAIYAN, N., SNAIDERO, N., BRIOSCHI, S., BIBER, K., YONA, S., EDINGER, A. L., JUNG, S., ROSSNER, M. J. & SIMONS, M. 2016. Age-related myelin degradation burdens the clearance function of microglia during aging. *Nature neuroscience,* 19**,** 995-998.

SAHATHEVAN, R., BRODTMANN, A. & DONNAN, G. A. J. I. J. O. S. 2012. Dementia, stroke, and vascular risk factors; a review. 7**,** 61-73.

SANTHAKUMAR, K., JUDSON, E. C., ELKS, P. M., MCKEE, S., ELWORTHY, S., VAN ROOIJEN, E., WALMSLEY, S. S., RENSHAW, S. A., CROSS, S. S. & VAN EEDEN, F. J. 2012. A zebrafish model

to study and therapeutically manipulate hypoxia signaling in tumorigenesis. *Cancer research*.

SATOH, J. I. 2018. Gene expression profiles of M1 and M2 microglia characterized by comparative analysis of public datasets. *Clinical and Experimental Neuroimmunology,* 9**,** 124-138.

SCHAAF, M., CHATZOPOULOU, A. & SPAINK, H. 2009. The zebrafish as a model system for glucocorticoid receptor research. *Comparative Biochemistry and Physiology Part A: Molecular & Integrative Physiology,* 153**,** 75-82.

SCHACHTELE, S. J., HU, S., SHENG, W. S., MUTNAL, M. B. & LOKENSGARD, J. R. 2014. Glial cells suppress postencephalitic CD8+ T lymphocytes through PD-L1. *Glia,* 62**,** 1582-1594.

SCHELTENS, P., BARKHOF, F., LEYS, D., PRUVO, J. P., NAUTA, J., VERMERSCH, P., STEINLING, M. & VALK, J. 1993. A semiquantative rating scale for the assessment of signal hyperintensities on magnetic resonance imaging. *Journal of the neurological sciences,* 114**,** 7-12.

SCHMIDT, R., SCHMIDT, H., HAYBAECK, J., LOITFELDER, M., WEIS, S., CAVALIERI, M., SEILER, S., ENZINGER, C., ROPELE, S. & ERKINJUNTTI, T. J. A. N. 2011. Heterogeneity in age-related white matter changes. 122**,** 171-185.

SCHUIERER, S., CARBONE, W., KNEHR, J., PETITJEAN, V., FERNANDEZ, A., SULTAN, M. & ROMA, G. 2017. A comprehensive assessment of RNA-seq protocols for degraded and low-quantity samples. *BMC genomics,* 18**,** 1-13.

SCHURCH, N. J., SCHOFIELD, P., GIERLIŃSKI, M., COLE, C., SHERSTNEV, A., SINGH, V., WROBEL, N., GHARBI, K., SIMPSON, G. G. & OWEN-HUGHES, T. 2016. How many biological replicates are needed in an RNA-seq experiment and which differential expression tool should you use? *Rna,* 22**,** 839-851.

SCHWARTZ, M., BUTOVSKY, O., BRÜCK, W. & HANISCH, U.-K. J. T. I. N. 2006. Microglial phenotype: is the commitment reversible? 29**,** 68-74.

SHATYA, A., BRIDGES, L., WILLIAMS, R., TRIPPIER, S., ZHANG, L., PEREIRA, A. C., NICOLL, J., BOCHE, D. & HAINSWORTH, A. 2021. Innate immune anti-inflammatory response in human spontaneous intracerebral haemorrhage. *Stroke***,** 3613-3623.

SHI, H., ZHOU, Y., JIA, E., PAN, M., BAI, Y. & GE, Q. 2021. Bias in RNA-seq library preparation: current challenges and solutions. *BioMed research international,* 2021.

SIEGER, D. & PERI, F. 2013. Animal models for studying microglia: the first, the popular, and the new. *Glia,* 61**,** 3-9.

SIGURGEIRSSON, B., EMANUELSSON, O. & LUNDEBERG, J. 2014. Sequencing degraded RNA addressed by 3'tag counting. *PloS one,* 9**,** e91851.

SIMPSON, J., INCE, P., HIGHAM, C., GELSTHORPE, C., FERNANDO, M., MATTHEWS, F., FORSTER, G., O'BRIEN, J., BARBER, R., KALARIA, R. J. N. & NEUROBIOLOGY, A. 2007. Microglial activation in white matter lesions and nonlesional white matter of ageing brains. 33**,** 670-683.

SIMPSON, J. E., HOSNY, O., WHARTON, S. B., HEATH, P. R., HOLDEN, H., FERNANDO, M. S., MATTHEWS, F., FORSTER, G., O'BRIEN, J. T. & BARBER, R. J. S. 2009. Microarray RNA expression analysis of cerebral white matter lesions reveals changes in multiple functional pathways. 40**,** 369-375.

SIMPSON, J. E., INCE, P. G., SHAW, P. J., HEATH, P. R., RAMAN, R., GARWOOD, C. J., GELSTHORPE, C., BAXTER, L., FORSTER, G. & MATTHEWS, F. E. 2011. Microarray analysis of the astrocyte transcriptome in the aging brain: relationship to Alzheimer's pathology and APOE genotype. *Neurobiology of aging,* 32**,** 1795-1807.

SONOHARA, K., KOZAKI, K., AKISHITA, M., NAGAI, K., HASEGAWA, H., KUZUYA, M., YOKOTE, K. & TOBA, K. 2008. White matter lesions as a feature of cognitive impairment, low vitality and

other symptoms of geriatric syndrome in the elderly. *Geriatrics & gerontology international,* 8**,** 93-100.

SOSA, S. M. & SMITH, K. J. 2017. Understanding a role for hypoxia in lesion formation and location in the deep and periventricular white matter in small vessel disease and multiple sclerosis. *Clinical Science,* 131**,** 2503-2524.

SRIRAM, K. & O'CALLAGHAN, J. P. 2007. Divergent roles for tumor necrosis factor-α in the brain. *Journal of Neuroimmune Pharmacology,* 2**,** 140-153.

STREIT, W. J., BRAAK, H., XUE, Q.-S. & BECHMANN, I. J. A. N. 2009. Dystrophic (senescent) rather than activated microglial cells are associated with tau pathology and likely precede neurodegeneration in Alzheimer's disease. 118**,** 475-485.

STROHL, K. 2007. Genetic Factors In The Acute Response To Hypoxia In Animals Models.

SUEMOTO, C. K., NITRINI, R., GRINBERG, L. T., FERRETTI, R. E., FARFEL, J. M., LEITE, R. E., MENEZES, P. R., FREGNI, F., JACOB-FILHO, W. & PASQUALUCCI, C. A. 2011. Atherosclerosis and dementia: a cross-sectional study with pathological analysis of the carotid arteries. *Stroke,* 42**,** 3614-3615.

SUN, C., MITCHELL, D. M. & STENKAMP, D. L. 2018. Isolation of photoreceptors from mature, developing, and regenerated zebrafish retinas, and of microglia/macrophages from regenerating zebrafish retinas. *Experimental eye research,* 177**,** 130-144.

SVAHN, A. J., GRAEBER, M. B., ELLETT, F., LIESCHKE, G. J., RINKWITZ, S., BENNETT, M. R. & BECKER, T. S. 2013. Development of ramified microglia from early macrophages in the zebrafish optic tectum. *Developmental neurobiology,* 73**,** 60-71.

T O'BRIEN, J. & THOMAS, A. J. T. L. 2015. Vascular dementia. 386**,** 1698-1706.

TAKASE, H., LOK, J. & ARAI, K. J. N. R. R. 2018. A radical scavenger edaravone and oligodendrocyte protection/regeneration. 13**,** 1550.

TANG, Y. & LE, W. J. M. N. 2016. Differential roles of M1 and M2 microglia in neurodegenerative diseases. 53**,** 1181-1194.

TOMIMOTO, H., IHARA, M., WAKITA, H., OHTANI, R., LIN, J.-X., AKIGUCHI, I., KINOSHITA, M. & SHIBASAKI, H. 2003. Chronic cerebral hypoperfusion induces white matter lesions and loss of oligodendroglia with DNA fragmentation in the rat. *Acta neuropathologica,* 106**,** 527-534.

TOPAKIAN, R., BARRICK, T., HOWE, F. & MARKUS, H. 2010. Blood–brain barrier permeability is increased in normal-appearing white matter in patients with lacunar stroke and leucoaraiosis. *Journal of Neurology, Neurosurgery & Psychiatry,* 81**,** 192-197.

TSAROUCHAS, T. M., WEHNER, D., CAVONE, L., MUNIR, T., KEATINGE, M., LAMBERTUS, M., UNDERHILL, A., BARRETT, T., KASSAPIS, E. & OGRYZKO, N. 2018. Dynamic control of proinflammatory cytokines Il-1β and Tnf-α by macrophages in zebrafish spinal cord regeneration. *Nature communications,* 9**,** 1-17.

TSINKALOVSKY, O., ROSENLUND, B., LAERUM, O.D. AND EIKEN, H.G. 2005. Clock gene expression in purified mouse hematopoietic stem cells. . *Experimental hematology***,** 100-107.

UENO, M., TOMIMOTO, H., AKIGUCHI, I., WAKITA, H., SAKAMOTO, H. J. J. O. C. B. F. & METABOLISM 2002. Blood–brain barrier disruption in white matter lesions in a rat model of chronic cerebral hypoperfusion. 22**,** 97-104.

UZUN, S., KOZUMPLIK, O. & FOLNEGOVIĆ-ŠMALC, V. J. C. A. 2011. Alzheimer's dementia: current data review. 35**,** 1333-1337.

VAN DIJK, E. J., PRINS, N. D., VROOMAN, H. A., HOFMAN, A., KOUDSTAAL, P. J. & BRETELER, M. M. 2008. Progression of cerebral small vessel disease in relation to risk factors and cognitive consequences: Rotterdam Scan study. *Stroke,* 39**,** 2712-2719.

VAN ROOIJEN, E., SANTHAKUMAR, K., LOGISTER, I., VOEST, E., SCHULTE-MERKER, S., GILES, R. & VAN EEDEN, F. 2011. A zebrafish model for VHL and hypoxia signaling. *Methods in cell biology*. Elsevier.

VAN ROOIJEN, E., VOEST, E. E., LOGISTER, I., KORVING, J., SCHWERTE, T., SCHULTE-MERKER, S., GILES, R. H. & VAN EEDEN, F. J. 2009. Zebrafish mutants in the von Hippel-Lindau tumor suppressor display a hypoxic response and recapitulate key aspects of Chuvash polycythemia. *Blood, The Journal of the American Society of Hematology,* 113**,** 6449-6460.

VAR, S. R. & BYRD-JACOBS, C. A. 2020. Role of macrophages and microglia in zebrafish regeneration. *International Journal of Molecular Sciences,* 21**,** 4768.

VENKAT, P., CHOPP, M. & CHEN, J. 2015. Models and mechanisms of vascular dementia. *Experimental neurology,* 272**,** 97-108.

VERHAAREN, B. F., VERNOOIJ, M. W., DE BOER, R., HOFMAN, A., NIESSEN, W. J., VAN DER LUGT, A. & IKRAM, M. A. 2013. High blood pressure and cerebral white matter lesion progression in the general population. *Hypertension,* 61**,** 1354-1359.

VERKHRATSKY, A. & BUTT, A. 2013. Neuroglia: definition, classification, evolution, numbers, development. Glial physiology and pathophysiology. Wiley, New York.

VESELÝ, B., ANTONINI, A. & REKTOR, I. 2016. The contribution of white matter lesions to Parkinson's disease motor and gait symptoms: a critical review of the literature. *Journal of Neural Transmission,* 123**,** 241-250.

VETTORI, A., GREENALD, D., WILSON, G. K., PERON, M., FACCHINELLO, N., MARKHAM, E., SINNAKARUPPAN, M., MATTHEWS, L. C., MCKEATING, J. A. & ARGENTON, F. 2017. Glucocorticoids promote Von Hippel lindau degradation and Hif-1α stabilization. *Proceedings of the National Academy of Sciences,* 114**,** 9948-9953.

VILLAMOR, E., KESSELS, C. G., RUIJTENBEEK, K., VAN SUYLEN, R. J., BELIK, J., DE MEY, J. G. & BLANCO, C. E. 2004. Chronic in ovo hypoxia decreases pulmonary arterial contractile reactivity and induces biventricular cardiac enlargement in the chicken embryo. *American Journal of Physiology-Regulatory, Integrative and Comparative Physiology,* 287**,** R642-R651.

VOIGT, A. P., MULLIN, N.K., WHITMORE, S.S., DELUCA, A.P., BURNIGHT, E.R., LIU, X., TUCKER, B.A., SCHEETZ, T.E., STONE, E.M. AND MULLINS, R.F. 2021. Human photoreceptor cells from different macular subregions have distinct transcriptional profiles. . *Human molecular genetics***,** 1543-1558.

VON BERNHARDI, R. 2007. Glial cell dysregulation: a new perspective on Alzheimer disease. *Neurotoxicity research,* 12**,** 215-232.

WAHLUND, L. O. & BRONGE, L. 2000. Contrast-enhanced MRI of White Matter Lesions in Patients with Blood-Brain Barrier Dysfunction. *Annals of the New York Academy of Sciences,* 903**,** 477-481.

WAISMAN, A., GINHOUX, F., GRETER, M. & BRUTTGER, J. 2015. Homeostasis of microglia in the adult brain: review of novel microglia depletion systems. *Trends in immunology,* 36**,** 625-636.

WALI, N., MERTEROGLU, M., WHITE, R. J. & BUSCH-NENTWICH, E. M. 2022. Total nucleic acid extraction from single zebrafish embryos for genotyping and RNA-seq. *Bio-protocol,* 12**,** e4284-e4284.

WALLER, R., BAXTER, L., FILLINGHAM, D. J., COELHO, S., POZO, J. M., MOZUMDER, M., FRANGI, A. F., INCE, P. G., SIMPSON, J. E. & HIGHLEY, J. R. 2019. Iba-1-/CD68+ microglia are a prominent feature of age-associated deep subcortical white matter lesions. *PLoS One,* 14**,** e0210888.

WALLER, R., WOODROOFE, M. N., FRANCESE, S., HEATH, P., WHARTON, S., INCE, P., SHARRACK, B. & SIMPSON, J. 2012. Isolation of enriched glial populations from post-mortem human CNS material by immuno-laser capture microdissection. *Journal of neuroscience methods,* 208**,** 108-113.

WANG, J. & CAO, H. 2021. Zebrafish and medaka: important animal models for human neurodegenerative diseases. *International Journal of Molecular Sciences,* 22**,** 10766.

WANG, J., HOU, J., ZHAO, H. & LIU, J. 2015. Synergistic use of geniposide and ginsenoside Rg1 balance microglial TNF-α and TGF-β1 following oxygen-glucose deprivation in vitro: a genome-wide survey. *Evidence-based complementary and alternative medicine: eCAM,* 2015.

WANG, X., LI, C., CHEN, Y., HAO, Y., ZHOU, W., CHEN, C. & YU, Z. 2008. Hypoxia enhances CXCR4 expression favoring microglia migration via HIF-1α activation. *Biochemical and biophysical research communications,* 371**,** 283-288.

WANG, X. & LIN, Y. 2008. Tumor necrosis factor and cancer, buddies or foes? 1. *Acta Pharmacologica Sinica,* 29**,** 1275-1288.

WANG, Y., MASHOCK, M., TONG, Z., MU, X., CHEN, H., ZHOU, X., ZHANG, H., ZHAO, G., LIU, B. & LI, X. 2020. Changing technologies of RNA sequencing and their applications in clinical oncology. *Frontiers in Oncology,* 10**,** 447.

WANG, Z., GERSTEIN, M. & SNYDER, M. 2009. RNA-Seq: a revolutionary tool for transcriptomics. *Nature reviews genetics,* 10**,** 57-63.

WARDLAW, J. M., SMITH, C. & DICHGANS, M. 2013. Mechanisms of sporadic cerebral small vessel disease: insights from neuroimaging. *The Lancet Neurology,* 12**,** 483-497.

WASHIDA, K., HATTORI, Y. & IHARA, M. 2019. Animal models of chronic cerebral hypoperfusion: from mouse to primate. *International Journal of Molecular Sciences,* 20**,** 6176.

WEIDEMANN, A., JOHNSON, R. J. C. D. & DIFFERENTIATION 2008. Biology of HIF-1α. 15**,** 621.

WELLER, R. O., HAWKES, C. A., KALARIA, R. N., WERRING, D. J. & CARARE, R. O. J. B. P. 2015. White matter changes in dementia: role of impaired drainage of interstitial fluid. 25**,** 63-78.

WHARTON, S. B., BRAYNE, C., SAVVA, G. M., MATTHEWS, F. E., FORSTER, G., SIMPSON, J., LACE, G. & INCE, P. G. 2011. Epidemiological neuropathology: the MRC cognitive function and aging study experience. *Journal of Alzheimer's Disease,* 25**,** 359-372.

WHARTON, S. B., SIMPSON, J. E., BRAYNE, C. & INCE, P. G. J. B. P. 2015. Age-Associated White Matter Lesions: The MRC C ognitive F unction and A geing S tudy. 25**,** 35-43.

WHO. 2022. *Dementia* [Online]. Available: https://www.who.int/news-room/fact-sheets/detail/dementia [Accessed 17 November 2022].

WILKINSON, K. & EL KHOURY, J. 2012. Microglial scavenger receptors and their roles in the pathogenesis of Alzheimer's disease. *International journal of Alzheimer's disease,* 2012.

WINEBERG, Y., BAR-LEV, T.H., FUTORIAN, A., BEN-HAIM, N., ARMON, L., ICKOWICZ, D., ORIEL, S., BUCRIS, E., YEHUDA, Y., PODE-SHAKKED, N. AND GILAD, S. 2020. Single-cell RNA sequencing reveals mRNA splice isoform switching during kidney development. *Journal of the American Society of Nephrology,* 31(10)**,** 2278-2291.

WINKLER, E. A., SAGARE, A. P. & ZLOKOVIC, B. V. J. B. P. 2014. The Pericyte: A Forgotten Cell Type with Important Implications for A lzheimer's Disease? 24**,** 371-386.

WON, Y. H., LEE, M.-Y., CHOI, Y.-C., HA, Y., KIM, H., KIM, D.-Y., KIM, M.-S., YU, J. H., SEO, J. H. & KIM, M. 2016. Elucidation of relevant neuroinflammation mechanisms using gene expression profiling in patients with amyotrophic lateral sclerosis. *PloS one,* 11**,** e0165290.

WONG, S. M., JANSEN, J. F., ZHANG, C. E., HOFF, E. I., STAALS, J., VAN OOSTENBRUGGE, R. J. & BACKES, W. H. 2019. Blood-brain barrier impairment and hypoperfusion are linked in cerebral small vessel disease. *Neurology,* 92**,** e1669-e1677.

WU, C., BENDRIEM, R. M., GARAMSZEGI, S. P., SONG, L. & LEE, C. T. 2017. RNA sequencing in post-mortem human brains of neuropsychiatric disorders. *Psychiatry and clinical neurosciences,* 71**,** 663-672.

WU, W.-K., LLEWELLYN, O. P., BATES, D. O., NICHOLSON, L. B. & DICK, A. D. 2010. IL-10 regulation of macrophage VEGF production is dependent on macrophage polarisation and hypoxia. *Immunobiology,* 215**,** 796-803.

XIE, W.-J., YU, H.-Q., ZHANG, Y., LIU, Q. & MENG, H.-M. 2016. CD163 promotes hematoma absorption and improves neurological functions in patients with intracerebral hemorrhage. *Neural Regeneration Research,* 11**,** 1122.

XIONG, B., YANG, Y., FINEIS, F. R. & WANG, J.-P. 2019. DegNorm: normalization of generalized transcript degradation improves accuracy in RNA-seq analysis. *Genome biology,* 20**,** 1-18.

XIONG, Y. Y. & MOK, V. J. J. O. A. R. 2011. Age-related white matter changes. 2011.

XU, J., WANG, T., WU, Y., JIN, W. & WEN, Z. 2016. Microglia colonization of developing zebrafish midbrain is promoted by apoptotic neuron and lysophosphatidylcholine. *Developmental cell,* 38**,** 214-222.

YAMADA, H., MARUO, R., WATANABE, M., HIDAKA, Y., IWATANI, Y. AND TAKANO, T. 2010. Messenger RNA quantification after fluorescence activated cell sorting using intracellular antigens. . *Biochemical and biophysical research communications* 425-428.

YAMADA, Y., HAMAKUBO, T. & KODAMA, T. 1998. Scavenger receptor family proteins: roles for atherosclerosis, host defence and disorders of the central nervous system. *Cellular and Molecular Life Sciences CMLS,* 54**,** 628-640.

YANG, F., GHIO, A. J., HERBERT, D. C., WEAKER, F. J., WALTER, C. A. & COALSON, J. J. 2000. Pulmonary expression of the human haptoglobin gene. *American journal of respiratory cell and molecular biology,* 23**,** 277-282.

YANG, G.-F., ZHANG, X., SU, Y.-G., ZHAO, R. & WANG, Y.-Y. 2021. The role of the deubiquitinating enzyme DUB3/USP17 in cancer: a narrative review. *Cancer Cell International,* 21**,** 1-11.

YANG, J., KIM, S. M., KIM, Y.-J., CHEON, S. Y., KIM, B., JUNG, K. C. & PARK, K. S. 2016. Accuracy of the fluorescence-activated cell sorting assay for the aquaporin-4 antibody (AQP4-Ab): comparison with the commercial AQP4-Ab assay kit. *PLoS One,* 11**,** e0162900.

YANG, Y., KIMURA-OHBA, S., THOMPSON, J. F., SALAYANDIA, V. M., COSSÉ, M., RAZ, L., JALAL, F. Y. & ROSENBERG, G. A. 2018. Vascular tight junction disruption and angiogenesis in spontaneously hypertensive rat with neuroinflammatory white matter injury. *Neurobiology of disease,* 114**,** 95-110.

YEE, W., KUMAR, J.N. AND MUTHUSAMY, P.D. 2018. Inclusion of 2-Mercaptoethanol in Lysis Buffer Could Interfere with Isolation of High Molecular Weight DNA from Freshwater Microalgae. *Indian journal of microbiology,* 58(1)**,** 109-113.

YI, S., JIANG, X., TANG, X., LI, Y., XIAO, C., ZHANG, J. & ZHOU, T. 2020. IL-4 and IL-10 promotes phagocytic activity of microglia by up-regulation of TREM2. *Cytotechnology,* 72**,** 589-602.

YOUSAF, T., DERVENOULAS, G., VALKIMADI, P.-E. & POLITIS, M. J. J. O. N. 2018. Neuroimaging in Lewy body dementia.

YU, X., GUO, C., FISHER, P. B., SUBJECK, J. R. & WANG, X.-Y. 2015. Scavenger receptors: emerging roles in cancer biology and immunology. *Advances in cancer research,* 128**,** 309-364.

ZAJICEK, A. & YAO, W.-D. 2021. Remodeling without destruction: non-proteolytic ubiquitin chains in neural function and brain disorders. *Molecular Psychiatry,* 26**,** 247-264.

ZHANG, D., TANG, J., ZHANG, J. & HU, C. X. 2019a. Responses of pro-and anti-inflammatory cytokines in zebrafish liver exposed to sublethal doses of Aphanizomenon flosaquae DC-1 aphantoxins. *Aquatic Toxicology,* 215**,** 105269.

ZHANG, F., ZHONG, R., LI, S., FU, Z., CHENG, C., CAI, H. & LE, W. 2017. Acute hypoxia induced an imbalanced M1/M2 activation of microglia through NF-κB signaling in Alzheimer's disease mice and wild-type littermates. *Frontiers in aging neuroscience,* 9**,** 282.

ZHANG, P., YAO, Q., LU, L., LI, Y., CHEN, P.-J. & DUAN, C. 2014. Hypoxia-inducible factor 3 is an oxygen-dependent transcription activator and regulates a distinct transcriptional response to hypoxia. *Cell reports,* 6**,** 1110-1121.

ZHANG, Y., PAN, N., SHENG, Y., ZHOU, M., WEN, Z., CHEN, Y., HUANG, F. & WANG, L.-X. 2019b. Hypoxia enhances IL-10-producing B cell generation through upregulating high-mobility group B1 on tumor cell-released autophagosomes. *Immunology letters,* 216**,** 36-42.

ZHAO, Y., KE, Z., HE, W. & CAI, Z. 2019. Volume of white matter hyperintensities increases with blood pressure in patients with hypertension. *Journal of International Medical Research,* 47**,** 3681-3689.

ZHAO, Z., NELSON, A. R., BETSHOLTZ, C. & ZLOKOVIC, B. V. 2015. Establishment and dysfunction of the blood-brain barrier. *Cell,* 163**,** 1064-1078.

ZHENG, Q., HUANG, T., ZHANG, L., ZHOU, Y., LUO, H., XU, H. & WANG, X. 2016. Dysregulation of ubiquitin-proteasome system in neurodegenerative diseases. *Frontiers in aging neuroscience,* 8**,** 303.

ZHU, L., LIU, X., NEMETH, D. P., DISABATO, D. J., WITCHER, K. G., MCKIM, D. B., OLIVER, B., LE, X., GORANTLA, G. & BERDYSZ, O. 2019. Interleukin-1 causes CNS inflammatory cytokine expression via endothelia-microglia bi-cellular signaling. *Brain, behavior, and immunity,* 81**,** 292-304.

ZHU, X., LI, J., YOU, D., XIAO, Y., HUANG, Z. & YU, W. 2022. Neuroprotective Effect of E3 Ubiquitin Ligase RNF8 Against Ischemic Stroke via HDAC2 Stability Reduction and Reelin-Dependent GSK3β Inhibition. *Molecular Neurobiology***,** 1-15.

ZWEMER, L. M., HUI, L., WICK, H. C. & BIANCHI, D. W. 2014. RNA-Seq and expression microarray highlight different aspects of the fetal amniotic fluid transcriptome. *Prenatal diagnosis,* 34**,** 1006-1014.